University of Southampton

Faculty of Engineering and the Environment
Institute of Sound and Vibration Research

A new framework for estimating noise impact of novel aircraft

by

Athanasios Synodinos

Thesis for the degree of Doctor of Philosophy

July 2017

Abstract

Air traffic demand is forecast to significantly grow during the next few years. To compensate for the associated potential increase of aviation environmental impact, ambitious aircraft noise and emissions reduction goals have been set by several organisations worldwide. Accommodating these goals requires planning new mitigation strategies involving technological advances, optimised flight operations, and novel aircraft concepts. Methods for predicting the impact of potential mitigation strategies is vital to support effective planning.

This thesis presents a new framework for estimating the noise impact of mitigation strategies (i.e. involving each or both of technological and operational changes) aspiring to: a) bypass the dependance on empirical flyover data and hence enable impact assessment of novel aircraft and operations, b) be independent of specific noise prediction methods and confidential inputs that are normally required by many noise prediction tools, c) have low computational requirements and thus be efficient in parametric studies, and d) provide inputs to emissions prediction tools, facilitating a more holistic strategic mitigation that considers various environmental concerns.

The crux of the framework developed is that rather than seeking absolute noise values, it computationally estimates the noise impact of mitigation strategies, starting from a baseline scenario for which noise levels are known. This eliminates the need for measurements whilst minimising complexity and dependance on confidential inputs. Noise and emissions interdependencies are incorporated by expressing noise changes as a function of thrust, which is a common influencing parameter. In addition, the framework provides means for deriving purely computational NPD curves, enabling the construction of noise exposure contour maps for future aircraft and contemporary operations.

The framework's applicability on innovative flight operations and its capability of including the interdependencies between noise and emissions is demonstrated by estimating the environmentally-optimum approach and takeoff angles for civil aircraft of different sizes. The applicability to novel aircraft is displayed through noise estimations (including noise exposure contours) for various electric aircraft featuring Distributed Electric Propulsion (DEP), as well as for a Blended-Wing-Body (BWB) aircraft.

The results obtained for future scenarios generally conform with the expected trends (deriving from e.g. higher-fidelity tools or historical trends) highlighting the framework's great potential and usefulness in contributing in effective planning and decision-making.

Contents

List of Figures

List of Tables

Declaration of Authorship

I, Athanasios Synodinos , declare that the thesis entitled *A new framework for estimating noise impact of novel aircraft* and the work presented in the thesis are both my own, and have been generated by me as the result of my own original research. I confirm that:

- this work was done wholly or mainly while in candidature for a research degree at this University;
- where any part of this thesis has previously been submitted for a degree or any other qualification at this University or any other institution, this has been clearly stated;
- where I have consulted the published work of others, this is always clearly attributed;
- where I have quoted from the work of others, the source is always given. With the exception of such quotations, this thesis is entirely my own work;
- I have acknowledged all main sources of help;
- where the thesis is based on work done by myself jointly with others, I have made clear exactly what was done by others and what I have contributed myself;
- parts of this work have been published as:
  - Synodinos, P. A., Self, R.H. and Torija, A.J., ‘Framework for predicting Noise-Power-Distance curves for novel aircraft designs’, Journal of Aircraft, (published online ahead of print 31 August 2017), doi: 10.2514/1.C034466
  - Barrett, S. R.H., Dray, L.M., Doyme, K., Gnadt, A., Schfer, A.W., Self, R.H., O’Sullivan, A., Synodinos, P. A., Torija, A.J., and Al’Zayat, K., ‘Electric aircraft - A potential solution for reducing aviation emissions?’, Submitted to Nature, 2017
  - Synodinos, P. A., Self, R.H. and Torija, A.J., ‘Noise assessment of aircraft with distributed electric propulsion using a new noise estimation framework’, Proceedings of the 24th International Congress on Sound and Vibration (ICSV), London, UK, 24 - 27 July 2017

  - Synodinos, P. A., Self, R.H. and Torija, A.J., ‘A new method for estimating community noise changes due to aircraft technology variations’, Proceedings of the 23rd International Congress on Sound and Vibration (ICSV), Athens, Greece, 10 - 14 July 2016
  - Synodinos, P. A., Self, R.H., Flindell, Ian, and Torija, A.J., ‘Estimating variation in community noise due to variation in aircraft operations’, Proceedings of the 10th European Congress and Exposition on Noise Control Engineering (EURONOISE), Maastricht, NL 31 May - 3 Jun 2015

Signed:..

Date:.........31 July 2017...

Acknowledgements

Despite working in the rail industry, I have always been devoted to music and sound, fascinated by aircraft, and intimately attracted by research. I would like to thank ISVR for giving me the marvellous opportunity to do a PhD in aircraft acoustics.

I feel grateful for every single second of this amazing, challenging and rewarding adventure in my late thirties. Daydreamers never learn.

In particular, I would like to express my deepest gratitude toward my supervisors, Dr. Rod Self and Dr. Antonio Torija, most importantly for their honest feedback and support, as well as for the inspiring discussions and scientific debates. Also, I would like to thank my internal examiners Dr. Alan McAlpine and Prof. David Thompson for providing their encouraging feedback halfway through this journey, as well as my external examiner Dr. Luca Benassi who turned my viva into an unforgettable and electrifying experience. It is my honour having my work read by the three of you.

Also: Thank you my dear colleagues, my lovely friends, for your great company, stirring support and uplifting conversations, as well as for sharing your knowledge with me. You are always welcome in my place in Greece!

Special thanks to music, coffee and Dale Cooper, special thanks to the woods, the rain and the walls.

I would also like to thank my charming family for always being there for me. Thank you for everything. Thanks to my friends for supporting me throughout the years.

Last but not least, I would like to thank my partner, Aliki, for being a fabulous human being, an inspiring teacher and psychologist, as well as a great artist. Thank you my dear for explaining all that noise to me.

Every day, once a day, give yourself a present. Don't plan it. Don't wait for it. Just let it happen. It could be a new shirt at the men's store, a catnap in your office chair, or two cups of good, hot black coffee.

Nomenclature

Abbreviations

A320	Airbus A320
A380	Airbus A380
ACARE	Advisory Council For Aeronautics Research In Europe
ANIS	Aircraft Noise Index Study
APM	Aircraft Performance Model
APU	Auxiliary Power Unit
AR	Aspect Ratio
ATM	Air Traffic Management
BADA	Base Of Aircraft Data
BLI	Boundary Layer Ingestion
BPR	Bypass Ratio
BWB	Blended-Wing-Body
CAA	Civil Aviation Authority
CCD	Cruise And Descent Cycle
CCO	Continuous Climb Operations
CDA	Continuous Descent Approach
CFM	Cfm International
CG	Centre Of Gravity
CO	Carbon Monoxide
CO_2	Carbon Dioxide
CP	Certification Point
DEFRA	Department For Environment, Food And Rural Affairs
DEP	Distributed Electric Propulsion
DP	Distributed Propulsion
DSP	Digital Signal Processing
e-A320	Concept Electric A320
EASA	European Aviation Safety Agency
ECAC	European Civil Aviation Conference
EEA	European Environment Agency
EEC	Eurocontrol Experimental Centre
EI	Emission Index
EIS	Entry Into Service
EPNL	Effective Perceived Noise Level

Symbols

A	Area
B	Constant
c	Speed of sound
C	Constant
C_D	Drag Coefficient
C_L	Lift Coefficient
c_p	Specific heat
D	Directivity
e	Batteries specific energy
e_i	Component i polytropic efficiency
$\dot{E}_k$	Kinetic Energy
E_p	Mass of gaseous pollutant p
f	Frequency
F	Force
F_∞	Rated thrust
f_b	Blade-passing frequency
f_d	Fan diameter
F_G	Gross thrust
F_N	Net thrust
h	Altitude
I	Acoustic intensity
k	Wave number
$\mathrm{L}_{A,max}$	Maximum A-weighted level
L_p	Sound Pressure Level, dB
L_w	Sound Power Level, dB
$\mathrm{L}_{eq,T}$	Equivalent continuous sound level
ℓ	Length of Engine/Propulsor
$\dot{m}$	Mass flow rate
M	Mach number
$\dot{m}_f$	Fuel flow rate
m	Mass
m_f	Mass of fuel burned
$\overline{m_m}$	Average a/c mass in cruise
n	Number of samples
N	Number of propulsors

FAA	Federal Aviation Authority
FAR	Federal Aviation Regulations
GE	General Electric
GTP	Global Temperature Change Potential
H_2O	Water Vapour
HC	Hydrocarbons
IAE	International Aero Engines
ICAO	International Civil Aviation Organisation
ISO	International Standards Organization
L/D	Lift-To-Drag Ratio
LAQ	Local Air Quality
LPR	Low Pressure Rotor
LTO	Landing And Take-Off Cycle
MLW	Maximum Landing Weight
MTOM	Maximum Takeoff Mass
MTOW	Maximum Takeoff Weight
NA	Number Above
NNI	Noise And Number Index
NOx	Nitrogen Oxides
NPD	Noise-Power-Distance
OASPL	Overall Sound Pressure Level
OEW	Overall Empty Weight
P & W	Pratt & Whitney
Pax	Passengers
PNL	Perceived Noise Level
PNLT	Tone Corrected Perceived Noise Level
PWL	Sound Power Level
QC	Quota Count
RF	Radiative Forcing
RFI	Radiative Forcing Index
RR	Rolls-Royce
SA	Sustainable Aviation
SEL	Sound Exposure Level
SFC	Specific Fuel Consumption
SOx	Oxides Of Sulfur
SPL	Sound Pressure Level
STOL	Short Takeoff And Landing
TA	Time Above
TeDP	Turboelectric Distributed Propulsion
VOC	Volatile Organic Compound

$N1$	LPR speed
p	Sound pressure
P	Pressure
p_{ref}	Reference effective acoustic pressure
p_{rms}	Effective (root-mean-square) pressure
$\mathcal{P}$	Propability
R	Distance source to receiver
Re	Reynolds number
RH	Relative humidity
t	Time
T	Time period; event duration
$T_{t,x}$	Stagnation temperature at location x
T_x	Temperature at location x
u	Particle speed
V_0	Flight Velocity (Airspeed)
V_j	Exhaust (jet) velocity
W	Acoustic power, Weight
x	Longitudinal distance
y	Lateral distance
z	Vertical distance; Flight altitude
Z	Number of blades

Greek Letters

α	Acceleration, Angle of Attack
γ	Heat capacity
δ_f	Flap deflection angle
$\Delta\tau$	Delay between signals
Δt	Time increment
η	Efficiency
θ	Polar angle
κ	Flight track specifier
μ	Bypass ratio
π_x	Pressure ratio across component x
ρ	Gas density
τ_x	Temperature ratio across component x
ϕ	Azimuthal angle
φ	Phase
ω	Angular frequency

Chapter 1

Introduction

Forecasts from global air transport stakeholders, such as leading manufacturers (Airbus [1], Boeing [2]), agencies (EASA [3], ICAO [4]), as well as government departments like the UK's Department for Transport (DfT) [5], anticipate that air traffic will significantly grow over the next few years. To compensate for the associated potential increase of aviation environmental impact [6, 7] ambitious interim-to-long term noise and emissions reduction goals have been elaborated by several organisations worldwide, such as ACARE [8, 9, 10] and NASA [11]. To illustrate the trends, Figure 1.1 shows the expected growth in air travel demand, as predicted by the UK DfT [5], along with the challenging targets for aviation set by ACARE for the year 2050, as published in their 'Flightpath 2050' document [8]. NASA technology goals for their N+3 timeframe (year 2030) are equally aggressive, aiming at reducing CO_2 by more than 70%, NO_x by more than 75% and certification cumulative noise (defined in Section 2.1.6) by 71 EPNdB, relative to the performance of year 2000 civil aircraft [11].

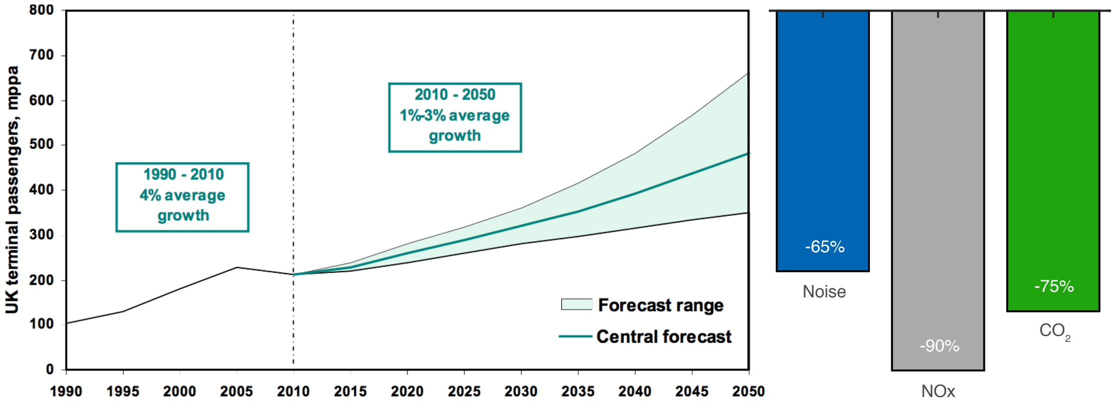

Figure 1.1: UK's DfT forecast of passenger numbers [5] and ACARE Flightpath 2050 objectives relative to the performance of year 2000 civil aircraft.

Delivering these demanding environmental goals requires developing radical mitigation strategies for civil aviation, including technological breakthroughs and design of novel aircraft able to perform innovative operations. A worth mentioning joint technology initiative aiming at developing and demonstrating innovative civil aviation technologies is Clean Sky 2 [12, 13] that involves Europe's aeronautics industrial leaders and public research organisations. A similar, UK based initiative is Greener by Design [14], which is formed by the Royal Aeronautical Society. In any case, it is clear that methods for predicting the corresponding outcomes of mitigation strategies, i.e. which technological and operational changes are likely to achieve the highest reduction of environmental impact around airports, are needed to support effective planning and decision making, under a wider Strategic Environmental Assessment (SEA) process.

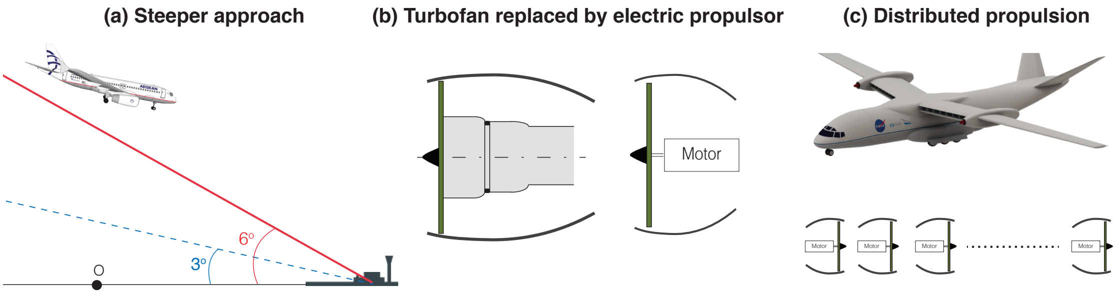
(a) Steeper approach (b) Turbofan replaced by electric propulsor (c) Distributed propulsion

Figure 1.2: Sketches of potential noise mitigation strategies.

Figure 1.2 shows one operational (the steeper descent) and two technological potential mitigation strategies. Current noise prediction tools would normally assess the noise impact of mitigation strategies by calculating absolute aircraft noise values, using either experimentally obtained (i.e. measured) data, typically Noise-Power-Distance (NPD) databases, or high-fidelity mathematical models. Prediction tools relying on measurements, like FAA's INM [15], are impractical in assessing the impact of future aircraft designs and contemporary operations; for example, although measurements are costly, they could be conducted, if needed, for the steeper descent; yet, it is impossible to obtain experimental data for non-existing concepts like cases (b) and (c) of Figure 1.2. Likewise, mathematical tools, such as ANOPP [16], attempt to simulate the complex aircraft noise generation and propagation mechanisms and typically require many inputs, some of which are proprietary to manufacturers; for instance, manufacturers of future electric propulsors may be reluctant in sharing their designs data. This poses limitations in the accuracy of mathematical tools, despite their fidelity level.

Normally, mitigation strategies have a simultaneous impact on noise and emissions, as illustrated in the sketch of Figure 1.3. An additional concern of existing aviation impact prediction tools, is that they often tend to focus on noise abatement and hence overlook the interdependencies between noise and other environmental concerns, like emissions [17]. Technology has reached a point where trade-offs between aircraft noise and fuel consumption (and thus, emissions) are inevitable, posing severe challenges to decision-makers on aircraft design and ATM. Cumpsty [18] and Hall [19] portray this interdependence conflict using the Airbus A380 engine case, where the fan diameter was

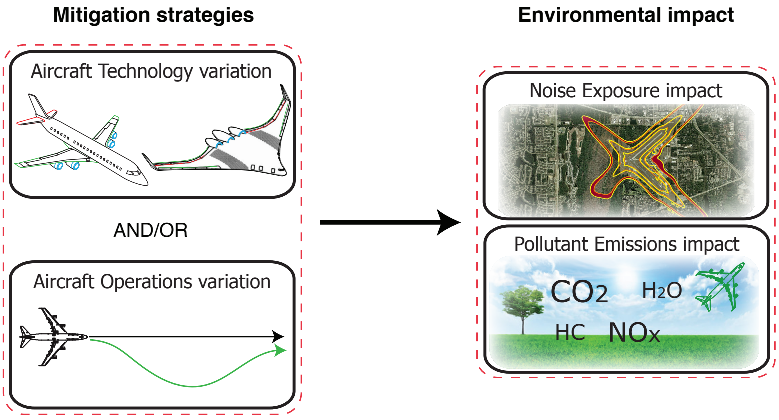

Figure 1.3: Measures for aviation have a twofold environmental impact.

increased to meet noise regulations, incurring fuel burn efficiency losses. Indeed, such conflicts may be further complicated because of the ambiguity in comparing the units of noise and emissions and explaining them in monetary or perceptual terms. For example, the noise level reduction resulting from a generous fuel burn efficiency sacrifice may be extremely costly or non-perceptible. Analogous difficulties emerge at ATM level; noise optimised trajectories may be inefficient in terms of emissions, due to longer flight times and/or increased fuel consumption.

1.1 Research aims

The research described in this thesis aims to develop a simplified framework for estimating the noise impact of aviation mitigation strategies (i.e. technological and/or operational changes), with the following features:

- Be able to give fast answers in order to quickly assess potential mitigation strategies, facilitate parametric studies and support the decision-making process.
- Allow integration with other aviation tools (e.g. emissions tools), in order to facilitate a holistic approach to environmental impact assessment that will include the interdependencies between noise and other environmental concerns, like emissions.
- Allow predicting or estimating the impact of introducing novel aircraft concepts and contemporary operations, bypassing the need for measurements, complex simulations and dependance on manufacturer's proprietary inputs and detailed source models (i.e. essentially rely on public domain information and data).

In accordance with ICAO's balanced approach to noise management [20], the latest roadmap of Sustainable Aviation (SA) [21] splits mitigation strategies into five categories: 1) land use planning, 2) community engagement, 3) operational restrictions,

4) adoption of new technologies and 5) Air Traffic Management (ATM) improvements. The proposed framework focuses on the two last mentioned, that refer to technological evolution (e.g. advances in engine design and performance, novel aircraft concepts) and modified airport operations (e.g. reshaped takeoff and approach flight profiles) respectively.

Figure 1.4 illustrates the perspective that leads to achieving the aims of this thesis. The underlying concept of the proposed noise estimation framework is rooted in the fact that a scenario (e.g. a mitigation measure) is assessed by determining noise variations with respect to a 'baseline' scenario, where the noise levels are known, or otherwise estimated. In other words the new framework has a comparative nature, where only the impact of a mitigation measure is sought and hence, any parameters defining absolute noise values become excessive, significantly reducing the amount of inputs required and hence dependance on confidential data. So as a simple example, the impact of a steeper descent is assessed based on the already measured noise levels of the conventional approach. This only requires the noise difference due to the steeper descent configuration (extended flaps etc.) to be calculated, as will be shown in the case study in Section 8.1 that investigates the environmental impact of steeper operations. Also, in order to support efforts to raise awareness of the interdependencies between noise and emissions and including the associated implications in decision making, the framework relates the estimated noise changes with thrust variations that are directly linked with fuel consumption and hence variation of CO_2 and NO_x emissions.

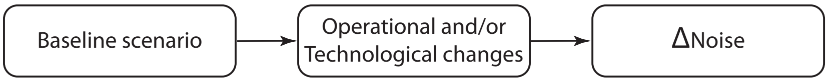

Figure 1.4: Main concept of the proposed noise estimation framework.

1.2 List of original contributions

The main contributions to knowledge are outlined below.

- A new framework was developed for estimating aircraft noise variation due to technological and operational changes, that can be adapted to differing levels of input data and required outputs.
- The framework was adapted for computational development of NPD curves, which allows to construct noise exposure contour maps around airports for novel aircraft and unconventional flight operations, and hence trace the associated noise impact.
- The noise impact of novel Blended-Wing-Body (BWB) aircraft and of various electric aircraft concepts was estimated. A parametric study was carried out seeking

the noise-optimum number of electric propulsors on Distributed Electric Propulsion (DEP) aircraft. Noise exposure contour maps were constructed for these future aircraft designs.

- The impacts of noise and emissions were linked through a common influencing parameter (thrust), aiming at facilitating the consideration of their interdependencies in decision making.
- A parametric study was undertaken investigating the environmentally-optimum (in terms of both noise and emissions) takeoff and approach slopes for aircraft of different sizes.
- The framework was adapted for estimating the individual noise source levels of existing aircraft, enabling parametric studies on individual sources.

1.3 List of publications

- Synodinos, P. A., Self, R.H. and Torija, A.J., 'Framework for predicting Noise-Power-Distance curves for novel aircraft designs', Journal of Aircraft, (published online ahead of print 31 August 2017), doi: 10.2514/1.C034466
- Barrett, S. R.H., Dray, L.M., Doyme, K., Gnadt, A., Schfer, A.W., Self, R.H., O'Sullivan, A., Synodinos, P. A., Torija, A.J., and Al'Zayat, K., 'Electric aircraft - A potential solution for reducing aviation emissions?', Submitted to Nature, 2017
- Synodinos, P. A., Self, R.H. and Torija, A.J., 'Noise assessment of aircraft with distributed electric propulsion using a new noise estimation framework', Proceedings of the 24th International Congress on Sound and Vibration (ICSV), London, UK, 24 - 27 July 2017
- Synodinos, P. A., Self, R.H. and Torija, A.J., 'A new method for estimating community noise changes due to aircraft technology variations', Proceedings of the 23rd International Congress on Sound and Vibration (ICSV), Athens, Greece, 10 - 14 July 2016
- Synodinos, P. A., Self, R.H., Flindell, Ian, and Torija, A.J., 'Estimating variation in community noise due to variation in aircraft operations', Proceedings of the 10th European Congress and Exposition on Noise Control Engineering (EURONOISE), Maastricht, NL 31 May - 3 Jun 2015

1.4 Thesis structure

Chapter 2 presents the theory behind the present research. Basic aircraft noise definitions are given followed by a description of the universally established noise and emissions metrics for aviation and the associated regulations, certification standards and abatement procedures. The last Sections of the Chapter look at aircraft aerodynamics and outline the standard procedure for calculating performance parameters and flight profiles that are directly linked with the environmental impacts of aircraft activity.

Chapter 3 reviews prominent existing aviation noise and emissions assessment tools. Also described are prevailing methods for predicting noise from individual aircraft noise sources. Such methods comprise an indispensable element of the proposed noise estimation framework.

Chapter 4 is devoted to historical trends of aviation that are extremely useful for approximating or forecasting some inputs to the proposed framework. Also presented in this Chapter are the expected noise benefits from specific imminent and future technological advances (e.g. nacelle acoustic liners) and innovative operations (e.g. the Continuous Descent Approach (CDA)).

Chapter 5 demonstrates the core methodology of the proposed noise estimation framework and explains the procedure for deriving purely computationally NPD curves. Also presented is an interdependencies matrix based on which thrust is used as the suitable parameter for linking the impacts of noise and emissions.

Chapter 6 presents two supplementary elements that constitute one way for calculating or estimating inputs to the framework presented in this thesis. These are the custom aircraft noise prediction tool, FANjET, along with a turbofan engine thermodynamic analysis.

Chapter 7 validates the proposed framework by comparing estimated NPD curves for existing aircraft to the published ones. The last part of the Chapter presents an error analysis indicating the framework's potential sources of error and discussing its limitations.

Chapter 8 presents the framework's functionality in innovative operational mitigation strategies by appraising the environmentally optimum descent and takeoff slopes for civil aircraft of different sizes. The effect of the interdependencies between noise and emissions is depicted by plotting both quantities concurrently.

Chapter 9 demonstrates the applicability of the framework to future aircraft concepts by estimating the noise impact of novel BWB and electric aircraft, while seeking the optimal number of electric propulsors on DEP systems. The Chapter also includes a detailed procedure for estimating the thrust requirements of the various electric aircraft configurations examined, since these requirements mainly determine the propulsive aircraft noise.

Chapter 10 presents the conclusions drawn from this research and discusses ways for extending the work undertaken in this thesis.

Chapter 2

Aviation and the Environment

This chapter gives the theoretical background behind this research. Basic noise definitions are first outlined, followed by an identification of aircraft noise sources and a description of the noise metrics for single aircraft events and fleets. Aircraft emission types and metrics are then reviewed, whereas the regulatory framework for aircraft noise and emissions is also presented. The last sections of this chapter discuss aircraft performance topics that are essential for estimating thrust requirements of an aircraft for a given operational procedure. Thrust (or engine power setting) is a parameter that relates to both noise and emissions and therefore is greatly involved in the methodology (Chapter 5) and the case studies (Chapters 7–9) of this thesis.

2.1 Aircraft noise

2.1.1 Noise definitions

The definitions presented in this section are based mainly on the textbooks from Kinsler [22], Bies [23] and Pierce [24]. The noise at distance R from a noise source that radiates acoustic power, W, is quantified with the acoustic intensity, I, which is the rate of acoustic energy flow through a unit area [22]. As distance increases, energy spreads over greater areas and hence intensity decreases. Spreading of sound energy from typical noise sources (and most aircraft noise sources, as discussed later) is not uniform in all directions. Thus, in the far field[1], intensity in a direction (θ, ϕ) is shaped by the noise source's directional sound radiation properties that are described by a directivity factor, D [23], so that

$$I(\theta, \phi) = \frac{W}{4\pi R^2} D(\theta, \phi)\,. \tag{2.1}$$

---

[1] The near field of a source is associated with complicated patterns of local pressure maxima and minima [23]. Thus, it is practically impossible to characterise it using just a specific function of directivity.

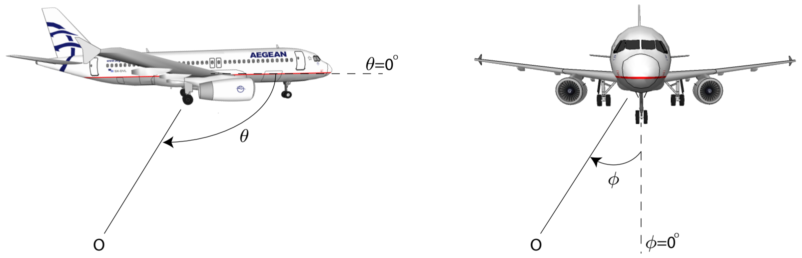

Figure 2.1: Illustration of polar and azimuthal angles.

The directivity factor, which is expressed in terms of the polar and azimuthal directivity angles, as per Figure 2.1, is defined as the ratio of the intensity in direction (θ, ϕ) and the mean intensity [23], which can be seen as the intensity of an omnidirectional source that emits the same acoustic power as the directional source:

$$D(\theta, \phi) = \frac{I(\theta, \phi)}{\bar{I}}\,. \tag{2.2}$$

Acoustic intensity is hard to measure; the easiest acoustic parameter to assess (e.g. with a microphone) is the root-mean-square (or effective) pressure [23], which, in the far-field relates with intensity with [22]:

$$p_{rms}^2 = I\,\rho c\,. \tag{2.3}$$

Due to the enormously wide range of audible pressures and intensities, it is convenient to describe these quantities using a logarithmic scale, named the sound levels [22] that have units of decibel (dB). The sound pressure level (SPL) is given by

$$\mathrm{L}_p(\theta, \phi, R) = 10 \log \frac{p_{rms}^2}{p_{ref}^2} = 10 \log \left[\frac{W D(\theta, \phi)}{R^2} C \right]\,, \tag{2.4}$$

where the reference pressure $p_{ref} = 20\ \mu$Pa represents the threshold of human hearing and constant $C = \rho c / (4 \pi p_{ref}^2)$.

Ignoring any atmospheric absorption effects, equation 2.4 implies that acoustic power variation from W_1 to W_2 induces a SPL change

$$\underset{W_1 \to W_2}{\Delta \mathrm{L}_p} = 10 \log \frac{W_2}{W_1}\,. \tag{2.5}$$

Similarly, a distance change from R_1 to R_2 yields:

$$\underset{R_1 \to R_2}{\Delta \mathrm{L}_p} = -20 \log \frac{R_2}{R_1}\,. \tag{2.6}$$

Equations 2.5, 2.6, show why aircraft noise is mainly an issue at regions around airports. Not only is distance R small at these regions, but also, as explained later, approach and takeoff aircraft configurations are associated with increased sound power W.

Sound power level (PWL) is defined as [23]:

$$\mathrm{L}_w = 10 \log \frac{W}{W_{ref}} \,, \tag{2.7}$$

where the reference power $W_{ref} = 10^{-12}$ Watts. The SPL and PWL are related with

$$\mathrm{L}_w = \mathrm{L}_p(\theta, \phi, R) + 10 \log \frac{R^2}{D(\theta, \phi) C W_{ref}} \,. \tag{2.8}$$

2.1.2 Addition of sources

As mentioned in Chapter 1, aircraft noise is the sum of various noise source contributions. If two noise sources produce pressures $p_1(t)$, $p_2(t)$ at a point in space, the total sound pressure $p_t(t) = p_1(t) + p_2(t)$. The p^2_{rms} term is the time average of $p^2_t(t)$ over a period T:

$$p^2_{rms} = \overline{p^2_t(t)} = \frac{1}{T} \int_0^T [p_1(t) + p_2(t)]^2 \, \mathrm{d}t = \overline{p^2_1} + \overline{p^2_2} + 2\overline{p_1 p_2} \,. \tag{2.9}$$

Incoherent sounds, such as broadband noise components, have randomly interfering wave fronts and it can be presumed that $\overline{p_1 p_2} = 0$ [24]. This reduces Equation (2.9) to $p^2_{rms} = p^2_1 + p^2_2$. So, the total SPL in terms of the SPLs of n incoherent sources is

$$\mathrm{L}_p = 10 \log \left(\sum_{i=1}^{n} 10^{\frac{\mathrm{L}_{p,n}}{10}} \right) \,. \tag{2.10}$$

With W_i being the acoustic power of source i, the total acoustic power produced by the n sources is given by [23]

$$W_{tot} = \sum_{i=1}^{n} W_i \,, \tag{2.11}$$

and the total PWL by

$$\mathrm{L}_w = 10 \log \left(\sum_{i=1}^{n} 10^{\frac{\mathrm{L}_{w,n}}{10}} \right) \,. \tag{2.12}$$

Coherent sounds, such as two identical tones, keep fixed relative phase relationship between them [23]. Thus, combining them creates constructive or destructive interference, depending on their relative phase $\varphi = \omega \Delta\tau$, which is determined by frequency ω and delay $\Delta\tau$ between them. This effect is expressed with a phase term $\cos(\varphi)$, so that

$$p^2_{rms} = p^2_1 + p^2_2 + 2 p_1 p_2 \cos(\varphi) \,. \tag{2.13}$$

If the fan tones from the engines of the aircraft in Figure 2.2 are coherent (which is an unrealistic assumption as discussed in the next paragraph), then delay $\Delta\tau$ can be calculated with:

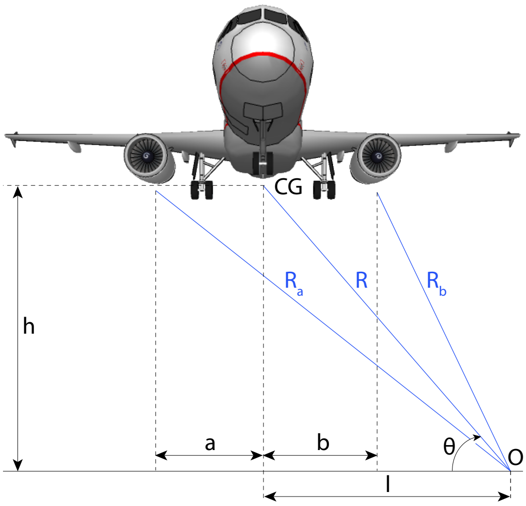

Figure 2.2: Path difference of (hypothetical) coherent aircraft noise sources.

$R_a = \sqrt{h^2 + R_{xya}^2}$ and $R_b = \sqrt{h^2 + R_{xyb}^2}$,

where, based on Figure 6.1:

$$R_{xya} = \begin{cases} \sqrt{y^2 + (l-a)^2} & \text{if } l \geq 0, \\ \sqrt{y^2 + (l+a)^2} & \text{if } l < 0. \end{cases},$$

$$R_{xyb} = \begin{cases} \sqrt{y^2 + (l+b)^2} & \text{if } l \geq 0, \\ \sqrt{y^2 + (l-b)^2} & \text{if } l < 0. \end{cases}$$

which leads to the delay $\Delta\tau = \dfrac{|R_a - R_b|}{c}$.

In principle, noise sources will have random relative phases between them and will therefore be incoherent [23]. In this context, aircraft noise calculation tools (e.g. NASA's ANOPP [16]) and metrics (e.g. $\mathrm{L}_{eq,T}$ in Equation 2.14) assume incoherent aircraft noise sources [25, 26]. It is worth justifying this assumption with the following arguments:

- Tones from multiple engines are practically unlikely to be coherent especially at high polar angles; that would require mechanically and aeroelastically identical blades, behaving in the exact same way under high-speed rotation loads. According to Smith [27] and ESDU [28] this is unlikely to occur in practice.
- Tones of turbine and fans have different frequencies, as implied by Zaporozhets [26] and shown in the estimated sources spectra in Figure 2.14.
- Potential coherent sources due to e.g. reflections experience reduced interference, especially at higher frequencies, due to atmospheric effects and turbulence [29, 26].

2.1.3 Noise propagation

Aircraft noise propagates from high altitudes over long distances before reaching the ground and thus transverses several atmospheric layers with fluctuating properties, such as temperature, relative humidity and density. Wind and turbulence can be seen as additional layers altering the speed of sound. Thus, propagating sound is refracted [23] and depending on the atmospheric properties, sound is strengthened or weakened. Sound is also absorbed by the atmosphere; in fact, atmosphere acts as a low-pass filter, since it more easily attenuates higher frequencies. Moreover, the perceived frequency is shifted due to the Doppler effect (i.e. due to the relative motion between source and receiver)

[24]. Sound ultimately arriving at an observer position has also been influenced by transmission and reflection effects (e.g. due to the ground or structures) and diffraction around structures [22].

These propagation effects are generally described by several models of varying fidelity and degree of accuracy. Models often incorporated in aircraft noise prediction tools are the SAE ARP 866A [30] and Sutherland [31] for atmospheric absorption, and NAU Soroka for ground reflections [26]. The Doppler shift is typically described by a function dependant on relative velocity [22]. One advantage of the proposed noise estimation framework is that it bypasses the need to model atmospheric influence on propagating sound, since it aims at delivering noise changes, rather than absolute noise values. Normally, technological and/or operational variations will be relatively small and hence any changes in propagation effects will be second order.

2.1.4 Aircraft noise metrics

A simple dB scale is insufficient to reflect the perceived noisiness for aircraft flyovers and the resulting annoyance [27]. Thus, various aircraft noise metrics have been developed referring to either a single event or to the cumulative, long-term noise exposure to aircraft noise, in which case they are taken as indicators of residential annoyance [32]. Noise metrics are typically subject to weightings related to human perception of sound, like the A-weighting [33]. Also, human exposure to aircraft noise is portrayed more meaningfully if noise metrics and other indices, such as the number of flights or the amount of people affected, are used conjointly [26]. For example, Clairbois et al.[34] enhanced the outcomes of their airport noise study by incorporating the amount of complaints in their results.

Single event noise metrics

Instantaneous sound level, $\mathrm{L}(t)$, is the sound level at an observer location at time t. The variation of $\mathrm{L}(t)$ with time during an aircraft noise event is termed the event's level time history and is typically described by a Gaussian bell-shaped curve.

Maximum sound level, $\mathrm{L}_{A,max}$, is the maximum, A-weighted instantaneous sound level and has units of dB(A). While it is easily measured and understood by the public, it is less descriptive of the annoyance caused, since it omits the event duration.

Equivalent continuous sound level, $\mathrm{L}_{eq,T}$, is the continuous steady level, which over the same time period T contains equivalent total acoustic energy as the actual fluctuating

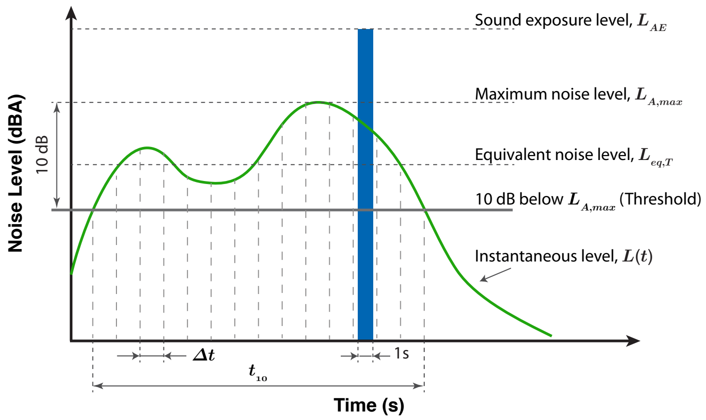

Figure 2.3: Graphic representation of single aircraft noise event metrics

noise [33]. Mathematically, it derives from integrating the time history [32]:

$$\mathrm{L}_{eq,T} = 10\log\frac{1}{T}\int_0^T 10^{\frac{\mathrm{L}(t)}{10}}\,dt = 10\log\left(\frac{1}{T}\sum_{i=1}^{n}10^{\frac{\mathrm{Lp}_i}{10}}\Delta t\right)\,, \tag{2.14}$$

where n and Lp_i are the total number of discrete measurements and associated SPLs.

The sampling interval, Δt, is set according to the event duration. It is apparent that only a portion of an aircraft movement encompass the significant contribution to the total noise exposure at an observer location. Hence, it is common practise to only include that portion in noise calculations. The significant part duration is normally specified by incorporating suitable threshold levels at which the event start/end limits are triggered. A typical threshold level is 10 dB below $\mathrm{L}_{A,max}$ named the 10 dB down-time, t_{10} [32]. Alternatively, an effective duration t_e is used, representing an hypothetical event of constant level containing the same acoustic energy as the event of interest [32]. A third option is to pre-define cut-off levels, such as the commonly used 55 dB(A) [35].

Sound exposure level (SEL), L_{AE}, is similar to $\mathrm{L}_{eq,T}$ but with $T = 1$. Thus, it is the one second long steady level containing equivalent total acoustic energy as the actual fluctuating noise. SEL accounts for both the event's duration and intensity [33].

Cumulative noise metrics

Equivalent sound level, $\mathrm{L}_{eq,T}$, due to N aircraft flyovers over a period T, is given by [33]

$$\mathrm{L}_{eq,T} = \overline{\mathrm{L}}_{AE} + 10\log(N) - 10\log(T)\,, \tag{2.15}$$

where $\overline{\mathrm{L}}_{AE}$ is the average SEL defined as

$$\overline{\mathrm{L}}_{AE} = 10\log\left(\frac{1}{N}\sum_{i=1}^{N}10^{\frac{\mathrm{L}_{AE,i}}{10}}\right)\,, \tag{2.16}$$

where $L_{AE,i}$ is the SEL corresponding to flyover i. Common variations of $L_{eq,T}$, which is globally the most commonly employed aircraft noise exposure metric [32], are: a) L_n that represents exposure due to night events and b) L_{dn} and L_{den} that describe 24-hour exposure by giving specific weighting to night and evening events.

Statistical percentile ratings (L_x) interpret the level exceeded for a specified percentage x% of the measurement time. The level exceeded for 10% of the measurement time, L_{10}, describes the typical high levels of noise events, whereas L_{90} express background noise. Yet, in the UK, L_x is most commonly used to assess road traffic noise exposure [33].

Perceived Noise Level (PNL) is a function of both frequency and level and rates aircraft noise in terms of human perceived noisiness. Perceived noisiness values (in Noys) derive from one-third octave band levels that are measured at suitable time intervals and then appropriately weighted and summed. These values are converted through published tables or contours of perceived noisiness [36] into PNL in PNdB.

Tone corrected PNL (PNLT) incorporates a correction in dB that depends on the tone frequency and the level difference between tonal and broadband content. PNLT embodies the fact that noise containing protrusive tones is often perceived as being more annoying, as the human hearing system tends to focus on tonal sounds [23].

Effective PNL (EPNL) additionally accounts for the duration and bell-shaped time history of an aircraft noise event. It has units of EPNdB and is a common aircraft noise annoyance indicator [37]. The recommended procedure to convert an aircraft noise event SPL time history into EPNL is described in the FAA (FAR) part 36 document [38]. A faster, empirical method to obtain good EPNL estimates is to add 13 dB to $L_{A,max}$ [23].

Noise and Number Index (NNI) is an annoyance indicator that relates the aircraft noise levels with the number of aircraft movements. It is based on studies showing that if noise levels increase, annoyance can remain constant provided that the number of movements decrease [39]. NNI is given by the empirical formula:

$$\mathrm{NNI} = \mathrm{L} + 15\log(N) - 80\,, \tag{2.17}$$

where L is the logarithmic average in PNdB of the peak noise levels for N aircraft movements whose peak noise level exceeds 80 PNdB, over a specific 12 hour period [33].

Number above (NA) is the number of aircraft noise events exceeding a given level of a noise metric. Likewise, Time above (TA) is the total time during which the SPL exceeds a given level. The benefit of these metrics is that they are easier understood by residents.

Health based noise exposure population indicators are proposed by the European Environment Agency (EEA) [40] that involve the total number of inhabitants per dwelling. These indicators consider the whole population rather than only a part of it, in an effort to be more comprehensive than other population indicators, such as the NA and TA.

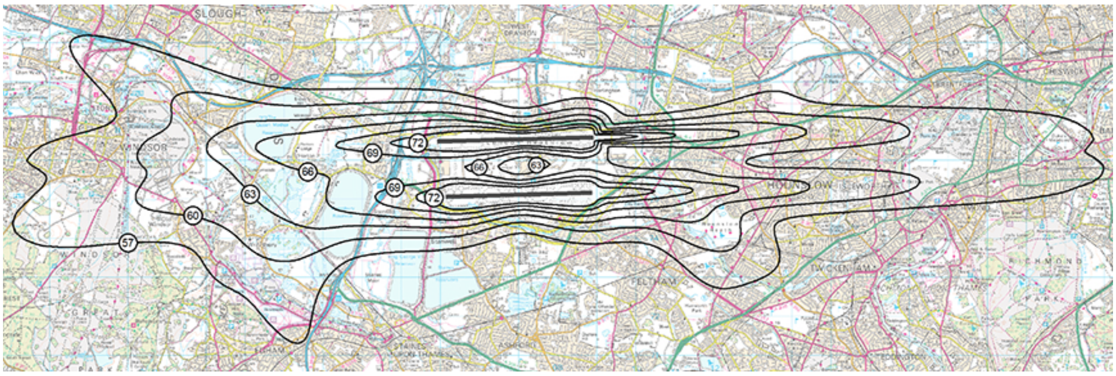

Figure 2.4: London Heathrow $L_{eq,T}$ noise exposure contours for year 2015 [42].

Noise exposure contours are lines around a certain location, usually an airport, representing fixed values of an aircraft noise metric. Metrics used in noise contours vary between countries and states [32]. For instance, the Sydney Airport uses N70 contours, that derive from the number of events above 70 dB(A), which according to Australian standards, is the lowest level interfering with conversation [41]. The UK uses $L_{eq,T}$ contours that replaced the NNI ones in 1990, when an Aircraft Noise Index Study (ANIS) suggested that NNI emphasises too much on the number of noise events [33]. Figure 2.4 shows $L_{eq,T}$ noise contours for London Heathrow [42]. The 55 dB and 70 dB $L_{eq,T}$ contours represent the lowest and high community disturbance levels respectively [33].

2.1.5 Noise-Power-Distance (NPD) curves

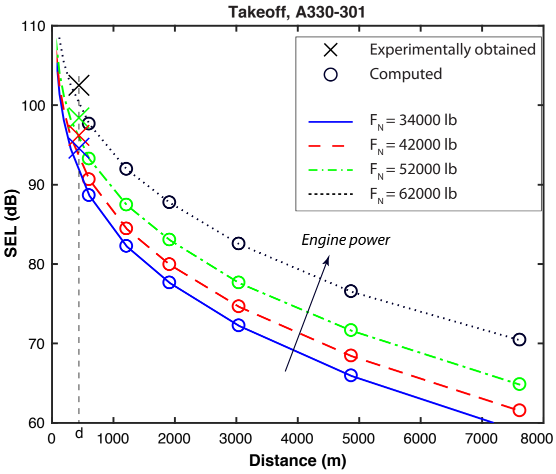

Figure 2.5: Takeoff SEL NPDs for the A330-301.

Noise-Power-Distance curves (NPDs) are important in the present thesis and are therefore presented extensively. Along with flight profiles, they are the main input for constructing noise exposure contours around airports [32]. NPDs provide the relationship between the noise level of a given aircraft at a reference flight speed and atmosphere, and the slant distance from the flight path at a number of engine power settings. Noise level of an aircraft is determined by its configuration (i.e. flap setting, thrust setting, etc.) that varies between operations [43]; hence, aircraft are assigned different NPDs for takeoff and landing. The noise levels are provided at ten standard slant distances in different single event noise metrics, including SEL and $L_{A,max}$. As an example, Figure 2.5 shows the Airbus A330-301 takeoff SEL NPDs. Each curve describes different engine power settings, i.e. different net thrust F_N per engine. The specific NPD engine power values are established based on the certification ratings of the given engine [32]. NPDs for most existing aircraft and conventional operations are available in the publicly accessible ICAO ANP Database [44].

The NPDs development procedure, which is detailed in the SAE AIR1845 document [45] and briefly described in the next paragraph, principally comprises of an experimental and a computational part. As will be shown in Chapter 5, the proposed noise estimation framework is used to bypass the experimental part, i.e. the need for noise measurements. This important achievement allows constructing noise contours for novel aircraft, starting from a baseline aircraft. The NPD development procedure is also exploited for estimating the noise levels of individual noise sources of the baseline aircraft, as will be demonstrated in Section 5.6.

Figure 2.6 sketches the experimental NPD development part: the test aircraft flies at fixed altitude and engine power setting j, at the cleanest possible landing or takeoff configuration (i.e. flap setting, landing gear state), generating PWL, $L_w(j)$. The resulting noise is measured at a location directly under the flight path, denoted O, and hence the slant distance, R_{SL}, equals the flight altitude. Point $P(j)$ and polar angle $\theta_P(j)$ describe the location where $L_{A,max}$ occurs, which is at distance R_P away from location O. The experiment aims at measuring the $L_{A,max}$ and SEL of the test flyover, for a set of pre-defined engine power settings, yielding the SEL NPD points marked with a cross in Figure 2.5. Then, accounting for effects of spherical spreading, atmospheric absorption and effective duration differences, measured noise levels are computationally propagated to the other NPD distances, yielding points marked with a circle in Figure 2.5. Further technical details and instructions on NPD curves usage are given in Appendix C.

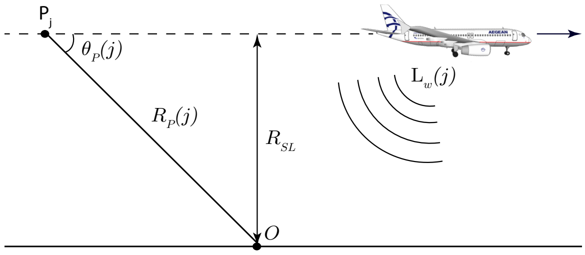

Figure 2.6: Sketch of the experimental procedure for developing NPD curves.

2.1.6 Aircraft noise certification

In order to satisfy the continuously stricter noise ceilings imposed to newer aircraft, as discussed in Chapter 1, aircraft are required to not exceed specific certification EPNLs at three reference points, termed flyover, sideline and approach certification points (CP). Meanwhile, older aircraft are required to be withdrawn at a specific ‘phase-out’ year. The exact levels and CP locations are defined in ICAO Annex 16 [46] and FAR Part 36 [47] according to the aircraft ‘Chapter’, i.e. its age and maximum takeoff weight (MTOW), as shown in Figure 2.7, which also shows a chronological progression of ICAO chapters.

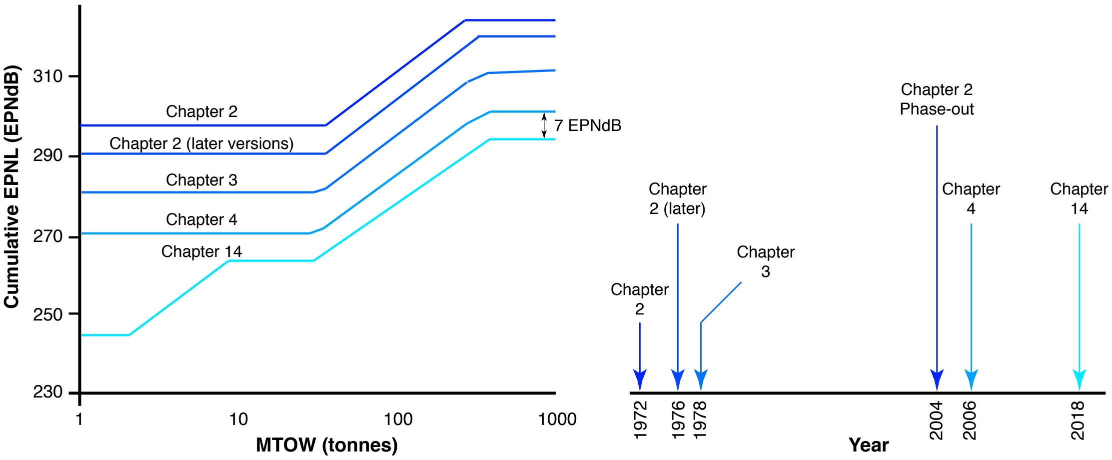

Figure 2.7: Noise certification cumulative EPNL per ICAO Chapter (left) and chronological progression of the ICAO Noise Standard. Data from [48].

Figure 2.8 depicts the CPs for aircraft classified as Chapter 3 and Chapter 4. These reference noise measurement points are defined as [46]:

- Sideline (or lateral): The point on a line parallel to and 450 m from the runway axis, where the highest noise measurement was recorded during takeoff. Typically, this occurs at a height of 1000 ft for civil jet-powered aircraft [49].
- Flyover (or takeoff): 6.5 km from the break release point of the takeoff roll, on the extended centerline of the runway.
- Approach: On the runway axis, 2 km from the runway threshold, or 2.3 km from the ILS landing point, under the 3° approach flight path. Thus, the aircraft passes above the approach reference point at a height of 120 meters.

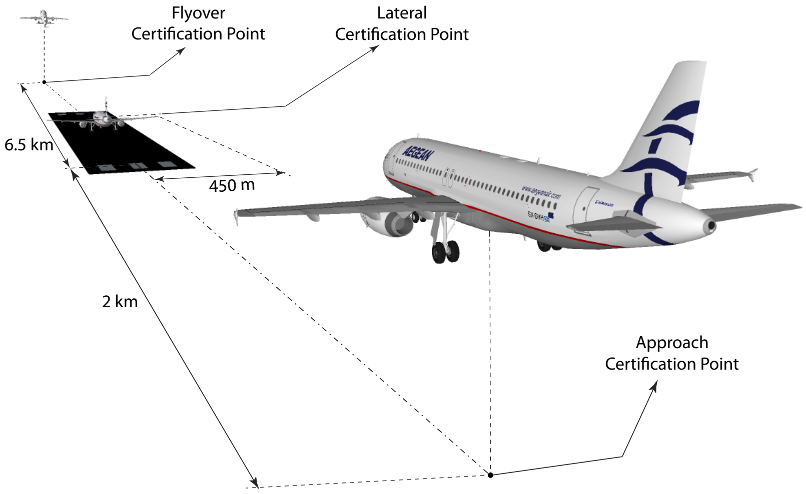

Figure 2.8: Illustration of the ICAO chapter 3 and 4 aircraft certification points.

Certification noise levels of aircraft certified under the ICAO and FAR regulations are freely available in the NoisedB database [50] and the EASA noise type certificates [51].

2.1.7 Aircraft noise sources

An aircraft is a complex set of noise sources, as it consists of various noise contributions whose properties vary during flight. As shown in Figure 2.9, aircraft noise is broadly categorised as engine (or propulsive) and airframe (or non-propulsive) noise [26]. A third noise source is the Auxiliary Power Units (APUs) that supply the aircraft with electrical and pneumatic power whilst on stand [27]; yet, it is neglected in the present research, not only because it is only important within the airport's area [25] where it mainly affects cabin noise prior to takeoff, but also because APUs tend to be replaced by electrical or pre-conditioned power sources [17].

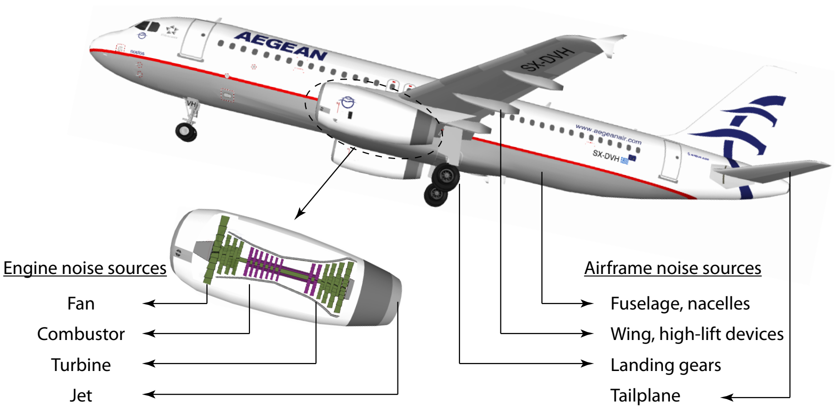

Figure 2.9: Aircraft noise sources

2.1.7.1 Engine noise sources

Engine noise is created by both the engine's moving parts and airflows traversing it and/or being released at high speed for the aircraft's propulsion. As stated earlier, this research emphasises on turbofan-propulsed aircraft; below are described the major noise sources of turbofan engines. An unfamiliar with jet engines operation reader may want to first refer to Section 6.2 that gives a brief description of jet engines working principles.

Fan noise

The fan of turbofan engines generates broadband and tonal noise components, radiated from both the inlet and exhaust ducts [27], as shown in Figure 2.10. Broadband fan noise has an aerodynamic origin as it arises from the turbulent flow through inhomogeneous pressure fields, such as the stationary and rotating blade rows and the wall boundary layers [27]. Discrete tones occur at the blade-passing frequency, f_b, and associated harmonics. With Z being the number of blades and $N1$ the rotor speed in rpm [26]:

$$f_b = \frac{N1}{60} Z \tag{2.18}$$

The buzz-saw noise (also refer to as combination tone) is generated during high engine power operational modes, such as takeoff, when the fan operates at supersonic tip speeds, forming shock waves [26]. Buzz-saw noise is radiated from the inlet duct and is audible not only in the ground, but also in the cabin section ahead of the fan. Its name derives from the fact that the experienced noise is similar to that of a sawmill as a result of the higher frequency harmonics being absorbed by the atmosphere or the fuselage.

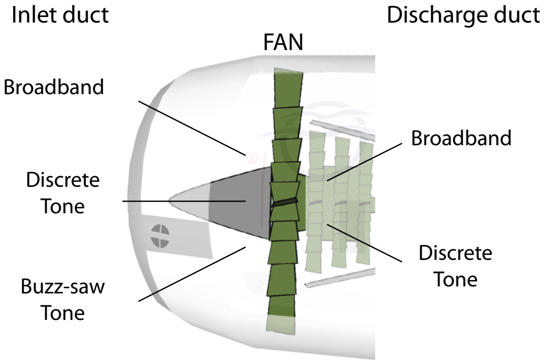

Figure 2.10: Fan noise components.

Fan noise intensity and tone frequencies depend not only on design and manufacture parameters, such as the number of rotor/stator blades, blade chord widths, rotor-stator spacing [25] and obstructions in the inlet duct [27] but also on operational-related parameters, like the airflow velocity and fan rotational speed. Theoretically, fan noise intensity is proportional to the fifth-power of airflow velocity [27].

Jet noise

Jet noise derives from the violent and turbulent interaction between high-velocity, high-temperature exhaust gases with ambient air. The shear layer between the jet and the atmosphere produces turbulent eddies that progressively grow downstream the jet, generating broadband noise, whose frequency decreases as velocity falls [27]. Turbofan engines have a secondary jet (referred to as cold jet) and thus, an additional shear layer between the two jets. Also, a broadband shock noise component occurs when supersonic exhaust streams exist [25]. This mainly occurs in turbojet or low BPR turbofan engines.

Similarly to all aircraft noise sources, jet noise characteristics depend both on manufacturing factors, such as the nozzle geometry, and operational parameters, such as the airspeed and engine power setting [26]. Theoretically, the jet noise intensity scales with the eighth power of jet velocity, as suggested by Lighthill's acoustic analogy (also known as the eighth power law) [52]. Yet, this is mostly valid for pure turbojet engines; scaling becomes more complicated in high BPR turbofans, where the interface between jets introduces additional possible noise sources [27]. Moreover, experimental work confirmed Lighthill's acoustic analogy only under certain conditions, i.e. for a stationary subsonic cold jet, at 90° to the jet axis, whereas the eighth power dependance reduces considerably under different conditions [53, 54]. Smith [27] specifies that the relationship may become as low as the third power of jet velocity.

Turbine noise

Similarly to the fan, the turbine generates both broadband and tonal noise components. Since the rotor-stator spacing in a turbine is narrower than in a fan [27], the turbine-blade-passing frequency tonal component dominates. Turbine noise typically increases with BPR as it is designed to handle greater internal power [37]. As discussed in Section 2.1.8, turbine noise contribution is insignificant compared to that of the jet or fan.

Combustion chamber noise

The combustor generates a low-frequency broadband noise [55, 26] that results from the chemical reactions related to fuel burn and the acceleration of the non-uniform density airflow at the combustion chamber outlet [56]. As turbofan engines technology evolves combustion noise is becoming notable, not only due to the advances that weaken other noise sources, but also because of the way that state-of-the-art combustors work [57]. The high temperatures in the chamber along with its location in the engine pose limitations on isolating and/or experimentally measuring combustion noise and thus, several sophisticated DSP methods are being introduced for that task [55].

2.1.7.2 Airframe noise sources

Airframe noise is generated by turbulence and friction resulting from the interaction of the airflow with its wetted area i.e. the aircraft areas (e.g. parts of the fuselage, wings, landing gears etc.) that come in contact with the airflow. Since these areas have various geometrical properties airframe noise is generally broadband, whereas experimental data suggest that airframe noise sources have similar spectra [26]. Less important low frequency tones are generated at cavities [58], such as landing gears bays, and at the trailing edge of the wing [59]. Theoretically, airframe noise intensity scales with the fifth or sixth power of aircraft speed but experiments suggest that this relationship may be overestimated [27]. Flap noise is additionally influenced by the flap deflection angle.

2.1.8 Significant noise sources

Based on data published by Airbus [60] Figure 2.11 depicts the relative contribution of each aircraft noise source to the noise of a typical medium-haul turbofan aircraft at takeoff and approach[2]. Clearly, the total aircraft noise level is essentially determined

---

[2] This data is from 2003 and is therefore rather old. Data for newer turbofan engines are not publicly available, but dominant sources are assumed to be generally the same, although relative levels may vary.

by the fan and the jet during takeoff, and the fan and airframe at landing. The jet's significance at takeoff reduces with increasing BPR due to the associated decrease in jet velocity and hence jet noise [27, 61]. Meanwhile, fan noise generally benefits from increasing BPR because of lower fan rotational speed and smaller FPR [18], however, these may be offset by higher fan tip speeds that increase fan noise [26, 62]. In addition, the large nacelles of high-BPR engines increase the aircraft weight and drag that, at some point, leads to noise penalties for the whole aircraft [63].

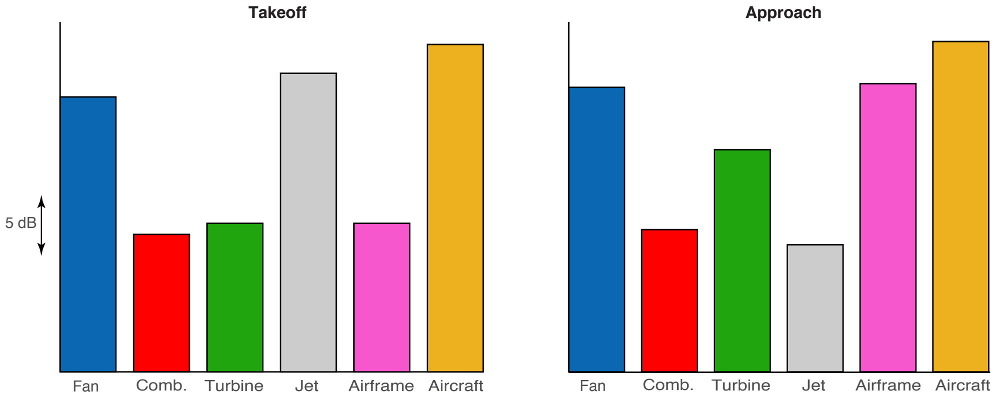

Figure 2.11: Relative aircraft noise source levels. Data from [60].

Airframe noise contribution is substantial during approach, not only because engines operate at low power modes at this flight phase, but also due to the approach aircraft configuration, i.e. extended landing gears and high lift device [27]. Research at DLR [64] showed that full slat/flap deployment increases airframe noise level by around 10 dB compared to the clean fuselage configuration. Whereas predictions in [25] suggest that landing gears are even noisier by about 8 dB. Needless to say that the contributions of the wings and fuselage are outweighed by that of the landing gears and high lift device.

The dominance of the fan, jet and airframe is also observed in Figure 2.12 that shows predicted average noise source and aircraft EPNLs at certification conditions, for Chapter 3 aircraft of different sizes, as published by NASA [65]. Also observed is the level increase of the dominant sources with aircraft size. Figure 2.12 also lists average values of BPR, MTOW and fan diameter corresponding to the aircraft size categories used in the plots; these are defined as (aircraft classification is further discussed in Section 2.5).

- Business Jet comprising of 15 models of 8 manufacturers
- Small Twin comprising of Boeing 737 and Airbus A320 models
- Medium Twin comprising of Boeing 757 and 767 as well as Airbus A330 models
- Large Quad comprising of Boeing 747 models.

Figures 2.13, 2.14 present a frequency-related analysis of aircraft noise sources contribution. The plots show spectra and SPL at CPs of a turbofan aircraft with BPR, $\mu = 6$,

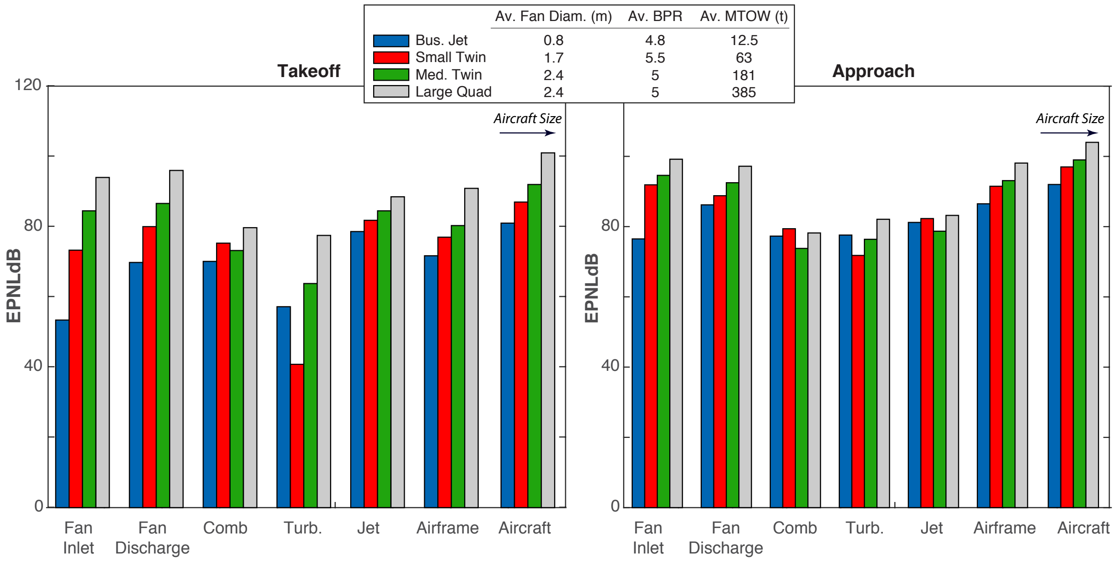

Figure 2.12: Noise sources EPNLs at approach and takeoff certification conditions, for different aircraft-size categories. Based on NASA data [65].

at landing and takeoff, as estimated using a simplified, own-developed aircraft noise prediction tool, FANjET (presented in Chapter 6). Inputs to the tool are spectra from Zaporozhets et al. [26], directivity data from ANOPP [16] and source noise levels from NASA [43]. The plots show that the jet and airframe dominate in the low frequency range, while the fan governs the high-frequency range. Prevailing high-frequency fan and turbine tones are also visible. Even so, as mentioned earlier, higher frequencies are more easily absorbed by the atmosphere, whereas often, tonal components are attenuated at source by liners [66]. Dashed lines denote A-weighted spectra and thus are representative of noise as perceived by humans. A-weighting degrades the predominant, low-frequency spectral content of airframe and jet noise, further exposing the fan contribution.

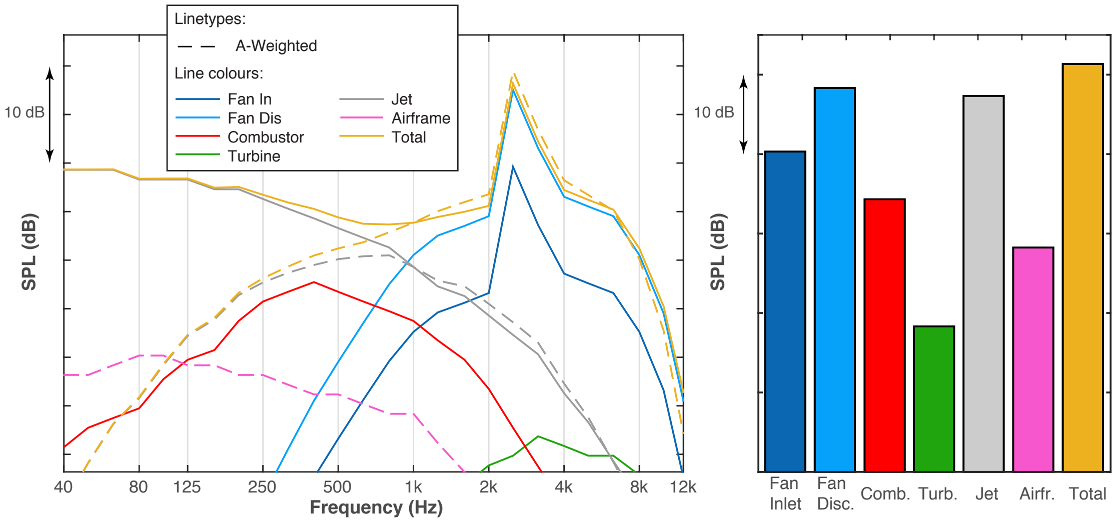

Figure 2.13: Estimated spectra and relative SPL for each noise source of turbofan aircraft ($\mu = 6$) at takeoff certification conditions.

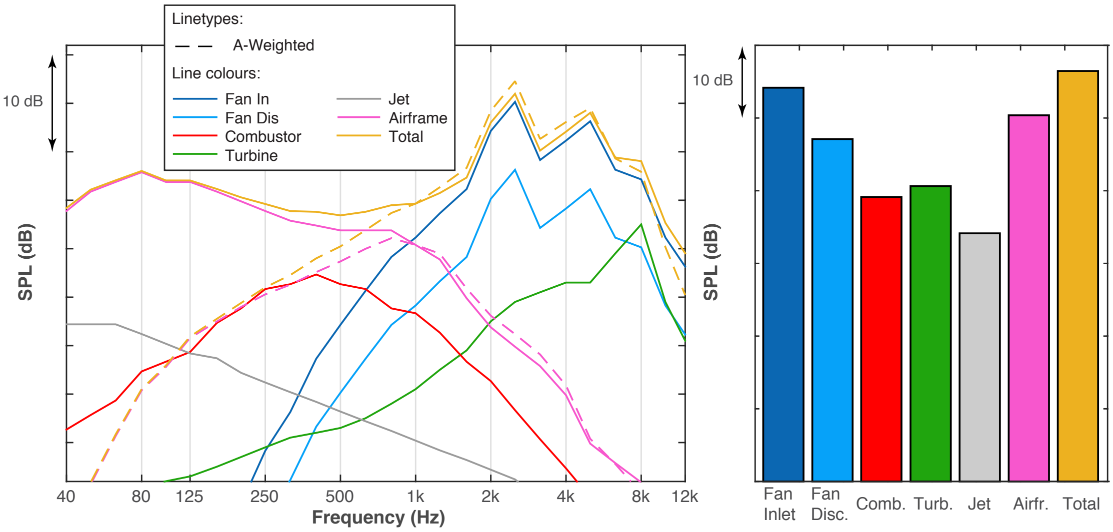

Figure 2.14: Estimated spectra and relative SPL for each noise source of turbofan aircraft ($\mu = 6$) at approach certification conditions.

2.1.8.1 Directivities

Aircraft engine noise sources are directional. Figure 2.15, which is based on Smith [27], sketches representative directivity patterns from typical low and high BPR engines, denoted with continuous and dashed lines respectively. The sketch implies that directivity patterns are affected by BPR changes. In fact, not only are they influenced by manufacturing factors, such as BPR, but also by operational parameters, as indicate the attached in Appendix G predictions by Zaporozhets [26]. For example, the top plots of Figure G.1 show that jet polar directivity pattern, which generally peaks around the middle of the backward quadrant, is influenced by both jet velocity and flight speed. Likewise, fan noise polar-emission angle, which has a strong forward and a weaker but noteworthy backward radiation, is a function of the aircraft operational engine mode.

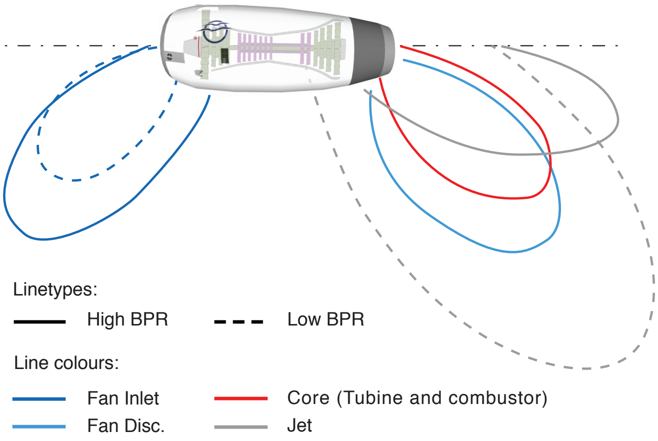

Figure 2.15: Typical directivity patterns from low and high BPR engines. Based on directivity patterns in [27].

Airframe noise is generally omnidirectional [26]. As indicated by Smith [27], this omnidirectionality is more true when landing gears are deployed, because although wings and landing gear noise is omnidirectional and practical identical [26], flap noise is stronger in the forward arc where the jet-flap interaction noise peaks [67].

2.2 Aircraft engine emissions

While aircraft noise has been an issue for almost half a century [27], it was only recently that aviation pollutant emissions, including those resulting from other airport related activities, such as APU and ground transport, became a concern regarding both air quality in the vicinity of airports and global climate change [68]. Contrary to noise, which is mainly a concern at areas around airports and whose effect is directly linked to the duration of an aircraft movement, pollutant emissions may have long-term environmental effects[3] [71, 72]. Aircraft engine emissions consists of several direct or indirect substances, the latter being products of pollutant reactions with the atmosphere [25]. They are distinguished as local air quality (LAQ) pollutants or greenhouse gases, depending on whether they occur during the Landing and takeoff cycle (LTO) or the Climb, Cruise and Descent cycle (CCD) respectively.

2.2.1 Gaseous emissions types

Carbon dioxide (CO_2) is the product of complete combustion of hydrocarbon fuels like gasoline and jet fuel [73]. CO_2 emission composes 70% of aircraft engine emissions and is the largest contributor of aviation to global warming [73]. It endures all along the flight and is directly proportional to engine power and fuel consumption (fuel properties determine the exact proportionality [72]), in contrast to other substances, such as Nitrogen oxides (NO_x) and carbon monoxide (CO) that also depend on engine properties and operating point [72]. CO_2 emission and distance travelled are not linearly related, e.g. takeoff requires higher engine power settings. Overall, the amount of emitted CO_2 depends on manufacturing parameters (such as the engine's thermodynamic efficiency), atmospheric conditions, the flight distance and operating procedures [68]. CO_2 is one of the six Kyoto gases[4] that are characterised as 'well-mixed' [72], due to their long lifetimes that make their impact global and unrelated to the exact location of emission.

In contrast, non-CO_2 emissions have a localised impact, although the affected location may not be where the emission occurred [72]. LAQ is mostly affected by NO_x, CO and unburned hydrocarbons (HC), which together with sulphur oxides (SO_x), volatile organic compounds (VOCs) and particulates and other trace elements, compose 1%

---

[3] Chronic noise exposure may have long-term health issues as well [69, 70], but these often depend on numerous external and subjective parameters.

[4] Termed after the fact that they are controlled under the Kyoto Protocol.

of the aircraft engine emissions [73] (the remaining 29% of fuel combustion is water vapour, H_2O). Being key ozone ingredients, NO_x have been at the centre of environmental concerns[5], while NO_2 in particular is one of the main ingredients of smog. NO_x are by-products of complex chemical reactions within the high temperature/high pressure combustor, like the one of modern gas-turbine engines. While in the hight-temperature combustor conditions, and more specifically in its hottest parts, nitrogen and oxygen in the air blend to form NO [73], which is then oxidized in the atmosphere, in the exhaust plume, to form NO_2 [74]. NO_x generation mechanisms are complex and involve not only ambient conditions but also engine performance parameters, such as the residence time (i.e. the time that substances remain at a given temperature) and the combustion temperature [11, 18]. The latter generates a trade-off between NO_x emissions and fuel efficiency, which, as previously stated, improves with combustion temperature. The amount of emitted NO_x is not directly related to fuel burn. It generally increases with engine power [61], i.e. more NO_x is generated at takeoff, when engine power is maximum. NO_x contribution to global warming through the formation of tropospheric ozone is considered negligible, as it is compensated by the fact that NO_x also facilitate the reduction of methane [75, 72].

HCs occur when fuel molecules overpass the flame zones and are expelled unburnt from the engine. They are responsible for the characteristic odour around airports [76], whereas many of them are hazardous [73]. H_2O is an important greenhouse gas, yet, the amount emitted by commercial aircraft is insignificant compared to ambient concentrations. Hence, its environmental impact is negligible [76]. SO_x are generated due to the interaction of oxygen and sulphur contained in HC fuels, during combustion. Although SO_x emission is mainly addressed through fuel specifications, the proportional relation between emitted amounts of SO_x and condensed hydrocarbons suggest that engine-technology solutions may be required as well [74]. Lastly, particulate matter that are products either of incomplete combustion or the oxidation of some fuel compounds, have both environmental and direct health impacts. Emission of SO_2 and particulate is directly proportional to fuel consumption.

2.2.2 Aircraft emissions metrics

According to ICAO [77], the mass of emitted pollutants is typically measured in grams (g) or kilograms (kg). Often, the fuel-use efficiency of a flight is better expressed in terms of fuel volume consumed per passenger per distance (for instance fuel/pax/100km) [25], to express the effects of aircraft capacity and number of empty seats, e.g. the effect of fully loaded aircraft versus half-empty ones.

---

[5] Nevertheless, the NO_x and ozone relationship may be location dependant, which complicates the establishment of engine NO_x emissions limits [74].

2.2.3 Emissions certification - Emission indices (EIs)

Commercial aircraft emissions are conveniently attributed and assessed at different flight phases, in order to distinguish between their impact at low and higher altitudes. ICAO [77] considers the altitude of 3000 feet (915 m) to be approximately the limit below which aircraft emissions affect LAQ. Aircraft activity is therefore quantified in terms of: a) the LTO cycle that consists of all phases occurring below 3000 feet, i.e. takeoff, initial climb, final approach and idle (taxiing or standing on the ground), and b) the CCD cycle that covers all remaining flight phases.

The LTO cycle serves as a certification tool for proving compliance with emissions standards around airports, as specified in ICAO Annex 16, vol. 2 [77]. Emissions certified are HC, CO and NO_x. As stated earlier, these pollutants are not directly linked with fuel burn. Rather, they are described by an experimentally obtained emission index (EI), which is defined as the ratio of the pollutant mass produced in grams and the mass of fuel consumed in kilograms [78]. EI for each pollutant, as well as the fuel flow, $\dot{m}_f$ are measured for each engine at default engine power settings and time periods, as specified in Table 2.1. EI for most civil aircraft engines, as well as $\dot{m}_f$ and fuel consumption within the LTO cycle, are accessible from the ICAO Engine Exhaust Databank [79]. As an example, Table 2.2 lists the emissions data for the Rolls-Royce Trent 892 engine.

Table 2.1: Parameters defining the ICAO reference landing and takeoff (LTO) cycle [77].

LTO Operation mode	**Default thrust setting (%)**	**Time in mode (minutes)**
Taxi, ground idle	7%	26
Approach	30%	4
Climb	85%	2.2
Takeoff	100%	0.7

As pointed out in [80], associating a single value of EI and $\dot{m}_f$ for each flight phase (i.e. the thrust settings of Table 2.1) is unrealistic and while is acceptable for certification purposes, may lead to inaccuracies in emissions assessment. The generic assumptions on the cycles' definition is an additional source of uncertainties. For instance, EIs do not account for the aircraft takeoff weight, which directly affects the thrust setting but varies

Table 2.2: Rolls-Royce Trent 892 engine emissions data, as obtained by the ICAO Engine Exhaust Databank [79].

Engine Model	**EI HC (g/kg)**				**EI CO (g/kg)**				**EI NOx (g/kg)**				**Fuel Flow (kg/sec)**				**Fuel LTO (kg)**
	T/O	**C/O**	**App**	**Idle**	**T/O**	**C/O**	**App**	**Idle**	**T/O**	**C/O**	**App**	**Idle**	**T/O**	**C/O**	**App**	**Idle**	
Rolls-Royce Trent 892	0.01	0	0	0.7	0.28	0.2	0.57	13.07	45.7	33.3	11.6	5.33	3.91	3.1	1	0.3	1281

according to the load type and distance flown. Figure 2.16 illustrates the disagreements between the ICAO NO_x EIs and EIs obtained experimentally at the Athens Airport, for different aircraft at takeoff [48]. One solution for reducing discrepancies is using EIs derived from specialised measurements, as described in [81] and [82]. Yet, these are only available for a few engines. Also, several authors propose alternate ways of assessing EIs, like Singh who proposes a specific equation for calculating NO_x EI [83]. Alternatively, EIs at non-default thrust settings can be obtained with linear interpolation, as proposed by DEFRA [84] and as performed in the case study in Section 8.1, that investigates the impact of steeper operations; the effect of interpolation is depicted in Figures 8.5, 8.8.

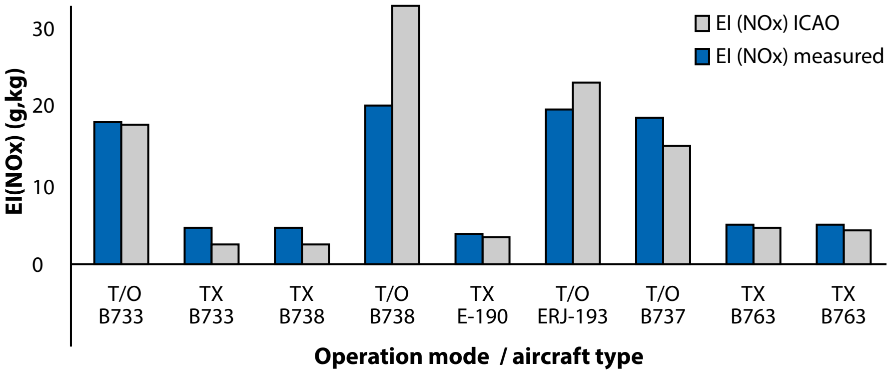

Figure 2.16: Comparison between published (by ICAO) and measured NO_x EIs for takeoff (T/O) and taxing (TX). Based on data in [48].

2.2.4 Specific fuel consumption (SFC)

SFC expresses the mass of fuel burned to produce one unit of thrust over a certain period of time. Hence, it is an indicator of an engine's fuel efficiency relative to thrust output. It is defined as the ratio of fuel mass flow rate and net thrust and has units of (kg s)/N:

$$SFC = \frac{\dot{m}_f}{F_N}\,. \tag{2.19}$$

The smaller the SFC the more efficient an engine is, as it produces more thrust for fixed $\dot{m}_f$. Dependance on $\dot{m}_f$ implies that SFC varies throughout the flight according to the thrust setting; it also depends on airspeed and altitude [18, 25]. For civil aircraft engines, SFC at cruise phase is often freely available and can be used to assess fuel consumption (e.g. if $\dot{m}_f$ is unavailable).

2.3 Emissions assessment

The methodology for assessing civil aircraft emissions and fuel consumption adopted in this research is in line with the ones typically used in the UK, recommended by the UK

DEFRA [84] and ICAO [48, 85]. This Section gives an overview of the methodology before presenting the different evaluation procedures that apply to the LTO and cruise phases.

2.3.1 Fuel consumption

Denoting N the number of engines and t_i the time on operating mode i associated with fuel flow $\dot{m}_{f,i}$, the mass of fuel consumed in kg is [84]:

$$m_{f,i} = \dot{m}_{f,i}\, t_i\, N\,. \tag{2.20}$$

Division by the number of passengers (pax) yields the fuel consumption in kg/pax:

$$m_{f,i,\mathrm{pax}} = \frac{m_{f,i}}{\mathrm{pax}}\,. \tag{2.21}$$

Emission of CO_2 is directly proportional to fuel consumption. One kilogram of typical fuel burned yields 3.15 kilograms of CO_2. Hence:

$$E_{CO_2} = 3.15\, m_{f,i}\,. \tag{2.22}$$

Rather than dividing directly CO_2 emissions with number of passengers, ICAO suggests calculating the amount of CO_2 associated to each passenger with [85]:

$$\mathrm{CO_2\ per\ pax} = 3.157\frac{(\mathrm{Total\ Fuel})(\mathrm{P1})}{(\mathrm{number\ of\ Y\ seats})(\mathrm{P2})}\,. \tag{2.23}$$

In Equation 2.23, P1, P2 are route-dependant factors specified in ICAO statistical databases that contain independently verified airline data [86]. The number of ‘Y’ seats is the total number of economy seats available on all flights serving a given city pair. Likewise, the total fuel is the average fuel consumed by all these flights.

2.3.2 Estimation of LTO cycle emissions

The emission of certification pollutant ε from an engine type j operating at mode i, is:

$$E_\varepsilon = m_{f,i}\, \mathrm{EI}_{\varepsilon,j}\,, \tag{2.24}$$

where $\mathrm{EI}_{\varepsilon,j}$ is the corresponding emission index. Division with number of passengers yields the emission of certification pollutant ε in kg/pax:

$$E_{\varepsilon,\mathrm{pax}} = \frac{E_\varepsilon}{\mathrm{pax}}\,. \tag{2.25}$$

As an example, NO_x emitted by an aircraft equipped with two Rolls-Royce Trent 892 engines at approach are calculated below, based on Tables 2.1 and 2.2.

$$E_{\mathrm{NOx},app} = \dot{m}_{f,app}\, t_{app}\, N\, \mathrm{EI}_{\mathrm{NOx},app} = 1 * (4 * 60) * 2 * 11.6 = 5.5\,\mathrm{kg}\,. \tag{2.26}$$

2.3.3 Evaluation of cruise emissions

Cruise fuel consumption can be evaluated by subtracting the LTO cycle consumption from the total fuel burned. Alternatively, emissions outside the LTO cycle are assessed based on the Eurocontrol Experimental Centre's (EEC) Aircraft Performance Model (APM), referred to as Base of Aircraft Data (BADA) [87]. BADA provides fuel flow rates for different aircraft and flight levels along with predicted aircraft trajectories. This leads to calculating fuel consumption, which is used to calculate emission of CO_2 through Equation 2.22, and certification gases emissions through EIs provided by e.g. NASA [88] and DEFRA [84]. With m_{avg} being the average aircraft mass during a cruise lasting time T, and L/D the lift to drag ratio, fuel consumption is also obtainable from [18]

$$m_f = \frac{m_{avg}\, g\, SFC\, T}{L/D}\,. \tag{2.27}$$

2.4 Aircraft operations

As described thus far, aircraft noise and emissions are controlled through standard certification procedures. This has motivated research and development on sustainable alternative aviation fuels [48], as well as on aircraft technological innovations that improved aircraft environmental performance. While these advances are mostly adopted at design stage, mitigation of aviation's environmental impact extends beyond the aircraft itself, to the operational level. Considering that aircraft design and manufacturing is a process that takes decades, mitigation at operational level is more flexible and adaptable to airport-specific plans. It is worth mentioning that ICAO's Balanced Approach to Aircraft Noise Management, which is adopted by numerous airports globally (e.g. Manchester, Sydney) encourages controlling airport noise[6] through not only technological and operational improvements, but also with land-use planning and management [20].

ICAO [86] uses the term 'operations' to describe a broader range of aviation activities:

- The actual flying of the aircraft,
- Any control and/or monitoring of the aircraft by the ATM system,

---

[6] Overall, ICAO's balanced approach is more noise oriented; however it also considers the interrelationships between noise and emissions.

- Any airport activities,
- Any planning activities out of the flight period

2.4.1 Noise abatement operations

Specific noise abatement operations have been designed aiming at reducing the departure noise impact, such as the Continuous Climb Operations (CCO) and ICAO's NADP 1 and NADP 2 [89, 75]. Analogous procedures exist for approach, e.g. the Continuous Descent Approach (CDA, also abbreviated CDFA), the steeper approach, the reduced landing flap and the displacement of runway thresholds [89, 48]. These procedures are described in detail in ICAO Doc 8168 [90].

Other procedures are based on noise preferential runways and routes, in order to reduce the number of population exposed, either by avoiding sensitive areas or by increasing their distance from the flight path. Software optimisation tools, such as Airbus ADAS [60], are often used to design optimum routes. Also, NASA has been researching and developing their Short takeoff and Landing (STOL) [91] technology to provide quieter operations. In fact, the concepts of Blended-Wing-Body (BWB) aircraft and Distributed Propulsion, examined in Chapter 9 of this thesis, evolved from the STOL requirements.

Noise mitigation operational procedures also include financial penalties and/or time-based operational restrictions, such as night curfews or night limits. Individual regions or airports may administer their own rules and operational bans, which is however inconvenient for network planners [27]. For example, the Quota Count (QC) restrictions used by London's airports impose night curfews on the number of aircraft movements at an airport [48]; each aircraft is associated with a QC rating depending on its landing and takeoff noise certification EPNLs. A certain noise quota 'budget' is allowed for the sum of aircraft movements, meaning that fewer operations are permitted for the noisiest aircraft. This 'budget' is airport specific, since individual regional authorities may establish their own QC levels.

Finally, it is worth mentioning some ground-based operational practices for reducing noise, such as limiting taxiing time, distance and engine power, as well as controlling APU usage and other airport related ground transport.

2.4.2 Emissions abatement operations

Often, operational procedures are associated with trade-offs between noise and emissions, as demonstrated in the case study of Chapter 8 that seeks the environmentally optimum takeoff and descent angle. Yet, some noise abatement operational procedures also lead into emission reductions. For example, CDA requires less engine power fluctuations than the conventional step descent, which also cuts down fuel consumption and emissions. It must be emphasised that in terms of lowest fuel consumption, aircraft performance is optimum at a certain altitude and airspeed whereas it is also affected by the aircraft weight [25]. Flight time at non-optimum conditions has a negative impact on fuel consumption and emissions, and therefore should be the minimum possible [18].

Furthermore, emissions mitigation operational procedures include balancing factors such as aircraft size and service frequency, especially for short-haul flights [92, 93]. For example, Givoni [92] concludes that for a fixed seating capacity, aviation environmental impact can be reduced by using larger aircraft. However this comes at the expense of service frequency, which could have detrimental effects on airlines competition and customer's satisfaction. Such contradictions imply that, just like technological advances, operational improvements are also engaged with compromises between conflicting parameters, highlighting the interdependencies issue mentioned in Chapter 1.

2.5 Aircraft classification

Due to the enormous number of aircraft models worldwide, it is often convenient to group aircraft with similar characteristics into a manageable number of categories. Various classification possibilities exist, like the earlier mentioned 'Chapters' that categorise aircraft according to their age and MTOW, for certification purposes. The ICAO division of aircraft according to flight distance into regional jets, short-haul, medium-haul and long-haul is the classification used when calculating emissions [94]. Long-haul aircraft have maximum range capability larger than 8000 km and are further subdivided into two-engine long-haul, including aircraft like the A330, and four-engine long-haul that refer to aircraft like the B747. The A320 and B737 are representative short-haul aircraft, whereas the Bombardier CRJ900 is an indicative regional jet. SA classifies aircraft according to their MTOW and size, into regional jets (subdivided into small or large), single aisle, twin aisle (subdivided into small, medium and large) and very large aircraft [21].

Case studies performed with the proposed noise estimation framework adopt the SA classification but omitting the subdivisions, since these are assumed to be unimportant in terms of noise and emissions. For example, it is assumed that the MTOW difference between small and large regional jets is too small to create significant noise and emissions differences, due to the fact that both have turbofan engines with similar geometrical and performance characteristics. Table 2.3 lists the aircraft-size categories considered in this research, sorted from smaller to larger, along with their defining performance properties and one corresponding representative aircraft model.

Table 2.3: Aircraft-size categories adopted in this research.

ID	Aircraft-size category	Reference aircraft	Reference MTOW (t)	Reference rated thrust (N)
1	Regional (turbofan) jets	Bombardier CRJ900ER	30	55
2	Single aisle turbofans	Airbus A320-232	80	120
3	Twin aisle turbofans	Airbus A330-301	250	300
4	Very large quad turbofans	Boeing B747-400	380	260

Other classification examples worth mentioning are the FAA and ICAO design groups that divide aircraft according to their wingspan [95] or their emissions [78], the ATC classification according to the approach speed, as well as the aircraft characterisation as light, medium or heavy depending on its wake vortex [96]. Additionally, depending on whether they are subject to regulation of airworthiness by EASA Regulations, aircraft are classified as 'EASA Aircraft' or 'non-EASA Aircraft' [97].

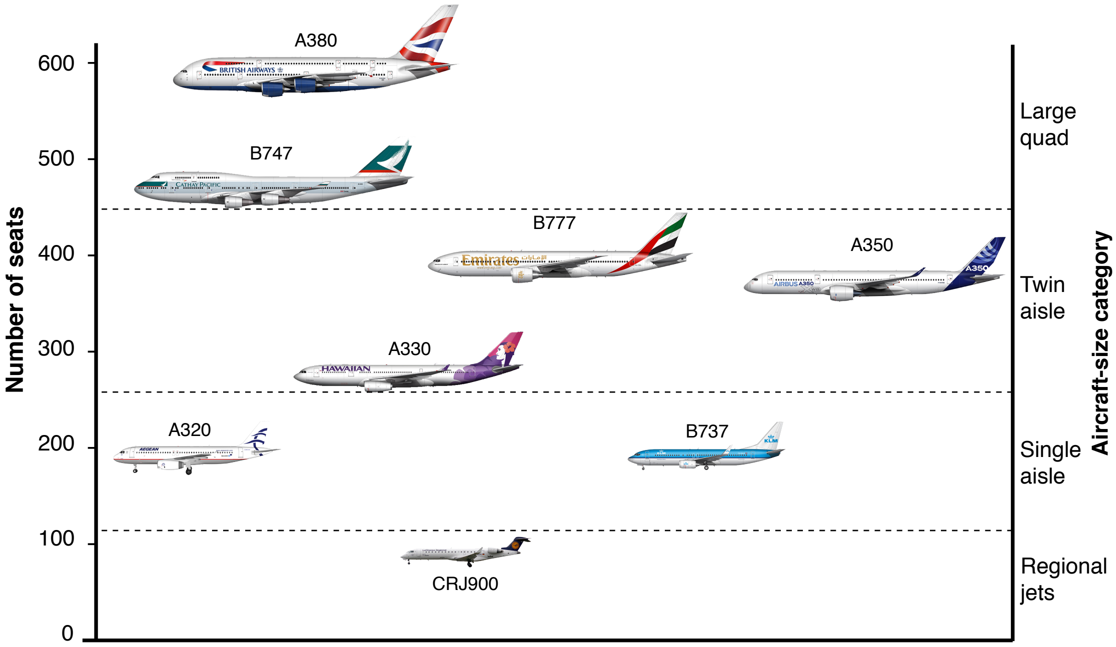

Figure 2.17: Typical existing civil aircraft belonging to the aircraft-size categories defined in this thesis.

2.6 Aerodynamic performance

As stated in the introduction of the present Chapter, the aerodynamic performance and thrust requirements of an aircraft is a key input for estimating its noise and emissions footprint through the proposed noise estimation framework. As shown in Figure 2.18, the forces acting on an aircraft in flight are its weight, W, along with the lift, L, drag, D and thrust, F. For simplicity, the aircraft is considered as a lumped mass with all forces acting on it's centre of gravity. This section gives a brief description of these forces and presents the widely used SAE-AIR 1845 procedure for calculating aircraft aerodynamic performance parameters.

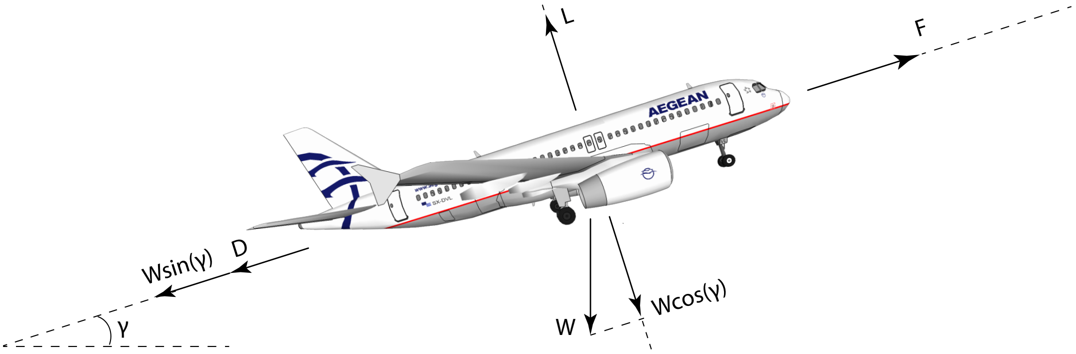

Figure 2.18: Forces on an aircraft climbing with a gradient γ.

2.6.1 Weight

Weight always points towards the earth centre and is the main force that the aircraft has to overcome. Aircraft weight is the sum of the weights of the aircraft structure, fuel and payload (cargo and passengers) and determines the aircraft operational boarders and overall performance (e.g. aerodynamics, airworthiness, environmental aspects, etc.) [98]. There are various types of aircraft weights, such as the Maximum Takeoff Weight (MTOW) and Maximum Landing Weight (MLW) that are publicly available (e.g. from the ICAO ANP Database [44]) and define the weight limits of a given aircraft for takeoff and touch-down. Another type of weight used in this thesis is the Operating Empty Weight (OEW), which is the weight of the empty aircraft (i.e. without the payload) including all items necessary for its operation (e.g. passenger seats and life vests, aircraft crew and their luggage, all necessary fluids like engine oil and coolant) [98].

2.6.2 Thrust

Thrust is the propulsive force generated by the aircraft engines. Figure 2.19 gives a schematic representation of conditions across a turbofan engine. V_0 is the flight velocity, $\dot{m}_a$ the mass flow of air passing through the engine, while A_0, A_j are the inlet and jet cross section areas respectively. Subscripts c and b represent quantities in the core and bypass stream respectively. It is convenient to describe the effect of the two jet velocities $V_{j,c}$, $V_{j,b}$ with one equivalent (often named 'mixed') jet velocity, V_j. An expression for V_j is derived in Section 2.6.3. With $(p_j - p_0)$ being the pressure difference across the engine and ignoring the extra mass due to the fuel flow[7], the net thrust is defined as

---

[7] According to Cumpsty [18], considering an engine on a pylon under a wing, $\dot{m}_a$ is naturally two orders of magnitude greater than the fuel flow, $\dot{m}_f$ passing down the pylon.

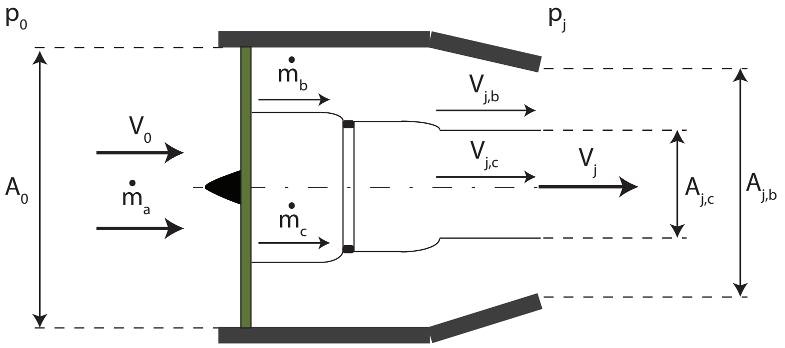

Figure 2.19: Schematic representation of conditions across a turbofan engine. Mass flow rate of fuel, $\dot{m}_f$, added in the combustor is not illustrated.

[98]:

$$F_N = \dot{m}_a(V_j - V_0) + A_j(p_j - p_0)\,. \tag{2.28}$$

The nozzle of typical civil aircraft turbofan engines is designed so that $p_j \approx p_0$ [99, 98], for most operating conditions. Thus, Equation 2.28 simplifies to the difference between the momentum fluxes entering and leaving the engine [18]:

$$F_N = \dot{m}_a(V_j - V_0)\,. \tag{2.29}$$

Dividing by the air mass flow yields the specific thrust

$$F_S = (V_j - V_0)\,, \tag{2.30}$$

which is an indicator of engine's physical size and efficiency [99]. The thrust of a stationary engine ($V_0 = 0$) is termed the gross thrust

$$F_G = \dot{m}_a V_j\,. \tag{2.31}$$

Equations 2.29, 2.31 imply that the same amount of thrust is achieved by decreasing the jet velocity (and hence greatly reduce jet noise[8]) while increasing the air mass flow. This is the core concept of turbofan engines that typically propulse current civil aircraft [61]; they are quieter (see Figure 4.1) and more efficient than turbojet engines [18].

The air mass flow rate is defined as [18] :

$$\dot{m}_a = \rho V A\,. \tag{2.32}$$

---

[8] Referring to Lighthill's eighth power law (see Section 2.1.7), decreasing jet velocity by 50% due to increasing BPR would lead to a jet noise reduction of $10\log(2^8) \approx 24$ dB.

Conservation of air mass flow rate suggests that $\dot{m}_a$ is the same at the engine inlet and exhaust. Also, according to Figure 2.19:

$$\dot{m}_a = \dot{m}_c + \dot{m}_b = \rho_{j,c} V_{j,c} A_{j,c} + \rho_{j,b} V_{j,b} A_{j,b}\,. \tag{2.33}$$

The turbofan engine BPR is defined as the ratio between the bypass and core mass flow rates:

$$\mu = \frac{\dot{m}_b}{\dot{m}_c} = \frac{\rho_{j,b} V_{j,b} A_{j,b}}{\rho_{j,c} V_{j,c} A_{j,c}}\,. \tag{2.34}$$

Modern commercial transport aircraft, such as the Boeing 777 and the Airbus A380 are equipped with high BPR engines, with $\mu > 6$ [25, 61]. Furthermore, according to Cumpsty [18], the optimum value of the ratio between bypass and core jet velocities is around 0.78. The two streams can either be mixed before being discharged from the engine, or expelled by separate co-axial nozzles, which is usually the case for high BPR engines. An alternative high BPR approach is to partially mix the flows before ejection [37]. Benefits from increasing BPR come with the cost of increased weight and drag, due to the large fan (and nacelle) dimensions. Also, as discussed in Section 9.1, very large BPR values introduce efficiency and design difficulties.

2.6.3 Equivalent single stream engines and mixed jet quantities

The thrust generated from a turbofan engine is the sum of the thrusts generated by each stream:

$$F_N = F_{N,c} + F_{N,b} = \dot{m}_c (V_{j,c} - V_0) + \dot{m}_b (V_{j,b} - V_0)\,. \tag{2.35}$$

To derive an expression for the mixed jet velocity, V_j, a ‘equivalent’ single stream engine is considered that produces the same thrust F_N as the turbofan engine, so that

$$\dot{m}_a (V_j - V_0) = \dot{m}_c (V_{j,c} - V_0) + \dot{m}_b (V_{j,b} - V_0) \tag{2.36}$$

Substituting using Equations for mass flow (Equation 2.33) and BPR (Equation 2.34) yields:

$$V_j = \frac{V_{j,c} + \mu V_{j,b}}{1 + \mu}\,. \tag{2.37}$$

Finally, SAE 1905 [100] gives a relationship for the equivalent (or mixed) jet temperature that can replace the individual streams exhaust temperatures, $T_{t,19}$, $T_{t,9}$:

$$T_j = T_{t,9} \left[\frac{1 + \mu \left(\frac{T_{t,19}}{T_{t,9}} \right)}{1 + \mu} \right]. \tag{2.38}$$

2.6.4 Propulsive and overall efficiency

With $\Delta\dot{E}_k$ being the rate of change in air kinetic energy through the engine and neglecting the effect of $\dot{m}_f$, propulsive efficiency η_p and overall efficiency η_o are approximated with [18]:

$$\eta_p = \frac{\text{Power to aircraft}}{\text{Power to jet}} = \frac{V_0 F_N}{\Delta\dot{E}_k} = \frac{V_0 \dot{m}_a (V_j - V_0)}{\frac{1}{2}\dot{m}_a (V_j^2 - V_0^2)} = \frac{2V_0}{V_0 + V_j} \,. \tag{2.39}$$

$$\eta_o = \frac{\text{Propulsive power}}{\text{Fuel power}} = \eta_p \eta_{th} = \frac{1}{SFC}\frac{V_0}{LCV} \,, \tag{2.40}$$

where η_{th} is the thermal efficiency.

In Equation 2.40, LCV is a fuel property, namely its lower calorific value. Overall efficiency consists of the thermal and propulsive efficiencies. The former increases by introducing advanced materials and design innovations, while the latter is mainly determined by the FPR [101]. As will be discussed in Chapter 9.1 low FPR increases η_p but causes problems in matching fan and turbine shaft speeds in modern high and ultrahigh BPR turbofan engines.

2.6.5 Lift

Lift is the upward force that acts perpendicular to the direction of flight [102]. Aircraft mainly generate lift through their lift-efficient, airfoil-shaped wings. As schematically shown in Figure 2.20, the airflow striking the wing is divided into streamlines at each wing side. The upper streamline moves faster than the one under the wing creating a pressure difference (pressure over the wing is lower) that in turn generates lift. Lift is defined by:

$$L = \frac{1}{2}\rho A V_0^2 C_L \,, \tag{2.41}$$

where A is the wing area and V_0 is the flight speed. C_L is the non-dimensional lift coefficient that depends on airfoil properties, such as its shape and inclination, as well as on flow conditions, such as viscosity and compressibility [103]. Lift coefficient is often provided by manufacturers; alternatively it can be determined experimentally or estimated through methods described in references [25] and [98].

2.6.6 Drag

Drag is a force acting parallel and opposite to the motion of the aircraft. The overall drag of an aircraft consists of three main components: the lift-induced drag, C_{Di}, the

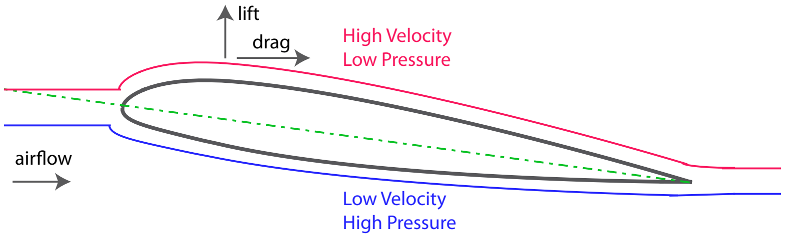

Figure 2.20: Schematic representation of lift generation in a typical airfoil.

profile drag, C_{Dp} and the wave drag, which is related to flow parts becoming supersonic and is typically less important. Lift-induced drag is the consequent rearward force from the lift generation and has therefore a direct relationship with the amount of lift and any effects at the wings. The profile drag results from the friction at the aircraft surfaces (e.g. the fuselage, wings, tail, nacelle, flaps and landing gears), and is therefore linked to the aircraft wetted area. Similarly to the lift force, drag is related to a drag coefficient C_D.

$$D = \frac{1}{2}\rho A V_0^2 C_D \,. \tag{2.42}$$

Equations 2.41, 2.42 lead to the lift to drag ratio, which is an indicator of the aircraft aerodynamic efficiency [102]:

$$\frac{L}{D} = \frac{C_L}{C_D} \,. \tag{2.43}$$

Drag coefficient and/or L/D ratio can be obtained from manufacturers, estimated using methods described in resources like [25] or [98] or determined experimentally.

2.7 SAE-AIR 1845 flight performance calculations

SAE AIR1845 document recommends procedures for calculating aircraft aerodynamic performance parameters and flight profiles during takeoff and approach. The first version of this document was published back in 1986 while the latest update [45] dates in 2012. A slightly altered version of these procedures is included in the ECAC Doc 29 [104] document. The procedure used in the case studies of the present thesis (Chapters 7, 9) is the one for calculating the corrected[9] net thrust, which is presented below.

For turbofan engines, ECAC Doc 29 [104] gives the following formula for the corrected net thrust per engine at a specific thrust rating:

$$\frac{F_N}{\delta_{am}} = E + FV_0 + G_A h + G_B h^2 + HT_{am} \,, \tag{2.44}$$

---

[9] Corrected refers to the thrust value at mean sea level.

where V_0 is the airspeed. In the Equations above, h is the aircraft altitude, T_{am} is the ambient temperature and δ_{am} is the ratio of the ambient air pressure at the aircraft altitude to the standard pressure. Whereas coefficients E, F, G_A, G_B, H depend on the engine thrust setting and are available for each aircraft and operation in the ANP Database [44]. The SAE-AIR 1845 version of this equation omits the $G_B h^2$ term.

The initial climb airspeed is calculated from:

$$V_c = C\sqrt{\mathrm{MTOW}}\,, \tag{2.45}$$

where C is a coefficient appropriate to the flap setting available in the ANP Database [44]. Considering a climb at constant speed, SAE-AIR gives the following Equation for the average geometric climb angle:

$$\gamma = \arcsin\left[K\left(N\frac{\overline{F_N/\delta_{am}}}{\overline{W/\delta_{am}}} - \frac{R}{\cos\epsilon}\right)\right]\,, \tag{2.46}$$

where ϵ is the bank angle (for takeoff and approach $\epsilon = 0$), N the number of engines and R the drag-to-lift ratio corresponding to a given flap setting, as provided by ANP Database [44]. Constant K depends on the airspeed and equals 1.01 when $V_0 \leqslant 200$ kt or 0.95 otherwise.

At approach conditions, the approach airspeed is given by:

$$V_A = D\sqrt{\mathrm{MLW}}\,, \tag{2.47}$$

where the coefficient D refers to the landing flap setting. With γ being the descent angle, the average corrected net thrust per engine is given by:

$$\overline{F_N/\delta_{am}} = \frac{\overline{W/\delta_{am}}}{N}\left(R + \frac{\sin\gamma}{1.03}\right)\,. \tag{2.48}$$

Lastly, it is necessary to mention the formula for the takeoff ground-roll, as it is used in the steeper takeoff case study in Chapter 8. With B being a flap-deflection dependant coefficient obtainable from the ANP database and assuming standard air temperature at mean sea level, the ground-roll distance is determined from:

$$s_r = \frac{B(W/\delta_{am})^2}{N(F_N/\delta_{am})}\,. \tag{2.49}$$

2.8 Breguet range equation

Breguet range equation expresses the distance travelled by an aircraft between takeoff and landing as [18]

$$s = -\frac{V_0\, L/D}{g\, SFC} \ln\left(1 - \frac{W_f}{W_{TO}}\right) , \tag{2.50}$$

where W_{TO} is the mass at takeoff and W_f the mass of the fuel consumed during the flight. Breguet range equation assumes steady-state cruise conditions (i.e. constant lift to drag ratio, overall efficiency and flight velocity) and is therefore more accurate for long-haul flights than for short-haul ones, where the remaining flight phases (e.g. taxiing, climb and descent) consist a larger portion of the overall flight duration.

While Breguet range equation is useful for evaluating the range (or fuel quantity required for a certain range) for new aircraft, it can also provide estimates of lift to drag ratio for current aircraft, as the remaining parameters of the equation are normally published [98]. In the present thesis, Breguet range equation is used in Chapter 9 for calculating the fuel weight, W_f, consumed by aircraft using conventional and future propulsion systems, for a fixed range. For that, Equation 2.50 is rearranged to yield

$$W_f = W_{TO}\left[1 - e^{\dfrac{-s\, g\, SFC}{V_0(L/D)}}\right] . \tag{2.51}$$

Considering that W_{TO} is the sum of the OEW, payload and fuel, Equation 2.51 can be re-written in terms of OEW and payload.

$$W_f = (W_{OEW} + W_{load})\left[\frac{1 - e^k}{e^k}\right] , \tag{2.52}$$

where

$$k = \frac{-s\, g\, SFC}{V_0(L/D)} . \tag{2.53}$$

Chapter 3

Existing prediction tools

This chapter reviews the most common existing tools for predicting noise and emissions for civil aviation. Existing noise prediction tools can be broadly divided into mathematical simulators and models relying on measurements, referred to in this thesis as 'engineering' and 'airport' tools respectively. Limitations of each are depicted, picturing the gap that the proposed noise estimation framework aims at filling in (see Figure 3.1). In summary, typical engineering tools are governed by the computational intensity and dependance on confidential information whereas airport tools lack experimental data, since it is impossible to produce data for all aircraft variants and novel designs. Also presented in this chapter are prevailing prediction methods for individual aircraft noise sources. Such methods are often incorporated into engineering tools, but most importantly, they comprise an indispensable element of the proposed framework, as will be discussed in Chapter 5. The final sections of this chapter are devoted to aircraft performance and integrated prediction tools.

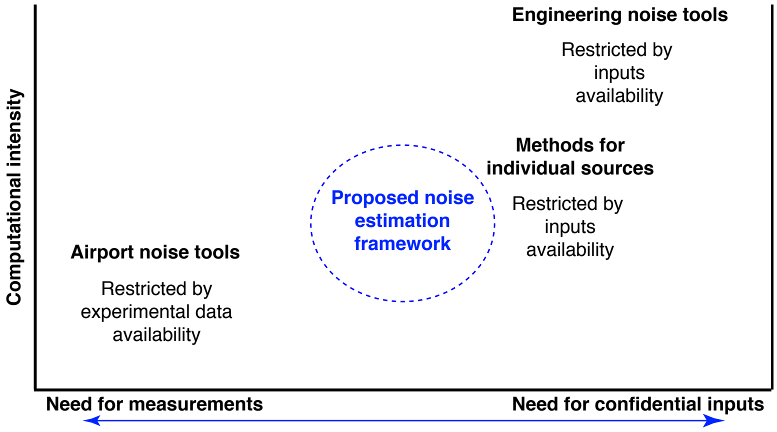

Figure 3.1: Sketch of the typical performance features of existing noise prediction tools and the aimed 'in-between' performance for the proposed framework.

In any case, complexity and accuracy level vary among prediction tools and are determined by numerous factors, like the number and precision of input parameters or the quality of employed noise databases and their validity at divergent technologies and airports. Generally, all tools involve uncertainty, which is governed by their fidelity level, the algorithms and structures adopted and the simplifications/assumptions made. Uncertainty, in combination with the different prediction methods used by each tool implies that predictions by different tools, under the same inputs, may deviate from each other, as reported by several authors [105, 106]. This underlines not only the importance of having some actual measurements, but also the need for an agreed standard prediction method, especially when absolute values are needed e.g. in noise contours production.

3.1 Airport noise prediction tools

3.1.1 Overview and limitations

Airport tools interpolate and/or extrapolate across existing, experimentally obtained noise data, typically NPD databases, in order to provide absolute noise values of aircraft events. Their primary aim is constructing, supporting and effectively communicating airport noise abatement programs. Based on measured data, they treat the aircraft as a single (lumped) directional noise source, whereas due to their low-computational intensity they produce predictions (e.g. from mixed fleet operations) in reasonable time.

However, measurements are expensive to perform, not only due to the direct flyover costs (including personnel, fuel and airport engagement) but also due to the uncertainties involved, arising from the fact that flyover measurements are often contaminated by unpredicted parameters, such as wind and slight trajectory or weight alterations[1]. Hence, to achieve statistically acceptable results, individual measurements must be repeated a few times, under similar meteorological conditions, further increasing cost. Consequently, it is practically impossible to produce experimental datasets for all aircraft types, variants (airframe and engine combinations) and configurations.

Another consequence of relying on experimental data is that there is no flexibility in handling terrain properties and effects, such as reflection and shielding. Most importantly, measured data are unfeasible for unconventional operations and/or novel designs that as said in Chapter 1 are indispensable for delivering the ambitious environmental goals for the near future. Thus, airport noise prediction tools are not applicable to such scenarios. Finally, airport noise tools are incapable of isolating the noise contribution from individual sources and thus, they cannot identify the critical noise sources, as well as the effect of source-oriented suppression technologies (e.g. nacelle liners).

---

[1] While such alterations are tracked by the aircraft systems, they introduce further calculations that involve uncertainties

3.1.2 Prevailing airport noise tools

INM

FAA's INM (Integrated Noise Model) [15] was first released in 1978 and is nowadays a solution used by numerous airports worldwide. As of May 2015, FAA has replaced INM with the AEDT system, which is described later on. It uses NPD data, along with the SAE [45], ECAC [104] and ICAO [107] recommendations in order to assess the noise impact from fleets around airports, in various metrics, typically noise exposure contours around airports. Hence, noise mitigation programs and operational plans can be developed and tested with INM, whereas often it is used combined with other software. For example, Boeing published noise footprints deriving from its proprietary software BCOP integrated with INM [108]. Similarly, the ACRP project [109] aims at implementing aircraft taxi noise modelling capability into INM.

In addition to the above described limitations that refer to all airport noise prediction tools, inconsistencies may arise from the fact that INM uses standard takeoff and landing flight profiles that may not correspond to the actual ones. Likewise, INM is bound to the errors deriving from the NPD derivation procedure, outlined in Chapter 7.3.6. Sometimes, INM underestimates noise at locations to the flight track side, especially at angles smaller than 20° due to lateral attenuation discrepancies [110]. Also, it is prone to issues related to atmospheric attenuation effects [111]. Finally, disagreements emerge due to the distance difference between the point of $L_{A,max}$ occurence and the slant distance that INM uses [110]; yet, this issue is addressed corrected in INM's latest version.

ANCON

Currently on its second version, the UK Civil Aviation Authority (CAA) modelling software, ANCON (Aircraft Noise Contour Model) [35, 112] is employed to produce annual noise contours for major airports in the UK, such as Heathrow and Manchester. It uses historical data, updated performance tables from manufacturers and NPD data, similarly to INM. The major difference between INM and ANCON is that the latter uses flight profiles deriving through airport Noise and Track Keeping (NTK) systems. NTK systems that are widely used in London airports, combine traffic control radar data with flight information and noise measurements from dedicated fixed or mobile monitors, in order to provide accurate flight profile modelling and regularly updated NPDs. Hence, discrepancies due to the aforementioned INM problem regarding standard flight profiles are notably reduced but still, some error may arise from constructing and averaging flight profiles of different aircraft types. Moreover, ANCON is mainly oriented to London Airports and aircraft operating there, and therefore, its database, which is adapted to the London experienced levels [112], may be ineffective when used in other airports.

ANOMS

Brüel & Kjær ANOMS [113] captures in real-time noise levels of all arriving and departing aircraft, in order to produce realistic airport noise reports and accurately predict the effectiveness of abatement solutions. ANOMS features flexibility, not only because it supports installation of additional modules addressing a wide range of concerns (e.g. ATC voice recorder, automated complaints tracker), but also because it integrates easily with other Brüel & Kjær software (e.g. tools monitoring airport emissions).

FLULA

Developed by EMPA (Swiss Federal Laboratories for Materials Testing and Research), the Swiss simulation model FLULA [114] has been growing continuously over the last 20 years [32]. FLULA attempts to exclude the earlier-mentioned influence of ground effects by developping their own noise database based on recordings obtained from an array of microphones at a height of 10 m above ground. However, FLULA, which accounts for spreading, absorption and delay effects, is only effective for noise assessments involving the 75 commercial and military aircraft models included in their noise database.

Other Airport models

It is worth mentioning the Sustainable Aviation (SA) Tools, which is a non-publicly available set of relatively simple tools that provide quick and rough noise estimations, as well as RANE [115], that is a simplified airport noise prediction model developed in the ISVR, University of Southampton. RANE uses the concept of noise cylinders around defined flight-tracks and was used in this research to produce noise exposure contours for novel aircraft (see Chapter 9) based on NPD curves generated through the proposed framework. Finally, also worth mentioning are noise prediction software proprietary to manufacturers, like the Airbus ADAS [60] and Boeing's BCOP [108].

3.2 Engineering noise prediction tools

3.2.1 Overview and limitations

Engineering models aim at providing absolute noise values of aircraft events by mathematically simulating sound generation and propagation effects. They consider the individual aircraft noise sources together with installation effects, such as wing reflections and liner attenuation, and thus allow assessment of each source contribution. The total aircraft noise level is calculated by summing all contributions at the observer location.

Generally, aircraft noise generation is hard to model, not only due to the vortices and complex airflows involved, but also because it varies with aircraft configuration (engine state, position of high-lift devices and landing gears) and trajectory (altitude, speed, rate of climb or descent). Likewise, modelling propagation through long distances involves uncertainties due to atmospheric variations and unpredictable meteorological factors. Last but not least, sound insulations and reflections at the receiver point as well as the Doppler effect and psychoacoustic parameters are sources of additional complexity for mathematically predicting aircraft noise impact.

Typically, engineering tools incorporate specialised methods for handling different tasks, such as the later described prediction methods of Stone [116] for jet noise, Heidmann [117] for fan noise and Fink [118] for airframe noise, as well as methods for simulating propagation effects like the SAE ARP 866A [30] for air absorption. Many of these methods are empirical and therefore limited by the availability and reliability of experimental data. Depending on their fidelity level and the accuracy sought, engineering noise prediction tools may end up handling hundreds of parameters and become extremely sophisticated, time consuming and impractical for generic use. Also, required inputs, such as noise sources directivity and spectral characteristics, as well as detailed design and performance data (e.g. number and geometry of fan blades, spacing between stator and rotor tips, etc.) are normally confidential or otherwise unavailable. Consequently, assumption or approximation may be required that may induce further discrepancies. Engineering tools are designed to feature noise impact prediction capabilities for novel aircraft and contemporary operations. Yet, in addition to the factors just mentioned, their accuracy is liable to the employed methods applicability to any new technologies involved.

3.2.2 Prevailing engineering noise tools

ANOPP

NASA's Aircraft Noise Prediction Program (ANOPP) [16] dates back to the early 1970s and is the earliest aircraft noise prediction software. It uses semi-empirical source noise and propagation methods to replicate (in a rather primitive way compared to today's technologies), flight dynamics as well as effects from atmospheric absorption and ground reflections. Its recently announced successor, ANOPP2 [119, 120], is equipped with a significantly improved noise propagation model; whereas it is more flexible, as it can combine several acoustic approaches and offer a range of fidelity levels. Moreover, the new version accounts for installation effects, which is an important factor for predicting noise from non-conventional configurations and future aircraft designs, such as the Hybrid Wing Body (HWB), which exploits its airframe for shielding the engine noise sources [119, 121].

In support of ANOPP, NASA has developed a set of complimentary and flexible programmes, namely FOOTPR and RADIUS [122] that allow inputs readjustment according to the user's requirements; this enables the assessment of several proposed alternative configurations and models. Being developed in 1981, these codes are now outdated; yet, according to [66], they are the basis for NASA's newer noise technologies.

Soprano

Anotec Consulting and Silence(r) [123, 106], which is the largest European Commission research project on aircraft noise reduction [123], have developed the Soprano programme in the early 2000s. It is versatile and adjustable because not only can it treat the aircraft either as a lumped or as a distributed noise source, but also the user has the option to decide which sources and effects will be included in calculations. Soprano features public methods for source modelling like the Stone [116] and Heidmann [117] methods as well as modules for propagation effects, such as the SAE ARP 866A [30] for atmospheric absorption. Similarly to ANOPP2, the user has the option to add new public, custom or private methods through a separate application, the 'Soprano Generators', whereas models can be combined with measured data. Moreover, it is possible to manually edit individual engine, aircraft and atmospheric conditions properties and therefore evaluate the impact of specific aircraft configuration or technology changes. Soprano outputs various single event or exposure metrics including noise exposure contours.

Soprano consists of three units. First, the pre-processor where the user selects the noise sources, flight and propagation effects along with the associated methods, resulting in the input files construction. Next, the main program (or core) reads the input files before executing the aircraft noise calculations and producing the outputs required by the post-processor, which presents the results in meaningful formats.

The latest, fourth version of Soprano is now part of a package named Aircraft Noise Studio (ANS) for Soprano [124]. It contains a significantly improved core and a new, redesigned pre-processor able to adapt to new projects.

Flight

Flight [25, 125], which is a multi-disciplinary aircraft performance software developed at the University of Manchester, comprises modules for estimating both the noise impact and environmental emissions of an aircraft journey. The noise module includes all noise generation, propagation and transmission features, including advanced effects like jet-by-jet shielding, ground reflection, noise scattering and time shift due to speed of sound. The software treats the aircraft as a lumped system only at aircraft-observer distances larger than ten times the fuselage length. The emissions module predicts CO_2, LTO emissions and contrail levels. Flight is also able to calculate avoidance trajectories. As claimed by the author [125], the current version of Flight is not applicable for preliminary aircraft design, due to the hundreds of inputs required, which would be hard to handle at multi-disciplinary level. Likewise, computations may become demanding when multiple aircraft movements are simulated concurrently.

PANAM

PANAM [126], which was recently developed by DLR, aims at providing rapid comparative noise assessment of different aircraft designs. It outputs the most common noise metrics and also features construction of real time noise contours. To reduce complexity, it omits high demanding CPU computational methods. Currently, it only accounts for airframe, jet and fan noise contributions. While jet and fan noise are predicted with the semi-empirical models of Stone [116] and Heidmann [117] respectively, airframe noise prediction is based on noise measurements and wind tunnel testing. PANAM neglects source aeroacoustic interactions and installation effects. SPL is computed on a reference sphere of 1m and then propagated, accounting for various effects, to the observer point.

AAM

The Advanced Acoustic Model (AAM)[127], which is developed under the Strategic Environmental Research and Development Program (SERDP), is a set of tools that calculates fixed wing or rotary wing aircraft noise in various noise metrics. AAM uses a combination of new methods and methods employed by ANOPP. Noise source modelling is done through the the Acoustic Repropagation Technique (ART) program that subtracts propagation effects (calculated within AAM) from measured noise levels.

3.3 Prediction methods for individual aircraft noise sources

The majority of existing engineering noise prediction tools use the aforementioned semi-empirical models of Stone [116], Heidmann [117] and Fink [118] for evaluating the jet, fan and airframe contributions. While various incorporate several, among the numerous available, ESDU methods. These prevailing methods are briefly described next.

Stone method for jet noise prediction

The Stone jet noise model dating back to 1980 [116] predicts jet mixing noise and jet shock noise of a single stream nozzle, accounting for forward velocity effects. It is a semi-empirical method that uses physical scaling laws and derives from the theory of

Lighthill [52], where the characteristic dimension ℓ is taken equal to $\sqrt{A_j}$, with A_j being the fully expanded jet area. The intensity at distance R would then be

$$I \propto \frac{\rho A_j V_j^8}{c_a^5 R^2}\,. \tag{3.1}$$

Provided that source-to-observer distance and directivity angle corrections are applied appropriately to avoid the consideration of the jet exhaust as a point source, Stone's method defines the one-third octave band total SPL spectrum at a directivity angle θ as the sum of the one-third octave band SPL of the jet mixing and shock components:

$$\mathrm{SPL} = 10\log(10^{\mathrm{SPL}_m/10} + 10^{\mathrm{SPL}_s/10})\,. \tag{3.2}$$

With S_m being the spectral directivity correction obtained from empirically-based tables, the jet mixing noise is calculated with:

$$\mathrm{SPL}_m(\theta, f) = \mathrm{OASPL}_m(\theta) + \Delta_K(\theta) + \Delta_D(\theta) + \Delta_S + S_m\,, \tag{3.3}$$

where OASPL_m is the overall mixing noise SPL, uncorrected for refraction, whereas $\Delta_K(\theta)$, $\Delta_D(\theta)$ and Δ_S describe effects of flight. These parameters are defined in [116]. Similarly, with S_s and OASPL_s being the analogous terms for jet shock noise, defined in [116], the corresponding SPL is:

$$\mathrm{SPL}_s(\theta, f) = \mathrm{OASPL}_s(\theta) + S_s\,. \tag{3.4}$$

A first updated version with improved modelling capabilities for dual stream (coaxial) nozzles was released by Stone in 1983 [128]. Further improvements and extensions are included in the two recently released versions of their code in 2004 [129] and 2009 [130], covering a wider range of single stream and dual stream nozzles and new jet noise reduction technologies, such as the chevron nozzles [131, 132]. Both of these versions are incorporated in NASA FOOTPR code, whereas according to [130], it will also be included in ANOPP. The new versions use the same Strouhal number, effective angle and source-to-observer distance and directivity angle corrections as the original version. The latest version [130] introduces the terms 'large scale mixing noise' that refers to lowest frequency noise component, generated well downstream of the nozzle exit and 'small scale mixing noise' that refers to high frequency noise component, generated near the nozzle exit. The intermediate middle-to-high frequency component is termed 'transitional/intermediate scale mixing noise'. Noise equations have similar form to the ones described in the original version; roughly, the changes are that jet velocity is replaced by a mixed velocity termed 'effective velocity for noise generation'; whereas area, density and the jet velocity term are adjusted to the appropriate jet region. Also, coefficients used in the original work are updated.

Heidmann method for fan noise prediction [117]

Dating back to 1979, Heidmann's semi-empirical method uses data obtained through single-stage fan tests for predicting the noise produced by a fan (or compressor) stage. The SPL due to each noise component of a fan (or compressor) stage is expressed as:

$$\mathrm{SPL} = \mathrm{SPL}_{Ref} - 20\log\frac{\Delta T}{\Delta T_0} - 10\log\frac{\dot{m}_a}{\dot{m}_0} - f(\mathrm{design})\,. \tag{3.5}$$

In Equation 3.5, $\dot{m}_a$ is the mass flow rate passing through the fan stage, whereas ΔT is the total temperature rise across it. Referring to the turbofan engine components numbering of the cross-section in Figure 6.3, $\Delta T = T_{t13} - T_{t2}$. Constants ΔT_0 and $\dot{m}_0$ are reference values. ΔT can be obtained from the fan total pressure ratio π_f:

$$\frac{\Delta T}{T_{t2}} = \frac{\pi_f^{\frac{\gamma-1}{\gamma}} - 1}{\eta_c}\,, \tag{3.6}$$

where T_{t2} is the total temperature at the fan inlet face, η_c is the fan adiabatic efficiency and γ is the heat capacity.

Equation 3.5 implies that noise differences between fan components is determined by function $f(\mathrm{design})$. This function is a sum of functions $F1$, $F2$, $F3$, $F4$ that have dB units and are calculated using unique equations for each noise component, as defined by Heidmann [117]. The last two parameters contain directivity and spectral information, the later being mainly affected (in a different way for each component) by the blade passing frequency, f_b. Term $F2$ involves design-related corrections for each component, while term $F1$ expresses the influence of the operating tip Mach number. It is apparent that knowing how parameters ΔT, $\dot{m}_a$ and the operating tip Mach number change suffices to have an estimate of the resulting fan noise variation using Heidmann's method.

Several authors have published updates and amendments to Heidmann's method, but without changing its structure. In 1996, Kontos et al. [133] recommended changes for adapting the model to advanced Ultra High Bypass (UHB) engines based on measured GE data. Similarly, Hough and Weir [134] modified the original module to lend itself to smaller engines. Finally, based on improved experimental setups using a low-speed wind tunnel that overcomes data contaminations associated with fan tests being static, Stone et al. [135] revised Heidmann's formulations in 2014.

ESDU Tools

ESDU provides a wide range of practical, empirical and analytical methods applicable to the aviation environmental impact prediction. Among these, ESDU Aircraft Noise Series [136] include methods for calculating or estimating noise from airframe and individual engine noise sources. All ESDU methods (ESDU 99006, ESDU 98019, ESDU 89041, ESDU 11002) for predicting the near and far field noise from single stream and coaxial jets, are based on interpolation/extrapolation across existing or custom databases of jet velocities, temperatures and jet noise spectra. Thus, they are limited within the bounds of the available data. Whereas ESDU 98008 [137] for the prediction of subsonic fan and compressor noise is actually a modified and improved version of the aforementioned Heidmann method. Airframe noise is estimated with ESDU 90023 [138], which is a semi-empirical model that uses ambient conditions and geometric properties of airframe elements, along with Strouhal numbers and Doppler effects. The ESDU Aircraft Noise Series also addresses combustion noise, propeller noise as well as noise shielding and noise attenuation from acoustic liners. Concerning sound propagation, ESDU provides methods for atmospheric attenuation, lateral attenuation and ground reflection.

Fink model for airframe noise prediction

With V_0 being the airspeed, Fink [118] expresses the acoustic power for each airframe component as:

$$W_{a,c} = KGV_0^a \,. \tag{3.7}$$

Empirically derived constants K and a, as well as the geometry function G are different for each airframe component. For example, exponent $a = 5$ for wings and tails, whereas $a = 6$ is assigned to flaps and landing gears. Constant K and function G are similarly defined. Furthermore, each airframe noise component is associated with different, empirically derived directivity and spectral functions.

3.4 Aircraft gaseous emissions prediction tools

Modelling the environmental impact of pollutant emissions is a demanding task, not only due to the noise and emissions interdependencies mentioned in Chapter 1, but also due to the emissions' complicated temporal and spatial distribution and long-term effects. The most prominent gaseous emissions prediction tools for aviation are concisely presented in this section.

ICAO Tools

ICAO has developed some publicly available tools to support decision-making in improving fuel efficiency and abate air travel CO_2 emissions. These are briefly described below, based on the latest user guides found at the ICAO website [139].

The ICAO Carbon Emissions Calculator, currently in its seventh version, is a simple tool for estimating CO_2 emissions per passenger in an air travel. Based on publicly available industry fuel consumption data[2], as well as on databases related to distance[3] and load factors[4], it only requires the user to input origin and destination airports. The ICAO Green Meetings Calculator uses the ICAO Carbon Emissions Calculator for generating optimum meeting venues, in terms of CO_2 emissions from attendees air travel. Finally, the ICAO Fuel Savings Estimation Tool is a simplified estimator of fuel savings (and not of absolute emissions values) due to operational improvements. Based on several assumptions related to factors such as the aircraft weight, engine thrust setting, meteorology and airframe/engine combinations, it appeals to airports that are not equipped with detailed modelling facilities or measurement tools.

EDMS

FAA's Emissions and Dispersion Modelling System (EDMS), whose first version was developed in the mid-1980s and is currently in its fifth version, appraises the air quality impacts of airport emission sources [140]. EDMS calculates emissions not only from aircraft movements in the vicinity of airports but also from APUs, ground support equipment, vehicles and stationary sources. It uses databases like the ICAO Engine Exhaust Databank [79] and the emission factors from MOBILE6 Vehicle Emission Modelling Software [141]. Since May 2015, EDMS has been replaced by the below presented AEDT tool.

AEM

Advanced Emission Model (AEM), developed by the EEC [142] assesses the fuel consumption and mass of certification emissions for specific trajectories and aircraft types. AEM, whose input is the aircraft and engine type as well as the flight profile, uses the ICAO Engine Exhaust Databank [79] for calculations below 3000 ft and combines BADA [87] and a revision of Boeing Fuel Flow Method 2 (BM2) for calculations above 3000 ft.

ESDU Tools

Section 27 of the ESDU Aircraft Performance Program [143] contains ESDUperf that predicts the aerodynamic takeoff and landing performance of an aircraft design. These predictions not only lead to pollutant emissions assessment but they also provide inputs to noise prediction tools.

---

[2] EMEP/CORINAIR database, which has data for 44 equivalent aircraft types

[3] ICAO Location Indicators database, combined with the Great Circle Distance (GCD)

[4] Traffic by Flight Stage database (TFS); it contains seats, passengers (with baggage) and cargo (freight and mail) information

3.5 Aircraft performance tools

Aviation noise and emissions prediction tools normally require flight profile information and engine performance data. In fact, as will be shown in Chapter 5, the proposed noise estimation framework may require inputs, such as the temperature at given engine locations in order to assess airflow velocities that determine engine noise. While the proposed framework addresses that through an engine thermodynamic analysis (as also explained in Chapter 5), required inputs can alternatively be obtained from specialised aircraft (or engine) performance tools.

Among numerous commercial aircraft analysis and/or engine performance software, such as Gasturb [144], Piano-X [145], APP [146] and GSP [147], it is worth describing NASA freely accessible handy tool, EngineSim [148]. EngineSim has been extensively used by the author of this thesis for understanding the behaviour of turbofan engines and the variation of certain thermodynamic (e.g. the conditions at each engine component) and performance (e.g. air and fuel flow) parameters with engine design and thrust. In contrast to the earlier mentioned commercial software that require detailed and numerous inputs, Enginesim incorporates standard turbojet, turbofan and ramjet models with modifiable geometry properties. Whereas it allows insertion of custom airspeeds and atmospheric conditions data.

3.6 Integrated tools

AEDT

It has already been mentioned that the main environmental consequences of aviation, namely noise and emissions, are interdependent. Thus, accurate aviation environmental impact assessment requires an integrated solution that consolidates both noise and emissions effects in a single tool. Such an integrated solution is FAA's Aviation Environmental Design Tool (AEDT) [149], whose second version was released on May 2015, replacing INM and EDMS. AEDT combines INM and EDMS capabilities in order to model aircraft performance and then predict emissions and noise from single flights or fleets. However, since it combines measurements-based software, it is associated with the aforementioned inflexibilities in terms of novel aircraft designs and contemporary operations.

Chapter 4

Historical Trends

Historical trends can be used as the basis for approximating, estimating or forecasting some of the few unknown inputs required by the proposed aircraft noise estimation framework. Noise impact estimation on future aircraft also requires knowledge of noise benefits for individual noise sources due to innovative technologies, such as the advanced liners and/or noise abatement operations, such as the steeper descent. Hence, this Chapter is devoted to aviation's historical trends and the noise benefits obtained from specific technological advances and altered operations.

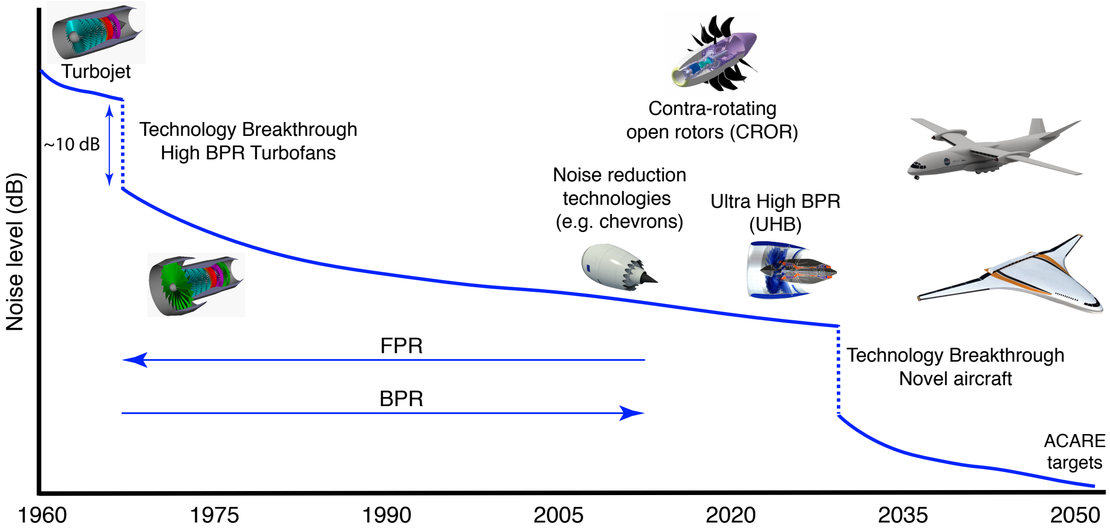

Figure 4.1: Trends in aircraft noise reduction. Dotted lines represent abrupt noise reductions due to technological breakthroughs.

4.1 Aircraft noise throughout the years

Figure 4.1 graphically represents the aircraft noise reduction trends throughout the years, along with the path towards achieving the challenging ACARE goals for 2050, presented

Table 4.1: Estimated noise reductions potential of imminent and future technologies and noise abatement operations. Based on [3, 132, 150, 151, 152, 153].

Noise reduction technologies	**Noise reduction potential at source (PWL)**
High lift devices treatment	Up to 3 dB (airframe noise)
Landing gears low noise design	Up to 5 dB (airframe noise)
Rotor speed optimisation	1-4 dB (fan noise)
Serrated nozzles (Chevrons)	2-3 dB (jet noise)
Advanced nacelle and liner technologies	1-4 dB (fan noise)
Ultra high BPR (UHB), geared turbofans	3-4 dB
Contra-rotating open rotors (CRORs)	4-7 dB
Variable area nozzle	2 dB
BWB fuselage	11 dB
Turboelectric distributed propulsion	Up to 12 dB less than N+3 goals (propulsion noise)
Noise abatement procedures	**SEL reduction potential**
NADP1, NADP2	Up to 5 dBA SEL
Continuous Descent Approach (CDA)	4 dBA SEL
Steeper descent	1-2 dBA SEL
Low power/low drag approach	Up to 5 dBA SEL
Good-practice landing gear deployment	3 dBA SEL
Reduced landing approach	1.5 dBA SEL
Displaced landing thresholds	4 dBA SEL

in Chapter 1. Technological breakthroughs leading to radical noise benefits, such as the introduction of high BPR turbofan engines in the early 1970s, are represented by vertical dashed lines. The noise benefit from increasing BPR is also shown; according to the latest EASA aviation environmental report [3], aircraft noise levels have been reducing by about 4 dB per decade since around 1990, when this progress reduced to about 2 dB per decade. This trend is expected to continue in the near future, but radical technological improvements (e.g. introduction of novel aircraft) are required to deliver the future noise targets.

4.2 Noise reduction technologies and operations

Table 4.1 summarises estimated noise reductions at source (unless otherwise stated) due to imminent and future aircraft noise reduction technologies and noise abatement operations, based on references [3, 132, 150, 151, 152, 153]. In the context of the proposed noise estimation framework, individual sources noise reduction due to such technologies (e.g. chevrons for jet noise) is an important input that must be incorporated into calculations, as will be shown in the case study of Section 7.1.3. Also, the noise reduction potential for the whole aircraft resulting from advanced technologies and operational procedures is useful to benchmark estimations performed with the proposed framework.

Table 4.2: Aviation related publicly available databases

Database Name	**Database content**
ICAO ANP Database	Aerodynamic & engine coefficients, performance data, NPD and Spectral data
ICAO & DGAC NoisedB database	Certified noise levels
EASA Engine Emissions Databank	Information on engines emissions
EASA Type Certificates (TCDS)	Aircraft & engine perform. data, certified noise levels
EEC Base of Aircraft Data (BADA)	Aircraft performance data
Jet Engine Specification Database	Gas turbine engines design & performance data
www.airliners.net	Aircraft Data, airlines, aviation news and photos

4.3 Engine parameters trends

This Section investigates the relationship between several parameters, based on trends deriving mainly from the publicly available aviation databases presented in Table 4.2, as well as from manufacturers websites and reports like the ICAO Environmental Report [48]. The scattered data are plotted along with the resulting trend lines that serve for estimating non-public parameters of existing and/or future aircraft involved in the case studies in Chapters 7-9 of this thesis. Trend lines can also be adjusted according to future technology expectations and practical assumptions.

Figure 4.2 plots the FPR against BPR for the turbofan aircraft size-categories defined in Section 2.5. Plotting these trends separately for each size category produced better fit. Categories with IDs 2 and 4 are plotted together, because what essentially differs between them is the number of engines and not their size.

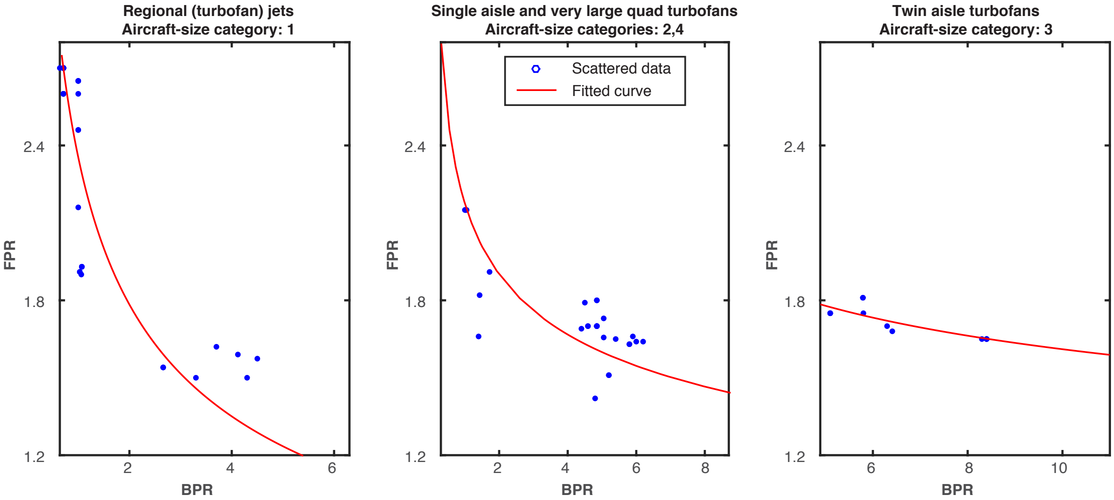

Figure 4.2: Trends between BPR and FPR for different aircraft-size categories.

Figure 4.3 shows the evolution of BPR and turbine entry temperature, T_{t4}, limit. Two technological breakthroughs are assumed; a) the increase of BPR due to the introduction of UHB engines at around year 2020 , and b) a steep increase of T_{t4} due to advanced materials technologies [153, 154]. Figure 4.4 shows the development of overall pressure ratio, OPR, (in turbofan engines, OPR is the pressure ratio between the fan face and the compressor exit [18], see Equation 6.25) and the associated benefits in engine efficiency, since, as mentioned in Section 2.2.4, the smaller the SFC the more efficient an engine is.

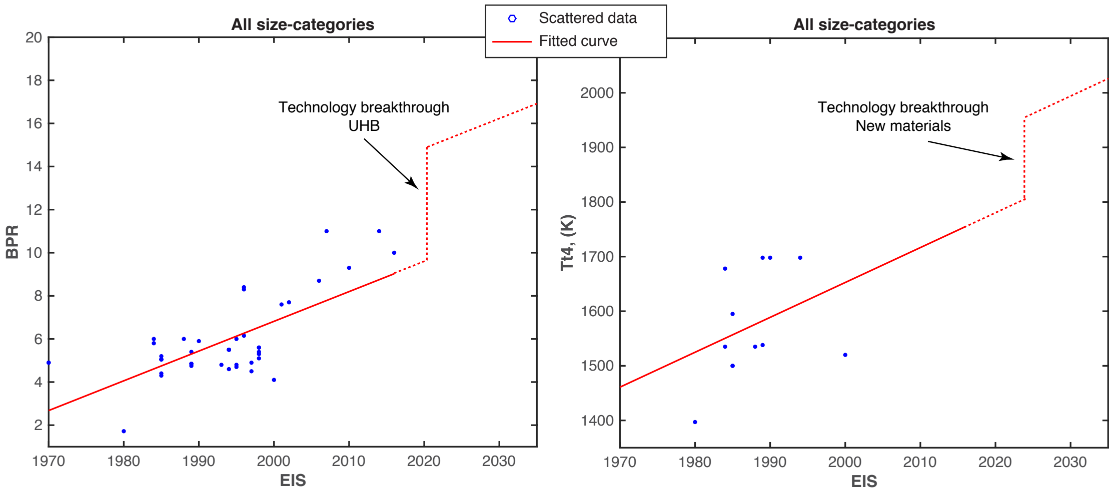

Figure 4.3: Evolution of BPR and turbine entry temperature.

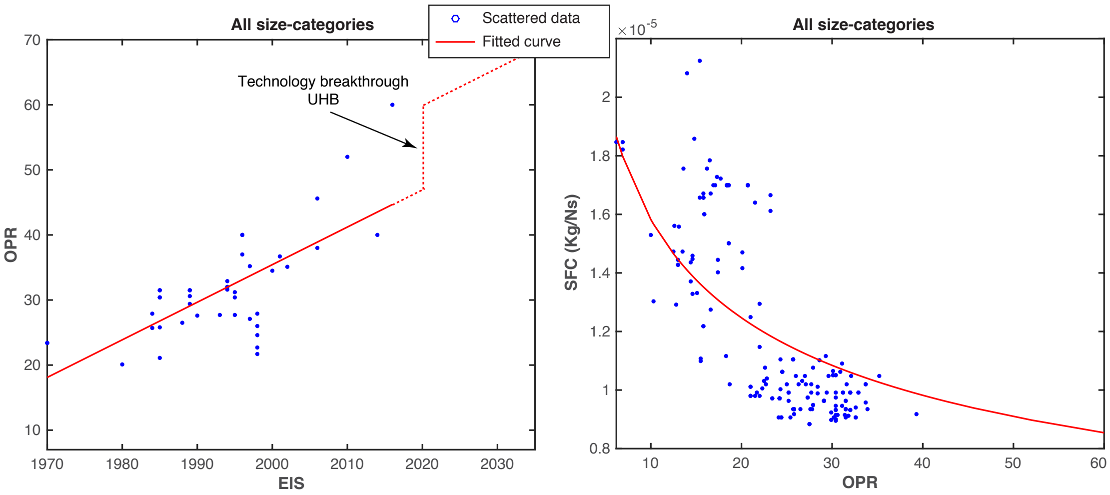

Figure 4.4: Trend of turbofan fan diameter with FPR.

Figure 4.5 shows the trends of BPR with SFC and static thrust, indicating that higher BPR engines are generally designed for producing more thrust. However, modern high BPR turbofan engines, such as the CFM LEAP that is used by the Airbus A320 Neo and the Boeing 737 Max have a static thrust of around 120 kN, as notified in Figure 4.5. Figure 4.7 suggests that fan diameter is a better indicator of the takeoff thrust.

As will be shown in Chapter 5, where the methodology of the proposed noise estimation framework is presented, fan diameter is an important parameter for estimating engine noise. In addition, it is a convenient parameter for briefly describing the performance of turbofan-propulsed aircraft, and/or estimating the size of the engines (or any other type of propulsors) on a novel aircraft. For example, in the electric aircraft noise estimation

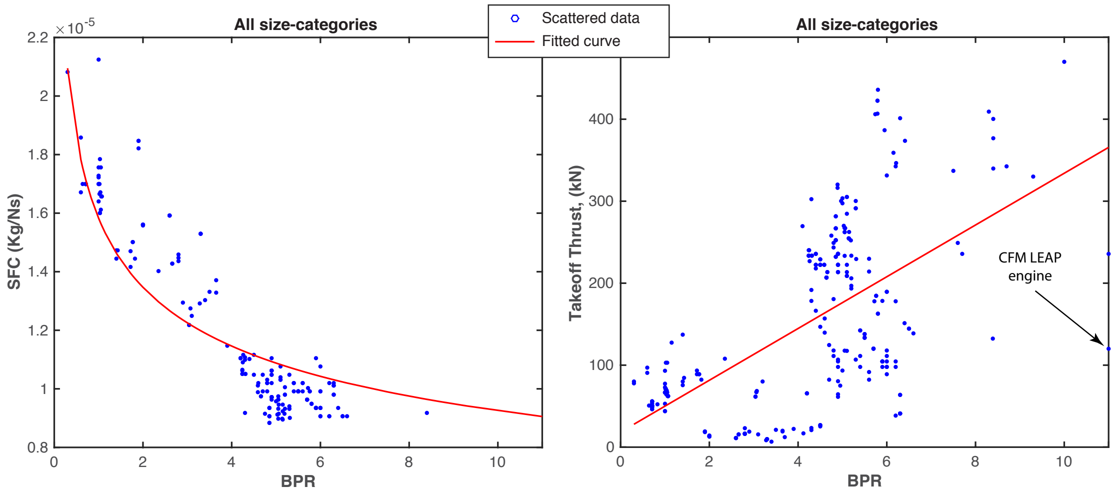

Figure 4.5: Trends of turbofan BPR with SFC (left) and static thrust.

study of Chapter 9 the design and performance parameters of the electric propulsors have been estimated based on their fan diameter. Hereafter are therefore plotted the trends of several design and performance parameters with fan diameter.

The left hand plot of Figure 4.6 describes how the static airflow depends on fan diameter (for all aircraft-size categories). The same Figure shows the trend of fan diameter with BPR. It is seen that BPR and fan diameter do not have a definite relationship; for example the BPR for a fan diameter of around 1.2 m ranges from 1 to 7. For that reason, it is important to make further assumptions and use critical thinking (e.g. relate with the thrust requirements of an aircraft, or the available space below the wing for mounting an engine, etc.), before using this trend diagram. Much clearer are the trends of fan diameter with engine takeoff thrust and maximum LPR speed in Figure 4.7. Figure 4.8 illustrate the weight and length increase of turbofan engines with fan diameter. Finally, Figure 4.9 depicts the trend between fan diameter and FPR.

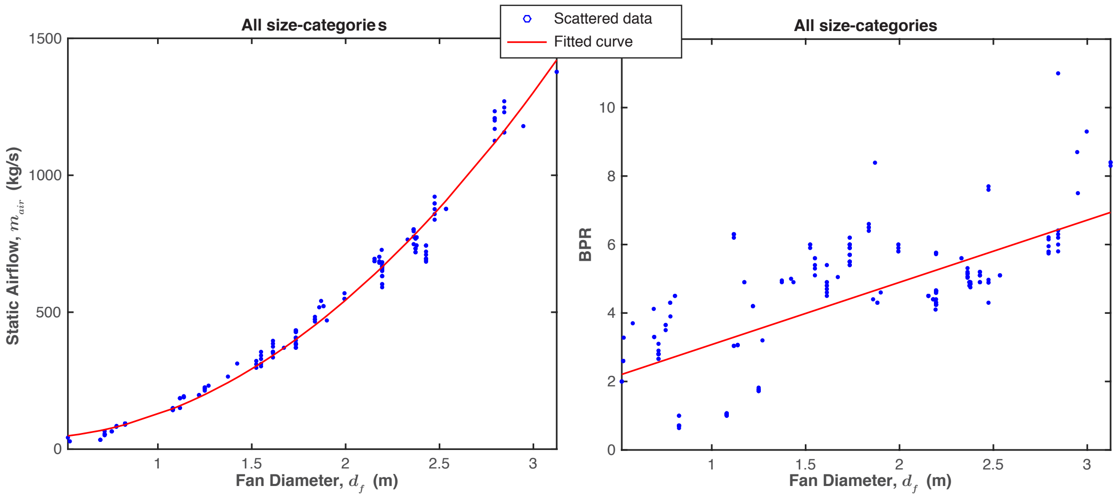

Figure 4.6: Trends of $\dot{m}_{air}$ and BPR versus fan diameter.

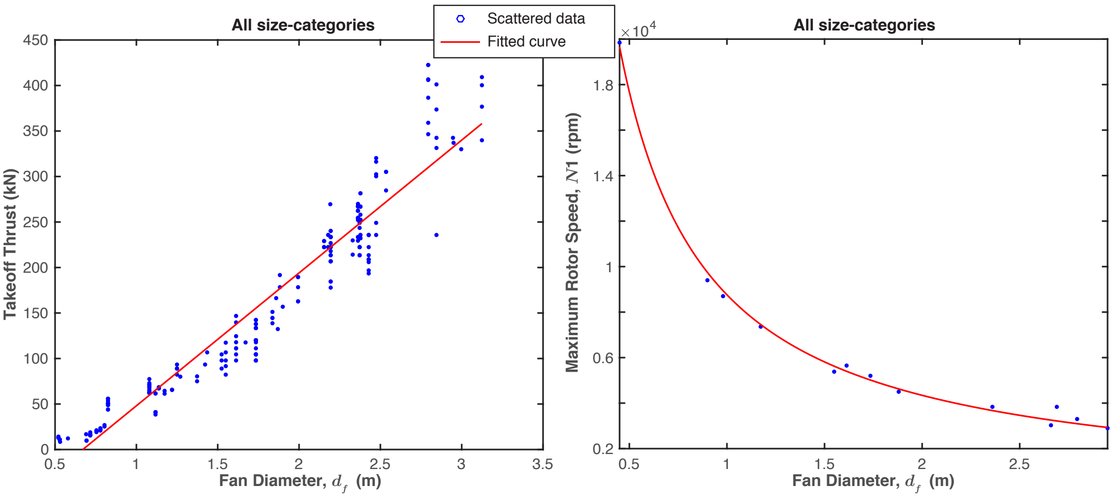

Figure 4.7: Trends of engine takeoff thrust and LPR speed with fan diameter.

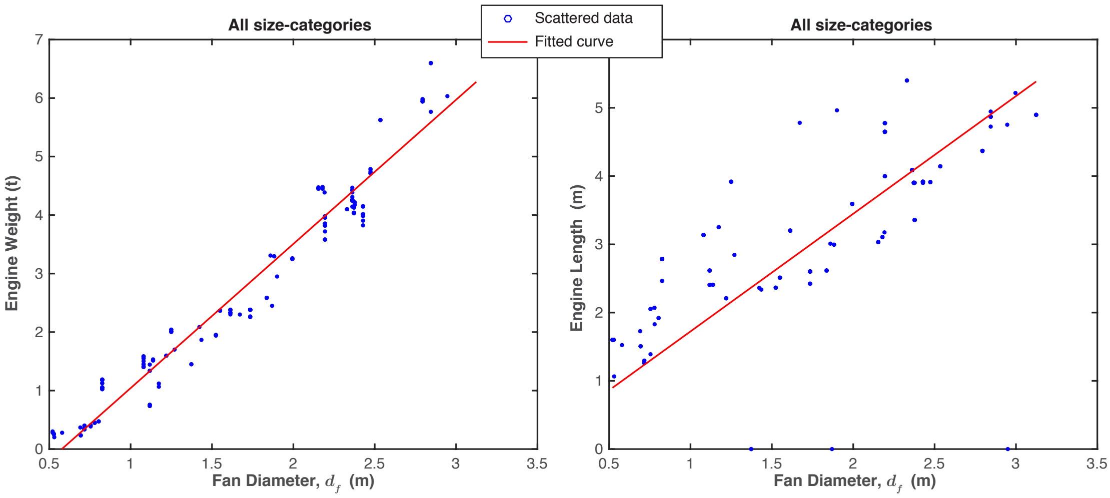

Figure 4.8: Turbofan engine weight and dimensions trends.

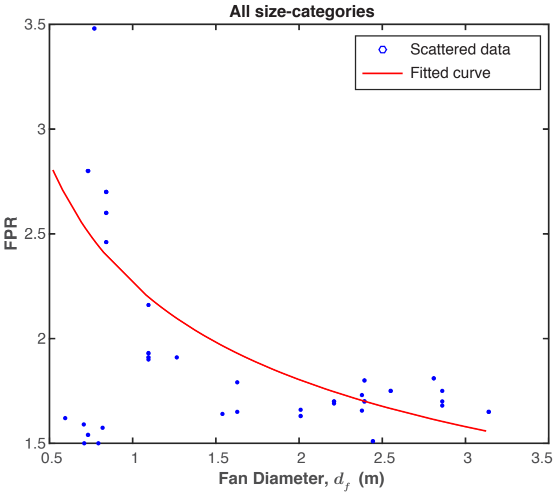

Figure 4.9: Trend of turbofan fan diameter with FPR.

Chapter 5

Methodology I: Core architecture

5.1 Overview

This chapter demonstrates the methodology of the proposed aviation noise estimation framework. As pointed out in Chapter 1, the framework estimates the noise impact of mitigation strategies starting from a baseline scenario where the noise levels are known, or otherwise estimated. For instance, with reference to Figure 5.1, rather than directly calculating or measuring the noise impact of a steeper descent approach, the framework estimates the noise level change ΔNoise relative to the conventional descent. Noise estimation is performed computationally, bypassing dependance on noise measurements or NPD data. Also, the fact that only noise changes are sought reduces computational complexity (parameters defining the absolute values become excessive) and the need for confidential inputs. This enables fast assessment of the noise impact of mitigation strategies, including novel concepts. The few unknown required inputs are: a) estimated based on the historical trends in Chapter 4, or b) approximated based on thermodynamic engine analysis, which is demonstrated in Chapter 6 or c) given the values of publicly available averages that represent the aircraft-size categories presented in Section 2.5.

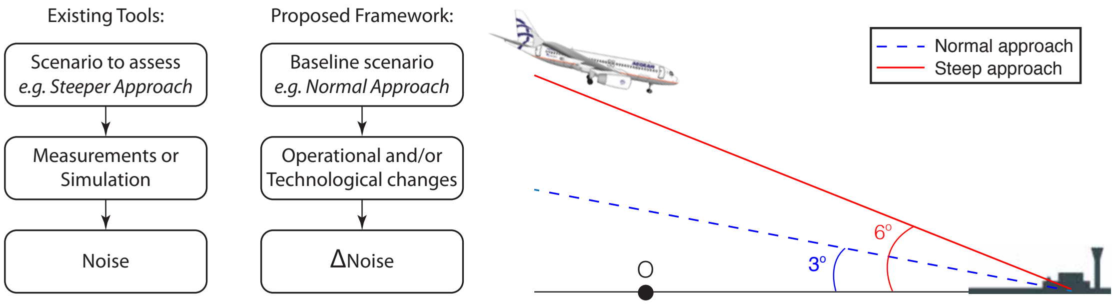

Figure 5.1: Left: Comparison between the flows of typical existing aircraft noise prediction tools and the proposed framework. Right: Vertical flight profiles of normal and steeper descent operations.

5.2 Linking parameter between noise and emissions

In order to relate noise with emissions it is required to detect and utilise a linking parameter. To achieve this, all parameters affecting noise and/or emissions are mapped in Table 5.1 along with their interdependencies. The resulting matrix notes the relationship between design and operating parameters (in the far-left vertical column) and parameters that affect noise and emissions (listed horizontally). The symbol X indicates dependence of vertical on horizontal parameters and vice-versa; so that both dependencies of e.g. fuel load on trajectory and wind on airspeed are noted. A weighting factor describing the relationships strength was originally used, but this was finally judged excessive for the purpose of the matrix. Ultimately, it is the number of relationships that determines how influential a given parameter is on noise and emissions. This analysis also enables trivial parameters to be defined and potentially neglected in calculations.

The interdependencies matrix implies that thrust is the most influential parameter for both noise and emissions. It determines the aircraft throttle setting and hence the engine fuel flow that relates to the CO_2 and LAQ emissions (see Section 2.3). Likewise, fuel flow sets the turbine inlet temperature that determines parameters affecting engine noise; as described in Chapter 2, these are the fan rotational speed, the jet velocity and the air mass flow rate. Airframe noise related parameters, such as airspeed and aircraft configuration (e.g. flap setting) are also thrust-reliant. Hence, it is convenient to express noise source changes as a function of thrust variation, as performed in Section 5.5.

5.3 The framework architecture

Figure 5.2 shows the flowchart of the proposed noise estimation framework, where elements are numbered for reference. The objective is to obtain the aircraft noise change (element 6) resulting from operational and/or technological changes (element 2). The processes to achieve the objective are described below.

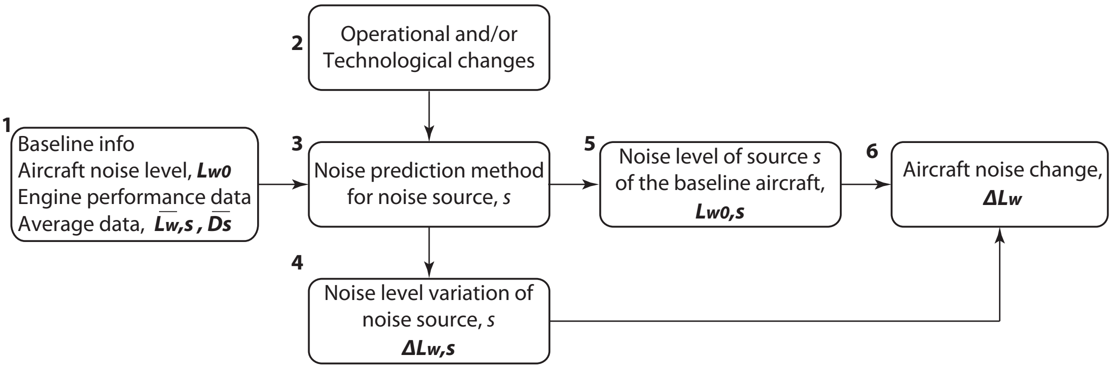

Figure 5.2: The proposed framework flowchart.

	Parameters affecting aircraft noise and emissions																															
	Noise																		Emissions			Operations			Aircraft and Performance						
	Generation						Propagation						Reception			Exposure									Weight						
Design or Operational Parameter	Ac. Power	Directivity	Frequency	Airspeed	A/c Config	Thrust	Air Absor.	Wind	Turbulence	Day or night	Humidity	Temperature	Reflections	Insulation	Back. Noise	Doppler	Seg. Length	Period T	CO2	Local Gases	Fuel burnt	Duration	Disatnce R	LTO cycle	No of PAX	Carriage	Fuel load	Wing Area	No of Eng.	Drag	**No of Dependencies**
Aircraft Conf.	X	X	X	X	■	X		X	X										X	X	X	X		X				X	X	X	**15**
Aircraft model	X	X	X		X	X													X	X	X			X	X	X	X	■	■		**12**
Airspeed	X	X	X	■	X	X		X	X							X	X	X	X	X	X	X								X	**15**
Altitude	X	X	X		X	X	X				X	X				X	X		X	X	X	X	X							X	**16**
Thrust	X	X	X	X	X	■	X	X	X		X	X							X	X	X	X		X	X	X	X	X	X	X	**21**
Trajectory		X	X	X	X	X	X									X	X	X	X	X	X	X	■	X			X				**15**
Weight	X		X	X	X	X													X	X	X			X	X	X	X	X	X	X	**15**

Table 5.1: Interdependencies matrix mapping the relationship between operational parameters and aircraft noise and emissions related factors. The total number of dependencies for each operational parameter is also shown.

5.4 Aircraft noise variation

This process yields the aircraft noise level change, which is the final output of the proposed noise estimation method (i.e. element 6 of the flowchart in Figure 5.2). According to the definitions in Chapter 2 the PWL of an aircraft consisting of n noise sources of acoustic power W_s is

$$\mathrm{L}w_0 = 10\log\left(\frac{\sum_{s=1}^{n} W_s}{W_{ref}}\right) \tag{5.1}$$

If acoustic power of sources j and f changes to $W_j + \Delta W_j$ and $W_f + \Delta W_f$ respectively, then PWL becomes:

$$\begin{aligned} \mathrm{L}w &= 10\log\left(\frac{\sum_{s=1}^{n} W_s + \Delta W_j + \Delta W_f}{W_{ref}}\right) = \\ &= 10\log\left[\frac{\sum_{s=1}^{n} W_s}{W_{ref}}\left(1 + \frac{\sum_{s=1}^{n} \Delta W_s}{\sum_{s=1}^{n} W_s}\right)\right] = \\ &= \mathrm{L}w_0 + 10\log\left(1 + \frac{\sum_{s=1}^{n} \Delta W_s}{\sum_{s=1}^{n} W_s}\right). \end{aligned} \tag{5.2}$$

Hence, the aircraft PWL change resulting from altering the acoustic power of n (or less) sources is expressed by the term:

$$\Delta \mathrm{L}w = 10\log\left(1 + \frac{\sum_{s=1}^{n} \Delta W_s}{\sum_{s=1}^{n} W_s}\right). \tag{5.3}$$

Acoustic power terms in Equation 5.3 can be written as function of the baseline PWL, $\mathrm{L}w_0$ and the PWL changes, $\Delta \mathrm{L}w_s$ calculated in Section 5.5. Equation 2.7 implies that

$$\sum_{s=1}^{n} W_s = W_{ref}\, 10^{Lw0/10}. \tag{5.4}$$

Also, the PWL of source s after a change $\Delta \mathrm{L}w_s$ is

$$\mathrm{L}w_{0,s} + \Delta \mathrm{L}w_s = 10 \log \left(\frac{W_s + \Delta W_s}{W_{ref}} \right) , \tag{5.5}$$

that can be solved for ΔW_s giving

$$\Delta W_s = W_{ref}\, 10^{\mathrm{L}w_{0,s}/10} \left(10^{\Delta \mathrm{L}w_s/10} - 1 \right) . \tag{5.6}$$

Hence, the aircraft PWL change in Equation 5.3 can be expressed as

$$\Delta \mathrm{L}w = 10 \log \left[1 + \frac{\sum_{s=1}^{n} 10^{\mathrm{L}w_{0,s}/10} \left(10^{\Delta \mathrm{L}w_s/10} - 1 \right)}{10^{Lw_0/10}} \right] . \tag{5.7}$$

Hence, inputs required to obtain the aircraft change, $\Delta \mathrm{L}w$, (flowchart element 6) are:

- The baseline aircraft PWL level, Lw_0, which is obtained from the publicly available NPD curves in ANP database [44], through the process described in Section 5.6.1.
- The noise variation, $\Delta \mathrm{L}w_s$ of individual sources that are estimated with the flowchart process 2-4 described in Section 5.5
- The individual noise source baseline levels, $\mathrm{L}w_{0,s}$, that are estimated with the flowchart process 1-5 described in Section 5.6.

Modelling the aircraft as a lumped source implies a uniform distance R between observer and each noise source. Hence, based on Equation 2.8, the SPL change due to $\Delta \mathrm{L}w$ is

$$\Delta \mathrm{L}p = \Delta \mathrm{L}w + 10 \log \left[\frac{D(\theta, \phi)}{D(\theta_0, \phi_0)} \right] - 20 \log \left(\frac{R}{R_0} \right) . \tag{5.8}$$

The lumped aircraft directivity is obtained from the directivity definition (Equation 2.2)

$$D(\theta, \phi) = \frac{\sum_{s=1}^{n} W_s D_s(\theta, \phi)}{\sum_{s=1}^{n} W_s} = \frac{\sum_{s=1}^{n} \left[10^{Lw_s/10} D_s(\theta, \phi) \right]}{10^{Lw/10}} . \tag{5.9}$$

With t and k being the time index and the total number of discrete SPL measurements respectively, and if Δt is the time increment, the SEL under the new conditions can be expressed as:

$$\mathrm{L}_{AE} = 10 \log \left[\sum_{t=1}^{k} 10^{\frac{Lp_t + \Delta Lp_t}{10}} \Delta t \right] . \tag{5.10}$$

Algebraic operations shown in Appendix B lead to the following SEL change expression:

$$\Delta \mathrm{L}_{AE} = 10\log\left[1 + \frac{C\Delta t \sum_{t=1}^{k}\sum_{s=1}^{n}\left[\frac{\Delta W_s D_{s,t}}{R_t^2}\right]}{10^{\mathrm{L}_{AE}/10}}\right], \tag{5.11}$$

where C is the constant defined in Equation 2.4, whereas L_{AE} refers to the conditions before the acoustic power changes.

5.5 Noise variation of individual sources (process 2-4)

The vertical flowchart process 2-4 estimates the noise variation of individual noise sources resulting from mitigation strategies, i.e. operational and/or technological changes. This is achieved through dedicated, publicly available noise prediction methods for individual aircraft sources (element 3), such as the ones presented in Section 3.3 of this thesis.

If method M predicts the noise level L_s of source s and L_s is a function of parameters $\zeta_0, \xi_0, ..., \psi_0$; then

$$\mathrm{L}_s = f(\zeta_0, \xi_0, ..., \psi_0)\,. \tag{5.12}$$

If parameters ζ_0, ψ_0 become ζ, ψ as a result of implementing a new mitigation strategy, while ξ_0 remains fixed, the noise level becomes

$$\mathrm{L}_s' = f(\zeta, \xi_0, ..., \psi)\,. \tag{5.13}$$

While is it hard to accurately assess L_s' due to the numerous parameters required, it is feasible to calculate, or at least obtain good estimates of the noise level change

$$\Delta \mathrm{Lw}_s = 10\log\left[\frac{f(\zeta, \xi_0, ..., \psi)}{f(\zeta_0, \xi_0, ..., \psi_0)}\right] \tag{5.14}$$

between these two conditions. This is because fixed parameters (e.g. geometry data) become redundant in incremental changes estimations. As shown later in Section 5.5.5, $\Delta \mathrm{Lw}_s$ is a function of few parameters estimated based on publicly available information.

5.5.1 Framework configuration

It must be emphasised that the proposed framework is independent of specific prediction methods and can use any potential new model for existing or new noise sources. Also, the aircraft is modelled as a single (lumped) directional source consisting of (user-defined) appropriate sources. In this context, the framework demonstrations in Chapters 7–9 only consider the significant noise sources of turbofan aircraft, i.e. the fan, jet and airframe, as discussed in Section 2.1.8; whereas the specific noise prediction methods employed are Heidmann's [117] for fan noise, Fink's [118] for airframe noise and Lighthill's acoustic analogy [52] for jet noise. Based on these methods, there is derived below the formulas describing the noise variation of these sources with thrust, which was found in Section 5.2 to be a common descriptive parameter for both noise and emissions.

5.5.2 Jet noise change with thrust variation

Taking into account Lighthill's acoustic analogy (Equation 3.1) and the definition of acoustic power in Section 2.1.1, the following can be written for the jet acoustic power:

$$W_j \propto \rho_j A_j V_j^8 \,. \tag{5.15}$$

Considering the definition of thrust in Section 2.6.2 and the relationship $\dot{m} = \rho_j A_j V_j$, thrust can be directly introduced in Equation 5.15. However, it is more convenient to introduce the gross thrust, F_G, instead (Equation 2.31) and account for flight speed effects by replacing V_j by an effective jet speed, V_e, such as the one proposed by Michel [155], given by

$$V_e = V_j \left(\frac{V_j - V_0}{V_j} \right)^{\frac{m-1}{n-2}} \,, \tag{5.16}$$

where exponents m, n depend on polar angle. This study adopts the values $m = 5.5$, $n = 8$ that correspond to unheated jets at $\theta = 90°$. Since $F_G \propto V_j^2$, relationship 5.15 ultimately becomes

$$W_j \propto F_G V_e^6 \,. \tag{5.17}$$

Thus, jet PWL change due to a change of gross thrust can be expressed as:

$$\Delta Lw_j = 10 \log \frac{F'_G}{F_G} + 60 \log \frac{V'_e}{V_e} \,, \tag{5.18}$$

where the values corresponding to the condition after the thrust change are denoted by an accent. The relationships above assume ideally expanded nozzle so that any jet velocity effects on jet area (described in reference [156]) are considered negligible, i.e. the effective jet area is assumed equal to the geometric area.

5.5.3 Airframe noise change with thrust variation

In contrast to the jet noise case, thrust variation, which mainly affects engine noise, does not have a direct effect on airframe noise, but an indirect one due to potential airspeed variation. This is confirmed by deriving the expression below for the PWL variation of airframe component c, starting from Fink's airframe noise method [118] (Equation 3.7)

$$\Delta Lw_{a,c} = 10 \log \frac{G'_c}{G_c} + 10a \log \frac{V'_0}{V_0} \,, \tag{5.19}$$

Each airframe component is associated with fixed values for constants a, K and a specific expression for function G, as detailed in ANOPP [16]. The only exception is flaps, where G varies with deflection angle. Thus, it is apparent that for a fixed aircraft, parameters influencing airframe noise are: a) airspeed, b) flap deflection angle, and c) landing gear state (deployed or retracted). The effect of angle-of-attack on slat trailing edge noise revealed in [64] is considered negligible for the purposes of the present research.

Assuming fixed landing gear state and airspeed, the PWL change relationship due to flap deflection angle variation is derived next. For flaps, ANOPP [16] gives $a = 5$ and

$$G_f = \frac{A_f}{{b_w}^2} \sin^2 \delta_f \,, \tag{5.20}$$

where A_f and b_w are the flap area and wing span respectively, whereas δ_f stands for the flap deflection angle in degrees. For a fixed flap type and airspeed, variables A_f, b_w, a and V_0 remain constant and hence cancel out when substituted in Equation 5.19. Therefore, flap PWL variation due to deflection angle change simplifies to:

$$\Delta Lw_{a,f} = 10 \log \frac{\sin^2 \delta'_f}{\sin^2 \delta_f} \,. \tag{5.21}$$

5.5.4 Fan noise change with thrust variation

The total temperature rise across a fan stage with isentropic efficiency η_c is given by [18]

$$\Delta T = \frac{{V_{j,b}}^2 - {V_0}^2}{2 c_p \eta_c} \,. \tag{5.22}$$

Inserting this in Heidmann's formula for fan noise (Equation 3.5), where, for now, the term $f(\text{design})$ is ignored, whereas $\dot{m}_a$ is substituted using Equation 2.31, yields a generic expression for the fan PWL variation with gross thrust

$$\Delta \mathrm{L}w_{f,0} = 20 \log \left(\frac{{V'_{j,b}}^2 - {V'_0}^2}{{V_{j,b}}^2 - {V_0}^2} \right) + 10 \log \left(\frac{F'_G}{F_G} \right) - 10 \log \left(\frac{V'_{j,m}}{V_{j,m}} \right) \,. \tag{5.23}$$

Assuming that the inlet velocity equals the aircraft airspeed, so that $\dot{m}_a \propto V_0 {d_f}^2$, Equation 5.23 can be recast in terms of the fan diameter, d_f, giving

$$\Delta\mathrm{L}w_{f,0} = 20\log\left(\frac{{V'_{j,b}}^2 - {V'_0}^2}{{V_{j,b}}^2 - {V_0}^2}\right) + 10\log\left(\frac{V'_0{d'_f}^2}{V_0{d_f}^2}\right)\,. \tag{5.24}$$

The generic fan noise change, $\Delta Lw_{f,0}$, is corrected to yield the change of individual fan noise components, using Heidman's function f(design), as shown in the next paragraph.

5.5.4.1 Evaluation of f(design) change for each fan noise component

As discussed in Section 3.3 function

$$f(\text{design}) = F1 + F2 + F3 + F4 \tag{5.25}$$

included in Heidmann's formula for fan noise (Equation 3.5) determines the noise characteristics and differences between fan noise components, as well as the effect of operational parameters on the noise generated. In summary, term $F1$ expresses the influence of the operating tip Mach number, term $F2$ represents a level correction related to the rotor-stator spacing, whereas terms $F3$ and $F4$ represent directivity and spectrum content functions respectively. Each fan component is assigned a different function f(design). Expressions for $F1$, $F2$, $F3$ and $F4$ for each fan noise component are given by Heidmann [117], however other authors have proposed revised versions, as discussed in Section 3.3.

Noise level differences arising from directivity and spectral properties alterations can be expressed as a $\Delta F3$ and a $\Delta F4$ respectively. Also, with RSS being a percentage rotor-stator spacing factor that depends upon whether the engine has inlet guide vanes or not [137], term $F2$ is given by [117]

$$F2 = -5\log\left(\frac{RSS}{300}\right) \tag{5.26}$$

and therefore, noise changes, e.g. due to altering the stators number can be expressed by a term

$$\Delta F2 = 5\log\frac{RSS}{RSS'}\,. \tag{5.27}$$

Term $F1$ is a function describing the effect of operational parameters on the noise generated by each fan component. It is a function of the operating tip Mach number, M_T and the relative operating tip Mach number, M_{TR}, which introduces the effect of flight speed. Function $F1$ is expressed by different formulas depending on the value of $M_{TR,D}$, which is the M_{TR} at maximum thrust setting. $M_{TR,D}$ is estimated with

$$M_{TR,D} = \frac{\pi d_f}{60c}N1_{\infty}\,, \tag{5.28}$$

where the maximum LPR speed, $N1_{\infty}$, is available in the EASA type certificates [51].

The remaining parameters in Equation 5.28 are publicly available and hence, $M_{TR,D}$ for the aircraft relevant to this thesis are calculated and outlined in Table 5.2. Since $M_{TR,D} > 1$ for all aircraft, the upcoming calculations for determining term $F1$ for each individual source, exclude cases where $M_{TR,D} \leqslant 1$.

Table 5.2: Values of $M_{TR,D}$ for representative aircraft.

Aircraft	CRJ900–ER	A320–232	737–400	737–800	A330–301	777–300	747–400
$\mathbf{M_{TR,D}}$	1.468	1.391	1.357	1.273	1.319	1.408	1.582

Fan inlet broadband noise

According to Heidmann, $F1$ for the inlet broadband noise component is given by:

$$F1 = \begin{cases} L + 20\log(M_{TR,D}) & \text{if } M_{TR} \leqslant 0.9\,, \\ L + 20\log(M_{TR,D}) - 20\log\left(\dfrac{M_{TR}}{0.9}\right) & \text{if } M_{TR} > 0.9\,, \end{cases} \tag{5.29}$$

where L is a reference level. Hence, the change of $F1$ between two engines is

$$\Delta F1 = \begin{cases} 20\log\left(\dfrac{M'_{TR,D}}{M_{TR,D}}\right) & \text{if } M_{TR}, M'_{TR} \leqslant 0.9\,, \\ 20\log\left(\dfrac{M'_{TR,D}\,M_{TR}}{M_{TR,D}\,M'_{TR}}\right) & \text{if } M_{TR}, M'_{TR} > 0.9\,, \\ -20\log\left(\dfrac{M_{TR,D}\,M'_{TR}}{0.9\,M'_{TR,D}}\right) & \text{if } M_{TR} \leqslant 0.9, M'_{TR} > 0.9\,, \\ 20\log\left(\dfrac{M'_{TR,D}\,M_{TR}}{0.9\,M_{TR,D}}\right) & \text{if } M_{TR} > 0.9, M'_{TR} \leqslant 0.9\,. \end{cases} \tag{5.30}$$

For a fixed engine (i.e. fixed $M_{TR,D}$), the change of $F1$ between two different throttle settings is:

$$\Delta F1 = \begin{cases} 0 & \text{if } M_{TR}, M'_{TR} \leqslant 0.9\,, \\ 20\log\left(\dfrac{M_{TR}}{M'_{TR}}\right) & \text{if } M_{TR}, M'_{TR} > 0.9\,, \\ -20\log\left(\dfrac{M'_{TR}}{0.9}\right) & \text{if } M_{TR} \leqslant 0.9, M'_{TR} > 0.9\,, \\ 20\log\left(\dfrac{M_{TR}}{0.9}\right) & \text{if } M_{TR} > 0.9, M'_{TR} \leqslant 0.9\,. \end{cases} \tag{5.31}$$

Fan exhaust broadband noise

Heidmann establishes term $F1$ for the exhaust broadband noise component as:

$$F1 = \begin{cases} L + 20\log(M_{TR,D}) & \text{if } M_{TR} \leqslant 1.0\,, \\ \\ L + 20\log(M_{TR,D}) - 20\log(M_{TR}) & \text{if } M_{TR} > 1.0\,, \end{cases} \tag{5.32}$$

where L is a reference level. Hence, the change of $F1$ between two engines is

$$\Delta F1 = \begin{cases} 20\log\left(\dfrac{M'_{TR,D}}{M_{TR,D}}\right) & \text{if } M_{TR}, M'_{TR} \leqslant 0.9\,, \\ 20\log\left(\dfrac{M'_{TR,D}\,M_{TR}}{M_{TR,D}\,M'_{TR}}\right) & \text{if } M_{TR}, M'_{TR} > 0.9\,, \\ -20\log\left(\dfrac{M_{TR,D}\,M'_{TR}}{M'_{TR,D}}\right) & \text{if } M_{TR} \leqslant 0.9, M'_{TR} > 0.9\,, \\ 20\log\left(\dfrac{M'_{TR,D}\,M_{TR}}{M_{TR,D}}\right) & \text{if } M_{TR} > 0.9, M'_{TR} \leqslant 0.9\,. \end{cases} \tag{5.33}$$

whereas, for a fixed engine (i.e. fixed $M_{TR,D}$), the change of $F1$ between two different throttle settings is:

$$\Delta F1 = \begin{cases} 0 & \text{if } M_{TR}, M'_{TR} \leqslant 1.0\,, \\ \\ 20\log\left(\dfrac{M_{TR}}{M'_{TR}}\right) & \text{if } M_{TR}, M'_{TR} > 1.0\,, \\ -20\log(M'_{TR}) & \text{if } M_{TR} \leqslant 1.0, M'_{TR} > 1.0\,, \\ \\ 20\log(M_{TR}) & \text{if } M_{TR} > 1.0, M'_{TR} \leqslant 1.0\,. \end{cases} \tag{5.34}$$

Fan inlet discrete tone noise

Term $F1$ for the inlet discrete tone noise is given by:

$$F1 = \begin{cases} L + 20\log(M_{TR,D}) & \text{if } M_{TR} \leqslant 0.72\,, \\ \\ L + 20\log(M_{TR,D}) + 50\log\left(\dfrac{M_{TR}}{0.72}\right) & \text{if } M_{TR} > 0.72\,, \end{cases} \tag{5.35}$$

where L is a reference level, which for comparison purposes is redundant.

It follows from the Equation above that the change of $F1$ between two engines is

$$\Delta F1 = \begin{cases} 20\log\left(\dfrac{M'_{TR,D}}{M_{TR,D}}\right) & \text{if } M_{TR}, M'_{TR} \leqslant 0.72\,, \\ 20\log\left(\dfrac{M'_{TR,D}}{M_{TR,D}}\right) + 50\log\left(\dfrac{M'_{TR}}{M_{TR}}\right) & \text{if } M_{TR}, M'_{TR} > 0.72\,, \\ 20\log\left(\dfrac{M'_{TR,D}}{M_{TR,D}}\right) + 50\log\left(\dfrac{M'_{TR}}{0.72}\right) & \text{if } M_{TR} \leqslant 0.72, M'_{TR} > 0.72\,, \\ 20\log\left(\dfrac{M'_{TR,D}}{M_{TR,D}}\right) - 50\log\left(\dfrac{M_{TR}}{0.72}\right) & \text{if } M_{TR} > 0.72, M'_{TR} \leqslant 0.72\,. \end{cases} \tag{5.36}$$

For a fixed engine (i.e. fixed $M_{TR,D}$), the change of $F1$ between two different throttle settings is:

$$\Delta F1 = \begin{cases} 0 & \text{if } M_{TR}, M'_{TR} \leqslant 0.72\,, \\ 50\log\left(\dfrac{M'_{TR}}{M_{TR}}\right) & \text{if } M_{TR}, M'_{TR} > 0.72\,, \\ 50\log\left(\dfrac{M'_{TR}}{0.72}\right) & \text{if } M_{TR} \leqslant 0.72, M'_{TR} > 0.72\,, \\ -50\log\left(\dfrac{M_{TR}}{0.72}\right) & \text{if } M_{TR} > 0.72, M'_{TR} \leqslant 0.72\,. \end{cases} \tag{5.37}$$

Fan buzz-saw noise

According to Heidmann's method, $F1$ for the inlet combination noise component is calculated for the sub-harmonics of the blade passing frequency f_b. The exact formulations depend on $M_{TR,D}$. Including only the $M_{TR,D}$ cases corresponding to the aircraft used in this thesis (see Table 5.2), the change of $F1$ between two different throttle settings is:

$$\Delta F1 = \begin{cases} 14.11(M_{TR} - M'_{TR}) & \text{for } \frac{1}{2} f_b \text{ and } M_{TR,D} > 1.146\,, \\ 147.51(M'_{TR} - M_{TR}) & \text{for } \frac{1}{4} f_b \text{ and } M_{TR,D} \leqslant 1.322\,, \\ 13.23(M_{TR} - M'_{TR}) & \text{for } \frac{1}{4} f_b \text{ and } M_{TR,D} > 1.322\,, \\ 67.54(M'_{TR} - M_{TR}) & \text{for } \frac{1}{8} f_b \text{ and } M_{TR,D} \leqslant 1.610\,, \\ 12.05(M_{TR} - M'_{TR}) & \text{for } \frac{1}{8} f_b \text{ and } M_{TR,D} > 1.610\,, \end{cases} \tag{5.38}$$

5.5.4.2 Overall level change of each fan noise component

An important observation from the Equations yielding $\Delta F1$ is that reference level L and term $M_{TR,D}$ cancel out, so that $\Delta F1$ only depends on M_{TR}. Assuming that inlet static density and speed of sound have their ambient values, ANOPP [16] defines M_{TR} as:

$$M_{TR} = \sqrt{{M_T}^2 + {M_0}^2}\,, \tag{5.39}$$

where M_0 is the axial flow Mach number that is approximated with the aircraft speed.

M_T can be obtained from Equation 5.28 using the operational LPR speed $N1$.

$$F_G \propto N1^2 \,, \text{or } F_G = \beta N1^2 \,, \tag{5.40}$$

where β is a constant that can be approximated by using the (publicly available) rated values of thrust and $N1$ into Equation 5.40. The assumed relationship 5.40 is justified by the following facts:

- Froude's Momentum Theory [25],
- Cumpsty's [18] suggestion that $\Delta P_{fan} \underset{\sim}{\propto} N1^2$ and $F_G \propto \Delta P_{fan}$,
- Hill's [157] suggestions that $T_{t4} \propto N1^2$ and $V \propto \sqrt{T_{t4}}$.

Solving Equation 5.40 for $N1$ and substituting in Equation 5.28 yields:

$$M_T = \frac{\pi d_f}{60c} \sqrt{\frac{F_G}{\beta}} \,. \tag{5.41}$$

Substituting into Equation 5.39 gives the relationship between M_{TR} and gross thrust. Knowledge of M_{TR} determines the applicable case in the above $\Delta F1$ Equations. The overall change of the PWL of fan component i due to a change of thrust is obtained by combining Equation 5.23 and the relevant Equation for $\Delta F1$:

$$\Delta \mathrm{L}w_{f,i} = \Delta Lw_{f,0} + \Delta F1_i \,. \tag{5.42}$$

5.5.5 Estimation of inputs to the noise sources variation equations

This section presents the methodology to estimate the unknown inputs to the noise variation equations for individual sources (i.e. Equations 5.19, 5.18, 5.23 given above). These are the mixed, core and bypass jet velocities, as well as the gross thrust. The methodology uses the concept of the equivalent single stream engine defined in Section 2.6.3. By definition [18], the rated jet mixed velocity of the equivalent engine is the ratio of the maximum static thrust, F_∞ that is available in the ANP Database [44], and the associated engine airflow $\dot{m}_{a,0}$ that is obtained from the databases listed in Table 4.2:

$$V_{j,m,\infty} = \frac{F_\infty}{\dot{m}_{a,\infty}} \,. \tag{5.43}$$

Then, the geometric jet area is calculated with[1]:

$$A_j = \frac{\dot{m}_{a,\infty}}{\rho_{j,\infty} V_{j,m,\infty}} \,, \tag{5.44}$$

---

[1] As mentioned in Section 5.5.2 any effective area effects [156] are ignored.

where $\rho_{j,\infty}$ is the fully expanded jet density that can be acquired from:

$$\rho_{j,\infty} = \frac{P_a}{\Re T_{tj,\infty}}\,, \tag{5.45}$$

where P_a is the atmospheric pressure, whereas $\Re$ denotes the specific gas constant of air. The total mixed jet temperature at rated thrust, $T_{tj,\infty}$, is calculated with Equation 2.38; the individual streams exhaust temperatures, $T_{t,19}$, $T_{t,9}$, that are required by that Equation are obtained from the turbofan engine thermodynamic analysis in Section 6.2. This is done under the assumption that the core stream jet temperature at rated thrust is equal to the operational limit of the LPT exit temperature, T_{t5}, which is available in the EASA TCDS certificates [51].

Having calculated A_j, then for any given net thrust F_N and airspeed V_0, the mixed jet velocity is the positive root of the polynomial

$${V_{j,m}}^2 - V_0 V_{j,m} - \frac{F_N}{\rho_j A_j} = 0\,, \tag{5.46}$$

that derives from the net thrust definition. Having acquired the mixed jet velocity, it is straightforward to calculate the gross thrust:

$$F_G = \rho_j A_j {V_{j,m}}^2\,. \tag{5.47}$$

An expression for the bypass stream jet velocity, which is the remaining parameter required for assessing the fan level change in Equation 5.23, is directly worked out starting from the fact that the total engine thrust is the sum of that generated by each stream. With μ being the BPR, the final expression is:

$$V_{j,b} = \frac{V_{j,m}(1+\mu) - V_c}{\mu}\,. \tag{5.48}$$

In the equations above, the jet density ρ_j and the core velocity V_c are estimated using the engine cycle thermodynamic analysis presented in Section 6.2.

5.6 Individual noise source baseline levels (process 1-5)

The proposed framework flowchart in Figure 5.2 shows that translating the individual noise source variations estimated in Section 5.5 (element 4) into variation of the whole aircraft requires the PWL, $\mathrm{L}w_{0,s}$, of each individual source, s, of the baseline aircraft (element 5). Levels $\mathrm{L}w_{0,s}$ are normally proprietary to manufacturers. Obtaining them experimentally is hard, due to difficulties in isolating each source contribution, whereas calculating them through engineering models could be impeded by lack of inputs and complexity. Hence, the framework approximates individual source levels $\mathrm{L}w_{0,s}$ through the horizontal flowchart process 1-5 that exploits three publicly available components:

- NPD data for the baseline aircraft, obtainable from the ANP database [44],
- Average noise levels of individual noise sources, for each aircraft-size category at takeoff and landing conditions, obtainable from the NASA dataset in [65],
- Noise prediction methods for each source, like the ones presented in Section 3.3.

The general idea involves reproducing $\mathrm{L}_{A,max}$ NPD curves for baseline scenarios and fitting them to the published ones. The variables in this fitting process are the sought baseline noise source levels $Lw_{0,s}$ that are initially assigned the values of the average levels $\overline{\mathrm{L}w_s}$ provided by NASA [65]. $\overline{\mathrm{L}w_s}$ are fine-tuned until the error ε between predicted and published NPD curves is minimum. The procedure is detailed below.

To begin with, the sought baseline noise source levels (flowchart element 5) are written as the sum of the averages and a correction α_s, respective to each source s:

$$\mathrm{L}w_{0,s} = \overline{\mathrm{L}w_s} + \alpha_s \,. \tag{5.49}$$

This is illustrated in Figure 5.3, where for each noise source, s, the blue bar represents the average, $\overline{\mathrm{L}w_s}$, whereas the sought (fine-tuned) baseline noise source level, $\mathrm{L}w_{0,s}$, is denoted by the red dotted bar. To avoid unrealistic results, two conditions are required; a) corrections α_s are restricted to within 3 dB, and b) the sum of $\mathrm{L}w_{0,s}$ should equal the baseline aircraft noise level

$$\mathrm{L}w_0 = 10\log\left(\sum_{s=1}^{n} 10^{\frac{\mathrm{L}w_{0,s}}{10}}\right) . \tag{5.50}$$

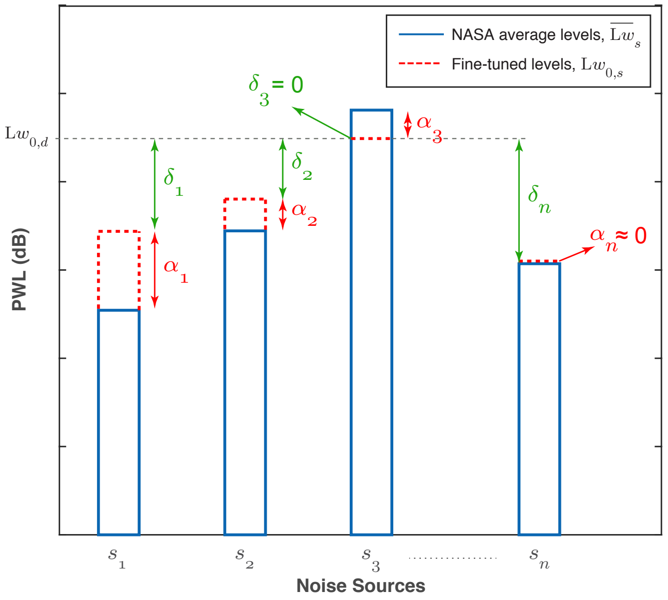

Figure 5.3: Graphical representation of correction α_s and level difference δ_s for each noise source s.

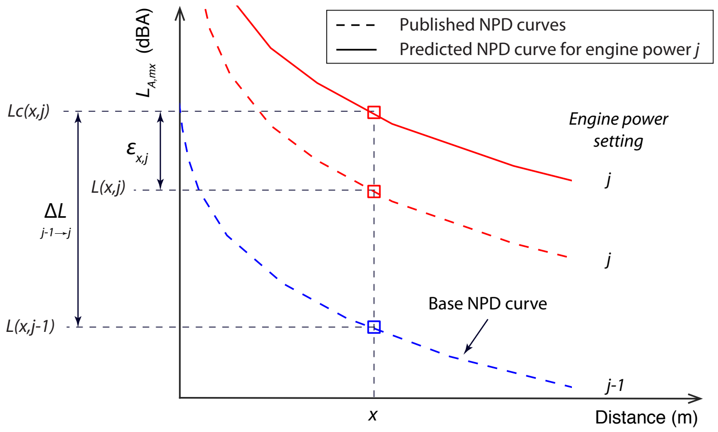

Figure 5.4: Graphical interpretation of the procedure to obtain individual noise source levels, $\mathrm{L}w_{0,s}$, of the baseline aircraft.

Next, with reference to Figure 5.4, a baseline point on the $\mathrm{L}_{A,max}$ NPD curves must be chosen, corresponding to an engine power setting $j-1$, distance x and maximum level $L(x, j-1)$. In choosing that point it must be considered that relative level differences between sources vary with engine power. Hence, since NASA averages correspond to certification conditions, they are only representative for certain NPD thrust settings. The theoretical net thrust, F_N, required by each aircraft at certification conditions can be estimated by the SAE-AIR 1845 [45] procedure described in Section 2.7. Alternatively, NASA [65] provides average F_N requirements for each aircraft-size category. The point chosen should belong to the NPD curve associated with thrust values around F_N.

5.6.1 Calculation of aircraft PWL from NPD curves

The level corresponding to the chosen NPD point is back-propagated (with Equation 2.8) to the aircraft yielding the aircraft PWL, $\mathrm{L}w_0$. Looking back in Figure 2.6 that sketches the NPD experimental procedure, the back-propagation distance R_p is a function of the polar angle θ_p at the time of $\mathrm{L}_{A,max}$ occurence, i.e.

$$R_P = \frac{R_{SL}}{\sin(\theta_P)}\,. \tag{5.51}$$

NASA [65] provides average values of angle θ_P. Aircraft lumped directivity D can be calculated with Equation 5.9 using source directivity data found in ANOPP [16].

5.6.2 Calculation of individual source levels from aircraft PWL

Having acquired $\mathrm{L}w_0$, fine-tuned levels $\mathrm{L}w_{0,s}$ from Equation 5.49 are shifted, in order to satisfy the condition in Equation 5.50. The shifting is required because levels $\mathrm{L}w_{0,s}$ actually give the relative differences between noise sources rather than the absolute levels. Hence, the logarithmic sum of the fine-tuned averages yields a 'fine-tuned' noise level, $\mathrm{L}w_R$, for the whole aircraft, that is different than $\mathrm{L}w_0$. The level difference, δ_s, of each source, s, from the dominant level, $\mathrm{L}w_{0,d}$, is indicated in green colour in Figure 5.3 and can be expressed as:

$$\Delta_{L0} = \begin{bmatrix} \delta_1 & \ldots & 0 & \ldots & \delta_n \end{bmatrix} . \tag{5.52}$$

Assuming that these differences do not vary with relatively small distance changes, then using Equation 5.50 the baseline PWL can be decomposed as:

$$\begin{aligned} \mathrm{L}w_0 &= 10\log\left(10^{\frac{\mathrm{L}w_{0,d}+\delta_1}{10}} + \ldots + 10^{\frac{\mathrm{L}w_{0,d}+\delta_n}{10}}\right) \\ &= 10\log\left[10^{\frac{\mathrm{L}w_{0,d}}{10}}\left(\sum_{i=1}^{n} 10^{\frac{\Delta_{L0,i}}{10}}\right)\right] . \end{aligned} \tag{5.53}$$

Solving for the dominant level $\mathrm{L}w_{0,d}$, which is the only unknown parameter in Equation 5.64 yields

$$\mathrm{L}w_{0,d} = \mathrm{L}w_0 - 10\log\left(\sum_{i=1}^{n} 10^{\frac{\Delta_{L0,i}}{10}}\right) . \tag{5.54}$$

Hence, the shifted (i.e. corresponding to the baseline aircraft PWL and hence satisfying Equation 5.50) individual noise source levels are given by

$$\mathrm{L}w_{0,s} = \mathrm{L}w_{0,d} + \Delta_{L0} . \tag{5.55}$$

5.6.3 Calculation of error ε

The next step is estimating the level variation $\Delta\mathrm{L}w_s$ of each noise source due to the engine power setting change from $j-1$ to j. This is done through the procedure in Section 5.5, i.e. flowchart process 2-4. Variation $\Delta\mathrm{L}w_s$ is then substituted into Equation 5.7 along with levels $\mathrm{L}w_{0,s}$ from Equation 5.55 to obtain the whole aircraft PWL variation, $\Delta\mathrm{L}w$ (flowchart element 6). Aircraft lumped directivity is updated with Equation 5.9 to reflect the corrected levels $\mathrm{L}w_{0,s}$. SPL variation $\Delta\mathrm{L}(x,j)$ can now be obtained from Equation 5.8, leading to calculating NPD level $\mathrm{L}c(x,j)$. This procedure is repeated for different corrections α_s until obtaining the minimum error ε at any distance x and engine power j

$$\varepsilon_{x,j} = \left|\mathrm{L}c(x,j) - \mathrm{L}_0(x,j)\right| . \tag{5.56}$$

The resulting levels $\mathrm{L}w_{0,s}$ are accepted as the source levels of the baseline aircraft.

5.7 Procedure for constructing computed NPDs

This paragraph demonstrates the procedure for generating NPD curves computationally. This is an important capability of the proposed noise estimation framework since it allows construction of noise exposure maps for new scenarios including novel aircraft and unconventional operations, despite the lack of experimental data. Examples of this capability are given in Chapters 7-9, where NPD curves are derived for electric aircraft concepts, an hypothetic HWB aircraft and for steeper operations.

5.7.1 Derivation of $\mathrm{L}_{A,max}$ NPD curves

Figure 5.5 demonstrates that $\Delta\mathrm{L}_p(d,j)$ can be added to an experimentally-known baseline NPD level $\mathrm{L}_{p,0}(d,j)$ (marked with a cross) to yield the aircraft L_p reflecting to the new scenario at the same power setting and slant distance, so

$$\mathrm{L}_p(d,j) = \mathrm{L}_{p,0}(d,j) + \Delta\mathrm{L}_p(d,j)\,. \tag{5.57}$$

The levels at the remaining engine power settings at the same distance d are obtained by adding the noise level variation resulting from changing the engine power setting from j to $j+1$, so that

$$\mathrm{L}_p(d,j+1) = \mathrm{L}_p(d,j) + \Delta\mathrm{L}_p(j \rightarrow j+1)\,. \tag{5.58}$$

In Equations 5.57, 5.58, changes $\Delta\mathrm{L}_p$ are estimated with Equations 5.7, 5.8 by following the methodology described earlier in this Chapter. Once levels $\mathrm{L}_p(d)$ are estimated for all NPD engine power settings, they are decomposed into $1/3^{rd}$-octave bands, as described in Section 5.7.3, and then propagated to the remaining NPD distances r through the SAE AIR1845 computational step (detailed in reference [45]). This yields all levels $\mathrm{L}_p(r)$ that are required to develop the complete $\mathrm{L}_{A,max}$ NPD curves.

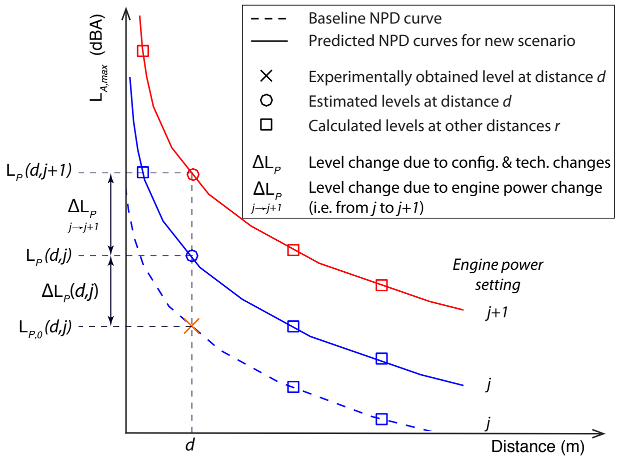

Figure 5.5: Schematic representation of deriving computational NPD curves.

5.7.2 Derivation of SEL NPD curves

SAE AIR 1845 [45] computes the SEL, L_{AE}, at NPD distances r with

$$\mathrm{L}_{AE}(r) = \mathrm{L}_{AE}(d) + [\mathrm{L}_p(r) - \mathrm{L}_p(d)] + 7.5\log(r/d)\,, \tag{5.59}$$

With reference to the test flyover of Figure 2.6, the SEL at slant distance d is [32]:

$$\mathrm{L}_{AE}(d) = 10\log\left(\int_{t_1}^{t_2} 10^{\frac{\mathrm{Lp(t)}}{10}}\,\mathrm{dt}\right)\,, \tag{5.60}$$

where the interval $[t_1, t_2]$ correspond to the flyover period when the instantaneous SPL,

$$\mathrm{L}_p(t) = Lw + 10\log\left[\frac{D(\theta(t))}{R(t)^2}\right] + C\,, \tag{5.61}$$

is within 10 dB of $\mathrm{L}_{A,max}$. Considering an airspeed of 160 knots and a time increment of 0.5 seconds, as recommended by the SAE AIR1845 procedure [45], distances $R(t)$ and polar angles $\theta(t)$ corresponding to each time increment of the test flyover are calculated. Hence, directivities $D(\theta(t))$ are obtained through interpolation across custom or existing directivity databases, like the one in ANOPP [16]. Resulting values of $\mathrm{L}_p(t)$ are inserted in Equation 5.61 to yield the SPLs required to calculate $\mathrm{L}_{AE}(d)$ with Equation 5.60. $\mathrm{L}_{AE}(d)$ is substituted in Equation 5.59 to give the $\mathrm{L}_{AE}(r)$ and develop the SEL NPDs.

5.7.3 Decomposition of NPD $\mathrm{L}_{A,max}$ into one-third octave bands

The SAE AIR 1845 computational part propagates calculated levels $\mathrm{L}_p(d)$ into the remaining NPD distances, by applying atmospheric attenuation effects. This requires sound levels to be in octave or $1/3^{rd}$-octave bands. This Section describes the procedure for decomposing any given NPD L_p into $1/3^{rd}$-octave bands.

The ANP Database [44] assign each aircraft two un-weighted spectral classes, one for approach and one for departure. ECAC Doc 29 [104] clarifies that these classes are average spectral shapes for aircraft with resembling spectral characteristics referring to the time when $\mathrm{L}_{A,max}$ occurs. Average spectral shapes, $\overline{S}$ consist of 24 one-third octave band levels $\overline{L_b}$, for the centre-frequencies from 50 Hz to 10 kHz, so that

$$\overline{S} = \left[\begin{array}{ccc} \overline{L}_{b,1} & ... & \overline{L}_{b,24} \end{array}\right]. \tag{5.62}$$

Each band's level difference from the maximum one, $\overline{L}_{b,max}$, can be expressed as:

$$\Delta S = \left[\begin{array}{ccccc} \sigma_1 & ... & 0 & ... & \sigma_n \end{array}\right]. \tag{5.63}$$

Assuming that relative differences, ΔS, between bands remain unchanged for small aircraft noise level changes, then any NPD level, L_p, can be decomposed into $1/3^{rd}$-octave bands with

$$\begin{aligned}\mathrm{L}_p &= 10\log\left(10^{\frac{\mathrm{L}_{b,max}+\sigma_1}{10}} + \ldots + 10^{\frac{\mathrm{L}_{b,max}+\sigma_{24}}{10}}\right)\\ &= 10\log\left[10^{\frac{\mathrm{L}_{b,max}}{10}}\left(\sum_{i=1}^{24} 10^{\frac{\Delta S_i}{10}}\right)\right]. \end{aligned} \tag{5.64}$$

Solving for the maximum $1/3^{rd}$-octave band level, $\mathrm{L}_{b,max}$, gives

$$\mathrm{L}_{b,max} = \mathrm{L}_p - 10\log\left(\sum_{i=1}^{24} 10^{\frac{\Delta S_i}{10}}\right). \tag{5.65}$$

Hence, the $1/3^{rd}$-octave band levels composing NPD level L_p will be:

$$S = \mathrm{L}_{b,max} + \Delta_S\,. \tag{5.66}$$

5.8 Methodology summary

This chapter described the methodology of the proposed noise estimation framework. The basic concept is that the noise impact of technological and/or operational changes is estimated by exploiting a) the already known noise levels of a baseline scenario, and b) the fact that variation of individual noise sources (due to changes) can be predicted accurately enough through (existing or new) specialised noise prediction methods (e.g. Heidmann's method for fan noise [117]), using as inputs publicly available aircraft noise and performance data. Table 5.3 summarises the inputs required by the proposed framework under the configuration (e.g. exact noise prediction methods, number of included sources) specified in Section 5.5.1 and used for the framework demonstrations in the following Chapters. Finally, Appendix A contains a more analytical flowchart of the methodology than the one presented earlier in Figure 5.2.

Table 5.3: List of inputs to the noise estimation frameowrk.

Engine design	**Baseline levels**	**Operational**
BPR	Aircraft NPDs	Trajectory
Fan diameter, d_f	Source noise levels	Airspeed
FPR, OPR		
Rated thrust, F_∞		
Airflow at rated thrust, $\dot{m}_{a,\infty}$		
Maximum LPR speed, $\mathrm{N1}_{max}$		
Maximum LPT exit temperature, $T_{t5,max}$		

Chapter 6

Methodology II: Supplementary elements

Having presented the core methodology of the proposed noise estimation framework, this chapter describes two supplementary elements that serve at calculating or estimating inputs to the framework. These are the own-developed noise prediction tool, FANjET, and the turbofan thermodynamic analysis tool. It must be emphasised that the explicit elements described in this Chapter do not constitute part of the proposed methodology. Any other methods providing the required inputs can be used instead.

6.1 FANjET: Fast Aircraft Noise Estimation Tool

FANjET is a custom, simplified aircraft noise prediction tool. Using as inputs publicly available aircraft noise and performance databases it outputs the most common metrics of aircraft noise (including noise exposure contours) and calculates the flight profiles. In the context of the proposed noise estimation framework, noise outputs are of no interest (clearly, it would be pointless to use the proposed noise estimation framework if accurate noise assessments were made directly through FANjET. This would mainly require knowledge of the noise at source, which is the output provided by the proposed framework). In contrast, flight profiles are essential in assessing operational mitigation strategies through the proposed framework. For example, FANjET is used in the steep operations case studies of Section 8.1 for simulating the steep trajectories (i.e. get quantity R_t in Equation 5.11 as well as the instantaneous location data that lead to $D_{s,t}$) and assessing the associated noise exposure impact, after having estimated the noise variation at source (i.e. quantity ΔW_s in Equation 5.11). Also, it is worth mentioning that FANjET was used throughout this study, not only as an experimentation tool (some representative example applications are described in Appendix H) but also for producing graphs, such as the aircraft noise sources contribution Figures 2.14 and 2.13.

Any custom databases referring to existing or new noise sources and/or aircraft can be incorporated in FANjET. By default FANjET uses:

- Polar directivity data from ANOPP [16, 134] and azimuthal directivity data for the Airbus A320, from Krebs et al. [158]. These directivity data are published in the form of indices in dB at pre-defined angles and are therefore subjected to interpolation and normalisation to yield the directivity factor D, as shown in Appendix E. It is important to note that aircraft pitch attitude and incidence angle are ignored in directivity angles calculations. While this is unrealistic at the climb and descent phases, it does not affect NPD curves computation, since this uses infinite, parallel to the ground flight paths passing directly over the observer.
- Sources noise levels from NASA [43] and sources spectra from Zaporozhets [26].

The next few Sections describe the sub-functions within FANjET.

6.1.1 Geometry function

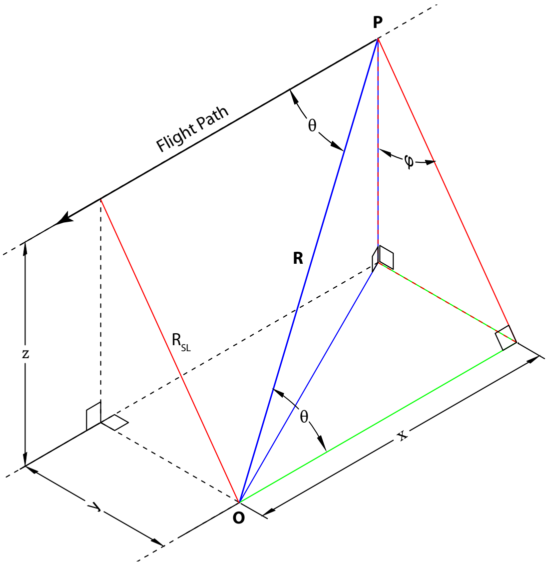

Figure 6.1: Reference system for aircraft noise modelling.

The geometry function calculates the instantaneous polar θ and azimuthal ϕ angles as well as the associated distance between aircraft or its individual noise sources and an observer in space or a grid of points. FANjET uses the coordinate system depicted in Figure 6.1. Considering a simple flyover, points P, O represent the aircraft (here, as a point source) and observer respectively, whereas R denotes the distance between them. Also, R_{SL} denotes the slant distance, which is the perpendicular (and shortest) distance from the observer to the flight path. Referring to Figure 6.1:

$$R = \sqrt{x^2 + y^2 + z^2}\,.$$

$$\phi = \tan^{-1}\left(\frac{y}{z}\right)$$

$$\theta = \cos^{-1}\left(\frac{x}{R}\right)$$

When the aircraft flight path is directly above the observer, as in the ICAO flyover and approach certification points described in Section 2.1.6, $y = 0$ and hence $\phi = 0$. Also, when the aircraft overflies the observer, $\theta = 90°$, since $x = 0$. Considering an aircraft flying from a point P_0 in space to a point P at constant acceleration a, its position on axis x,y,z at time t is given by the equation of motion [159]:

$$x(t) = x_0 + u_{0x}t + \frac{1}{2}a_x t^2\,,$$

$$y(t) = y_0 + u_{0y}t + \frac{1}{2}a_y t^2\,,$$

$$z(t) = z_0 + u_{0z}t + \frac{1}{2}a_z t^2\,,$$

where subscript 0 denotes the initial position and velocity values. Acceleration can be substituted with [159]

$$a = \frac{u_x^2 - u_{0x}^2}{2(x - x_0)}\,, \tag{6.1}$$

leading to expressions in terms of coordinates and velocities. For instance, with reference to Figure 6.2, in the x-direction:

$$x(t) = x_0 + u_0\cos(\gamma)t + \frac{(u^2 - u_0^2)\cos^2(\gamma)}{4(x - x_0)}t^2\,. \tag{6.2}$$

Substituting $\cos(\gamma) = \dfrac{x - x_0}{S}$, the above equation becomes:

$$x(t) = x_0 + \frac{x - x_0}{S}u_0 t + \frac{(x - x_0)(u^2 - u_0^2)}{4S^2}t^2\,. \tag{6.3}$$

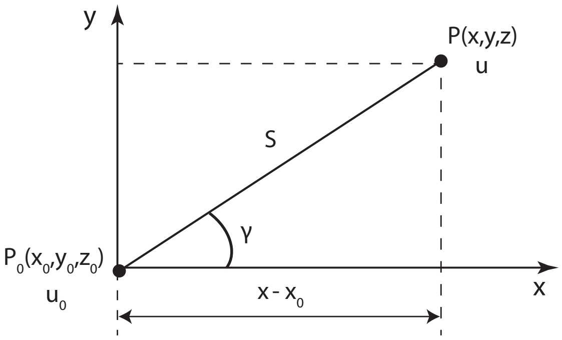

Figure 6.2: Simple geometry of two points in space

6.1.2 Aircraft function

In summary, aircraft function contains:

- The option to specify the aircraft noise sources included in calculations.
- The option of modelling the aircraft as a lumped or distributed noise source (see Section 6.1.3).
- The option to include or not spectral information (see Section 6.1.4).

6.1.3 Noise source modelling

As previously mentioned, aircraft noise at an observer position can be calculated either by adding all individual source contributions at the observer point, in which case the aircraft is considered a distributed system, or by modelling the aircraft as a single (lumped) directive source. On a distributed system, the SPL for each individual source i is evaluated through Equation 2.4; this requires knowledge of the relative distances between sources. These are often published by manufacturers but are also available in resources such as the EASA Type Certificates (TCDS) website [51], or aviation sites, e.g. reference [160].

$$\mathrm{L}_{p,i} = 10\log\left(\sum_{i=1}^{m}\frac{W_iD_i}{R_i^2}C\right). \tag{6.4}$$

The SPL experienced by the observer due to the distributed aircraft model is calculated with[1]

$$\mathrm{L}_{p} = 10\log\left(\sum_{i=1}^{m}10^{\frac{L_{p,i}}{10}}\right). \tag{6.5}$$

The lumped model considers all noise sources collocated at the same aircraft point, more conveniently, it's CG. Distance R becomes identical for all sources whereas according to Equation 2.11, the total acoustic power, W_{tot}, is the sum of the individual sources acoustic powers. Likewise, based on Equation 2.1, the total intensity in direction (θ,ϕ) due to m noise sources is

$$I_{\theta,\phi} = \frac{1}{4\pi}\sum_{i=1}^{m}W_iD_{i,\theta,\phi}\,, \tag{6.6}$$

Hence, according to Equation 2.2 the lumped aircraft directivity is given by

$$D_{\theta,\phi} = \frac{\sum\limits_{i=1}^{m}W_iD_{i,\theta,\phi}}{\sum\limits_{i=1}^{m}W_i}. \tag{6.7}$$

---

[1] As justified in Section 2.1.2, sources are assumed incoherent to each other.

The SPL at the observer due to the lumped aircraft is:

$$\mathrm{L}_p = 10\log\left(\frac{W_{tot}D_{\theta,\phi}}{R^2}C\right). \tag{6.8}$$

The proposed noise estimation framework can use either modelling approach. Any deviations deriving from the lumped source model tend to vanish at relatively large distances (e.g. the distances between aircraft and certification points). Hence, in airport noise case studies, such as the ones performed in this thesis, both modelling approaches will produce identical results. The lumped source model is normally superior in terms of computational speed, as proved in Chapter 7 (see Table 7.3).

6.1.4 Incorporation of spectral properties

In accordance with the spectral classes discussion in Section 5.7.3, source spectral characteristics are introduced to the model through spectral functions, S_b, for each band b (usually one-third octave bands from 50 Hz to 10 kHz). Spectral functions may refer to the whole aircraft (for most existing civil aircraft these are available in the ICAO ANP Database [44]) or to individual noise sources (typical functions can be found in NASA's ANOPP [16]). In the former case, function S_b is multiplied by the aircraft SPL (Equation 6.5 or 6.8), yielding the aircraft SPL for each band

$$L_{p,b} = L_p S_b\,. \tag{6.9}$$

In the latter case, function $S_{i,b}$ is introduced in Equation 6.8 yielding source's i SPL for each band

$$\mathrm{L}_{p,i,b} = 10\log\left(\sum_{i=1}^{m}\frac{W_iD_iS_{i,b}}{R_i^2}C\right). \tag{6.10}$$

If n is the number of bands, the total SPL experienced by the observer is

$$\mathrm{L}_p = 10\log\left(\sum_{b=1}^{n}10^{\frac{L_{p,b}}{10}}\right). \tag{6.11}$$

It must be noted that spectral distribution varies with aircraft operational parameters, such as flight speed and thrust setting. Such detailed data are not publicly available.

The Doppler shift can optionally be included through a factor $\dfrac{\omega}{(1-M\cos\theta)}$, where ω is the frequency and M is the Mach number.

6.2 Turbofan engine thermodynamic analysis

This Section presents the thermodynamic analysis of turbofan engine cycle through which are estimated some inputs to the proposed framework, as described in Chapter 5. For that, it is required to first present the turbofan engine principles of operation, define the engine stations and outline the assumptions made. It must be noted that this analysis can be realised by specialised gas turbine performance simulation software, such as Gasturb [144].

6.2.1 Turbofan engine layout and principle of operation

The basic operation of turbofan engines is described with reference to the schematic diagram of Figure 6.3. The atmospheric air sucked by the fan enters the intake section of the engine; a part of it is being compressed by a compressor, before entering a combustion chamber, where it is mixed with fuel and burned. The resulting (due to combustion) high-temperature high-pressure gas enters a turbine and expands, generating mechanical work, a portion of which drives the fan and compressor. The remaining energy is expelled backwards in the exhaust nozzle, producing forward propulsive thrust, as implied by Newton's third law of motion. The compressor, combustor and turbine processes and prepares the air intake to do some work and for that reason is referred to as the engine's core [18, 61]. The other part of the sucked air bypasses the core and is slightly accelerated (due to the fan) before being expelled from the nozzle, creating additional thrust as described in Section 2.6.2.

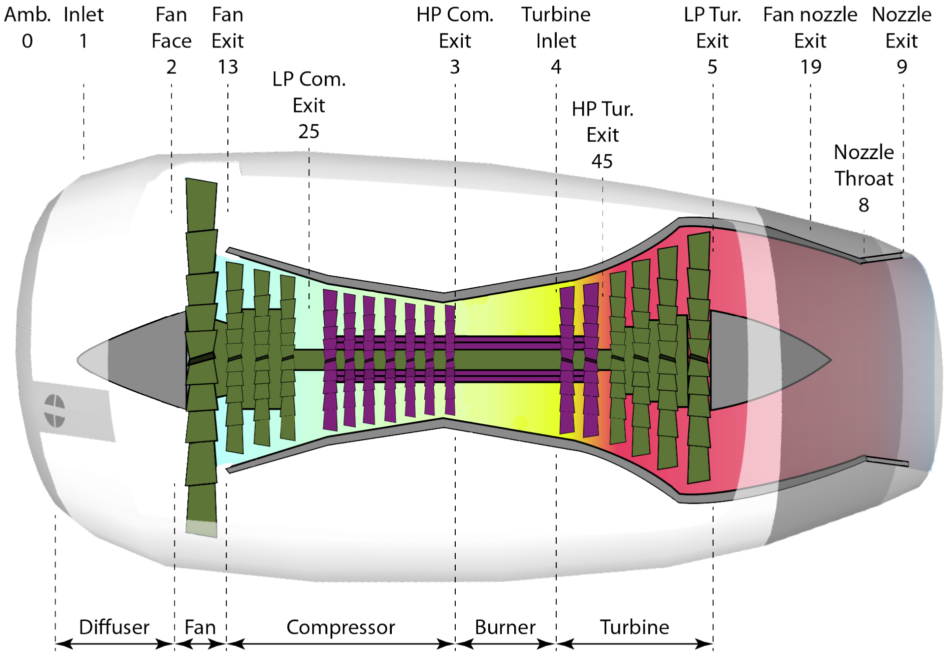

Figure 6.3: Schematic diagram demonstrating the turbofan engine operation and station numbers. Based on artwork in [161].

6.2.2 Engine station numbers

In order to analyse the engine cycle it is convenient to use a numbering system for referring to the conditions across each engine component. Figure 6.3 illustrates the adopted numbering system that conforms with the internationally recognised SAE ARP 755C recommendations [162]. A brief description of each station is outlined below[2]:

- Station 0: Ambient conditions, i.e. the static pressure and temperature far upstream of the engine inlet.
- Station 1: The engine inlet, which reduces the incoming flow Mach number.
- Station 2: The fan face.
- Station 13: The fan exit in the bypass stream.
- Station 25: The interface between low (LPC) and high pressure compressor (HPC).
- Station 3: The exit of the HPC.
- Station 4: The exit of the burner.
- Station 45: The interface between high (HPT) and low pressure turbine (LPT).
- Station 5: The exit of the turbine.
- Station 19: The bypass exhaust nozzle exit.
- Station 8: The nozzle throat.
- Station 9: The core exhaust nozzle exit.

6.2.3 Stagnation quantities and ratios

Analysing the engine cycle, the conditions across the engine components are more conveniently expressed in terms of stagnation (or total) rather than static variables. Stagnation temperature, T_t, is the temperature the moving flow would have if brought adiabatically to rest from an initial Mach number, M, [18]. It is defined as [157]:

$$T_t = T\left(1 + \frac{V^2}{2c_pT}\right) . \tag{6.12}$$

Introducing the Mach number and writing the specific heat, c_p, as $\gamma R/(\gamma - 1)$ leads to the stagnation to static temperature ratio:

$$\frac{T_t}{T} = 1 + \frac{\gamma - 1}{2} M^2 . \tag{6.13}$$

---

[2] Intermediate stations, like station 4.1 that refers to the nozzle vanes exit are irrelevant to this study and thus are not included in the list.

Table 6.1: Subscripts defining stagnation ratios $\pi_i = \dfrac{P_{t\beta}}{P_{t\alpha}}$, and $\tau_i = \dfrac{T_{t\beta}}{T_{t\alpha}}$

Component	**Subscript i (identifies π, τ)**	**Subscripts α, β (identify T_t, P_t)**
Diffuser	d	0 and 2
Fan	f	2 and 13
Compressor	c	2 and 3
Burner	b	3 and 4
Turbine	t	4 and 5
Exhaust nozzle	n	5 and 9

Assuming isentropic processes, stagnation pressure, P_t, which is the pressure measured by a stationary probe placed in the flow, is related with static pressure, P with [18]:

$$\frac{P_t}{P} = \left(1 + \frac{\gamma - 1}{2} M^2\right)^{\frac{\gamma}{\gamma-1}} . \tag{6.14}$$

The stagnation temperature and pressure across component i are typically expressed in ratios denoted by τ_i and π_i respectively. With subscripts α and β referring to the quantities entering and leaving component i respectively, Table 6.1 summarises the notation used. For instance, stagnation quantities in the burner are denoted as follows:

$$\pi_b = \frac{P_{t4}}{P_{t3}} \text{ and } \tau_b = \frac{T_{t4}}{T_{t3}} . \tag{6.15}$$

6.2.4 Ideal and non-ideal cycle assumptions

Table 6.2 catalogues and describes the assumptions associated to the analysis of the ideal turbofan cycle. These assumptions facilitate the analysis, as shown in Section 6.2, while enabling the estimation of further parameters like the $T_{tj,\infty}$ in Section 5.5.5.

Several cycle losses can be introduced in the thermodynamic analysis, typically through suitable efficiency factors. Frictional losses in the shafts can be introduced through a shaft mechanical efficiency. Stagnation pressure losses at the burner due to heat addition and wall friction and losses due to incomplete combustion can be reflected using a burner efficiency, which however, is very close to unity for modern engines [18]. Generally, the losses associated with a non-isentropic (e.g. due to viscous skin friction) process can be reflected through a polytropic efficiency e_i in the relationship between τ_i and π_i. For instance, Cumpsty [18] expresses the temperature ratios across the compressor and the turbine as

$$\tau_c = \pi_c^{\frac{\gamma-1}{e_c\gamma}} \text{ and } \tau_t = \pi_t^{\frac{e_t(\gamma-1)}{\gamma}} . \tag{6.16}$$

Mattingly et al. [163] explain that using polytropic efficiencies has two advantages: a) it simplifies calculations, and b) it removes isentropic efficiency [157] bias when handling

Table 6.2: Ideal gas turbine cycle assumptions

Assumption	Mathematical expression
Fully expanded core nozzle	$P_9 = P_0$
Negligible stagnation pressure losses in the diffuser (inlet)	$P_{t0} = P_{t2}$
Adiabatic diffuser flow	$T_{t0} = T_{t2}$
Fan behaves isentropically	$\pi_f = \tau_f^{\frac{\gamma}{\gamma-1}}$
Compressor behaves isentropically	$\pi_c = \tau_c^{\frac{\gamma}{\gamma-1}}$
Low Mach number heat addition in the burner	$P_{t3} = P_{t4}$
Turbine behaves isentropically	$\pi_t = \tau_t^{\frac{\gamma}{\gamma-1}}$
Adiabatic nozzle flow	$T_{t5} = T_{t9}$
Negligible stagnation pressure losses in the nozzle	$P_{t5} = P_{t9}$
Fully expanded fan nozzle	$P_{19} = P_0$
Fan exit static temperature equals the ambient static	$T_{19} = T_0$
Heat capacities are assumed constant	$\gamma = 1.4$
Negligible burner fuel to air ratio	$f \ll 1$
Steady flow, fluid behaves as a perfect gas	
One-dimensional flow across each engine component	
Uniform velocity profiles at inlet and exhaust planes	

multistage components because it indicates a level of technology rather than a component performance, which is expressed in terms of the isentropic efficiency

$$\eta = \frac{\pi^{\frac{\gamma-1}{\gamma}} - 1}{\tau - 1}\,. \tag{6.17}$$

To give representative efficiency values, Table 6.3 lists efficiencies of the GE-90 engine.

Table 6.3: GE-90 engine efficiencies (η), as published by General Electric [164].

	Intake	Fan polytropic	Compressor polytropic	Turbine polytropic	Nozzle isentropic	Mechanical	Fuel combustion
η	0.980	0.930	0.910	0.930	0.950	0.990	0.990

6.2.5 Thermodynamic engine analysis

The analysis is performed based on the procedures described by Mattingly et al. [163], Kerrebrock [156] and Hill [157], and with reference to the numbering system and schematic representation of Figure 6.3. If M_0 is the flight Mach number, the ambient static conditions at station 0 and the stagnation conditions at the entrance to the engine inlet (station 1) are related with:

$$\tau_r = \frac{T_{t0}}{T_0} = 1 + \frac{\gamma - 1}{2} M_0^2 \tag{6.18}$$

$$\pi_r = \frac{P_{t0}}{P_0} = \tau_r^{\frac{\gamma}{\gamma-1}} \tag{6.19}$$

Under the assumptions catalogued in Table 6.2, the flow from the ambient to station 1 is considered isentropic and additionally, the diffuser flow is regarded as adiabatic. Thus, the following can be written:

$$T_{t1} = T_{t0} \text{ and } P_{t1} = P_{t0} \tag{6.20}$$

$$\tau_d = \pi_d = 1 \tag{6.21}$$

$$T_{t2} = T_{t0} \text{ and } P_{t2} = P_{t0} \tag{6.22}$$

$$T_{t2} = T_0 \left(1 + \frac{\gamma - 1}{2} M_0^2\right) \tag{6.23}$$

$$P_{t2} = P_0 \left(1 + \frac{\gamma - 1}{2} M_0^2\right)^{\frac{\gamma}{\gamma-1}} \tag{6.24}$$

With η_c, e_c being the compressor adiabatic and polytropic efficiencies respectively, and π_c denoting the OPR, the conditions across the compression stage (stations 2, 3) are:

$$P_{t3} = \pi_c P_{t2} \tag{6.25}$$

$$\tau_c = \pi_c^{\frac{\gamma-1}{\gamma e_c}} \tag{6.26}$$

$$T_{t3} = \tau_c T_{t2} \tag{6.27}$$

$$\eta_c = \frac{\pi_c^{\frac{\gamma-1}{\gamma}} - 1}{\tau_c - 1} \tag{6.28}$$

Similarly, conditions across the fan are described with

$$P_{t13} = \pi_f P_{t2} \tag{6.29}$$

$$\tau_f = \pi_f^{\frac{\gamma-1}{\gamma e_f}} \tag{6.30}$$

$$T_{t13} = \tau_f T_{t2} \tag{6.31}$$

$$\eta_f = \frac{\pi_f^{\frac{\gamma-1}{\gamma}} - 1}{\tau_f - 1} \tag{6.32}$$

where π_f, e_f are the engine FPR and fan polytropic efficiency respectively.

Looking at the combustion then under the assumption $\pi_b = 1$:

$$P_{t4} = P_{t3} \tag{6.33}$$

$$\tau_b = \frac{T_{t4}}{T_{t3}} \tag{6.34}$$

The conditions across the turbine are described with [156]:

$$\tau_t = 1 - \frac{1}{\eta_m(1+f)}\frac{\tau_r}{\tau_\lambda}\left[\tau_c - 1 + \mu(\tau_f - 1)\right] \tag{6.35}$$

$$T_{t5} = \tau_t T_{t4} \tag{6.36}$$

$$\pi_t = \tau_t^{\frac{e_t\gamma_t}{\gamma_t - 1}} \tag{6.37}$$

$$P_{t5} = \pi_t P_{t4} \tag{6.38}$$

$$\eta_t = \frac{(1-\tau_t)}{1-\tau_t^{\frac{1}{e_t}}} \tag{6.39}$$

Quantities f and τ_λ in Equation 6.35 are defined next. With h_{pr} being the fuel heating value, fuel to air mass flow ratio, f, is defined as [163]:

$$f = \frac{\dot{m}_f}{\dot{m}_c} = \frac{\tau_\lambda - \tau_r\tau_c}{\frac{\eta_b h_{pr}}{cpcT_0} - \tau_\lambda} \tag{6.40}$$

For turbofans, f is very small [157] and can be ignored, as suggested in Table 6.2.

Accounting for specific heats variation within the engine, Mattingly et al. [163] define τ_λ as the ratio

$$\tau_\lambda = \frac{c_{p,4}T_{t4}}{c_{p,0}T_0}\,, \tag{6.41}$$

between the turbine inlet total temperature, T_{t4}, which is linked with the throttle setting, and the static temperature, T_0. This ratio is an indicator of the engine performance and limitations (e.g. due to the material withstanding temperatures) [157]. Cumpsty [18] points out that the engine analysis accuracy can be improved by using different specific heat values for the cold (i.e. fan and compressor) and hot (i.e. burner and turbine) parts of the engine. For example, Mattingly et al. [163] use $c_{p,c} = 1.055$ kJ/kg and $c_{p,t} = 1.244$ kJ/kg for the cold and hot specific heats respectively and ratios of specific heats $\gamma_c = 1.4$ and $\gamma_t = 1.3$. A larger variety of values can be obtained from published tables, such as the ones in [157] that give the air specific heat for varying temperatures.

Assuming that the maximum inlet total temperature, $T_{t4,max}$, is associated with the maximum thrust setting, then T_{t4} can be directly expressed as a function of throttle setting th percentage:

$$T_{t4} = T_{t4,max}\frac{th}{100}\,. \tag{6.42}$$

Nevertheless, $T_{t4,max}$ is typically publicly unavailable; rather, EASA TCDS [51] supply the operational limit of the temperature at the LPT exit $T_{t5,max}$. Hence, T_{t4} is estimated by recasting Equation 6.35 while substituting from Equations 6.18, 6.36 and 6.41:

$$T_{t4,max} = T_{t5,max} + \frac{T_{t0}}{\eta_m}[\tau_c - 1 + \mu(\tau_f - 1)]\,. \tag{6.43}$$

In the ideally expanded nozzle, friction losses are negligible and the nozzle adiabatic so:

$$\tau_n = 1 \tag{6.44}$$

$$T_{t9} = T_{t5} \tag{6.45}$$

$$T_{t9} = T_9\left(1 + \frac{\gamma - 1}{2}M_9^2\right) \tag{6.46}$$

$$\pi_n = 1 \tag{6.47}$$

$$P_{t9} = P_{t5} \tag{6.48}$$

$$P_9 = P_0 \tag{6.49}$$

The core and bypass jet velocities that are directly related with engine noise (e.g. see Equation 5.23), can be calculated through the equations below given by Mattingly [163]:

$$M_9 = \sqrt{\frac{2}{\gamma_t - 1}\left[\left(\frac{P_{t9}}{P_9}\right)^{\frac{\gamma_t - 1}{\gamma_t}} - 1\right]} \tag{6.50}$$

$$M_{19} = \sqrt{\frac{2}{\gamma_c - 1}\left[\left(\frac{P_{t13}}{P_0}\right)^{\frac{\gamma_c - 1}{\gamma_c}} - 1\right]}\,, \tag{6.51}$$

from where the core and fan velocities are obtained with:

$$V_9 = M_9 a_0 \tag{6.52}$$

$$V_{19} = M_{19} a_0\,. \tag{6.53}$$

Alternatively, with η_n and η_{nf} being the core and fan nozzle adiabatic efficiencies, Hill [157] gives the below Equations for the core and fan velocities.

$$V_9 = \sqrt{2\eta_n \frac{\gamma_t}{\gamma_t - 1} R T_{t5}\left[1 - \left(\frac{P_0}{P_{t5}}\right)^{\frac{\gamma_t - 1}{\gamma_t}}\right]} \tag{6.54}$$

$$V_{19} = \sqrt{2\eta_{nf} \frac{\gamma_c}{\gamma_c - 1} R T_{t13}\left[1 - \left(\frac{P_0}{P_{t13}}\right)^{\frac{\gamma_c - 1}{\gamma_c}}\right]} \tag{6.55}$$

Further expressions for the jet velocities are derived in Appendix D.

Chapter 7

Validation: Predictions for existing aircraft

This chapter is divided in three parts. The first part investigates the validity of the proposed framework by comparing estimated to published NPD curves of existing aircraft. The second part demonstrates the framework's capability on performing noise impact parametric studies of improvements on existing aircraft. The last part of this chapter is dedicated to error analysis, where the framework's potential sources of error are identified and discussed, whereas the error range is established.

7.1 Comparison between estimated and published data

For validating the proposed framework, estimated takeoff and approach NPD curves for existing aircraft of different sizes are compared to published ones. As described in Section 2.1.5, NPD noise measurements are performed with the test aircraft having the cleanest possible configuration (e.g. flap setting, landing gears position, etc.). However, the exact configuration of the test aircraft at each NPD thrust setting is not clarified. This could be an important source of error in estimating NPD curves and validating the proposed framework, since flaps are a prevailing airframe noise source, as discussed in Section 2.1.7. Therefore, before generating estimated NPD curves, some assumptions are made regarding the aircraft configuration at different NPD thrust settings and operations.

7.1.1 Aircraft configuration assumptions

Presuming that landing gears deployment/retraction moment is independent of thrust setting, then it is only required to make assumptions regarding the variation of flaps settings with engine power setting. Theoretical takeoff and approach thrust requirements for each aircraft can be either calculated using the SAE-AIR 1845 [45] methodology (see Section 2.7), or approximated with average thrust values provided by NASA [65]. Default flap deflection angles associated with the standard takeoff and approach flight profiles for each aircraft are included in the ANP Database [44].

Equations 2.45, 2.47 give the default theoretical takeoff and approach airspeed as a function of aircraft MTOW, according to the SAE-AIR 1845 flight performance calculations. The ANP Database [44] suggests that coefficients of these Equations (i.e. C and D) are inversely proportional to flap deflection angle. In other words, airspeed is inversely proportional to flap deflection angle. During NPD measurements aircraft need to maintain a standard airspeed of 160 knots. Hence, it can be assumed that for maintaining that airspeed under increased engine power settings, flap deflection angles should increase as well. In practice, this behaviour can be justified by considering that the increased drag due to the extra flap deflection compensates for the increased thrust. Thus, larger engine power settings than the default are associated with progressively larger flap angles (than the default), and vice versa.

Yet, it should also be considered that engine power affects attitude as well. A combination of high engine power setting and flap deflection angle could result in unsafe attitude angle. Hence, for NPD engine power settings much larger than the default, it is assumed that the test aircraft uses default flap settings with the airspeed being controlled by spoilers [165]. Based on the fact that spoilers are located on top of the wings, their impact on airframe noise is considered small due to shielding effects.

7.1.2 Comparison results

Table 7.1 summarises the engine performance inputs to the proposed framework for the aircraft included in the validation study. It is reminded that these inputs correspond to the particular configuration for the proposed framework defined in Section 5.5.1.

Comparisons between published and estimated (using the methodology described in Chapter 5) NPD curves are depicted in Figures 7.1 – 7.14. The baseline NPD point is denoted with a cross. The continuous and dashed lines refer to the estimated and published NPD curves respectively. The maximum root-mean-square error (denoted max rmse in the Figures) between published and estimated curves is noted in each plot. These errors are further discussed in the error analysis in Section 7.3. With respect to that analysis, the dotted lines in the plots reflect the effect of reducing Lighthill's acoustic analogy to lower powers of jet velocity (see Section 7.3.5). This effect is only investigated in the cases when the max rms error exceeds 2 dB. The bar plots at the right of the figures illustrate the fine-tuned (as described in Section 5.6) relative levels of individual baseline noise sources, along with the average values published by NASA [65]. It is important to remind here that individual baseline levels are relative and not absolute because they describe the level differences between sources with respect to the NASA average values (see Section 5.6). Absolute values that are not directly involved in the methodology of the proposed noise estimation framework, can be obtained by appropriately shifting relative levels using the methodology described in Section 5.6.2.

Table 7.1: Engine performance inputs for the aircraft used for validation.

Aircraft	**CRJ900**	**A320-232**	**737-400**	**737-800**	**777-300**
BPR	5.13	4.82	6	5.3	5.7
Fan diameter (m)	1.2	1.61	1.5	1.55	2.8
FPR	1.93	1.73	1.64	1.67	1.85
OPR	24.8	27.7	30.6	32.3	40.8
Rated thrust (kN)	64.5	117.0	104.5	115.2	407
Airflow (kg/s)	190	355	322	342	1200
Max. LPR speed, N1, (rpm)	7400	5650	5490	5382	3300

Aircraft	**A330-301**	**747-400**	**747-8**	**A380-841**
BPR	5.3	5.1	8.6	7.5
Fan diameter (m)	2.44	2.36	2.66	2.95
FPR	1.83	1.73	1.65	1.95
OPR	33.7	30.1	44.7	45
Rated thrust (kN)	300	254	302.5	311
Airflow (kg/s)	833	800	1042	1140
Max. LPR speed, N1, (rpm)	3542	3835	3026	2900

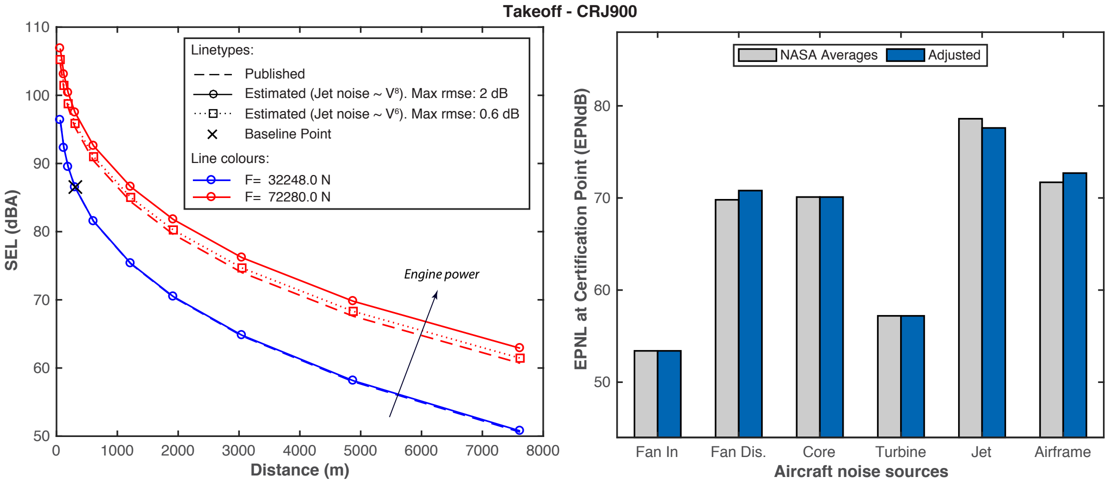

Figure 7.1: Published and estimated NPDs for the Bombardier CRJ900ER at takeoff, along with associated average and adjusted relative source levels.

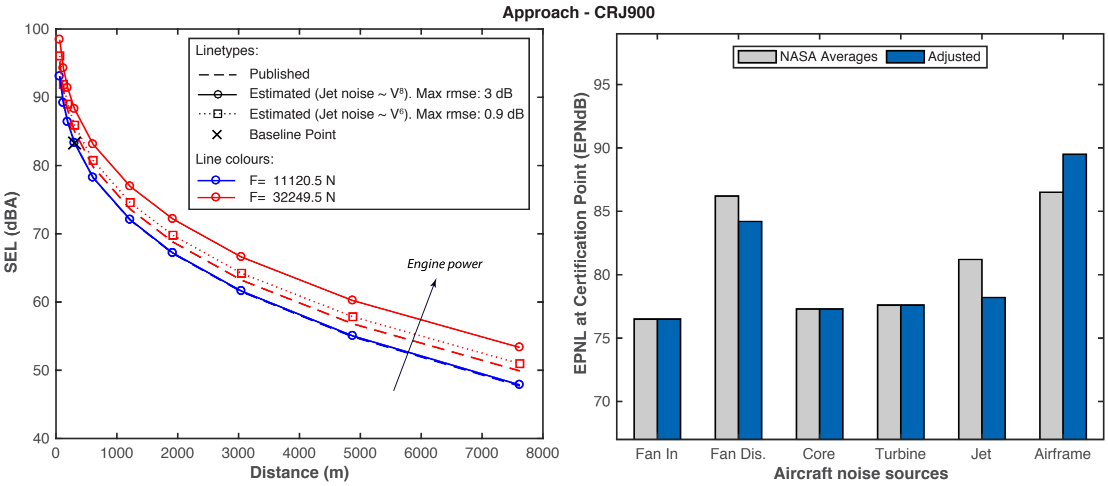

Figure 7.2: Published and estimated NPDs for the Bombardier CRJ900ER at approach, along with associated average and adjusted relative source levels.

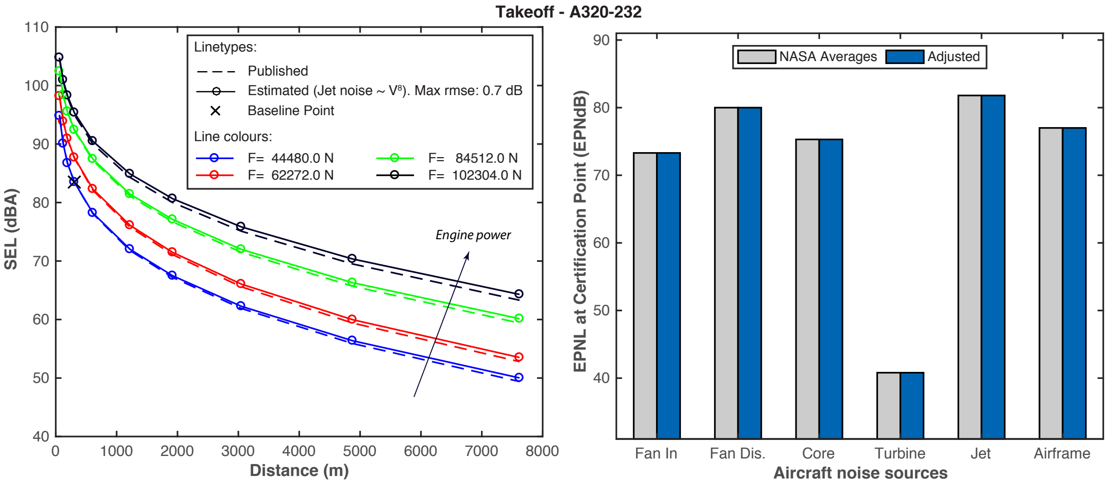

Figure 7.3: Published and estimated NPDs for the Airbus 320-232 at takeoff, along with associated average and adjusted relative source levels.

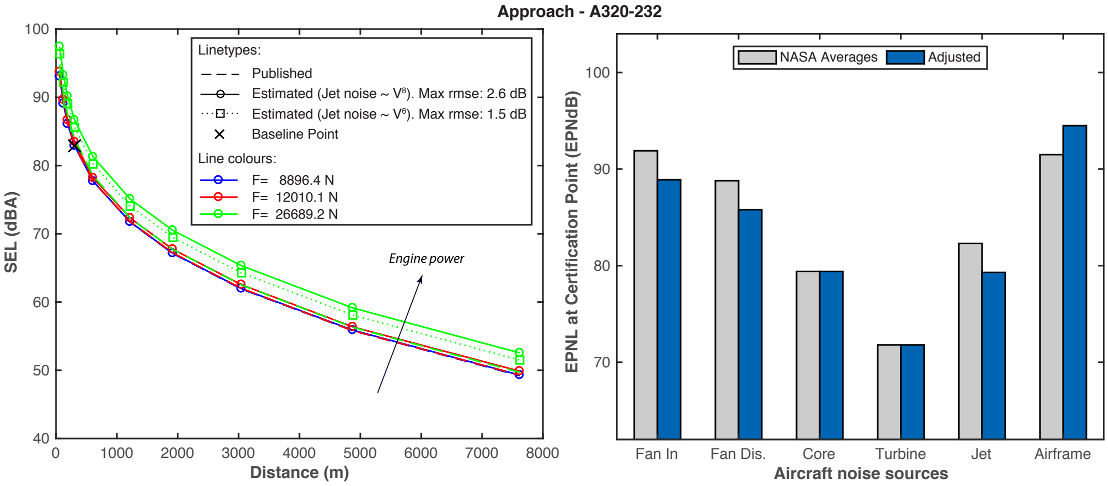

Figure 7.4: Published and estimated NPDs for the Airbus 320-232 at approach, along with associated average and adjusted relative source levels.

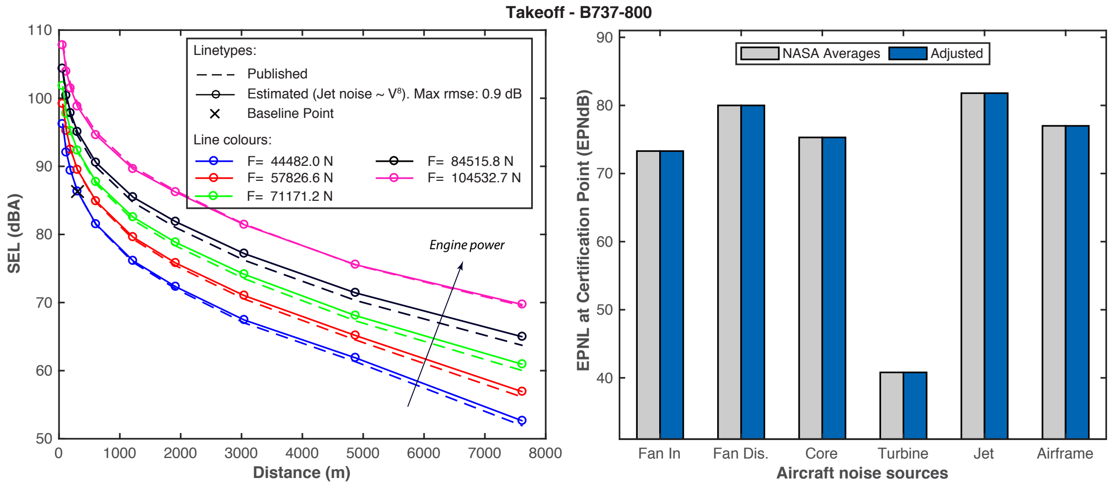

Figure 7.5: Published and estimated NPDs for the Boeing 737-800 at takeoff, along with associated average and adjusted relative source levels.

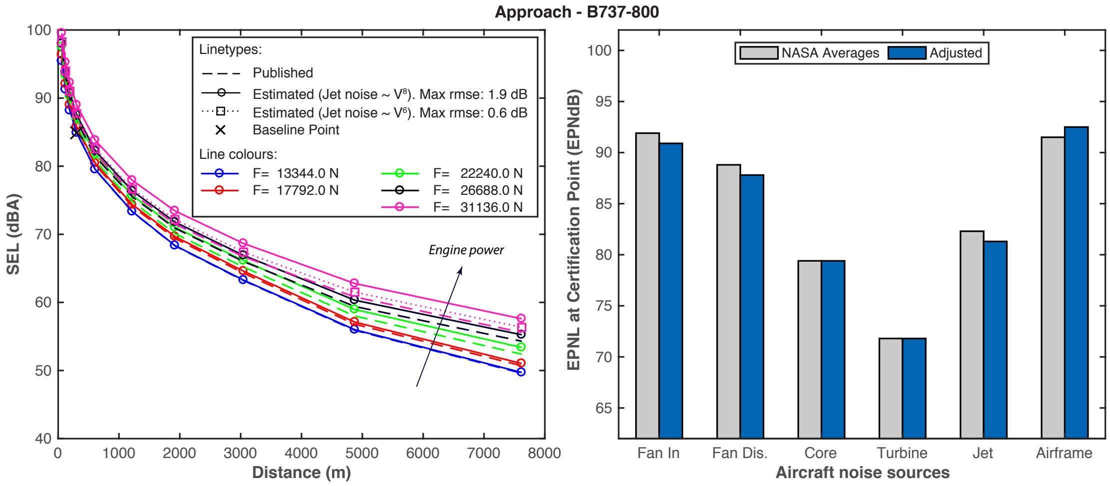

Figure 7.6: Published and estimated NPDs for the Boeing 737-800 at approach, along with associated average and adjusted relative source levels.

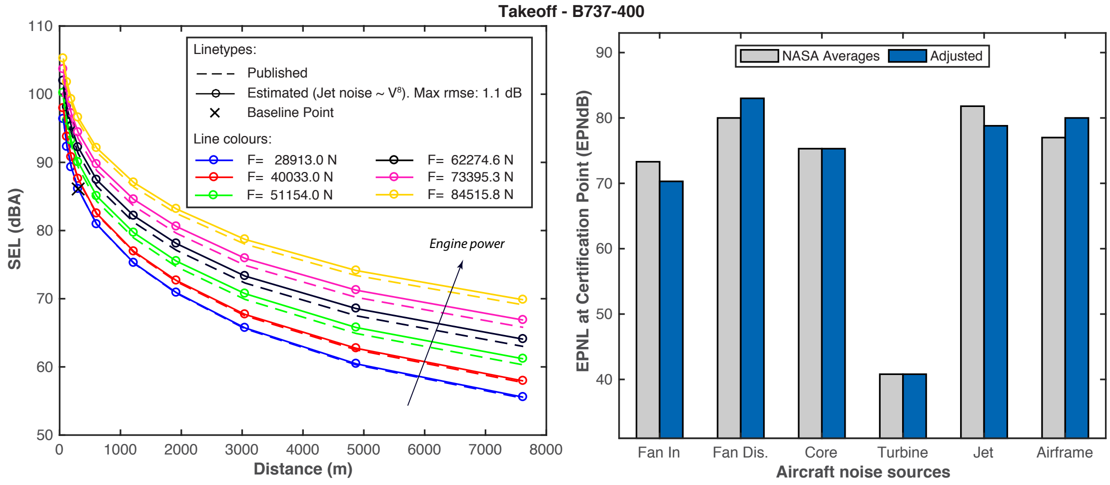

Figure 7.7: Published and estimated NPDs for the Boeing 737-400 at takeoff, along with associated average and adjusted relative source levels.

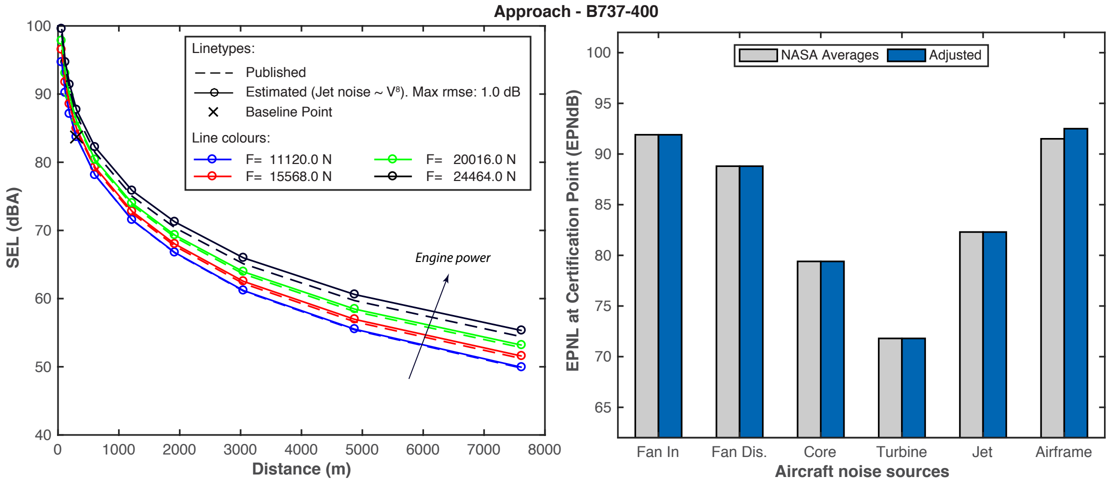

Figure 7.8: Published and estimated NPDs for the Boeing 737-400 at approach, along with associated average and adjusted relative source levels.

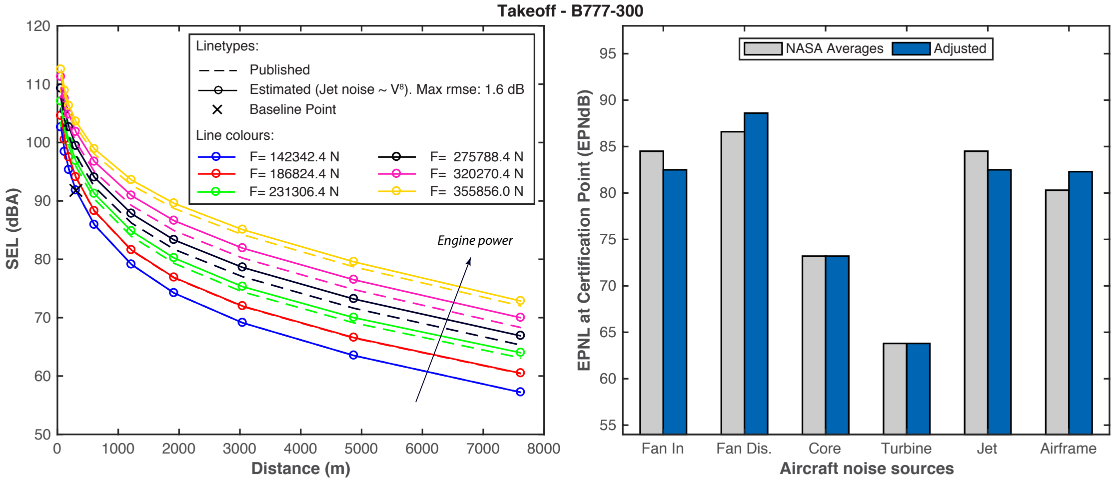

Figure 7.9: Published and estimated NPDs for the Boeing 777-300 at takeoff, along with associated average and adjusted relative source levels.

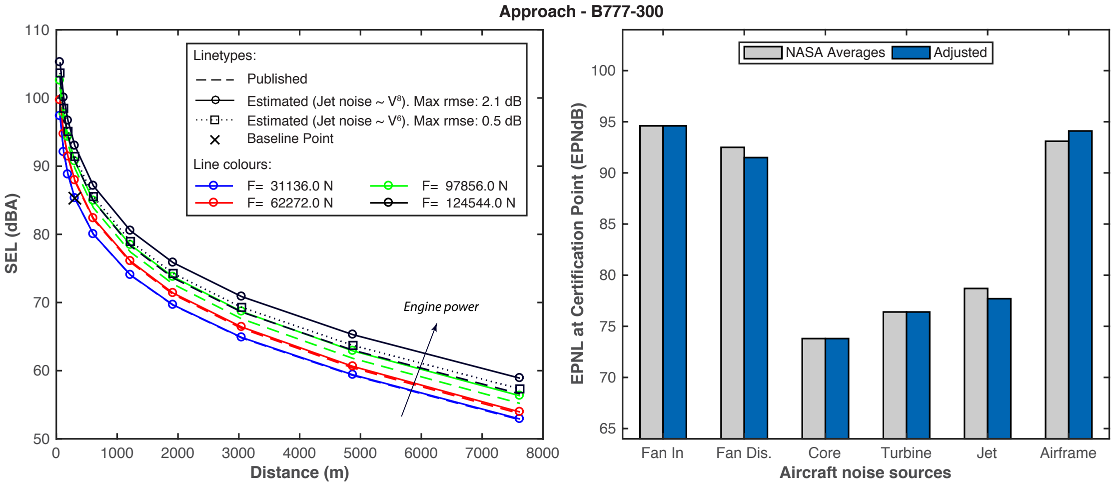

Figure 7.10: Published and estimated NPDs for the Boeing 777-300 at approach, along with associated average and adjusted relative source levels.

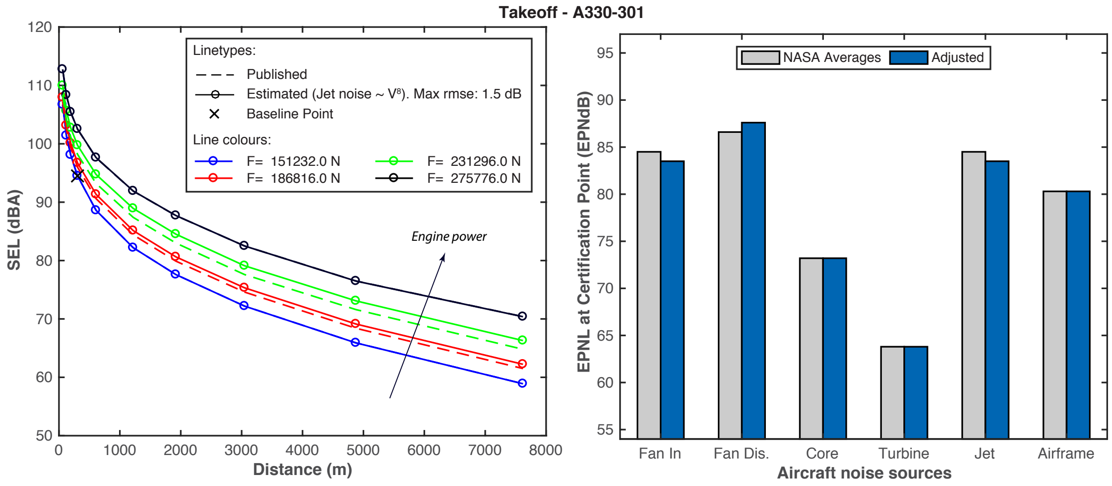

Figure 7.11: Published and estimated NPDs for the Airbus 330-301 at takeoff, along with associated average and adjusted relative source levels.

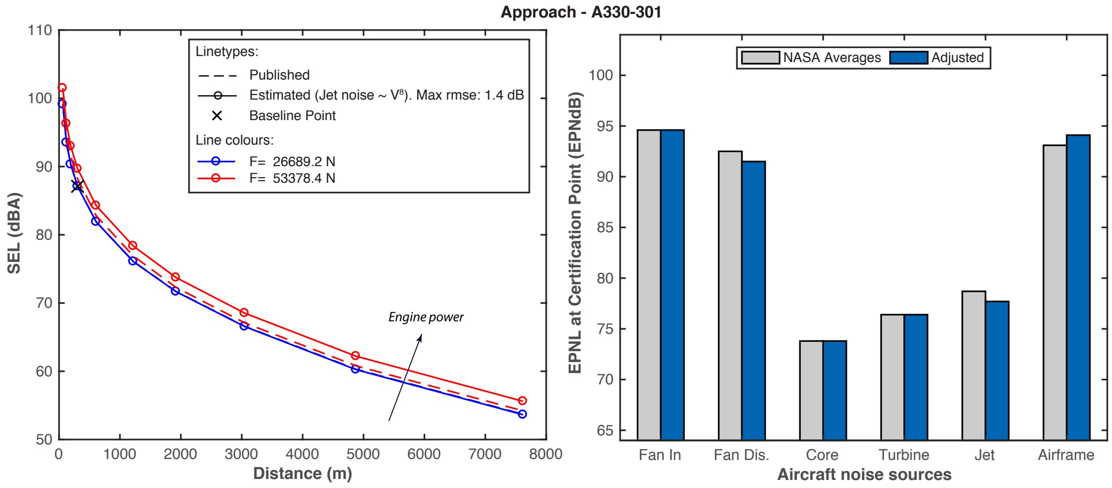

Figure 7.12: Published and estimated NPDs for the Airbus 330-301 at approach, along with associated average and adjusted relative source levels.

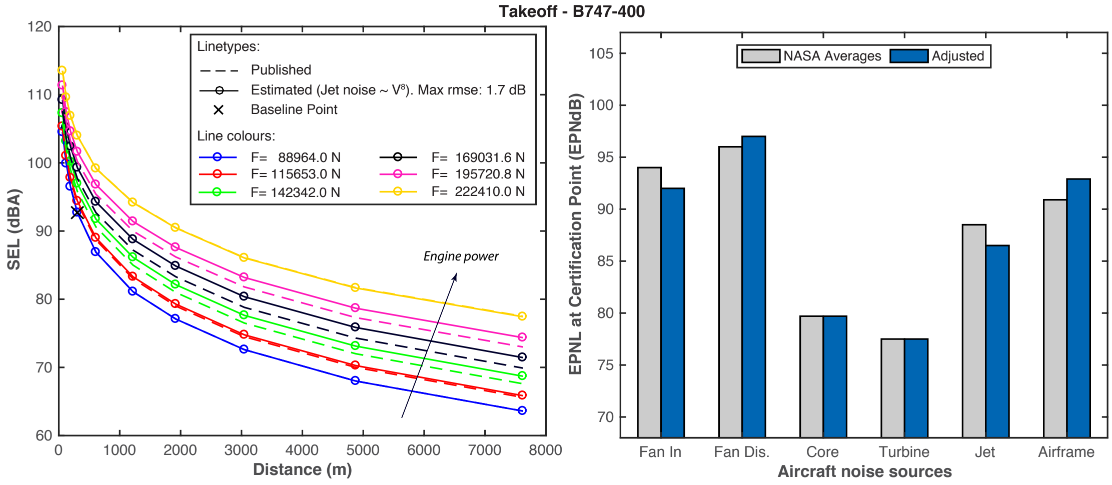

Figure 7.13: Published and estimated NPDs for the Boeing 747-400 at takeoff, along with associated average and adjusted relative source levels.

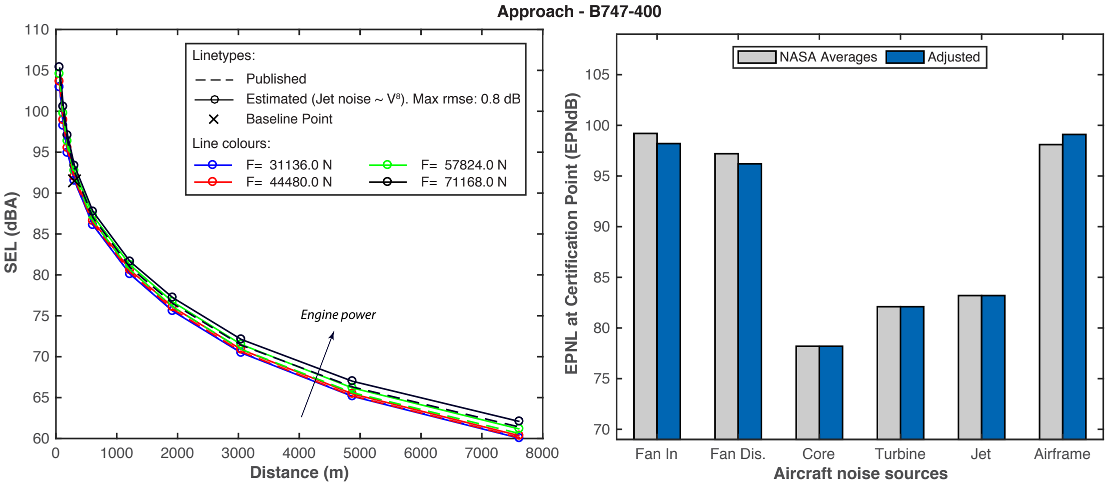

Figure 7.14: Published and estimated NPDs for the Boeing 747-400 at approach, along with associated average and adjusted relative source levels.

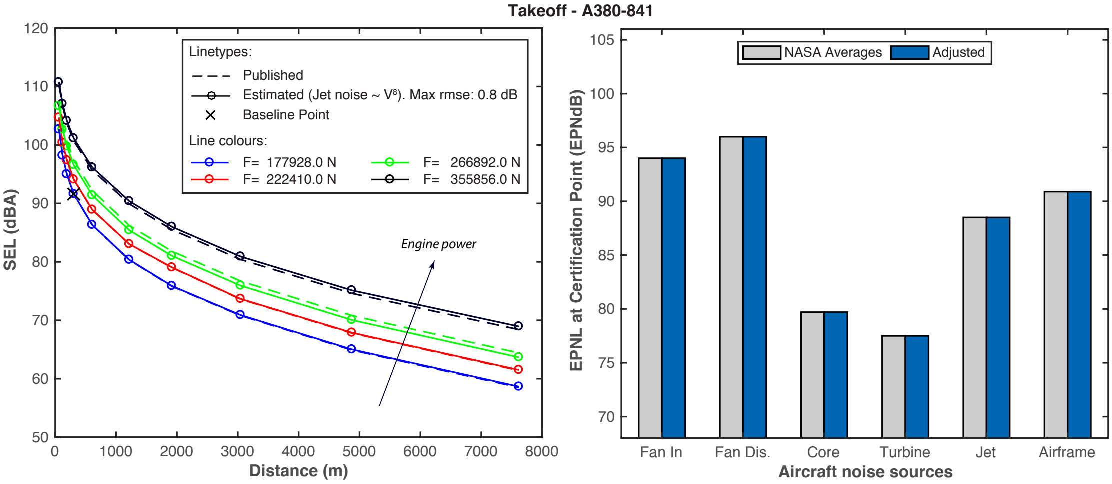

Figure 7.15: Published and estimated NPDs for the Airbus A380-841 at takeoff, along with associated average and adjusted relative source levels.

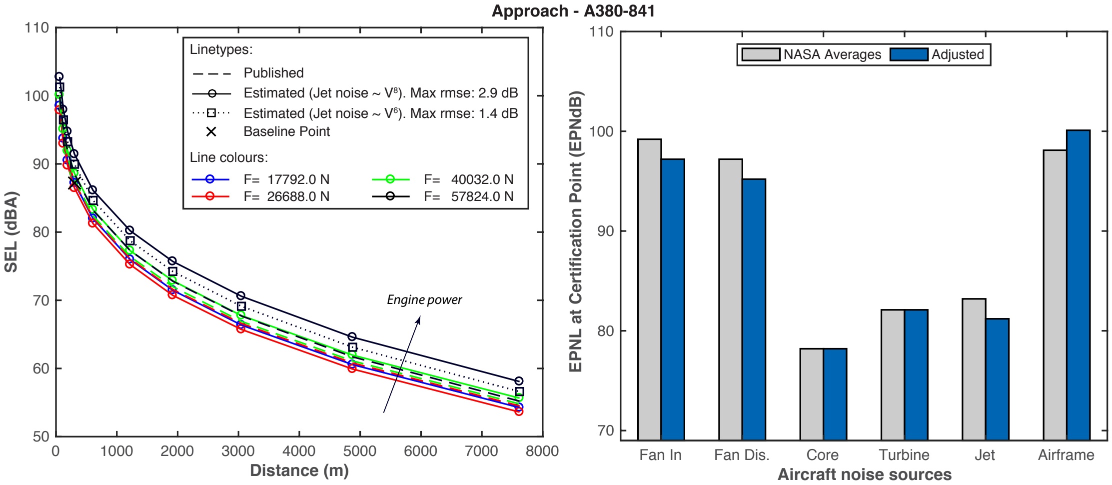

Figure 7.16: Published and estimated NPDs for the Airbus A380-841 at approach, along with associated average and adjusted relative source levels.

7.1.3 Estimating NPD curves for next generation aircraft based on predecessor's data

To validate the capability of the proposed framework to estimate NPD curves for next generation aircraft, takeoff NPD curves are estimated for two Boeing models, the B737-800 and the B747- 8, using as baseline aircraft their predecessors, the B737-400 and the B747-400 respectively. Conforming with the methodology described in Chapter 5, noise sources level changes ΔLw_s due to geometry and performance differences between the current and previous generation models are estimated using the procedure in Section 5.5. Yet, noise sources level reductions due to technological advances (e.g. chevrons, improved liners, etc.) must be accounted as well. Normally, noise level reductions from such advances are available in literature and hence are added manually to each source s level change ΔLw_s. A 1 dB reduction in airframe noise was assumed for the Boeing 737-800, to account for the split scimitar winglets [166, 167]. Likewise, the Boeing 747–8F features the following technological advances [168]:

- The chevron on the trailing edge of the bypass and core jet nozzles that enhances the mixing between the air streams and reduces jet noise. References [169, 132, 131, 170, 171] agree that chevrons offer a jet noise reduction of around 2 to 3 dB. Neise [172] suggests that the jet noise reduction due to chevrons varies from 1 dB, for low BPR engines, to 3 dB for high BPR turbofans. Based on these references, and since the B747-8 engine, the GE Genx-2B67 has BPR of 8, the effect of chevron is represented by a 2 dB jet noise reduction.
- Advanced liner technology that significantly weakens fan tonal components [121].
- Improvements that reduce discharge broadband fan noise by about 0.5 dB [171].

Under these assumptions, the plots in Figure 7.17 compare published (dashed lines) with estimated (continuous lines) NPD curves for the B737- 800 and the B747- 8. The baseline points are marked with a cross and belong to the NPD curves of their predecessors, the B737-400 and the B747-400. In both cases, maximum observed rms error is about 1 dB.

7.2 Noise impact parametric studies

This section demonstrates the framework's capability of performing noise impact parametric studies. The simplified example described below investigates the effect of increasing the BPR of the conventional A320-232 engines on aircraft SEL at takeoff. Table 7.2 lists the basic performance parameters of the A320-232 and of three hypothetical A320 variations with larger BPRs, named A320-h1, A320-h2, A320-h3. The parameters for these A320 variations derive from the historical trends presented in Chapter 4. Additional engine performance data, such as the temperatures in the engine are ignored in

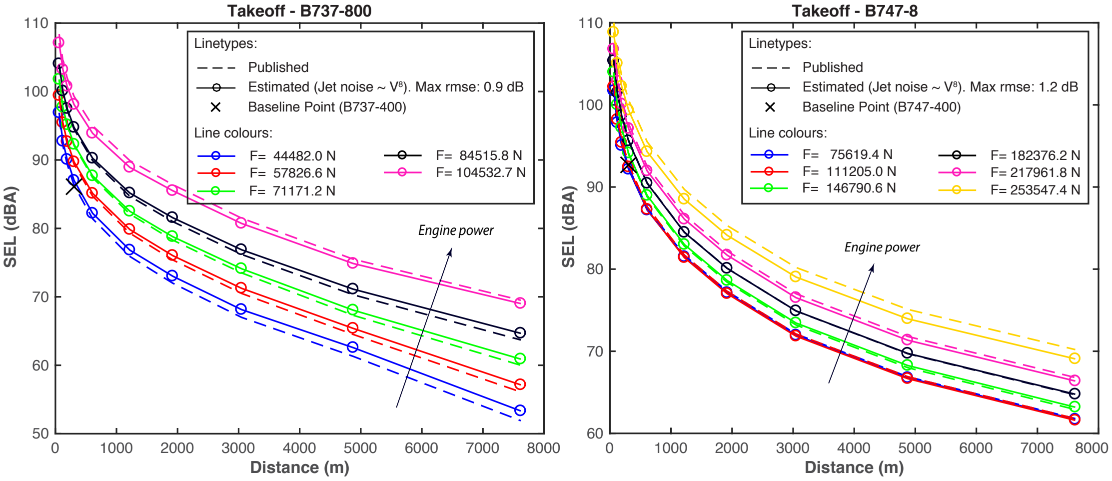

Figure 7.17: Estimated takeoff NPD curves for the Boeing 737-800 and the 747-8. Baseline aircraft are their predecessors, i.e. the B737-400 and the B747-400 respectively.

this simplified study. Also, effects of BPR increase on weight, drag and fuel consumption are ignored and hence thrust requirements remain fixed for all aircraft in Table 7.2.

Table 7.2: List of engine parameters that differ between the engines of the A320-232 and the hypothetical A320.

Aircraft	A320-232	A320-h1	A320-h2	A320-h3
BPR	4.82	6	7	8
Fan Diameter (m)	1.613	1.8	1.9	2.0
FPR	1.73	1.65	1.6	1.5
OPR	27.7	30	32.5	35
N1, max (rpm)	5650	4874	4574	4343

Figure 7.18 plots the estimated noise reduction trends with BPR. Estimated trends agree with the historical trends in the SA noise roadmap [21] and in the ICAO Doc 10017 [132]. Figures 7.19, 7.20 show estimated takeoff NPD curves for the hypothetical A320s. Approach NPDs are indecipherable due to the small noise reductions involved and are therefore not presented.

As a final note, it is worth mentioning that the framework allows numerous other parametric study possibilities, including the direct alteration of noise source levels, as a result of technological improvements. For example, it is possible to investigate the effect of improving the attenuation capability of liners by directly reducing fan noise. Normally, this example would give an optimum value, since noise attenuation benefits come at the cost of increased weight; advanced lining materials are generally heavier, e.g. Haynes 25 has a density of around 9000 kg/m^3 [169].

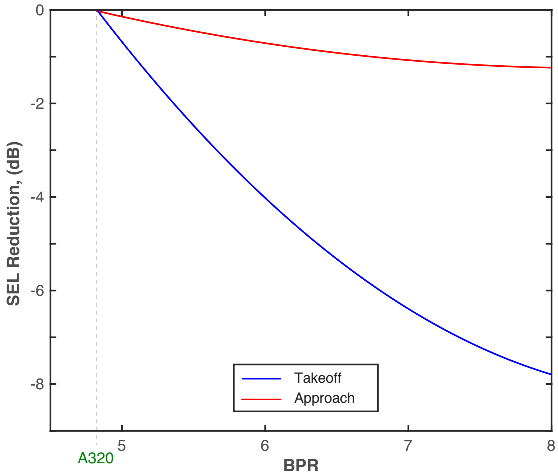

Figure 7.18: Estimated noise reduction trends with BPR.

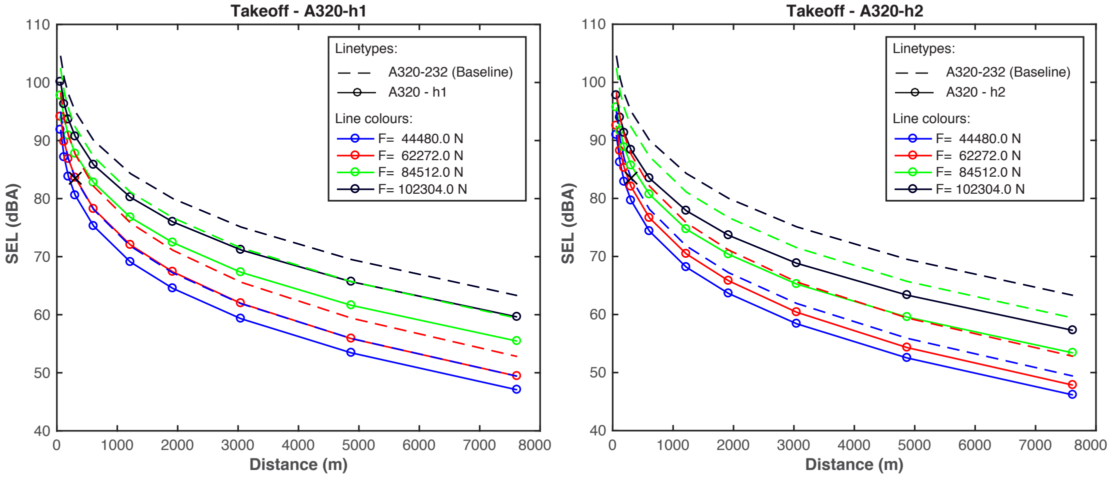

Figure 7.19: Comparison between published NPD curves for the A320-232 and estimated ones for an hypothetical A320 that has engines with larger BPR.

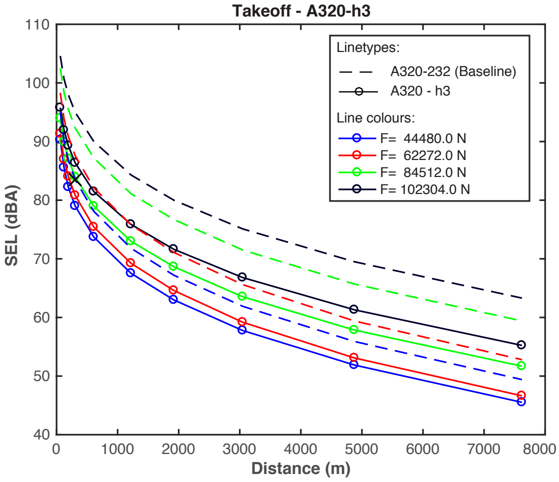

Figure 7.20: Comparison between published NPD curves for the A320-232 and estimated ones for an hypothetical A320 that has engines with larger BPR.

7.3 Error Analysis

7.3.1 Error due to number of included noise sources

As described in Section 5.5.1, the framework specific configuration for producing the results in Chapters 7–9 involves a lumped aircraft model consisting of the significant noise sources of turbofan aircraft; as discussed in Section 2.1.8 these are the fan, jet and airframe. This simplified configuration aims at reducing complexity and the number of inputs required. The relatively small error obtained in the comparisons earlier in this chapter imply that this configuration is adequate for giving a descriptive representation of the aircraft as a noise source.

Figure 7.21 shows the maximum rms error between estimated and published NPD curves, for the various aircraft involved in this study, and for different framework configurations. The black trend line represents the above-mentioned three sources configuration; so, it essentially summarises the rms error obtained in the comparisons in Section 7.1. The trend line does not exceed 2 dB, confirming that acceptable error is produced if the aircraft is modelled as a lumped noise source consisting of only these sources.

The remaining curves in this figure refer to cases where the framework includes two out of the three significant sources. It is seen that the impact of omitting the airframe noise contribution (red curve) is negligible at takeoff, whereas it gets more important at approach. In contrast, ignoring the fan and jet contributions at takeoff results into large errors. These behaviours are in accordance to the dominant sources discussion of Section 2.1.8. Moreover, due to the jet noise reduction with BPR, the error from omitting the jet (blue line) reduces with increasing aircraft size (Table 7.1 shows that large aircraft tend to have high BPR engines), while the opposite is observed for the fan (green line).

As a last point, the effect of this simplification on emissions estimation must be examined. As described in Chapter 2, emissions are represented by specific engine design properties and operational parameters and therefore, optimisation in terms of engine components number is non-applicable. Hence, modelling the aircraft as a fan, jet and airframe does not affect emissions estimations.

7.3.2 Error due to lumped model

Figure 7.22 plots the SPL time histories at takeoff and landing certification conditions as obtained from FANjET when the aircraft is modelled as a lumped or distributed sound source. Also plotted are the time histories when the aircraft is modelled with the two most important sources for each operation. Plots in Figure 7.22 suggest that results generated with either modelling approach are identical. Normally, the lumped model is computationally faster, because it only deals with one noise source, and hence one

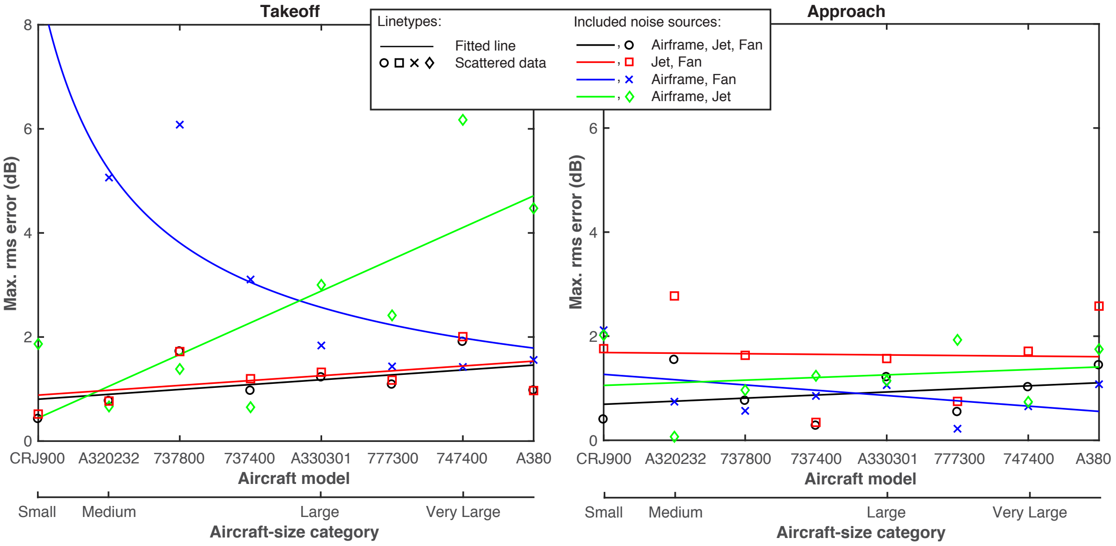

Figure 7.21: Maximum rms error between estimated and published NPD curves when including different noise sources, as a function of aircraft–size category.

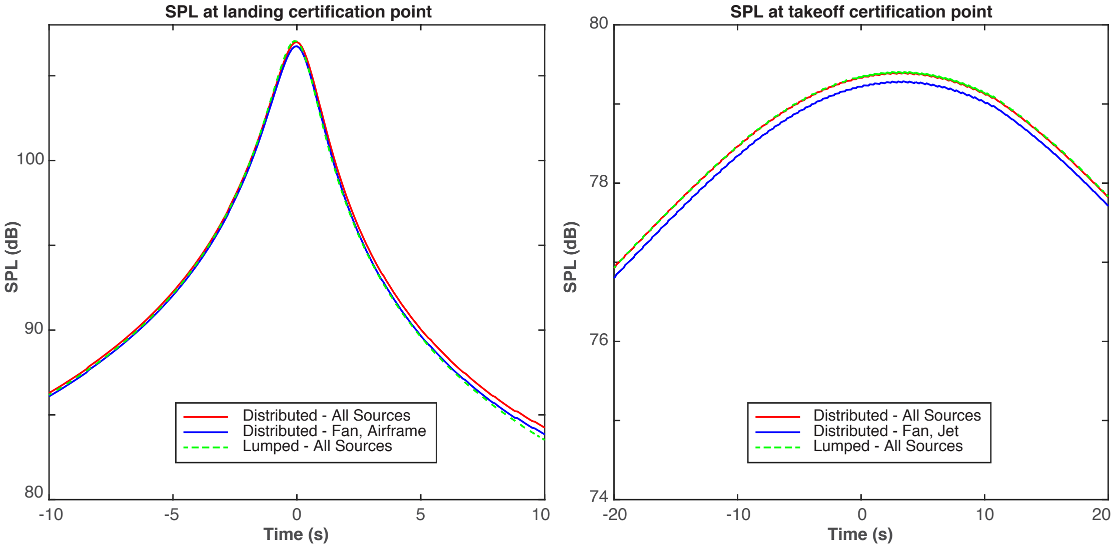

Figure 7.22: Time history at landing (left) and takeoff certification points when modelling the aircraft as a lumped or distributed noise source.

directivity factor and one distance between observer and aircraft. This agrees with the computation times listed in Table 7.3 that refer to noise estimations for a simple flyover. For statistical reasons, time measurements are repeated eight times.

7.3.3 Error from using average data

The good agreement between estimated and published NPD curves implies that error introduced from using average directivity and noise data is acceptable. Using average

Table 7.3: Estimation times for a simple flyover using the lumped and distributed noise source models.

	Time (ms)									Difference
Iterat. No	1	2	3	4	5	6	7	8	Average	(%)
Lumped	8.3	5.8	4.2	4.7	8.2	5.8	4.6	4.4	5.7	-65%
Distributed	29.3	18.5	14.9	15.6	17.9	14.3	13.9	18.8	17.9	

values offers the following benefits: a) aircraft of similar noise and performance characteristics are represented by only one base aircraft, b) dependence on explicit aircraft details is bypassed, c) average noise levels for individual aircraft noise sources (fan, jet, etc) that are publicly available can be used (in contrast, such data are normally proprietary to manufacturers for specific aircraft), d) this approach is very useful and completely valid in the study of future aircraft designs, where only the specifications of a generic (or representative) aircraft of a particular category are considered, and e) the overall complexity of the method is reduced.

7.3.4 Sensitivity analysis of estimated engine performance inputs

Section 5.5.5 described the process for obtaining the necessary engine performance inputs to the proposed framework. This process involves estimation of certain parameters. Typically, these are the total mixed jet temperature $T_{tj,m0}$, the FPR and the engine airflow, $\dot{m}_{air,0}$, at rated thrust. Figure 7.23 illustrates the maximum rms error, in dB, between estimated and published NPD curves if the value of these parameters deviate from their estimated value by up to ±20%. The estimated noise is found to be most sensitive to variations in $\dot{m}_{air,0}$; a 20% decrease to $\dot{m}_{air,0}$ increases the maximum rms error by 4 dB. In contrast a ±20% variation to the total mixed jet temperature $T_{tj,m0}$ or the FPR would cause level differences within 1 dB. This practically means that there is a larger tolerance in estimating the two last mentioned parameters.

7.3.5 Error due to noise prediction methods

It was pointed out earlier that noise prediction methods for individual aircraft noise sources are indispensable for the framework functionality. As aircraft and propulsion system design evolves, some methods tend to become inaccurate and even obsolete. For example, Fink's method may be unsuitable for modelling the noise characteristics of advanced high-lift devices, such as Krueger flap. Moreover, future aircraft designs may feature different and/or new significant noise sources. Although the proposed framework's accuracy relies on the level of adaptation of noise prediction methods to new technologies and/or the development of new ones, it is independent of specific such methods. New methods for (existing or new) individual aircraft noise sources (e.g. higher fidelity

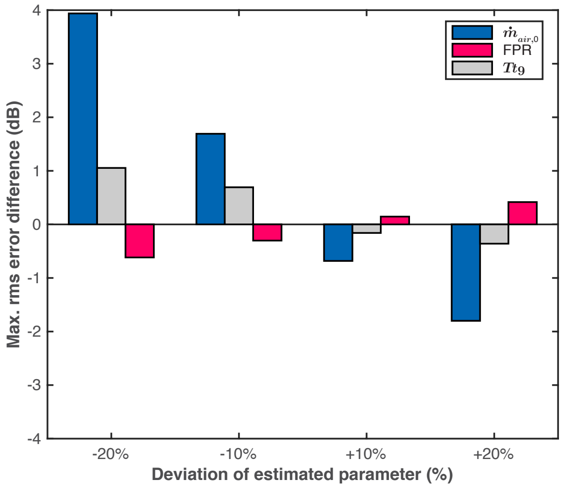

Figure 7.23: Sensitivity analysis of the estimated engine performance inputs.

methods incorporated into NASA's next generation aircraft noise prediction program, ANOPP2 [120], such as the recently developed Boeing methods for Kruger flap [173] and landing gear [174]) can be introduced within the proposed framework in order to improve accuracy. Also, installation effects due to different configurations (e.g different engine positioning) can be included by either using appropriate higher fidelity methods, or applying empirically-based corrections (e.g. see BWB example in Section 9.6, where corrections are directly applied on noise radiated within the shielding range).

To demonstrate the dependence of the framework's accuracy on noise sources prediction methods, this section investigates the effect of reducing the 8th power dependence between the jet noise intensity with jet velocity, suggested by Lighthill. Besides, it was discussed in Section 2.1.7 that this dependence is only valid under certain conditions (e.g. for pure turbojet engines). Figure 7.24 shows the maximum rms error between estimated and published NPD curves for the various aircraft involved in the present thesis, when the dependence is reduced to the 7th and 6th power. Interestingly, it is seen that these reduced relationships, that are represented by the red and blue fitted lines respectively, produce smaller error at approach, indicating that these could be more valid for low engine power settings. The effect at takeoff is generally smaller. Further investigating this dependence goes far beyond the scope of this thesis.

7.3.6 Error due to baseline scenario

Baseline aircraft noise levels

Typically, baseline aircraft noise levels are published NPD points obtained through the standard field measurements specified in the SAE AIR1845 documentation (see Section 2.1.5). These experimentally obtained levels may be contaminated due to: a) pilots

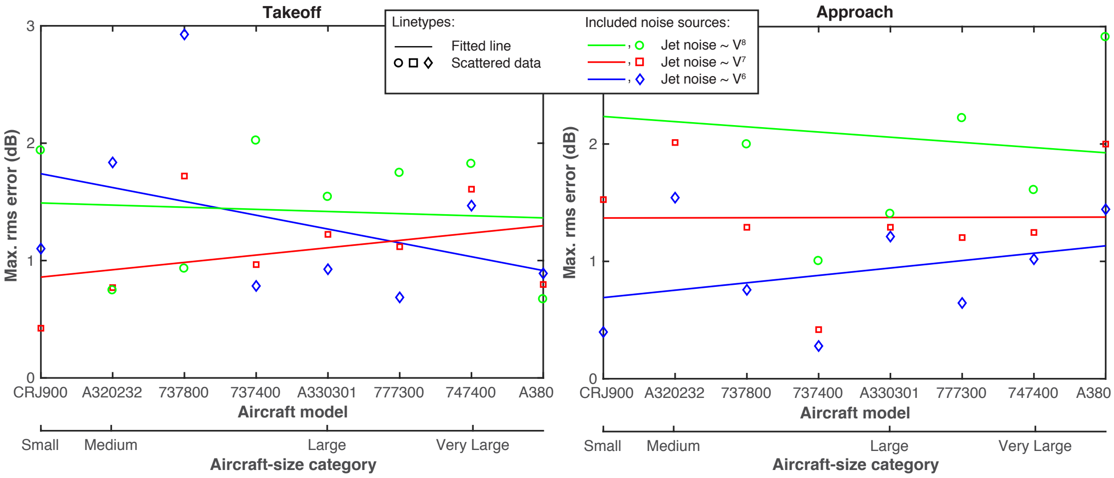

Figure 7.24: Error arising from using Lighthill's acoustic analogy.

failing to accurately maintain the nominal flight profile, engine power setting and configuration, b) inaccuracies in recording the test aircraft position and synchronising it with noise measurements, and c) varying atmospheric conditions during testing.

Errors embodied in the baseline scenario noise levels do not affect the effectiveness and validity of the framework, for two reasons: a) baseline error only affects the base point and does not scale within the framework, and more importantly b) the proposed framework does not intend to predict absolute noise values. In contrast, it has a comparative nature where only changes in noise level are estimated and hence baseline scenario errors do not prevent its ability to correctly render trends.

To support these arguments, an example is given below involving steeper takeoff, which is an operational mitigation strategy (the environmental impact of steeper operations is thoroughly investigated in the next Chapter using the proposed framework). Figure 7.25 plots the variation of SEL with takeoff angle using two different baseline points. The blue curve represents the variation when a published (exact) baseline point is used. The red circles depict the same variation but starting from a baseline level shifted upwards by 5 dB. It is seen that the results of this parametric study remain unaffected by the baseline points.

Baseline individual noise source levels

In contrast to the aircraft baseline level, relative levels between the individual noise sources of the baseline aircraft significantly affect the framework's estimations. The procedure to estimate these noise source levels essentially involves fitting of predicted NPD curves to published ones, as described in Section 5.6. This implies that NPD uncertainties (described later in Section 7.3.8) could influence the resulting noise source levels. Also, the fact that the fitting process is based on average levels could suggest

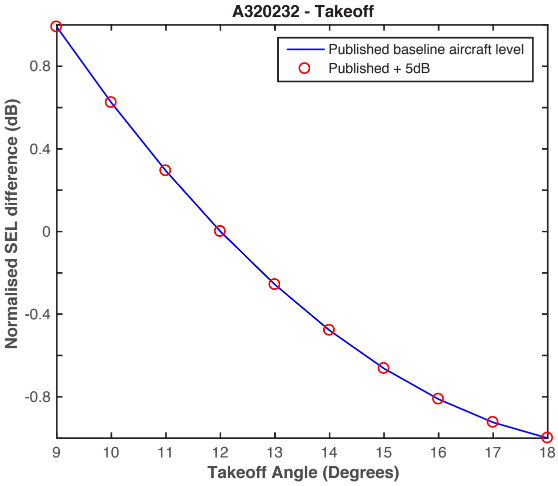

Figure 7.25: Effect of aircraft baseline level on estimated noise levels.

further uncertainties. Finally, the fact that noise source levels for all aircraft within a given size category are derived through small variations of the same average levels (provided by NASA) implies the assumption that all aircraft (within that category) have the same dominant noise sources. Although this is a reasonable assumption to make, since parameters affecting noise (e.g. maximum static thrust, BPR, fan diameter) are generally similar for turbofan engines applicable to each aircraft size-category, some exceptions could exist. This section investigates the sensitivity of aircraft noise estimations to relative noise sources uncertainties.

Figures 7.26 and 7.27 show the SPL change at certification conditions due to a ±2 dB variation in individual noise sources, for aircraft of different sizes. Also plotted is the SPL change due to a concurrent ±2 dB variation of all sources. At takeoff, an increase/decrease by 2 dB in one of the dominant noise sources (jet or fan discharge) results into an overall SPL increase of 1 dB. Airframe variation has an impact of less than 0.5 dB in all aircraft-size categories. The exact opposite situation is observed at approach, where airframe noise dominates. As would be expected, larger errors are tolerable when estimating non-dominant individual sources of the baseline aircraft. Clearly, larger errors occur if all dominant sources are concurrently over or under estimated. However the possibility of underestimating one dominant source while overestimating another could also be considered; such a case would lead in reducing or cancelling out the overall error. For instance, overestimating the jet noise of the A320-232 by 2 dB while underestimating the fan noise by 1 dB produces a SPL change of about 0.7 dB.

7.3.7 Error from the thermodynamic engine cycle analysis

As demonstrated in Section 5.5.5, engine stream velocities are approximated through the turbofan engine cycle thermodynamic analysis described in Chapter 6.2. This analysis

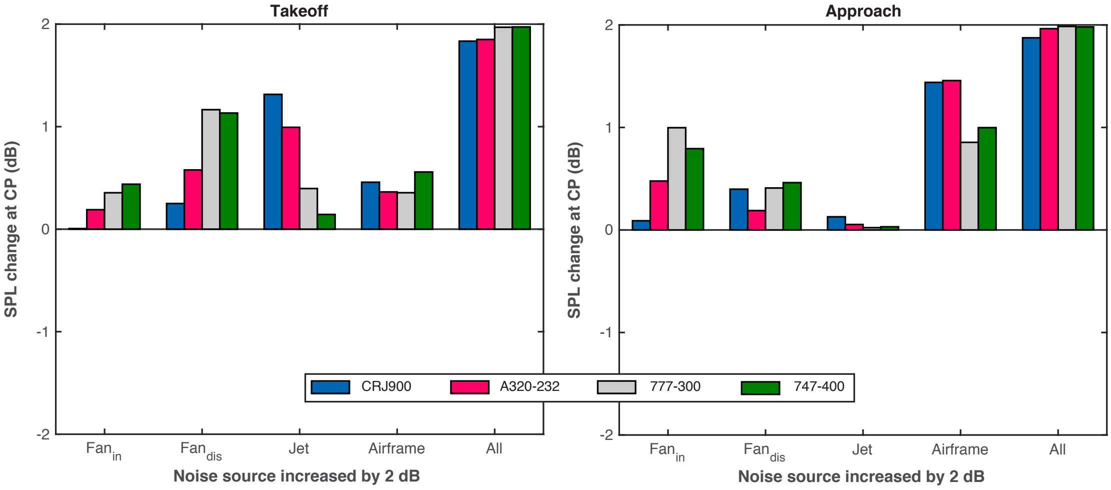

Figure 7.26: Noise sensitivity analysis for increasing baseline aircraft noise sources by 2 dB.

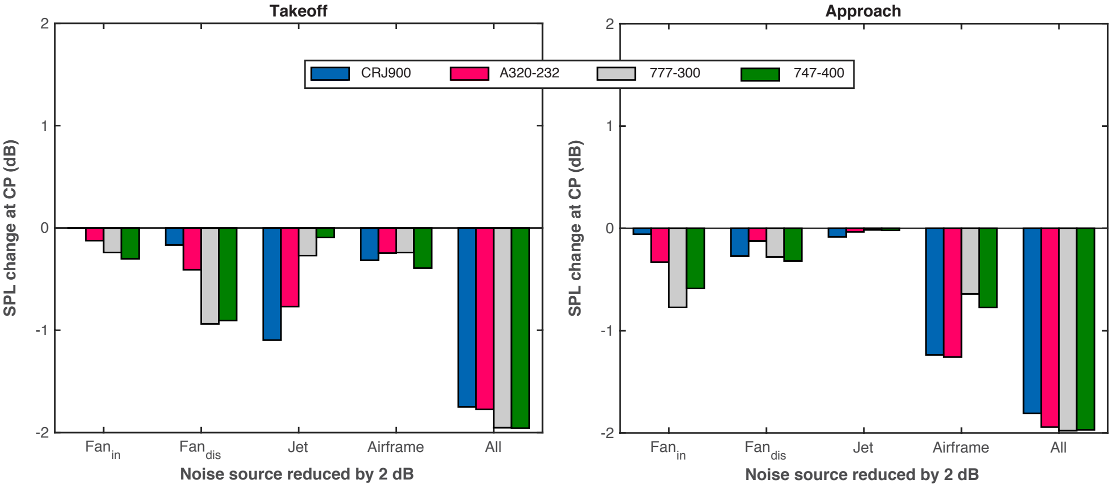

Figure 7.27: Noise sensitivity analysis for decreasing baseline aircraft noise sources by 2 dB.

involves two possible sources of error: a) the ideal gas turbine cycle assumptions listed in Table 6.2, and b) the fact that the rotating machinery components are assigned fixed, empirically derived polytropic efficiencies that represent a technology level rather than a certain engine. According to [163, 156, 157], the former produce insignificant approximation error. Concerning the latter, the average variation of jet velocities resulting from altering efficiencies by 10% was found to be less than 3%. This produces an average noise level error in the order of 0.1 dB. Overall, it is judged that the thermodynamic engine cycle analysis performed delivers sufficiently accurate inputs to the framework.

7.3.8 Error from NPD development uncertainties

Generating NPD curves through the proposed noise estimation framework incorporates the computational part of the standard SAE AIR1845 procedure in order to generalise estimated noise levels to all NPD distances. Uncertainties associated with that procedure need to be mentioned and are therefore discussed in this section. It should be noted that any error deriving from these uncertainties is irrelevant to the proposed framework. Any improved procedure for developing NPD curves can be used instead to eliminate error.

Two potential sources of uncertainty of the standard SAE AIR1845 are identified:

- SAE AIR1845 documentation clarifies that SEL NPD data is extrapolated from the measured initial levels to other distances by adding the corresponding atmospheric and distance attenuation. This requires knowledge of spectral data. NPD curves for most existing aircraft are derived based on average spectral shapes for aircraft with resembling spectral characteristics. Moreover, these average spectra are normally representative for just the time of $L_{A,mx}$ occurrence. Even in the ideal case when average spectra data is available for the full time history of the test flyover, some discrepancies have been reported between NPD data and field measurements, especially in the larger distances and at frequencies above 4 kHz [111, 26]. This implies that NPD data are likely to incorporate discrepancies that may be severe for some aircraft types, particularly at larger distances.
- The procedure assumes that the polar angle when $L_{A,mx}$ occurs is independent from distance, which means that the effect of atmospheric absorption at large distances on that polar angle is neglected. Although an empirical factor is used to correct that, uncertainty still remains due to the fact that the same factor is used for all aircraft and distances.

7.3.9 Other sources of error

Generally, results can also be affected by the directivity data used. It must be reminded that in this thesis, the same ANOPP directivity data are used for all aircraft types and operations, although as stated in Section 2.1.8.1, directivity is influenced by numerous factors, such as jet velocity and flight speed.

There is of course a mathematical error associated with the way the framework estimates changes in noise sources (i.e. Equations in Section 5.5). However, the examples presented in this Chapter demonstrated that if appropriate noise prediction methods for individual aircraft noise sources are used, then the error is likely to be small.

Also, errors may occur from omitting or failing to accurately account for the noise impact of technological interventions on individual noise sources, such as the effect of chevrons and liners on jet and fan noise respectively. As was shown in the case study in Section 7.1.3, this effect is considered with the addition of noise reductions to these noise sources based on data found in literature. Alternatively, the impact of new noise reduction technologies can be approximated or assumed e.g. based on historical trends or data available for similar sources.

Looking at the NPD curves comparisons in Section 7.1.2, the published approach NPD curves for all above aircraft show very small noise variations with engine power setting. For example, published approach NPD curves (dashed lines) for the A320-232 in Figure 7.4 almost coincide. Estimated NPD curves (continuous lines) are overestimated. This behaviour is observed at most estimated approach NPD curves. This could be due to:

- Heidmann's method overestimating fan noise changes. I.e. engine power changes may actually have less impact on fan noise. In fact, Stone [135] reports general non-agreements between measurements and predictions through Heidmann's method, especially in low fan speeds. Also, according to ESDU 98008 [137] Heidmann's method could produce a maximum rms error of 5 dB. Employing alternate/newer methods for fan noise may reduce these disagreements at approach.
- Airframe noise dominating over the remaining sources by more than what suggested by the NASA averages. In practise, this would mean that aircraft noise at approach is almost unaffected by engine noise changes (due to engine power changes). Hence, since airspeed (and thus airframe noise) is fixed for different NPD engine power settings, approach NPD curves almost coincide.
- The coefficients used for estimating the effective jet velocity through Mitchel's method [155] (described in Section 5.5.2). In fact Viswanathan [175] propose smaller values for coefficient m ranging between 3.2 and 3.6.

Chapter 8

Applications I: Operational changes

As discussed in the early chapters of this thesis, aviation mitigation strategies involve technological changes (e.g. cutting down source levels) or operational modifications (e.g. increasing the distance between flight path and noise sensitive areas). This chapter demonstrates the framework potential at estimating the impact of operational mitigation strategies by appraising the environmentally optimum descent and takeoff slopes for civil aircraft of different sizes. Steep takeoff and approach procedures are anticipated as promising operational solutions for reducing the noise footprint and improve the local air quality (LAQ) around airports. The particular aircraft models chosen for this study are the Airbus A320-232 and a larger aircraft, the Boeing 777-300.

8.1 Steep approach

According to ICAO [90] and FAA [176], the standard descent angle in the final approach for civil aircraft is 3°. Figure 8.1 illustrates approach profiles for the Airbus A320-232 at slopes ranging from 3° to 6°. These profiles were calculated with the SAE-AIR 1845 [45] aircraft performance procedure by assuming continuous descent approaches (CDA) rather than traditional step approaches and an ideal airport (i.e. with sufficiently long runways, ideal weather conditions, no obstacles, etc.). Figure 8.1 suggests that increasing the approach slope not only elongates the distance between the aircraft flight path and the ground (e.g the approach certification point, CP), but also shortens the time period where the aircraft is near the ground. Steep approach procedures are therefore likely to condense the approach noise foot-print and reduce the area of communities exposed to aircraft noise during approach. Figure 8.1 also implies that steep approach could shrink the time between landings at busy airports, since the distance covered at approach configuration is shortened while average descend airspeed remains roughly the same.

Faster landing procedures may also lead to reducing descent phase fuel consumption and improve LAQ in the vicinity of airports.

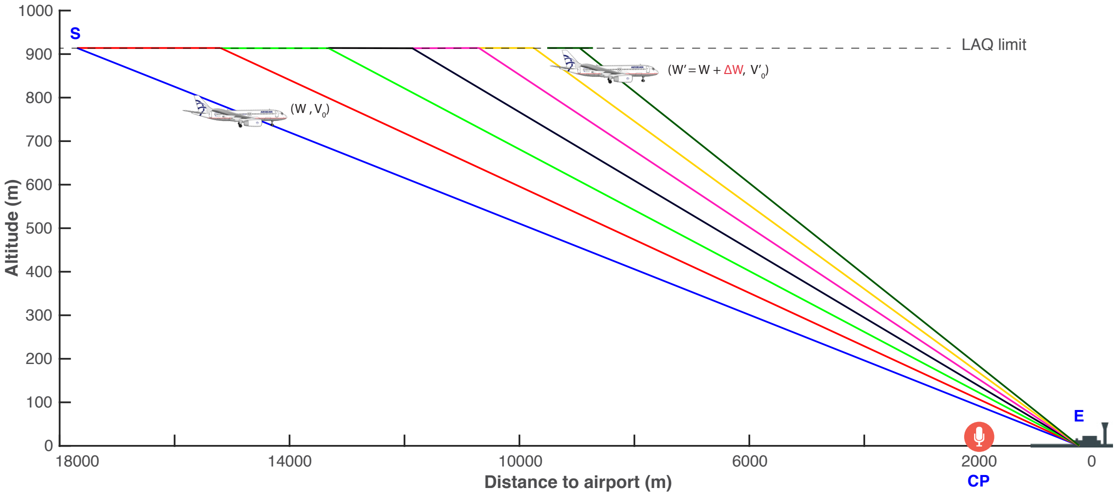

Figure 8.1: Vertical approach profiles at different slopes for the A320-232.

However, the steep approach benefits come with some drawbacks that were first discussed in the late 1960s when the steep approach concept emerged [177, 178]. Back then, it was found unattractive, not only because of the pilot's disapproval of high descent rates due to safety concerns [179], but also due to claims that the noise change near the, unavoidable (at that time) transition from steep to 3° approach was negligible [178]. Since then, aircraft technology has evolved making steep approach safe and feasible so that nowadays, it is been reconsidered as a way of exposing less populated areas to aircraft noise. In fact, London City airport already includes a glide slope of 5.5° in their 2013 - 2018 noise action plan [180]. Yet, this imposes aircraft performance restrictions that limits the types of aircraft that can use the airport.

Assessing the steeper approach impact is not straightforward. Although at first sight it may seem that doubling the descent angle and thus the distance between aircraft path and observer position (e.g. the approach CP) can lead to a SPL reduction of almost 6 dB, the situation is complicated by the fact that under normal flying circumstances, a steep approach is likely to be accompanied by increase of noise at source [181, 177]. This can be attributed to several intermingling factors: Firstly, it is generally acknowledged [181, 182, 165, 177] that fulfilling the steep approach requires additional drag[1]. For example, flight-tests by Toebben et al. [182] demonstrate that steep descent of a Boeing 737-800 requires increased flap deflection angles, whereas flyability tests for various aircraft described by Mollwitz et al. [165] show that steep approach is associated with deployed landing gears that provide additional drag. To prevent aircraft stalls, the additional drag must be compensated by increased engine power (i.e. additional thrust), which results in increased engine noise. Secondly, as earlier discussed, increasing flap deflection angle raises airframe noise. Moreover, to realize steep approaches, some aircraft may need

---

[1] Or more generally, altered aircraft lift to drag ratio (L/D), by modifying both or any of C_L, C_D.

to be equipped with special devices, such as microdrag generators that increase drag [183], clam shells that enable the aircraft to descend at a faster rate [181] and ventral airbrakes that serve at maintaining the appropriate approach speed [184]. Due to their high-lift nature these special devices are likely to raise airframe noise. To complicate the situation even further, Mollwitz et al. [165] suggest that steep approach decreased airspeed is controlled by spoilers, at least for some flap deflection angles. Hence, airframe noise benefits from decreasing airspeed could be outweighed by the noise of spoilers.

Clearly a key point for achieving accurate prediction of the steep approach noise impact is to reliably estimate the associated noise change at source, i.e. the acoustic power change ΔW. Indeed, this is performed below using the proposed noise estimation framework.

8.1.1 Steep approach with an Airbus A320

In agreement with the discussion above, estimating the steep approach noise impact of a A320 requires estimating its configuration and thrust requirements for the examined descent angles. One way of approximating these parameters is extracting them from literature. For instance, according to simulations with an Airbus 310-200 in reference [181], the steep descent at 5.5° requires increasing wing drag (e.g. through flaps) by about 55% or 3.2 kN. Therefore a thrust increase of the same amount can be assumed to avoid stall. Likewise, airspeed can be estimated from Mollwitz's flyability study [165].

Alternatively, the change of thrust and airspeed with approach angle can be estimated through the SAE-AIR 1845 [45] aircraft performance calculations, presented in Section 2.7. This is the methodology adopted in the present study. More specifically, airspeed is calculated with Equation 2.47; whereas Equation 2.48 gives the thrust variation with descent angle. Inputs to these equations are coefficient D that represents different flap settings on approach and coefficient R that describes the aircraft L/D per flap setting. These coefficients are aircraft-specific and are included in the ANP database [44] for the standard flap settings of existing aircraft. As previously mentioned, steep approach operations require greater flap deflection angles than the standard ones, which means that associated coefficients D, R must be estimated. ANP data suggest that coefficients vary almost linearly with flap position; therefore, D and R at any hypothetical flap deflection angle are estimated through linear extrapolation. While hypothetical flap settings are introduced to fulfil the L/D requirements of steep operations, it is assumed that no additional device affecting the aircraft L/D are mount on the aircraft; which means that aircraft weight remains unchanged.

Table 8.1 summarises the configurations, airspeed and thrust variation, ΔF_N, necessary to fulfil CDA descents at several steep slopes with the test A320-232. The notation 'FULL+' represents hypothetical flap settings for the A320-232 associated with descent slopes higher than 5°, for which coefficients D, R are obtained through linear extrapolation. It is seen that estimated ΔF_N value corresponding to the 5.5° case is close to the above mentioned value found in literature. It must be noted that these values reflect to the descent phase only and do not include the horizontal cruise of Figure 8.1, which is only considered for fuel burn comparison between descent trajectories.

Table 8.1: Airbus A320-232 configuration for various CDA descent slopes.

Descent Angle (degrees)	**Gear**	**Flaps ID**	**Average Airspeed V_0 (kt)**	**Duration (s)**	**Thrust Change ΔF_N (kN)**
3°	Down	3D	144.89	243.3	0
3.5°	Down	3D	143.37	209.7	0.45
4°	Down	3D	141.84	184.6	0.94
4.5°	Down	FULL	140.31	165.0	1.45
5°	Down	FULL	138.78	149.39	2.01
5.5°	Down	FULL+	137.25	136.61	2.59
6°	Down	FULL+	135.72	125.97	3.20

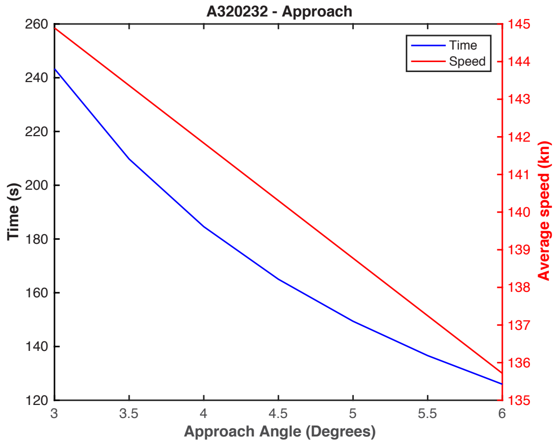

Figure 8.2: Effect of approach angle on descent duration and average airspeed.

8.1.1.1 A320 steep approach noise impact

As already discussed, the noise impact assessment of changes (e.g. mitigation strategies) through the proposed noise estimation framework is performed with respect to a known baseline scenario. For the examined case, the baseline point will be on the NPD curve representing the amount of thrust required for the A320-232 conventional, 3° CDA; using the SAE-AIR 1845 [45] methodology, this thrust is found to be 16 kN. Hence, the base NPD curve derives through interpolation between the 12 kN and the 26.6 kN approach NPD curves for the A320-232 (shown in Figure 7.4). Clearly, interpolation is not essential in the A320-232 case, since NPD curves are very close to each other.

The aircraft acoustic power level, L_w, at conventional CDA approach configuration is extracted using that NPD curve and following the procedure described in Section 5.6.1.

Ultimately, with reference to Figure 2.6:

$$\mathrm{L}_w = \mathrm{L}_{A,max} + 10\log\frac{R_p^2}{D(\theta_p)CW_{ref}}. \tag{8.1}$$

NASA measurements in [65] and simulations with FANjET suggest that for the A320-232, $\theta_p \approx 95°$ and hence, $R_p \approx R_{SL}$; hence, distance R_p is only calculated next for the sake of generality. The typical slant distance corresponding to NPD development flyovers is $R_{SL} = 300$ m [45]. Thus, using Equation 5.51, $R_p = 301$ m whereas NPD curves suggest that $\mathrm{L}_{A,max} \approx 73$ dB.

The aircraft acoustic power change, ΔW, due to the steep approach is estimated with the proposed framework, i.e. the methodology described in Chapter 5. The engine acoustic power change due to the above calculated thrust change, ΔF_N, as well as the impact of aircraft configuration and airspeed variations on airframe acoustic power are estimated with the procedure in Section 5.5. To reduce complexity, landing gears are considered to be deployed at the same horizontal distance from the airport independently of descent angle and thus, their noise impact remains fixed for all profiles. Extraction at different lateral distances would induce a new configuration change between standard and steeper descent and an additional level change, ΔLw_a, obtainable through Fink's method for airframe noise. Also, airframe noise variation due to attitude change is ignored.

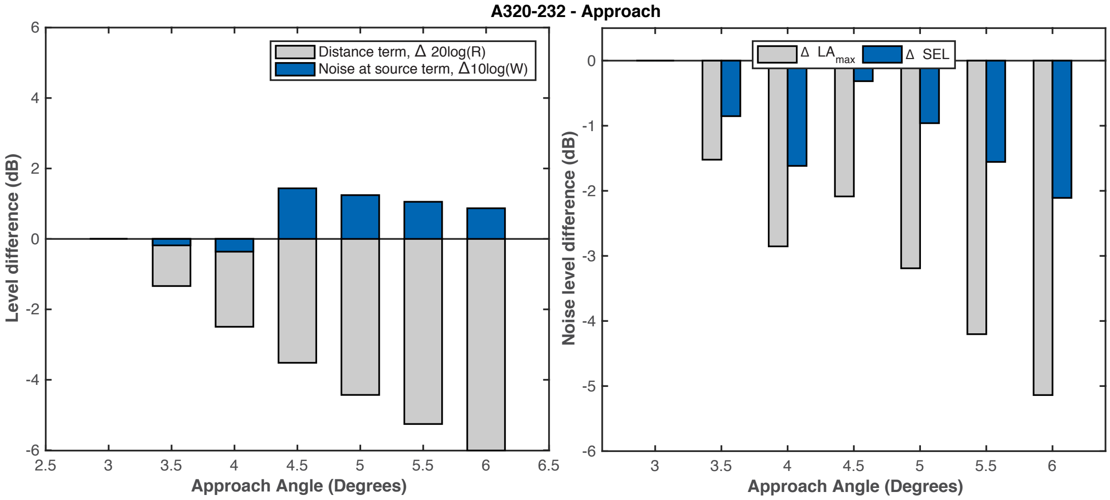

Figure 8.3: Left: Level difference due to variation of noise at source and of the distance between aircraft and CP with approach angle. Right: Noise level difference at the approach CP between conventional and steeper approach profiles.

The left plot of Figure 8.3 depicts the noise at source variation with approach angle and the noise benefits from increasing the distance, R, between aircraft and CP. The noise increase at source at slopes steeper than 4° is a result of the increased flap deflection angles at these flight profiles. The right plot of the same Figure gives the overall noise impact per approach angle; it shows the maximum instantaneous noise and exposure level change at the approach CP for each descent angle, as calculated using the geometry of Figure 8.1 and Equations 2.4 and 2.14. Clearly, the noise impact decreases with slope angle. Yet, a more holistic impact assessment requires to also examine the emissions impact of the steeper approaches, as shown below. Integrated plots containing both noise and emissions impact for all cases examined in this study are summarised in Section 8.3.

8.1.1.2 A320 steep approach emissions impact

As described in the emissions assessment methodology of Section 2.3, critical parameters for emissions calculations are the engine power setting, the time period operating at that setting, as well as the associated fuel flow, $\dot{m}_f$, SFC and EIs. Effects of altitude, descent angle and ground speed on $\dot{m}_f$, SFC and EI described in references [18, 25, 80, 185] are considered negligible and irrelevant to the purpose of this thesis. If needed, these effects can be incorporated in emissions calculations, if suitable relationships are available.

In contrast, influence of thrust variation, ΔF_N, on SFC and the NO_x EI needs to be embodied into calculations, because Equations 8.3 and 8.6 imply that the variation of these parameters is essential for trustworthily estimating fuel consumption and NO_x emission per flight profile. If appropriate engine data are available, NO_x and SFC variation can be predicted through dedicated engine performance tools (e.g. Piano-X [145]) that can also reveal effects of ΔF_N, on combustor temperature (that, as mentioned earlier determines NO_x emissions). Alternatively, NO_x and SFC changes can be estimated either through simpler, generic engine performance tools (e.g. NASA EngineSim [148]), or based on historical trends and/or experimental databases, such as the ICAO emissions databank [79] and data in [81] and [82]. Among these options, the present study uses experimental databases, although these have the disadvantage (mentioned in Section 2.3) of only providing a single value of $\dot{m}_f$ and EI for each flight phase.

Table 8.2: Fuel flow and NO_x Emission Indices at the LTO thrust settings, for the A320-232 engine, the V2527-A5 [79].

	Takeoff	**Climb**	**Approach**	**Idle**
% of rated thrust, F_∞	100	85	30	7
$\dot{m}_f$ (kg/s)	1.053	0.880	0.319	0.128
EI_{NOx} (g/kg)	26.5	22.3	8.9	4.7

The NO_x EI corresponding to each approach profile thrust setting is estimated through interpolation on the ICAO databank EIs listed in Table 8.2 (other experimental databases could have been used instead, such as the ones in references [79, 81]). Values in Table 8.2 are plotted in the left graph of Figure 8.4, suggesting that variation of EI with thrust is more accurately described by a quadratic relationship, since the NO_x EI is somewhat more sensitive to thrust changes at high engine power settings. In that context, interpolation used for acquiring NO_x EIs is quadratic. The A320-232 thrust requirement for fulfilling the conventional, 3° CDA approach was found earlier to be 16 kN, which corresponds to around 14% of F_∞, since the rated thrust of the A320-232 engine (the V2527-A5) is $F_\infty = 117$ kN [44]. Interpolation yields a value of 5.88 for the NO$_\text{x}$ EI at 14% of F_∞. The NO$_\text{x}$ EIs corresponding to the thrust settings used in the steeper CDA approach profiles are calculated similarly using the thrust changes in Table 8.1, and are listed in Table 8.3. It is seen that the maximum ΔF_N among the examined profiles (which occurred between the 3° and 6° profiles and is 3.2 kN, or 2.8% of F_∞) induce a NO$_\text{x}$ EI variation of around 20%, which is small but not negligible.

Table 8.3: Estimated NO$_\text{x}$ EIs per descent angle, for the A320-232 engine.

Approach angle	3°	3.5°	4°	4.5°	5°	5.5°	6°
EI$_{NOx}$ **(g/kg)**	5.88	6.05	6.22	6.41	6.60	6.81	7.03

The variation of SFC is extracted similarly. The engine rated thrust, F_∞, and the fuel flow that is obtainable from the ICAO databank [79] (reproduced in Table 8.2) yield the SFC at each ICAO thrust percentage, $F_\%$, with Equation 8.2. The SFC at any other thrust setting is approximated through quadratic fit, resulting in the curves in the right plot of Figure 8.4.

$$SFC_{ICAO} = \frac{\dot{m}_f}{F_\infty F_\%} 100\,. \tag{8.2}$$

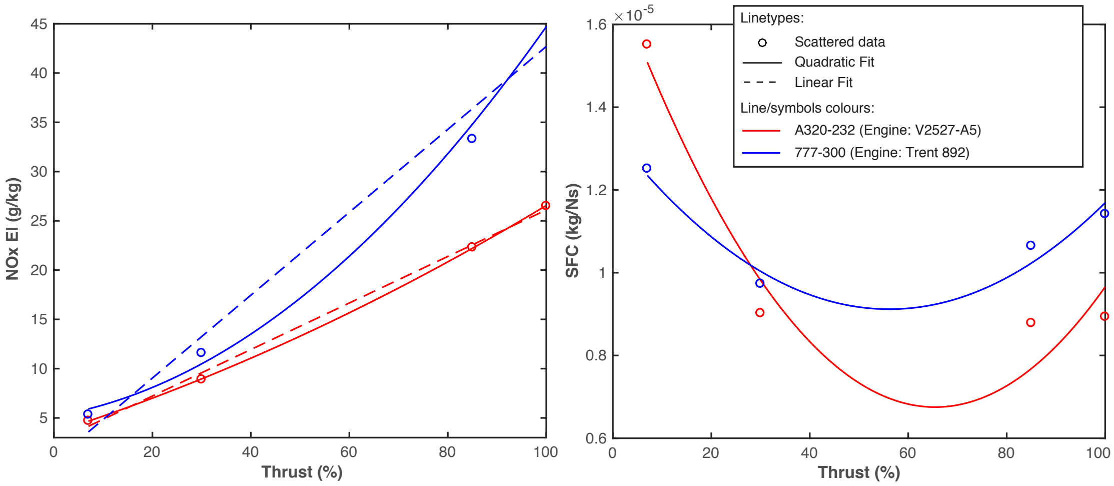

Figure 8.4: Estimated variation of NO$_\text{x}$ EI (left) and SFC with thrust for the engines of the A320-232 and the 777-300.

SFC variation with thrust leads to estimating variation of fuel flow rate with thrust variation, using algebraic operations starting from Equation 2.19:

$$\Delta\dot{m}_f = SFC\,\Delta F_N + \Delta SFC\,F_N + \Delta SFC\,\Delta F_N\,. \tag{8.3}$$

An expression for the fuel burn per descent angle is deduced from Equation 2.20:

$$m_f = (\dot{m} + \Delta\dot{m}_f)(T + \Delta T)\,, \tag{8.4}$$

where T, ΔT are the conventional descent duration and the duration change per approach profile respectively. To objectively compare profiles fuel consumption is assessed between points S and E of Figure 8.1. Equation 2.22 yields the amount of emitted CO_2

$$E_{CO_2} = 3.15\, m_f\,. \tag{8.5}$$

With $EI_{NOx,\sigma}$ being the above-approximated NO_x EI at engine power setting σ, the NO_x emission change is estimated based on Equation 2.24:

$$\Delta NO_x = EI_{NOx,\sigma}\, \Delta E_f\,. \tag{8.6}$$

Figure 8.5 depicts the fuel consumption and emissions impact of various steep approach profiles for the A320-232. While fuel consumption increases with approach angle, descent at 5° seems to optimise NO_x emission. The dashed red line represents the NO_x estimations if the ICAO NO_x EI is used for all approach angles, revealing the importance of accounting for the variation of EI with engine power. As already mentioned, the impact in terms of both noise and emissions is discussed in Section 8.3.

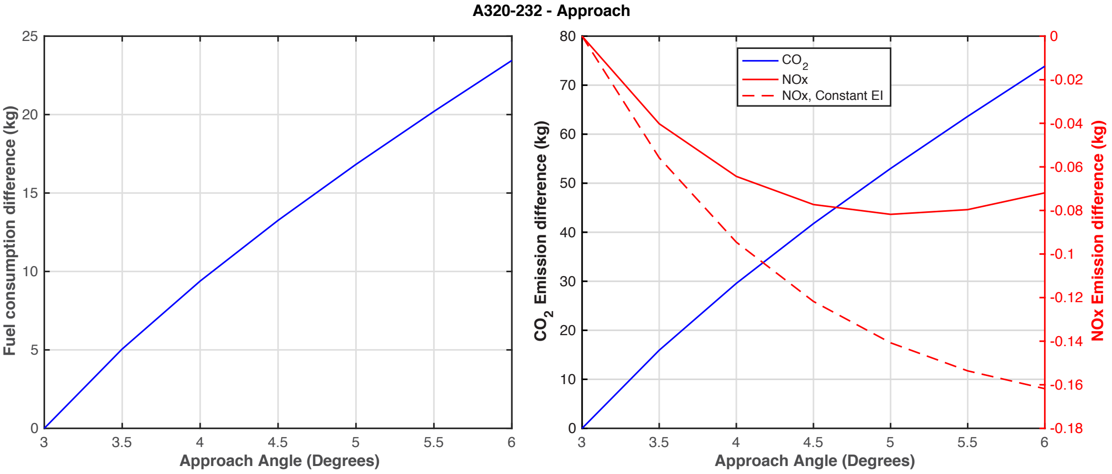

Figure 8.5: Variation of fuel consumption (left) and of emitted amount of CO_2 and NO_x among different steep CDA approach profiles for the A320-232.

8.1.2 Steep approach with a Boeing 777-300

Following the same methodology as for the A320-232, this Section investigates the environmental impact of steep approach for a larger aircraft, the Boeing 777-300. Table 8.4 outlines the relevant details per descent angle. The notation 'L_30_D+' represents hypothetical flap settings for the 777-300 associated with descent slopes higher than 5°, for which coefficient R has been obtained through linear extrapolation. Moreover, ICAO and interpolated values for NO_x EI are listed in Tables 8.5 and 8.6 respectively. Figures 8.7 and 8.8 show the corresponding noise and emissions plots.

Table 8.4: Boeing 777-300 configuration for various CDA descent slopes.

Descent Angle (degrees)	**Gear**	**Flaps ID**	**Average Airspeed V_0 (kt)**	**Duration (s)**	**Thrust Change ΔF_N (kN)**
3°	Down	L_25_D	156.07	228.61	0
3.5°	Down	L_25_D	152.71	198.22	4.11
4°	Down	L_25_D	149.35	175.48	8.52
4.5°	Down	L_30_D	145.99	157.85	13.21
5°	Down	L_30_D	142.63	143.78	18.17
5.5°	Down	L_30_D+	139.27	132.31	23.34
6°	Down	L_30_D+	135.91	122.79	28.86

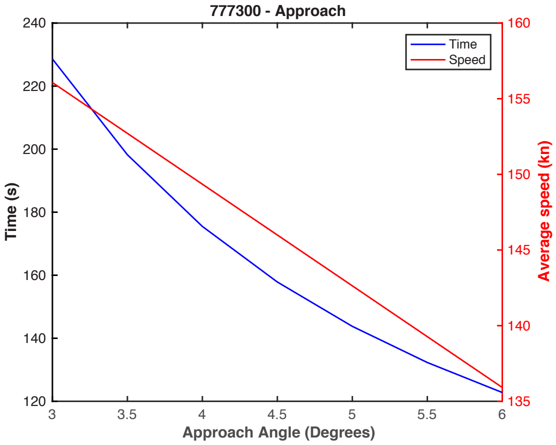

Figure 8.6: Effect of approach angle on descent duration and average airspeed.

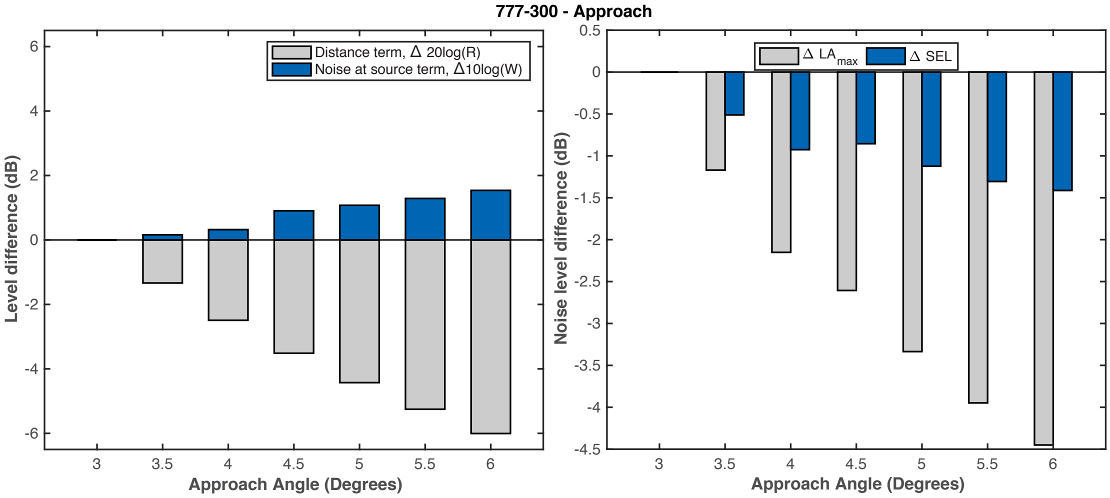

Figure 8.7: Left: Visual representation of level difference due to variation of noise at source and of aircraft to CP distance. Right: Variation of noise level at the approach CP for different steep approach profiles, compared with the conventional descent for the 777-300. Negative values indicate noise reduction.

Table 8.5: Fuel flow and NO_x EIs at the LTO thrust settings, for the 777-300 engine, the RR Trent 892 [79].

	Takeoff	**Climb**	**Approach**	**Idle**
% of rated thrust, F_∞	100	85	30	7
$\dot{m}_f$ (kg/s)	3.91	3.10	1.00	0.30
EI_{NOx} (g/kg)	45.7	33.3	11.58	5.33

Table 8.6: Estimated NO_x EIs per descent angle, for the 777-300 engine.

Approach angle	3°	3.5°	4°	4.5°	5°	5.5°	6°
EI_{NOx} (g/kg)	7.88	8.30	8.75	9.23	9.72	10.25	10.80

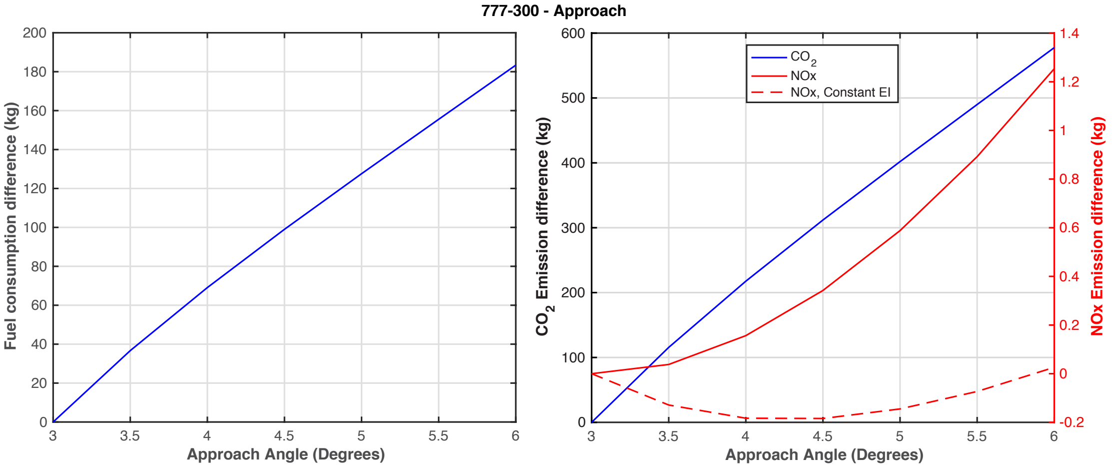

Figure 8.8: Variation of fuel consumption (left) and of emitted amount of CO_2 and NO_x among different steep CDA approach profiles for the 777-300.

8.2 Steep takeoff

This Section investigates the environmental impact of various steep takeoff profiles using the same aircraft as in the steep approach study, i.e. the Airbus A320-232 and the Boeing 777-300. Typically, takeoff operation is split into three segments [45, 32]; the ground roll, the initial climb and the continuing climb. The noise impact is extracted by examining the takeoff operation from the start of the ground roll (i.e. the brake release point) until climbing to an altitude where the SPL becomes lower than 20 dB from the maximum experienced SPL. In contrast, emissions impact assessment requires including different takeoff segments and sub-segments. Fuel consumption requires not only including the ground-roll, which differs among takeoff profiles as explained later, but also setting fixed start and end mission points for all profiles, to ensure objective comparison. Hence, the accounted takeoff period starts from the start of roll and ends at a common point at altitude h. Likewise, NO_x emissions estimation starts from the brake release point, but ends at the LAQ emissions altitude limit, i.e. 3000 ft.

8.2.1 Steep takeoff with an Airbus A320

Figure 8.9 gives a visual representation of the examined takeoff profiles for the A320-232, up to the common mission point, E. Just like in the steep approach study, these profiles derived through the SAE-AIR procedure [45]. Also shown in the Figure are the takeoff segments, whereas CP denotes the takeoff certification point (defined in Section 2.1.6). The procedure for deriving these profiles and the associated assumptions are described next.

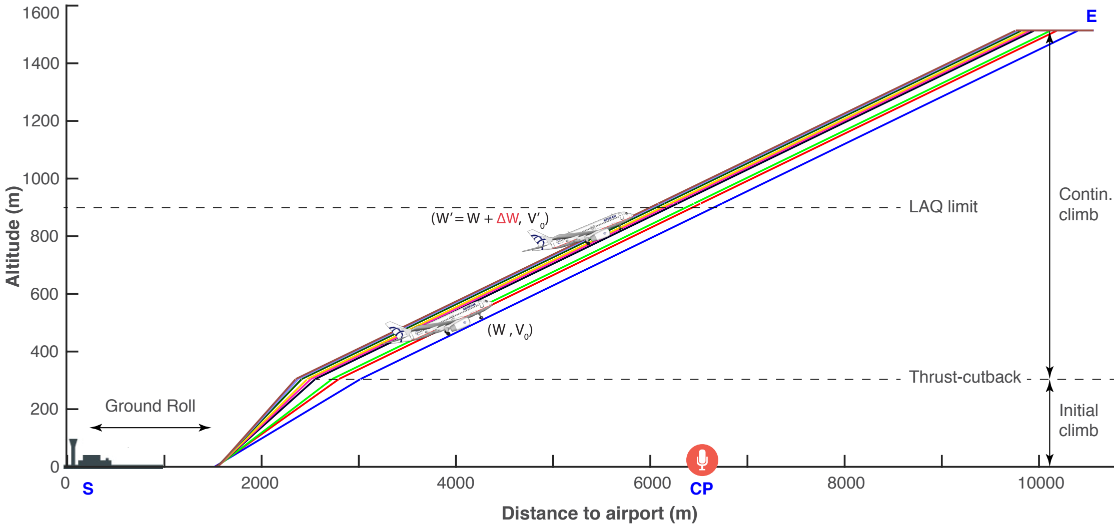

Figure 8.9: Vertical takeoff profiles at different slopes for the A320-232.

Initial climb

The initial climb segment represents the initial sharp climb at constant speed to the thrust-cutback altitude (1000 ft). It is described before the ground roll segment because it establishes the initial climb speed, V_0, that in turn determines the ground roll distance, as explained below.

The average geometric initial climb angle is calculated using Equation 2.46, as suggested by SAE-AIR 1845. Ignoring the negligible effect of the bank angle term $\cos\epsilon$ the Equation becomes:

$$\gamma = \arcsin\left[K\left(N\frac{\overline{F_N/\delta_{am}}}{\overline{W/\delta_{am}}} - R\right)\right] . \tag{8.7}$$

Assuming a fixed aircraft (i.e. fixed parameters W and N), Equation 8.7 suggests that, in contrast to the steep approach case, takeoff angle value is not a direct input; rather, it is determined by the combination of thrust, F_N and flap setting that is associated with coefficient R. Increasing flap deflection angle (i.e. increasing coefficient R) decreases climb angle, whereas the opposite stands for increasing the thrust. Hence, the various takeoff profiles examined in this study are defined by appropriately varying these two parameters. According to the EASA Type Certificates (TCDS) [51], the A320-232 theoretical thrust for a conventional takeoff (i.e. the base thrust) is close to the 100% of the rated thrust; which practically restricts further increasing takeoff thrust for obtaining steeper climb angles, γ. Thus, to enable a wider range of possible takeoff angles in this case study and to incorporate the acoustic effects of increasing engine power, the base thrust is assumed to be 90% of the rated thrust.

Table 8.7 lists the initial climb segment details of the various takeoff profiles resulting from different thrust – flaps combinations for the Airbus A320-232. Profile ID 4 represents the default takeoff configuration for that aircraft. The initial climb airspeed, V_0, which remains fixed throughout the segment, is calculated with Equation 2.45, where flaps -dependant takeoff coefficient C is obtained through extrapolation, as described in Section 8.1.1 for the approach coefficient D. It is seen that steeper takeoff profiles are associated with larger initial climb airspeed, V_0.

Table 8.7: Variation of takeoff angle and initial climb airspeed due to different Airbus A320-232 configurations at the initial climb segment.

Profile ID	**Flaps ID**	**Thrust Change** ΔF_N (kN)	**Airspeed** V_0 **(kt)**	**Duration (s)**	**Takeoff Angle** γ (°)
1	FULL	- 8.84	152.38	24.07	9.29
2	3_D	-5.89	156.50	19.87	10.98
3	2_D	-2.95	160.05	18.25	11.70
4 (default)	1+F	0.00	163.02	15.34	13.70
5	2_U	2.95	165.41	14.44	14.35
6	1	5.89	167.22	13.79	14.88
7	1_A	8.84	168.45	12.95	15.75
8	ZERO_A	11.79	169.11	12.33	16.51
9	ZERO	14.73	169.18	11.95	17.04

Ground roll

Assuming zero runway slope, the SAE-AIR procedure [45] determines the ground-roll distance from

$$s_g = \frac{B\,W^2}{N\,F_N}\,, \tag{8.8}$$

where W and F_N are the aircraft gross weight and net thrust at takeoff respectively, and N is the number of engines. B is an aircraft-specific coefficient included in the ANP database [44] that depends on on flap deflection angle. In this study, it is convenient to assume that W is the aircraft MTOW, whereas F_N is obtained from Table 8.7.

However, the following consideration is vital for correctly estimating the ground roll distance. Table 8.7 suggests that thrust increases with takeoff angle, whereas Equation 8.8 shows that rolling distance decreases with thrust. This could lead to the odd conclusion that rolling distance decreases with takeoff angle. The origin of this confusion is that Equation 8.8 derives empirically based on conventional operations and hence calculates the distance required for the aircraft to reach the default takeoff airspeed, V_0, and perform the conventional takeoff. Clearly, an aircraft operating at higher engine power would reach that airspeed quicker, i.e. at a shorter distance. However, Table 8.7 implies that steep operations involve altered takeoff airspeeds. To account for that, distances s_g are multiplied by a correction factor $V_0/V_{0,d}$, where $V_{0,d}$ is the default takeoff airspeed.

Table 8.8 outlines the rolling distance, average rolling speed and rolling duration for the takeoff profiles examined. The rolling duration is calculated based on the average rolling speed, i.e. from rest to the initial climb speed, which is listed in Table 8.7.

Table 8.8: Variation of ground rolling parameters with takeoff profile.

Profile ID	**Rolling distance (m)**	**Av. rolling speed (kt)**	**Rolling duration (s)**
1	1261	76.18	32.17
2	1277	78.25	31.72
3	1289	80.03	31.31
4 (default)	1296	81.51	30.91
5	1299	82.71	30.53
6	1297	83.61	30.17
7	1292	84.23	29.83
8	1299	84.55	29.87
9	1302	84.59	29.91

Continuing climb

In the continuing climb phase the aircraft accelerates while performing a milder climb with retracted flaps, until reaching the cruise altitude. As already mentioned, the examined profiles start and end at fixed points S (break-release point) and E (at an arbitrary altitude $h = 5000$ ft) to ensure objective comparison mainly on fuel consumption.

The airspeed at the end of the initial climb determines the maximum engine power at the cutback point, termed the maximum climb thrust[2]. Maximum climb thrust for each takeoff profile is calculated through the SAE-AIR procedure [45] and more specifically, by entering the airspeed and altitude along with the ‘maximum climb’ coefficients of ANP database [44], into Equation 2.44. To determine the end point of the continuing climb segment for each profile requires calculating the respective horizontal distances from the airport. Since the altitude is known (5000 ft), it suffices to calculate the continuing climb angle through Equation 8.7. For simplicity, it is assumed that flaps are retracted after

---

[2] It must be noted that additional thrust reduction is possible at cutback, down to a safe minimum level. This means that climb thrust could have been further varied manually. Nevertheless, this would generate a new set of trajectories per initial takeoff angle and the case study would go beyond its scope, which essentially is to demonstrate capabilities of the proposed framework. Hence, aircraft is assumed to climb at the maximum climb thrust corresponding to each takeoff profile.

cutback to the default 'Zero' flap setting [104], independently of takeoff angle. Thus, the climb angle will only be a function of the maximum climb thrust. Moreover, for the sake of consistency (ignoring this step would induce negligible effect due to the small fuel consumption differences at the first segment), aircraft weight, W in Equation 8.7 is adjusted according to the fuel burned at the first segment. Table 8.9 outlines the aircraft configurations and flight details at the climb segment, for each takeoff profile.

Table 8.9: Airbus A320-232 configurations and flight details for each steep takeoff profile at the continuing climb segment.

Profile ID	**Flaps ID**	**Thrust Change** ΔF_N (kN)	**Av. Airspeed** V_0 **(kt)**	**Duration (s)**	**Climb Angle** (°)
1	ZERO	0.097	176.78	51.14	7.53
2	ZERO	0.059	179.88	50.30	7.52
3	ZERO	0.027	182.54	49.60	7.52
4 (default)	ZERO	0.000	184.77	49.03	7.51
5	ZERO	-0.022	186.56	48.58	7.51
6	ZERO	-0.038	187.92	48.24	7.51
7	ZERO	-0.049	188.84	48.02	7.51
8	ZERO	-0.055	189.33	47.90	7.50
9	ZERO	-0.056	189.38	47.89	7.50

8.2.1.1 A320 steep takeoff noise and emissions impact

The noise and emissions impact of each segment is combined to yield the overall impact of the various takeoff angles. $L_{A,max}$ is the maximum noise level experienced at the CP among all segments. In contrast, noise exposure levels are added logarithmically to yield the overall takeoff SEL. Figure 8.10 depicts the noise at source variation with takeoff angle and the noise influence from varying the distance, R, between aircraft and CP, for the two climb segments. Noise at source varies in accordance with the flap settings and thrust requirements listed in Tables 8.7, 8.9.

The total fuel consumption difference is the sum of fuel burn difference during each segment, whereas the same procedure gives the difference on CO_2 and NO_x emissions. The variation of NO_x EI with thrust is calculated through the interpolation procedure implemented in the steep approach case in Section 8.1.1.2 and listed in Table 8.10. The noise and emissions impact of various steep takeoff profiles for the Airbus A320-232 are plotted on Figures 8.12 and 8.13 respectively.

Table 8.10: Estimated NO_x EIs per takeoff profile for the A320-232 engine at the takeoff climb segments.

Profile ID		1	2	3	4	5	6	7	8	9
EI$_{NOx}$	**In. climb**	23.82	24.48	25.15	25.81	26.47	27.13	27.79	28.46	29.12
(g/kg)	**C. climb**	15.34	15.33	15.32	15.32	15.31	15.31	15.30	15.30	15.30

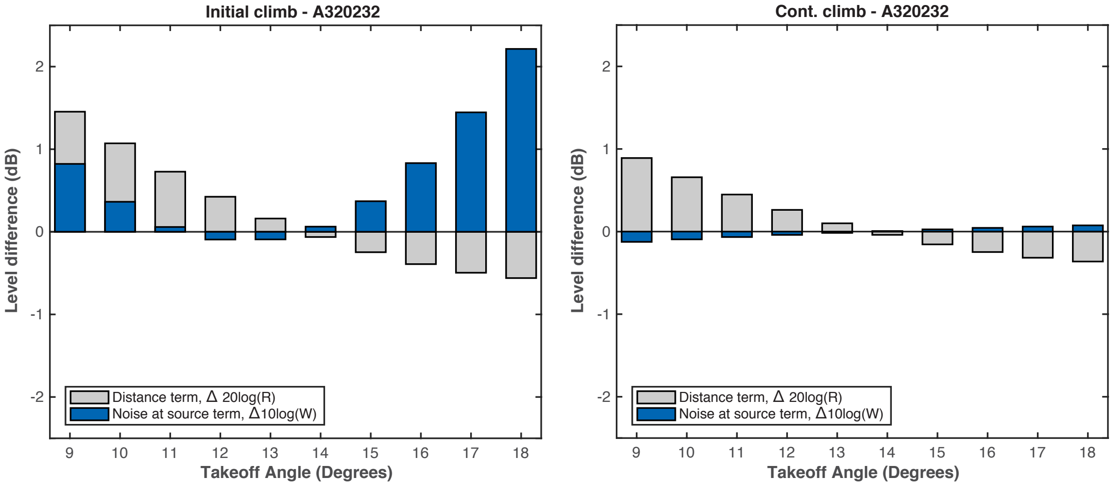

Figure 8.10: Level difference due to variation of noise at source and of the distance between aircraft and CP with takeoff angle, for the initial and continuous climb takeoff segments.

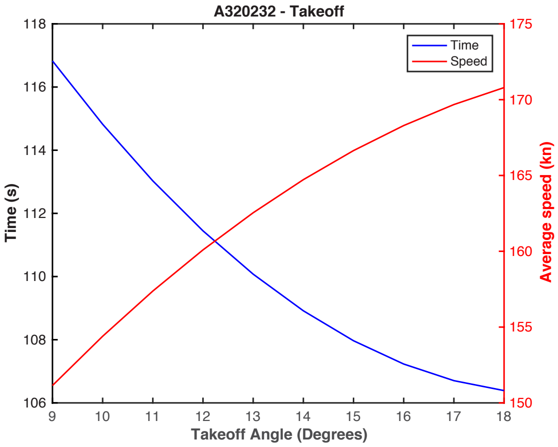

Figure 8.11: Duration and average airspeed for different steep departure profiles, for the A320-232.

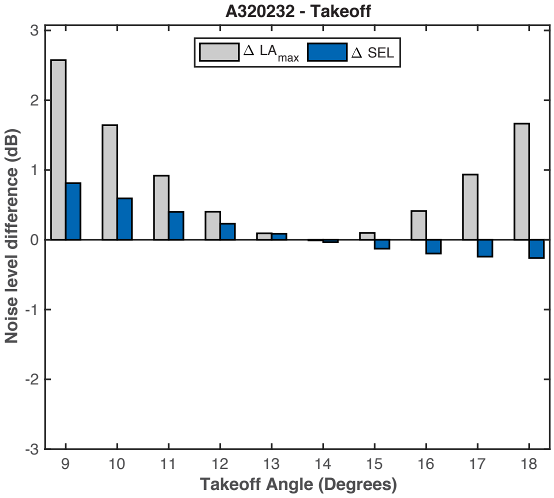

Figure 8.12: Variation of noise level at the takeoff certification point for different steep takeoff profiles for the A320-232.

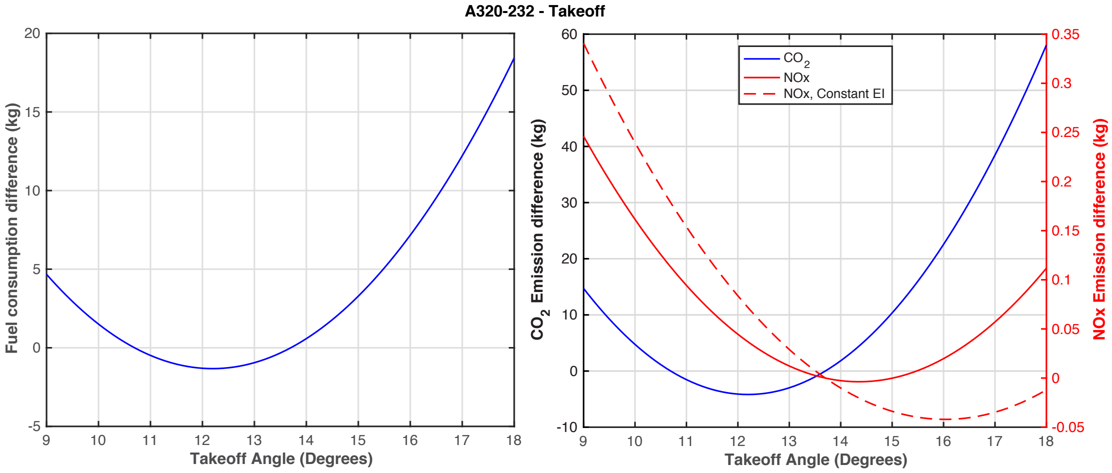

Figure 8.13: Variation of fuel consumption (left) and of emitted amount of CO_2 and NO_x among different steep takeoff profiles for the A320-232.

8.2.2 Steep takeoff with a Boeing 777-300

As in the steep approach case, the environmental impact of steep takeoff is also investigated for a larger aircraft, the Boeing 777-300. Figure 8.14 gives a visual representation of the examined takeoff profiles, from the break-release point, S, up to the common mission point, E. The ground roll differences among profiles are more visible than in the A320-232 case. Aircraft configurations and performance parameters for the three takeoff segments are evaluated through the same procedures as for the A320-232 case and are summarised in Tables 8.11 – 8.14. Figures 8.15, 8.17 and 8.18 illustrate the corresponding noise and emissions plots. Figure 8.17 implies that steeper takeoff slopes (at around 9° – 10°) than the default offer small noise benefits, whereas Figure 8.18 shows that the default takeoff profile is optimised in terms of fuel consumption. It is reminded that the concurrent effect of noise and emissions is discussed in Section 8.3.

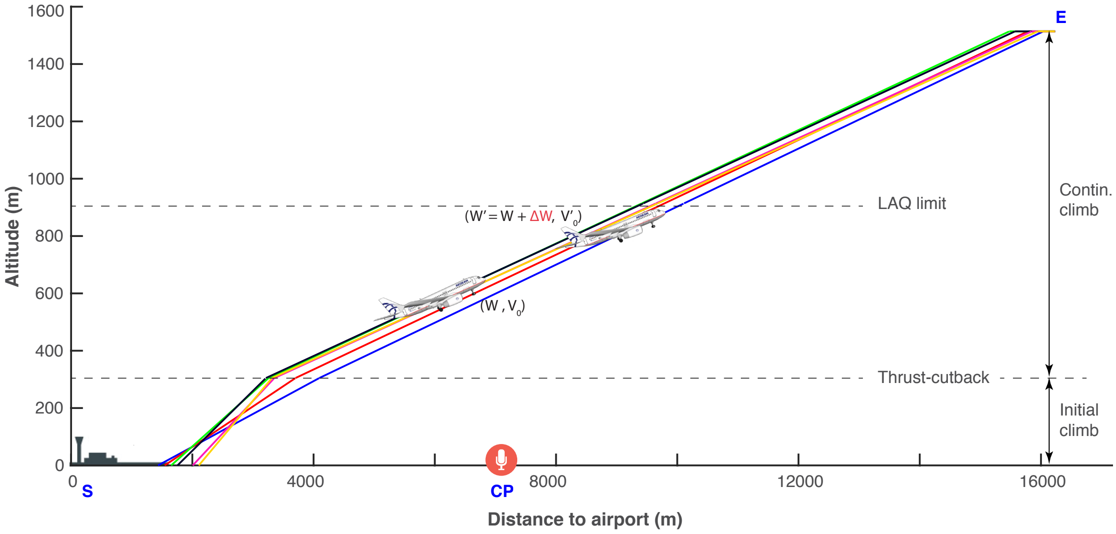

Figure 8.14: Vertical takeoff profiles at different slopes for the 777-300.

Table 8.11: Variation of ground rolling parameters with takeoff profile for the Boeing 777-300.

Profile ID	**Rolling distance (m)**	**Av. rolling speed (kt)**	**Rolling duration (s)**
1	2115	83.56	49.20
2	2247	89.15	48.99
3 (default)	2375	94.61	48.80
4	2500	99.94	48.62
5	2802	105.14	51.80
6	2922	110.22	51.53

Table 8.12: Variation of takeoff slope and initial climb airspeed due to different Boeing 777-300 configurations at the initial climb segment.

Profile ID	**Flaps ID**	**Thrust Change** ΔF_N (kN)	**Airspeed** V_0 **(kt)**	**Duration (s)**	**Takeoff Angle** γ (°)
1	L_30_D	-27.40	167.13	47.94	4.24
2	L_25_D	-13.70	178.30	33.83	5.63
3 (default)	T_20_U	0.00	189.22	21.91	8.21
4	T_15_U	13.70	199.88	18.61	9.16
5	T_05_U	27.40	210.29	16.21	10.00
6	T_00_U	41.10	220.44	13.71	11.30

Table 8.13: Boeing 777-300 configurations and flight details for each steep takeoff profile at the climb segment.

Profile ID	**Flaps ID**	**Thrust Change** ΔF_N (kN)	**Av. Airspeed** V_0 **(kt)**	**Duration (s)**	**Climb Angle** (°)
1	ZERO	3.48	187.85	62.60	5.78
2	ZERO	1.72	196.23	60.61	5.72
3 (default)	ZERO	0.00	204.41	58.84	5.65
4	ZERO	-1.68	212.41	57.26	5.59
5	ZERO	-3.32	220.21	55.83	5.53
6	ZERO	-4.92	227.83	54.56	5.47

Table 8.14: Estimated $\mathrm{NO_x}$ EIs per takeoff profile for the Boeing 777-300 engine at the takeoff climb segments.

Profile ID		1	2	3	4	5	6
EI$_{NOx}$	**In. climb**	39.77	41.53	43.31	45.07	46.84	48.61
(g/kg)	**C. climb**	24.66	24.47	24.28	24.10	23.93	23.76

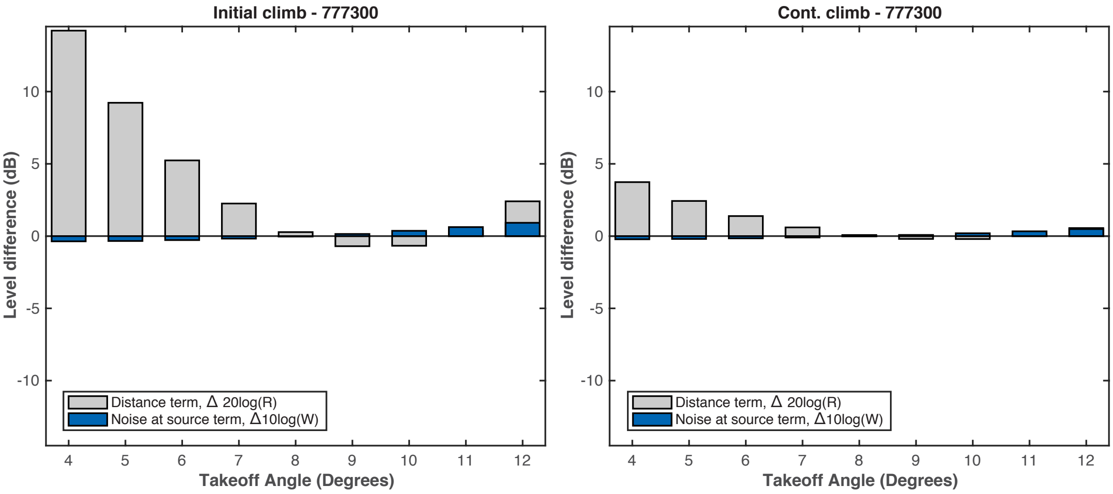

Figure 8.15: Visual representation of level difference due to variation of noise at source and of aircraft to CP distance for the 777-300 at takeoff.

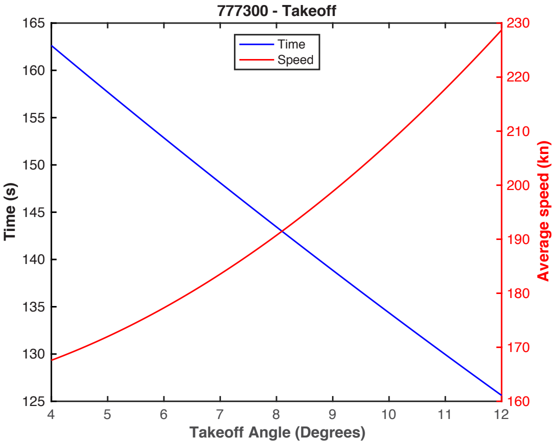

Figure 8.16: Duration and average airspeed for different steep descent profiles, for the Boeing 777-300.

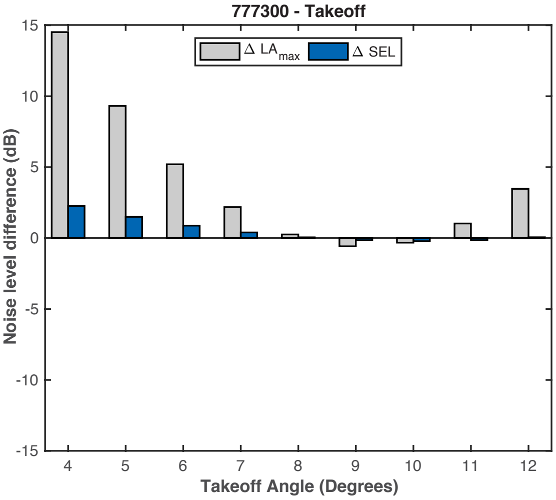

Figure 8.17: Variation of noise level at the takeoff certification point for different steep takeoff profiles for the Boeing 777-300.

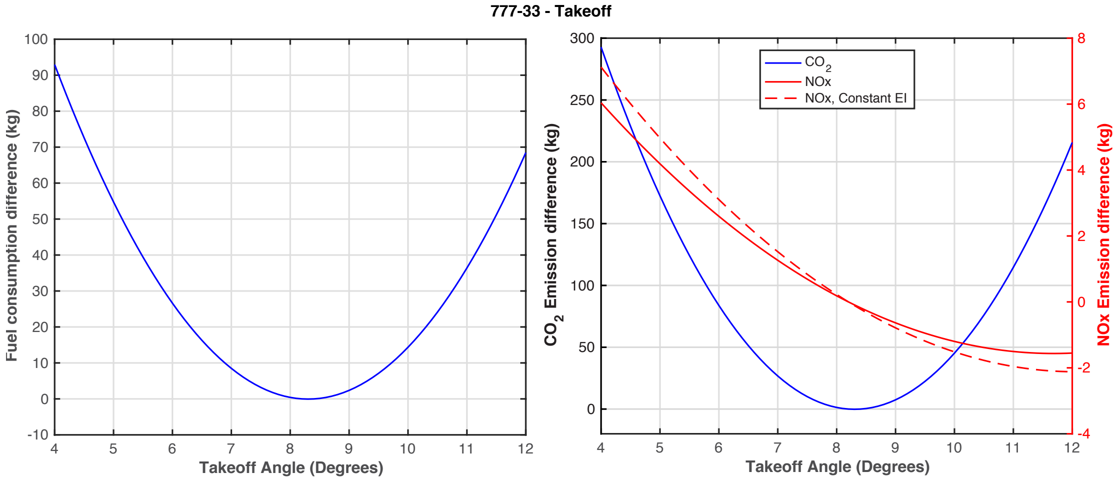

Figure 8.18: Variation of fuel consumption (left) and of emitted amount of CO_2 and NO_x among different steep takeoff profiles for the Boeing 777-300.

8.3 Steep operations noise and emissions interdependencies

This Section summarises the steep operations estimations through the proposed framework. Moreover, it reveals the effect of the interdependencies between noise and emissions by plotting concurrently the variation of their impact with steep operation angle in Figure 8.19. To implement the concurrent plots, noise and emissions changes are normalised to unity. It must be noted that normalisation may not be the optimum way of comparing the effect of noise and emissions; other existing (e.g. units related to cost or annoyance) and/or new units may express more realistically trade-off effects. Also, it should be considered that the environmental impact of mitigation strategies is to some extend airport-specific; for example, their effectiveness depends on factors related to the population around an airport, e. g. the number of residents and the location of residential areas with respect to the airport. Hence, weightings expressing the effect of such factors could also facilitate a more objective comparison between the impact of noise and emissions. The subject of objectively assessing these interdependencies is a recommended future expansion of this work (see Chapter 10).

In Figure 8.19, blue and red curves respectively represent the CO_2 and NO_x variation with operation slope, whereas the green curve depicts the noise exposure impact. Generally, it is seen that for all operations, noise benefits are 'paid' with increased fuel consumption. The default takeoff configurations can be roughly characterised as the environmentally-optimum ones, since they offer a balanced trade-off between noise and emissions impact. More specifically, in the A320-232 takeoff case, increasing the takeoff angle by 3-4°, i.e. at around 17° induces a SEL reduction of around 30% but increases fuel consumption and CO_2 emission by around 60% and NO_x emission by more than 35%. Likewise, the takeoff SEL impact for the 777-300 can be improved by 10% at a

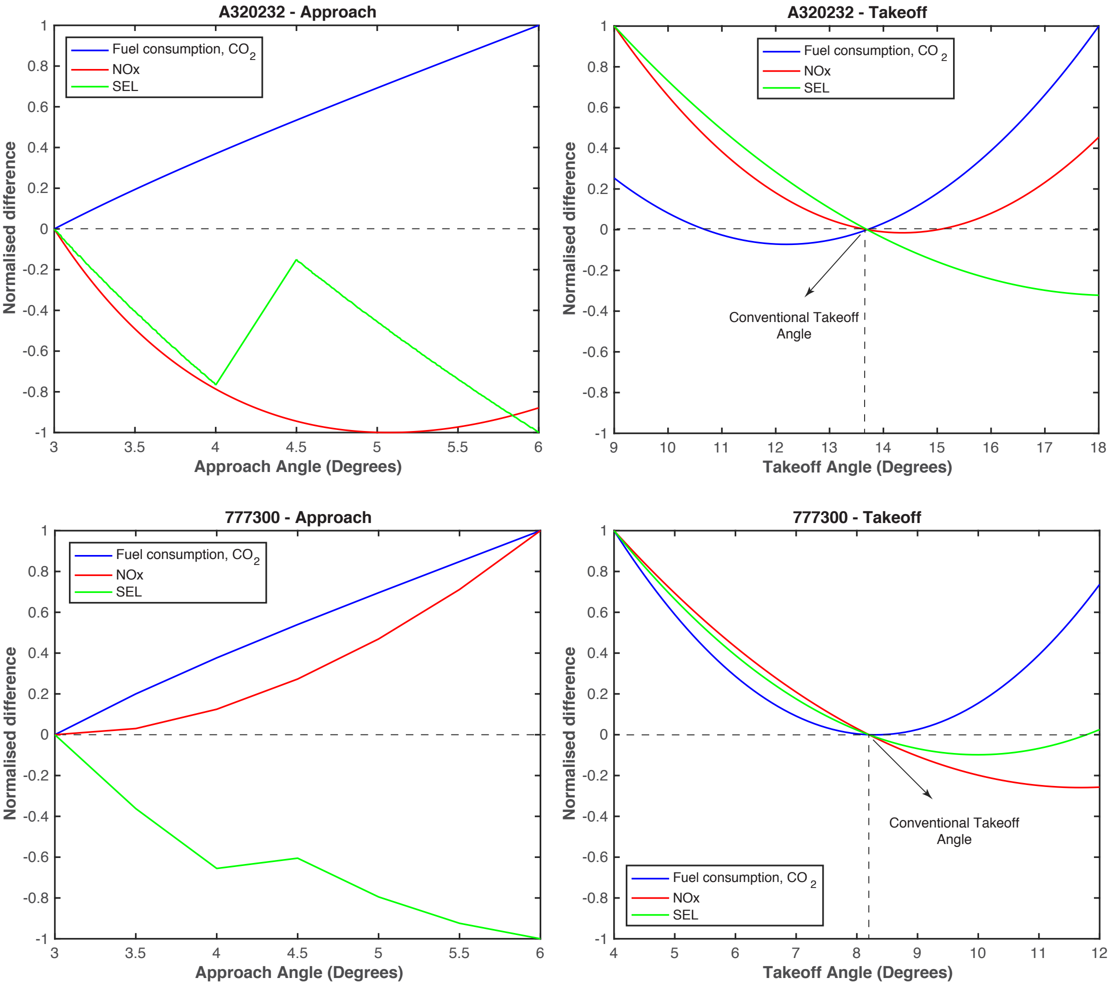

Figure 8.19: Estimated normalised noise exposure and emissions at different descent and takeoff angles, for the Airbus A320-232 and the Boeing 777-300.

takeoff angle of around 10°. Although this also results into a 20% NO_x emissions reduction, it comes at the expense of a 20% increase of fuel consumption. Similarly, SEL at approach decreases with approach angle at the expense of increased emissions of CO_2 and NO_x. The abrupt SEL increase occurring at 4.5° results from the increased flap deflection angles required for fulfilling the approach at slopes steeper than 4°.

8.4 Computed NPD curves for the steep operations.

NPD curves are computed for the above-defined steep operations performed by the Airbus 320-232 and the Boeing 777-300. NPD curves can be produced for each individual steep approach or takeoff angle, but here, only one representative case is shown for each operation. These are: a) approach at 5.5°, and b) takeoff at 15° for the Airbus 320-232 and 11° for the Boeing 777-300.

According to the NPD computation methodology presented in Section 5.7, inputs required to generate NPD curves for the steep operations are the corresponding acoustic power changes for each aircraft, along with the corresponding directivity and spectra data at the time of $L_{A,max}$. The acoustic power changes were previously estimated. Whereas the proposed framework uses by default the spectra data available in the ANP database [44] along with the ANOPP [16] directivity data. Using the default directivity and spectral data should not produce significant error in capturing trends, due to the relatively small thrust changes associated with the steep operations. However, it is reminded that the framework supports importing any existing/new spectra or directivity database. The polar angle between aircraft and CP at the time of $L_{A,max}$ occurrence is calculated for each operational profile with FANjET.

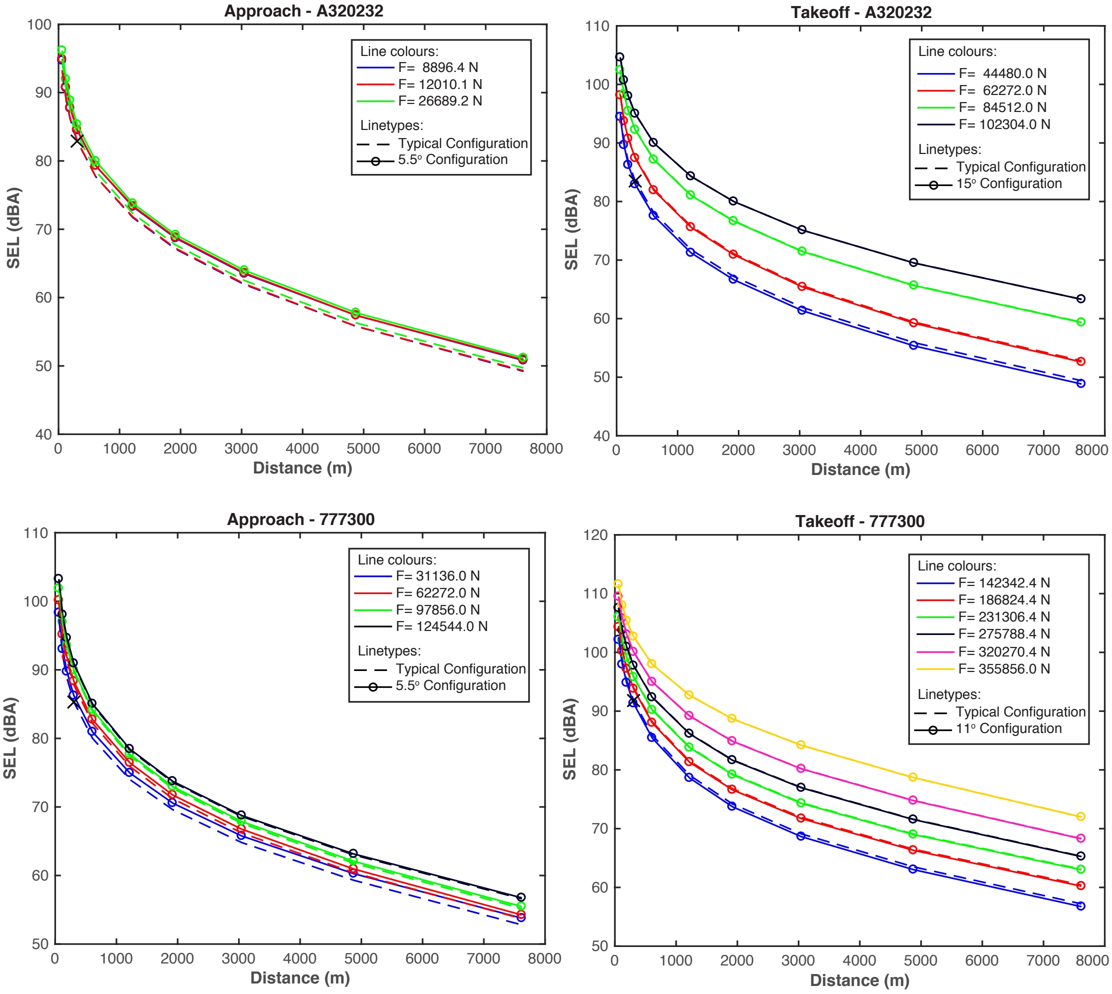

Figure 8.20: Estimated NPD curves for the A320-232 and the 777-300 at steep descent (left) and steep takeoff configuration. Dashed lines represent published NPDs for the conventional operations.

Figure 8.20 shows the generated NPD curves for both aircraft at steep approach and takeoff. For comparison, also plotted (with dashed lines) are the NPD curves for the respective conventional operations. At takeoff, where engine noise dominates, unconventional configurations (i.e. different flap deflection angles) generate small noise difference for the whole aircraft. This difference practically vanishes at higher engine power settings, where engine dominance is more definite. A clearer noise increase at source of about 1-2 dB is observed in the approach cases. This is because airframe noise is more important at approach.

8.5 Final remark

Before moving on to the next Chapter, is it important to remind the reader that the purpose of the case study presented in this (and the next) Chapter is not to accurately predict the absolute values of the optimum approach and takeoff angles. Rather it aims at demonstrating the capability of the proposed framework on estimating the impact of operational mitigation strategies and capturing the correct trends in parametric studies. While the case study involved a number of assumptions and simplifications, comparison with predictions for steep approaches (that also contain uncertainty) by authors like Toebben [182] and Filippone [181], summarised in Figure 8.21, provides sufficient evidence to validate the captured noise trends. Similar trends were found by Mollwitz [186] and Koenig [187], but these are not directly comparable to the ones found in this study, since Mollwitz uses different flight profiles (descent is steep from 8000 ft to 1500 ft but final approach is performed at 3°), whereas Koenig measures noise at a distance of 8 nm to the runway threshold, which is much further than the approach CP. Likewise, noise benefits from steep takeoff profiles, as well as the general tradeoffs between fuel consumption and noise benefits found in this case study are also affirmed by Koenig [187] and Torres [75]. Most importantly, this case study highlighted the potential of the proposed framework on providing NPDs for unconventional operations and configurations. As already mentioned, this is one of the novelties presented in this thesis.

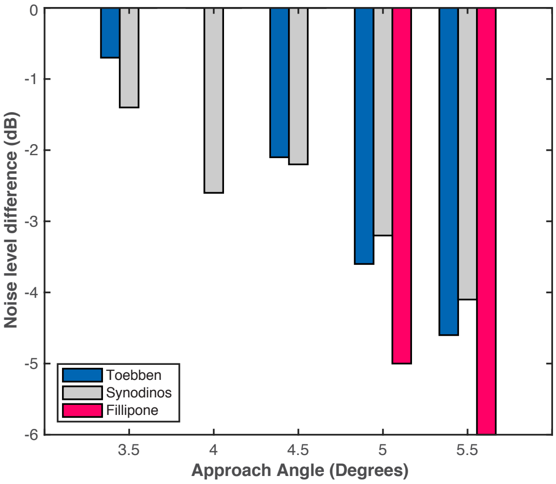

Figure 8.21: Comparison between steep descent noise predictions.

Chapter 9

Applications II: Predictions for novel aircraft

As already discussed, revolutionary aircraft concepts and propulsion systems, as well as drastic technology improvements are indispensable for meeting the longer term environmental goals (e.g. NASA N+3) presented in Chapter 1. Figure 9.1 shows the numerous aircraft layouts and configurations that have been studied for meeting these goals [188]; comprehensive overviews of these aircraft concepts can be found in references [14, 98, 189, 153]. This chapter presents impact estimations for novel aircraft concepts, performed with the proposed noise estimation framework. The largest part of the chapter investigates the environmental impact of Distributed Electric Propulsion (DEP) aircraft using different propulsion systems of varying number of electric propulsors. DEP definitions are initially given before identifying the noise sources on DEP aircraft and deriving the associated relationships for estimating their noise level variation with thrust (as performed in Section 5.5 for conventional aircraft). The DEP aircraft case study concludes by presenting the procedure for estimating their aerodynamic performance, and ultimately, their environmental impact. The last few paragraphs of this chapter include a simplified noise impact study of Blended Wing Body (BWB) designs.

9.1 Impact of Distributed Electric Propulsion aircraft

9.1.1 Overview

The concept DEP aircraft used in this case study is named e-A320. It uses the fuselage of the A320-232, which is the baseline aircraft, and a DEP system; so essentially, the conventional propulsion system (i.e. turbofans) on a A320-232 is replaced by a DEP system. Different e-A320 variants are examined, featuring DEP system with different

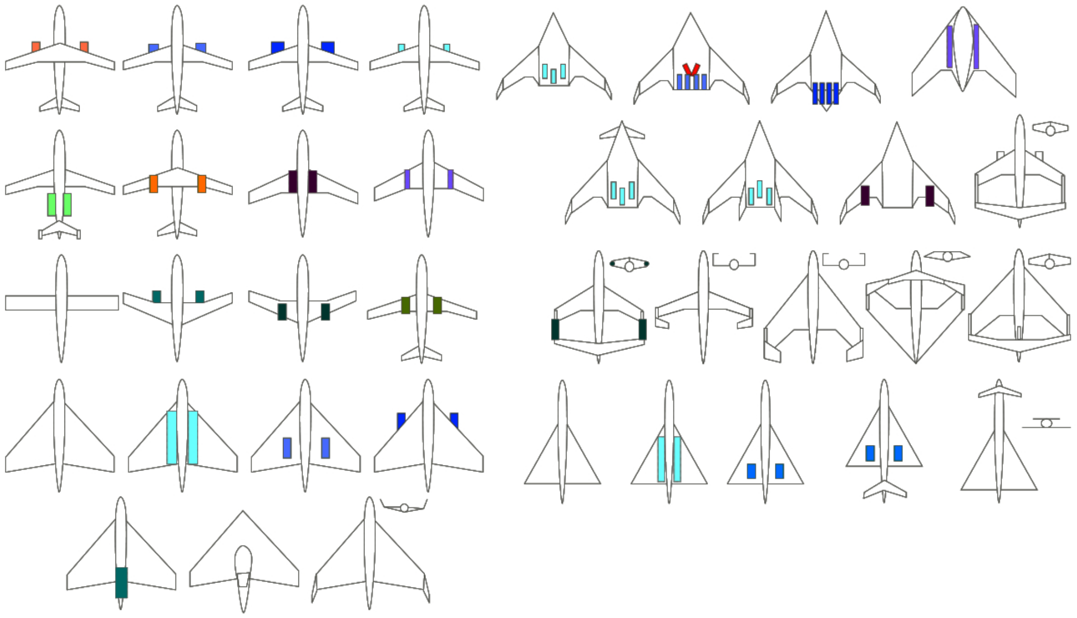

Figure 9.1: Configurations and designs studied for quieter aircraft [188].

power supply units (turboshaft engine(s) or batteries) and number of electric propulsors. The basic characteristics of the e-A320 are:

- Entry into service (EIS) planned for the year 2035,
- range capacity of 900 nm, complying with the results of market demand analysis performed by Bauhaus Luftfahrt [190], and
- identical passenger capacity to the conventional A320, i.e. 150 passengers.

Before presenting the DEP aircraft case study, it is worth discussing briefly the motivation behind replacing conventional turbofans with electric propulsors. Turbofans have been evolving towards high and ultrahigh BPRs achieving notable fuel consumption and noise benefits. As mentioned in Section 2.6.4, propulsive efficiency increases by lowering FPR, which however reduces the fan shaft speed. Felder [101] mentions that below a lower FPR limit of around 1.5, issues arise in matching the fan and turbine shaft speeds, in systems where the turbine drives the fan directly. This power transmission problem can be solved by decoupling the propulsive device (e.g. fan) from the power generator (e.g. turbine), either by introducing a gearbox or by transmitting the power electrically, using power inverters. The former is associated with design difficulties (e.g. due to the weight and dimensions of the gearbox). The second solution provides total independence between generator and fan shaft speeds, offering not only efficiency benefits since both operate at its optimum speed at each flight phase, but also enabling abundant design possibilities and propulsion configurations.

9.1.2 Distributed Electric Propulsion (DEP)

Distributed propulsion (DP) is the spanwise dispersion of propulsive thrust among multiple propulsors (e.g. small turbofans, hybrid fuel cell-gas turbine engine [154], electric propulsors) [191], aiming at improving performance in terms of aerodynamics, noise and emissions [189]. DP concepts have been proposed by NASA from as early as the 1970s [192]. Since then, several DP architectures have been proposed [189] that can be basically distinguished in those adopting the BWB designs (see Figure 9.2 (a) and (b)) and those mounted on advanced tube-and-wing morphologies (see Figure 9.2 (c) and (d)). Nowadays, DP systems are anticipated as one of the best options for powering future aircraft [189] that are envisioned to have significantly smaller noise footprint during takeoff and landing as well as reduced energy consumption and emissions impact. The benefits of DP are discussed in more detail in references, such as [11, 91, 101, 193].

Propulsors within a DP system can either be self-powered (e.g gas turbine engines) or powered by a common power producing unit (e.g. a turboshaft engine or a set of batteries). The former case may result in low efficiencies and increased fuel consumption [194]. In the more efficient latter case, performance is further improved by transmitting the power to the propulsors electrically (e.g. by electric motors) rather than mechanically, i.e. forming a Distributed Electric Propulsion (DEP) system [195]; DEP is adopted by numerous future DP aircraft designs and is therefore the DP arrangement examined in this case study.

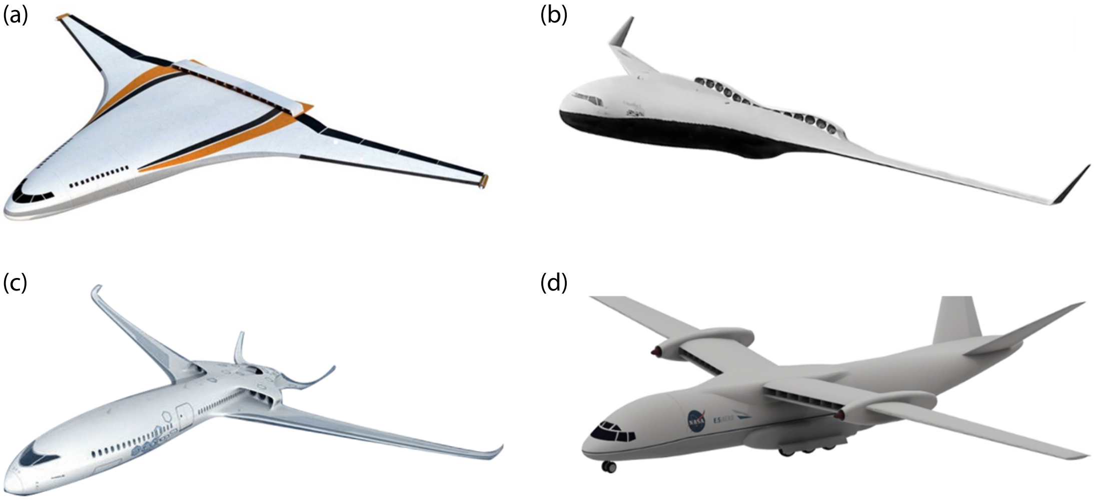

Figure 9.2: Aircraft concepts using DEP systems. (a) NASA N3-X, (b) Cranfield BW-11, (c) Airbus, Rolls-Royce and Cranfield DEAP, also known as e-Thrust, and (d) ESAero TeDP.

Figure 9.2 presents some prevailing aircraft concepts featuring DEP. Sorted according to size, these are the Airbus E-Thrust [196, 197] (100 passengers, according to [198]), the ESAero TeDP [199] (150 passengers, mission similar to the current Boeing 737-800 or Airbus A320), the NASA N3-X (300 passengers, mission similar to the current Boeing

777-200) [11] and the Cranfield BW-11 [194] (555 passengers or more, mission characteristics similar to the Airbus A380). The E-Thrust is one aspect of the Airbus, Rolls-Royce and Cranfield University Distributed Electrical Aerospace Propulsion (DEAP) project [198, 200], that also features the E-Fan prototype, illustrated in Figure 9.4 [201]. Also, it is worth mentioning the NASA STARC-ABL concept that has a mission similar to the ESAero TeDP [202]. Targeting years later than 2035, all these aircraft are not only envisioned to reduce noise and emissions, but also to offer Short Takeoff and landing (STOL) capabilities, as mentioned in Section 2.4.1. Moreover, it can be seen in Figure 9.2 that these aircraft feature motor driven fans in a continuous nacelle, which increases boundary layer ingestion (BLI) benefits (presented in Section 9.6.1) and reduces overall engine drag (in comparison to a turbofan engine nacelle) [203, 204].

9.1.3 Advantages of DEP

The numerous advantages of distributed electric propulsion are extensively presented by Felder [101]. The most prominent advantages, independently of the vehicle design (i.e. tube-and-wing or BWB) and DEP architecture (i.e. TeDP or other) are:

- Decoupling of propulsive device (i.e. fans) from the power generator (as explained earlier) and hence overall efficiency improvement. Also, power inverters can be seen as a flexible gearbox, able to adapt to the optimum ratio for specific operations or particular flight circumstances. For example, in the event of a fan failure, other fans operation can be easily modified to continue producing symmetric thrust.
- Electric fans can be scaled down, in contrast to gas turbine engines that contain non-scalable parts. Hence, the overall propulsion system weight decreases with number of propulsors (this is showed later in Figure 9.11).
- Multiple smaller fans are easier to integrate into an aircraft.
- Electric fans can be powered directly by batteries, facilitating the path towards producing totally electrical aircraft.
- Very high BPR[1] can be reached that cannot be attained with conventional turbofans (e.g. due to fan dimension constrains), at no nacelle drag cost [153].
- Boundary layer ingestion (BLI) benefits that are more relevant to BWB configurations, as discussed in Section 9.6.1.

---

[1] BPR in DP systems is often described [203, 191] in terms of an effective BPR (eBPR). In TeDP systems, eBPR is defined as the ratio of mass flow rate through all fans to rate through the engine core [101]. However, as discussed in the concluding Chapter of this thesis, BPR could be redefined in the future to reflect properties of electric aircraft and/or other novel DP aircraft concepts.

9.1.4 DEP architectures

Among several DEP architectures, such as a number of hybrid solutions described by Isikveren in [198] and [189], as well as various power transmission system options summarised in [205], this case study focuses on aircraft featuring: a) Turbo-Electric (TeDP), and b) All-Electric propulsion systems. This is because these architectures are the ones adopted by most novel aircraft concepts found in literature. This Section is devoted in briefly describing these architectures and outlining prominent aircraft using them.

9.1.4.1 Turboelectric Distributed Propulsion (TeDP)

Figure 9.3 (B) shows the component chain of a TeDP system. This DEP system is powered by one (or more) traditional gas turbine engine (e.g. turboshaft). A generator converts the mechanical power to electrical, which is then supplied to the electric motors that drive the fans. The TeDP system can use either conventional (i.e. kerosene) or advanced (e.g. hydrogen) fuel. Overall, although this propulsion arrangement exploits benefits of DP, such as the decoupling of the fan and turbine, it does not avoid the production of combustion emissions. Aircraft concepts designed to use the TeDP architecture are the NASA N3-X, the STARC-ABL, the BW-11 and the ESAero TeDP.

9.1.4.2 Hybrid-Electric and All-Electric Propulsion

One way of reducing the emissions impact of a TeDP system, is replacing the gas turbines by alternate, typically electric power sources, such as batteries, resulting in an hybrid-electric or a totally electric aircraft. The difference between a totally electric (often termed All Electric [206, 48] or Universally Electric [207, 190]) and an Hybrid-Electric aircraft is that the former features exclusively electric propulsion and power systems (e.g. batteries) and hence are envisaged to provide capability for zero in-flight emissions. Whereas an Hybrid-Electric aircraft uses electric power but incorporates at least one additional power source using standard kerosene or other advanced fuels like LH2 [194]. Hybrid-Electric propulsion is one among several solutions belonging to the so-called dual-energy propulsion and power systems (DESPPS) [207].

The interest in electric aircraft is not new. Since 1973, when the MB-E1 electric aircraft completed a 9 minutes flight, various small experimental electric aircraft have been produced, such as the Cessna 172(e) and the Electrolight 2 [198]. Future electric aircraft are conceived to have mission characteristics similar to current short/medium-haul aircraft. Representative All-Electric aircraft prototypes (not featuring the DP technology) are the E-Fan (see Figure 9.4) [201] and the Bauhaus Luftfahrt Ce-Liner [190], whereas the Airbus E-Thrust in Figure 9.2 is a Hybrid-Electric aircraft that uses DP. The component chain of DEP All-Electric (or Hybrid-Electric) system is illustrated in Figure 9.3 (C).

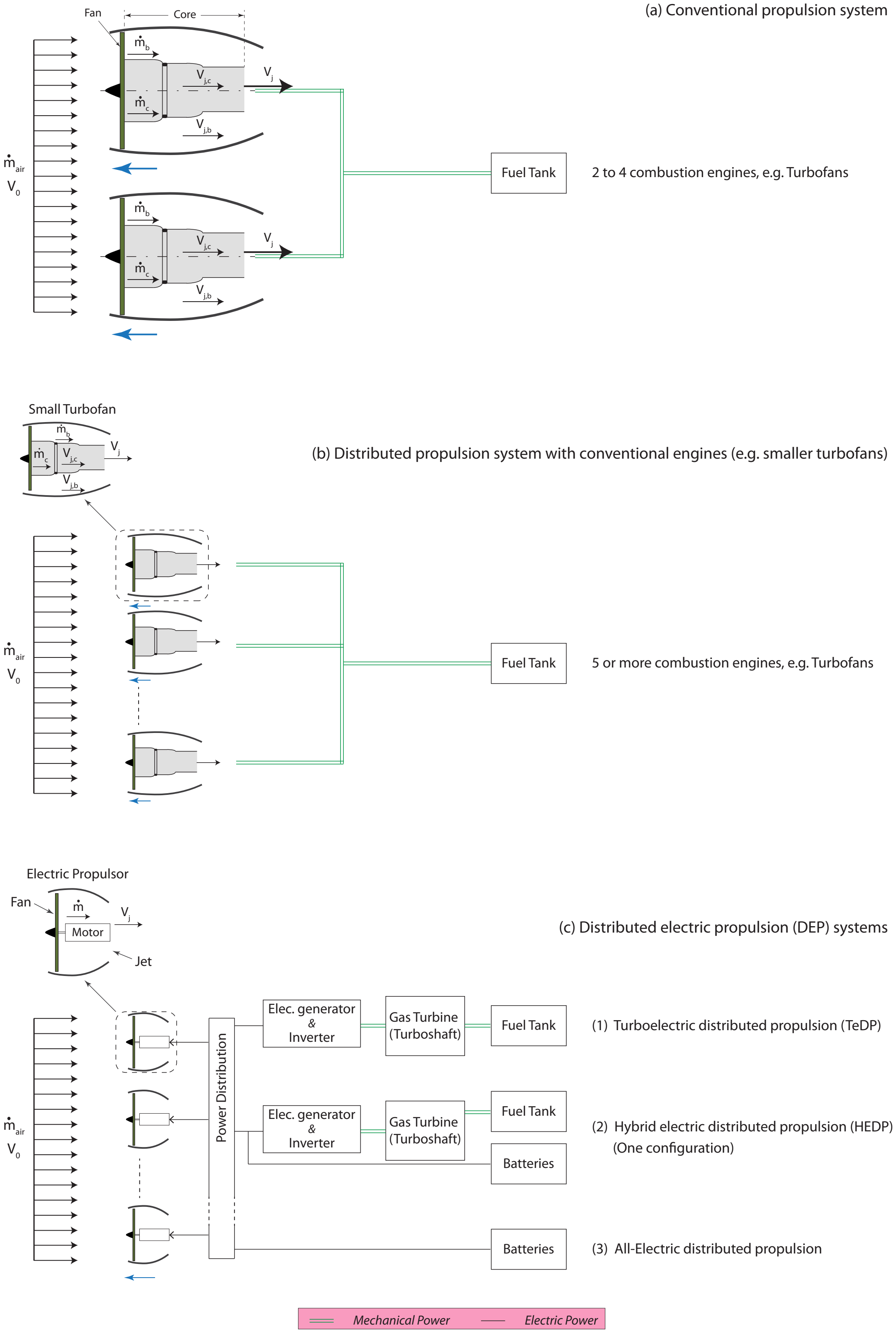

Figure 9.3: Components chain schematic of (a): Conventional propulsion system, (b) DP with conventional engines, (c) DEP systems: (1)Turboelectric (TeDP), (2) Hybrid-Electric and (3) All-Electric. Also shown are cross-sections of typical turbofan engines and electric propulsors, indicating their main components. The set of black arrows represents the airflow and the blue arrows the thrust generated by each engine/propulsor.

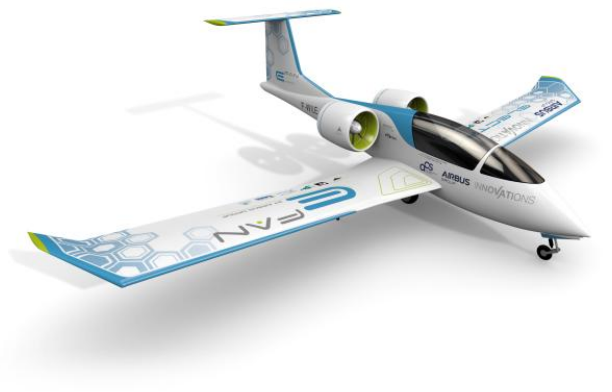

Figure 9.4: Airbus E-Fan prototype All-Electric aircraft [201].

9.2 Noise sources on a DEP aircraft

9.2.1 Power generator noise

The noise contribution of the power generator of DEP aircraft is negligible, independently of power unit type (i.e. batteries or turboshaft engine). In a totally electric aircraft, this is due to the low noise features of battery systems. Whereas turboshaft engines in TeDP systems are designed to produce minimum thrust and therefore have small exhaust velocity and reduced noise impact. Moreover, numerous TeDP aircraft are conceived to have their power generator buried within the aircraft (e.g. in the wing), minimising community noise impact, but possibly resulting in cabin noise issues. However, cabin noise is irrelevant to this thesis.

9.2.2 Propulsor noise

Electric propulsors in a DEP system consist of a fan, a jet (nozzle) and a motor, as illustrated in Figure 9.3. These components are the potential noise sources of the system. Noise associated with BLI effects is mostly relevant to BWB configurations and hence is discussed in Section 9.6.1. The noise contribution from the motor is assumed negligible, based on NASA predictions in [208], so that the significant noise sources of each propulsor are the fan and the jet.

Equations 5.18 and 5.23 for the jet and fan PWL variation with thrust were derived in Chapter 5 and used in the applications of Chapters 7 and 8. These need to be adapted to reflect the fan arrays of a DEP design. Assuming that all propulsors in an array are identical and produce the same thrust, then from Equation 5.17, the total acoustic power from N propulsors is

$$W_j \propto N F_G V_e^6 \,. \tag{9.1}$$

Therefore, the array jet PWL change due to gross thrust F_G variation is

$$\Delta Lw_j = 10\log\frac{N'}{N} + 10\log\frac{F'_G}{F_G} + 60\log\frac{V'_e}{V_e}\,, \tag{9.2}$$

where the values corresponding to the condition after the thrust change are denoted with a dash. The array fan PWL variation Equation derives in a similar manner, based on Equation 5.23, giving:

$$\Delta Lw_{f,0} = 10\log\frac{N'}{N} + 20\log\left(\frac{V_j'^2 - V_0'^2}{V_j^2 - V_0^2}\right) + 10\log\frac{F'_G}{F_G} - 10\log\frac{V'_j}{V_j}\,. \tag{9.3}$$

It is reminded that the function f(design) specified by Heidmann [117] must be accounted for, as described in Section 5.5.4.1.

9.3 Establishment of required parameters for estimating the environmental impact of the various e-A320s

This Section defines the required parameters and considerations for estimating the noise and emissions impact of TeDP and All-Electric e-A320s, as well as the effect of varying the number (and hence dimensions) of electric propulsors. The hybrid electric concept is not assessed, since the power generator weight and hence the overall aircraft performance depends on the Degree of Hybridisation (DOH) (i.e. the ratio between electric and conventional delivered power) [207]; optimising the DOH, which is crucial in hybrid electric designs, goes far beyond the interests of the present thesis.

Equations 9.2 and 9.3 imply that parameters required for noise estimations are the jet velocity and gross thrust. In fact, jet velocity can be assessed from Equation 5.46, if the gross thrust is known. It is important to remind that rated thrust (i.e. thrust requirements) is normally a known input to the noise estimation framework developed in this thesis; it is either public (as is for existing civil aircraft) or obtained through aircraft design and/or performance tools. In order to accomplish the distributed propulsion case study, thrust requirements for the e-A320 must be established, based not only on drag and weight considerations but also on safety regulations. Hence, broad drag and weight estimation models are developed in Sections 9.3.5, 9.3.7, whereas safety considerations on deciding thrust requirements are discussed in Section 9.3.4.

Emission characteristics depend on the DEP system type. The amount of pollutants emitted from a TeDP aircraft is a function of the SFC of the turboshaft engine. Whereas the All-Electric variation will have zero in-flight emissions (addressing emissions associated with the batteries production is not an objective of this thesis, but should be included in integrated global environmental impact studies).

9.3.1 Propulsors size and performance

The conventional A320-232, also referred to as the baseline aircraft or baseline A320, has wing span 35.80 m and fuselage width of around 4 m. It is sensible to assume that 60% of the wing length should remain clean for safety or other reasons (this conforms with the ESAero TeDP design in Figure 9.2). Hence the available space for installing propulsion arrays under each wing is set at $L = 6$ m. Propulsors maximum diameter is constrained to 2 m by the baseline A320 height. Moreover, in accordance with TeDP design studies in references [101, 204, 209], the minimum possible propulsors fan diameter, d_f, is set at 0.35 m. In that context, Table 9.1 outlines the geometry and performance data of the electric propulsors forming the various propulsion arrays examined in this study. The performance data in Table 9.1 are based on the efan propulsor [154] and engine performance trends in references [51, 210].

Table 9.1: Estimated geometry and performance data for the electric propulsors constituting the various DEP arrays examined in this study.

Aircraft type	**A320-232**	**e-A320**					
Number of propulsors	2	2	4	6	8	10	12
Fan diameter (m)	1.61	2.0	1.4	1.0	0.73	0.5	0.38
Rated thrust (kN)	117	106	55	37	28	22	18
Airflow (kg/s)	355	458	233	155	118.5	95	76.5
Nozzle area (m^2)	1.4	1.57	0.81	0.54	0.42	0.34	0.27
Fan speed (rpm)	565 0	4386	6142	8602	12047	16872	23630
FPR	1.73	1.65	1.65	1.65	1.65	1.65	1.65

9.3.2 Estimation of nacelle surface area

The nacelle area, S_{ncl}, is required for drag and weight estimations in the following sections. While it increases with fan diameter, its complex shape makes accurate calculations difficult. Although S_{ncl} could be approximated through several semi-analytical methods [25], estimating its relationship with engine dimensions fulfils the scope of the present analysis. This is achieved by considering the nacelle as a body of revolution, most conveniently a cylinder, and subtracting the inlet and outlet areas.

The dimensions of that cylinder are defined through the turbofan engine sketch of Figure 9.5. The minimum and maximum nacelle cross-section areas are denoted d_{min} and d_{max} respectively. It is assumed that the fan diameter equals the inlet diameter, i.e. $d_f = d_{in}$. Kroo [211] suggests that typically, the inlet cross section area, $A_{in} \approx 0.7A_{max}$; hence $d_{max} \approx 1.2\, d_{in}$. Also, it can be assumed that the average diameter of the nacelle is $d_{av} = 1.1d_f$. Finally, looking at the trends in Chapter 4 it can be seen that roughly, the length ℓ of conventional turbofan engines is 1.7 times the fan diameter. A smaller estimate of $\ell \approx 1.5d_f$ is adopted for the electric propulsors to account for the fact that they only consist of a fan and motor.

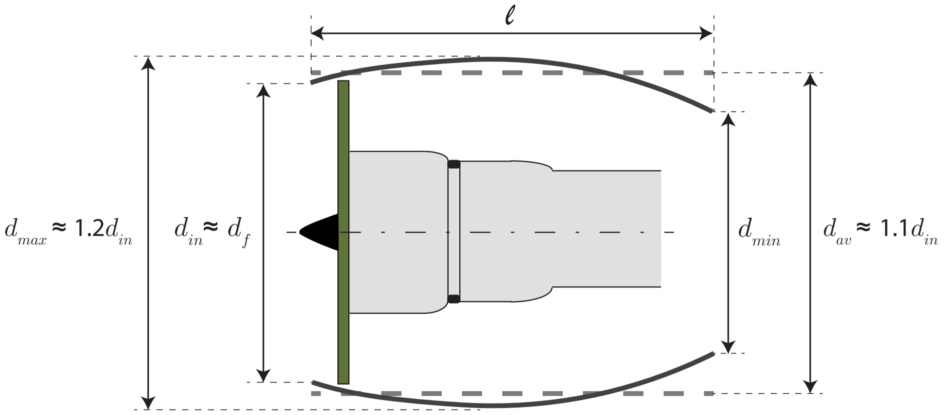

Figure 9.5: Approximation of turbofan nacelle shape as a cylinder of diameter d_{av} and length ℓ.

Based on these approximations, the nacelle can be represented by a cylinder of equivalent area with diameter d_{av} and length ℓ. Thus, the nacelle surface area is the cylinder's area without the inlet and outlet surfaces:

$$S_{ncl} \approx 1.1\,\pi d_f \ell \approx 1.87\,\pi d_f^2 \,. \tag{9.4}$$

9.3.3 Definition of thrust requirements

Referring to the schematic representations of Figure 9.3, this study involves replacing the turbofan engines of a conventional aircraft (i.e. configuration a) by a DEP system consisting of N electrically driven propulsors (i.e. one of the configurations c). Considering that the fuselage geometry is kept unchanged, Figure 9.3 implies that changing the aircraft propulsion system is likely to affect its total weight and drag, and consequently, its thrust requirements. The number of propulsors, N, within the DEP system plays a crucial role, because it determines not only the propulsors size (and hence their weight, drag and hence thrust requirements), but also the engine noise radiation and energy consumption. The number of engines also influences the minimum engine thrust requirements, $F_{min}(N)$, dictated by safety regulations. Under these considerations, if a turbofan engine generating thrust F is replaced by an array of N propulsors, the gross thrust provided by each propulsor should be given by a function

$$F_p = \frac{F + \Delta F_D + \Delta F_W}{N}\,, \tag{9.5}$$

with

$$F_p \geqslant F_{p,min}(N)\,,$$

where ΔF_D, ΔF_W represent the thrust variation due to drag and weight alterations respectively. The next sections describe own-developed methods for determining $F_{p,min}(N)$ and estimating the variations ΔF_D, ΔF_W in Equation 9.5.

9.3.4 Safety-induced thrust requirements, $F_{p,min}$

According to the FAR 25 [212] and EASA CS-25 [213] airworthiness regulations for multiengine aircraft, the minimum engine thrust of conventional twin or quad engine aircraft is dictated by the one engine out condition. This represents the necessity of the aircraft to be capable of meeting the climb demands, under several circumstances, with one engine inoperative. Therefore, if F_{clmb} is the maximum climb thrust required by a N engine aircraft, the minimum thrust provided by each engine must be

$$F_{p,min} = \frac{F_{clmb}}{N - n}\,, \tag{9.6}$$

where n is the number of inoperative engines; for conventional aircraft, $n = 1$. Quantity F_{clmb} is mainly determined by the MTOW and can be estimated through the SAE-AIR 1845 [45] procedures presented in Section 2.7 (or through the revised version by ECAC [104]), as performed in the steep takeoff case study of Chapter 8.

Considering a conventional twin engine (i.e. $N = 2$) aircraft like the A320-232, Equation 9.6 suggests that $F_{p,min} = F_{clmb}$. Thus, with both engines operating the A320-232 is capable of producing twice the normally required thrust. Overproducing thrust is translated into oversized engines, since it is generally acknowledged that engine dimensions and weight (and therefore drag) are roughly proportional to the thrust output (this is also implied by the trends of Figures 4.8 and 4.9 in Chapter 4). Hence, it can be concluded that the overall propulsive efficiency of twin (or quad) engine aircraft is sacrificed for complying with the current safety regulations.

Equation 9.6 suggests that $F_{p,min}$ becomes smaller than F_{clmb} as the number of engines increases; this is because the thrust loss due to one engine failure decreases with number of engines. The dashed curves in the left plot of Figure 9.6 show this behaviour for various values of n; the thrust values in the vertical axis apply to the A320-232. Clearly, the mandatory excessive amount of thrust produced per engine for safety reasons decreases with number of engines. Hence, a DEP (or DP in general) system can lead to reducing propulsive efficiency loss arising from safety constraints.

Meanwhile, increasing the number of engines also raises the probability of one engine failing, implying that the FAR 25 one engine out condition is unsuitable for DP aircraft. If the probability of one engine failure is $\mathcal{P}$, with $\mathcal{P} << 1$ then the probability of one engine failing among N engines is $\mathcal{P}N$. The probability of multiple engines failing during a single flight is dramatically smaller; assuming that the events of each engine failure are

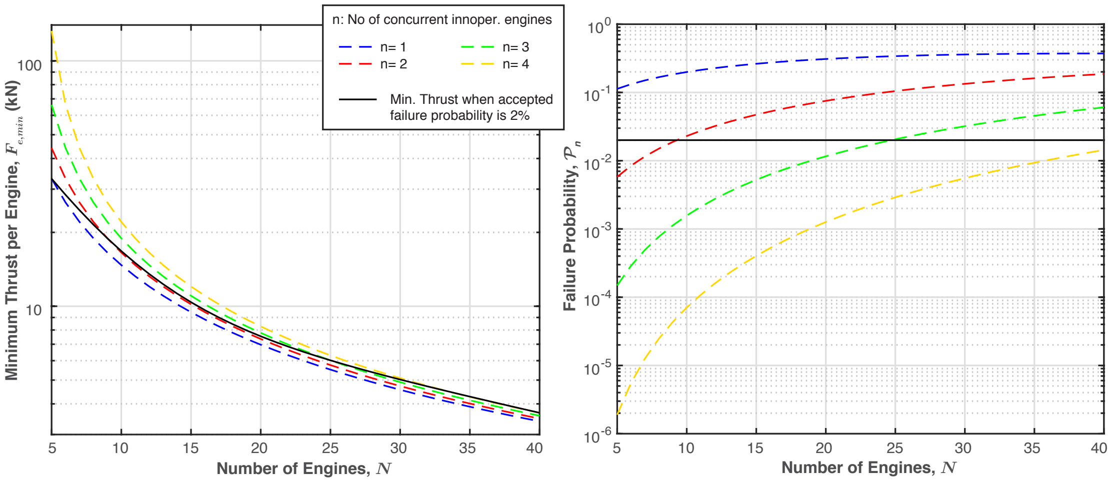

Figure 9.6: Left: Minimum thrust per engine satisfying the n engines-out condition. Right: Probability of n engines failing concurrently in a N engines DP system.

independent of each other (this may not be a totally realistic assumption, since these events could be a result of a common cause) then according to the binomial distribution [214], the probability of n engines becoming inoperative is

$$\mathcal{P}_n = \binom{N}{n} \mathcal{P}^n (1 - \mathcal{P})^{(N-n)} \,, \tag{9.7}$$

where the binomial coefficient

$$\binom{N}{n} = \frac{N!}{(N-n)!n!} \,. \tag{9.8}$$

Since $\mathcal{P} << 1$, it is apparent that $\mathcal{P}_n$ is in effect n orders of magnitude smaller than $\mathcal{P}$, as illustrated in the right plot of Figure 9.6. Normally, failure probability $\mathcal{P}_n$ should increase with flight duration; yet, this influence is considered negligible for the scope of this thesis and is not included in Equation 9.7.

In summary, increasing the number of engines results into reducing the safety-related minimum required thrust per engine while increasing the probability of one engine failing. These contradicting facts imply that a different way of determining the minimum thrust requirements of each engine must be introduced for DP systems. Since this topic is irrelevant to the present thesis, it is assumed in a simplified way that the maximum accepted failure probability is $\mathcal{P}_n = 2\%$[2]. This requirement is represented by the continuous horizontal line in the right plot of Figure 9.6. This plot suggests that to meet this requirement, the number of concurrently inoperative engines n must be adjusted as seen in Table 9.2. For the A320-232, the minimum thrust per engine among N engines

---

[2] The assumed failure probability is very high. Realistic values are available in FAA's Advisory Circular AC 25.1309-1A [215].

satisfying the $\mathcal{P}_n = 2\%$ condition is represented by the continuous curve in the left plot of Figure 9.6. Using the $N - n$ pairs of Table 9.2, the thrust $F_{p,min}$ can be obtained from Equation 9.6.

Table 9.2: Number of inoperative engines among N engines if accepted failure probability is $\mathcal{P}_n < 2\%$.

No of engines N	**No of concurrent inoperative engines satisfying** $\mathcal{P}_n < 2\%$ n
1 to 4	1
5 to 9	2
10 to 25	3
26 to 40	4

9.3.5 Drag considerations

Airframe geometry remains the same between the baseline A320 and the e-A320, irrespectively of DEP system (i.e. TeDP or All Electric) and/or number of propulsors. Hence, wing and body skin-friction drag remains fixed (assuming the same cruise airspeed) so that only engine drag varies with number of propulsors. Moreover, civil aircraft aerodynamic drag breakdowns in references [216, 217] show that skin-friction drag (and hence nacelle drag) is insignificant during takeoff and landing, where lift-induced drag clearly dominates. It becomes important during cruise, where it comprises about half the total aircraft drag, but still, engine drag is small compared to the wing and body drag. Figure 9.7, which is reproduced based on reference [217], shows representative takeoff and cruise drag breakdowns for a civil aircraft. Hence, below estimated propulsors drag variation with fan diameter has small effect in terms of the whole aircraft thrust requirements. However, it is included in the present case study, because drag variation is a crucial parameter in aircraft design that should generally be considered.

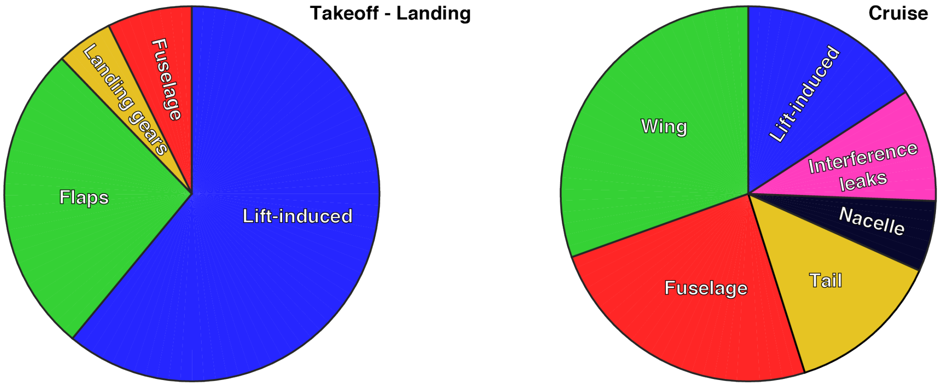

Figure 9.7: Typical aircraft drag breakdowns at different flight phases [217].

9.3.6 Propulsors drag

The drag in dimensionless form of each propulsor can be calculated from the expressions for nacelle drag [218, 211]

$$C_D = k\, c_f\, S_{ncl}\,, \tag{9.9}$$

where k is a constant and S_{ncl} is the wetted area of the nacelle, which is assumed equal to the total nacelle surface area. Skin friction coefficient, c_f, is given by different empirical formulas depending on whether the flow is laminar or turbulent; this is dictated by the Reynolds number

$$Re = \frac{\rho V_0 \ell}{\mu}\,. \tag{9.10}$$

For a given airspeed, V_0, and atmospheric conditions (μ is the air kinematic viscosity), Re is only a function of the nacelle length, ℓ, so that ultimately, $c_f = f(\ell)$. Air kinematic viscosity inside the landing and takeoff altitude range is assumed to be $\mu \approx 1.33 \times 10^{-5}$ m^2/s [219]. Assuming an airspeed $V_0 = 90$ m/s then $Re > 10^5$ for any typical nacelle length. This Reynolds number implies turbulent flow [220], and hence the skin friction coefficient is obtained from the empirical formula[3] [156]:

$$c_f = \frac{0.0592}{Re^{0.2}}\,. \tag{9.11}$$

Substituting S_{ncl} from Equation 9.4 in Equation 9.9 and separating the operational factors and constants from the engine dimension parameters, the nacelle drag coefficient is given by

$$C_D = \mathbb{A} {d_f}^{1.8}\,, \tag{9.12}$$

where

$$\mathbb{A} = 0.1 k \pi \left(\frac{\mu}{\rho V_0}\right)^{0.2}\,. \tag{9.13}$$

The propulsors array drag can be calculated with Equation 2.42 using the above obtained drag coefficient and the array area, which is approximated as a rectangular prism using the sketch of Figure 9.8. The right part of Figure 9.8 plots the drag (in normalised form) variation of the propulsors array with propulsors number. Also indicated in the plot is the normalised drag of the A320 propulsion system (i.e. the two turbofans), that is calculated using the publicly available dimensions of its engines. It is observed that an array of more than 4 propulsors offers propulsion system drag reduction, compared to the conventional A320.

---

[3] Several other approximation formulas can be used [218, 220]e.g. the Prandtl-Schlichting empirical formula $c_f = \frac{0.455}{[\log(Re)]^{2.58}}$.

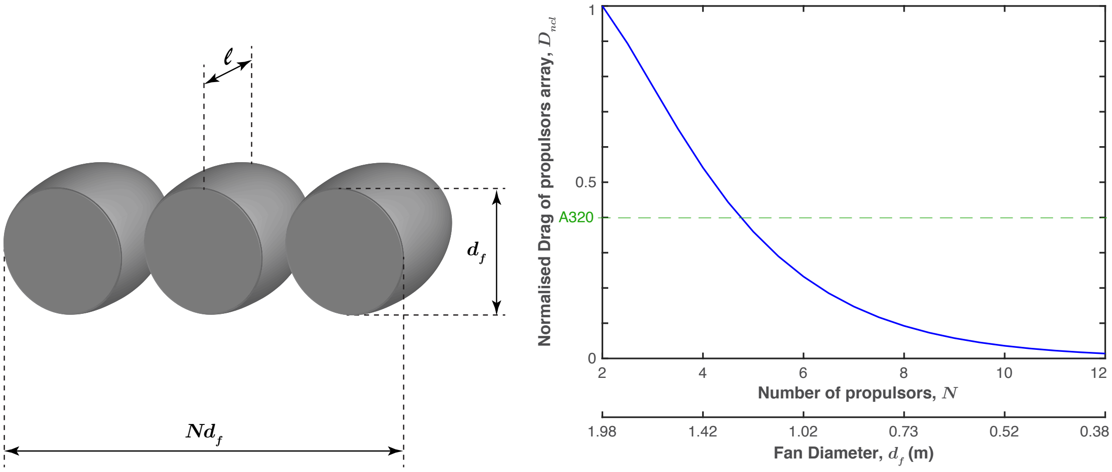

Figure 9.8: Left: Sketch used for approximating the propulsors array as a rectangular prism of the indicated dimensions. Right: DP system drag at different number (and sizes) of propulsors. The green dashed line represents the baseline A320-232.

9.3.7 Weight considerations

The weight plays an important role in the thrust requirements of an aircraft. This section estimates the weight difference between the conventional A320 and the e-A320s variations. Since all e-A320s use the airframe of the A320, weight differences arise only from the propulsion system. With reference to Figure 9.3, Table 9.3 lists the component weights of the TeDP and the All-Electric DEP architectures, along with the weight of the A320 turbofan, which is decomposed in order to quote the core and fan weights separately. The core weight is extracted from Figure 9.9.

The rest of this section describes the procedures for obtaining the weight values in Table 9.3. As explained earlier, weight variations are normally resolved by aircraft design and/or performance tools that ultimately establish the thrust requirements of a certain aircraft. Normally, thrust is an input to the noise estimation framework developed in this thesis. Therefore, the procedures presented below aims at obtaining rough estimates of the weight variation with number of propulsors, in order to accomplish the distributed propulsion case study.

9.3.7.1 Weight of conventional A320 turbofan engines

Figure 9.9 is reproduced based on reference [101] and shows estimated weight of turbofan cores as well as of different electric generator and motor types as a function of shaft power. The core weight of the conventional A320 turbofan engines can be extracted from that Figure, provided that the A320 power requirements are known.

Table 9.3: Weight breakdowns for the A320-232 and the e-A320 variants. Propulsion systems weights are estimated. Energy requirements (fuel or batteries) are for a 900 nm, 150 Pax mission at 0.78 M and include safety reserve.

Aircraft A320-232 (Baseline aircraft)

System	**Component**	**Weight (t)**
Propulsion	Core (x2) (from Figure 9.9)	1.5
	Fan** + Lining + remaining* (x2)	3.3
	Engine Dry (x2)	4.8
	Nacelle + Pylon (x2)	2.88
	Misc (x2)	0.32
	Total Propulsion:	**8**
Payload	Fuel Tank (including 3 t reserve)	9
	150 Passengers	15
OEW		42.6
	Total Aircraft:	**74.6**

* E.g. fuel and ignition systems, lubrication system, bleed air system [221]

** Includes LPT section [221]

Aircraft TeDP e-A320

System	**Component**	**Weight (t)**	
Propulsion	Electric propulsors array (min, max)	4.49	6.97
	Turboshaft	1.7	
	Electric generator	0.3	
	Inverter	0.18	
	Total Propulsion (min, max):	**6.67**	**9.15**
Payload	Fuel Tank (including 3 t reserve)	9	
	150 Passengers	15	
OEW		42.6	
	Total Aircraft:	**73.27**	**75.75**

Aircraft All - Electric e-A320

System	**Component**	**Weight (t)**	
Propulsion	Electric propulsors array (min, max)	4.49	6.97
	Total Propulsion (min, max):	**4.49**	**6.97**
Payload	Batteries ($e = 1500$ Whr/kg)	23.78	25.55
	150 Passengers	15	
OEW		42.6	
	Total Aircraft:	**85.86**	**90.12**

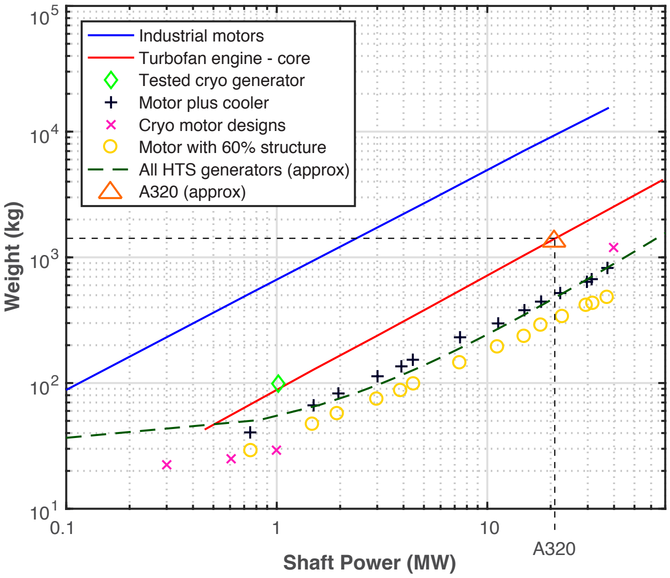

Figure 9.9: Weights of various types of turbofan cores, motors and HTS generators as functions of power, based on future technological expectations. The plot is reproduced based on reference [101].

The maximum power is drained during takeoff and therefore power requirements are established based on the takeoff phase configuration. Power is calculated with

$$P_{max} = N\, V_c\, F_\infty\,, \tag{9.14}$$

where the A320 takeoff speed $V_c = 163$ kn, was calculated in Section 8.1 and listed in Table 8.7. The rated thrust, F_∞, is used rather than the net takeoff thrust F_N (where engines normally operate just below its rated thrust) because the power should cover the event of requiring 100% of thrust.

Ultimately, the A320 maximum power requirements are found to be 19.7 MW. It can be assumed that an additional 5% of power is provided for various other reasons, yielding 21 MW. Hence, using Figure 9.9, the total core weight (2 turbofans) is approximated at 1.5 t. Subtracting the core weight from the engine dry weight, which is 2.4 t [51], yields the weight of the remaining engine components (i.e fan, lining). Also, the nacelle and pylon weight is approximately 0.6 times the engine dry weight [211], i.e. 1.44 t. Hence, the total weight (2 engines) of fan, nacelle (and pylon) and lining is 7.68 t. To cover the weight of any additional components (denoted Misc in Table 9.3) associated with the propulsion system, the total weight is rounded up to 8 t.

9.3.7.2 Fuel requirements of the A320

The fuel requirements of the conventional A320 for the 900 nm mission are then estimated. According to the aircraft technical database in [160], the Operating Empty Weight (OEW) of the A320 is 42.2 t, whereas ICAO [222] suggests that for short-range trips, the average mass of a passenger with luggage is 100 kg, which gives an overall passenger weight of 15 t. At cruise, the SFC is 0.596 lb/(lbf·h) [210] and the airspeed is 0.78 M at 37,000 ft (or 233 m/s) [160]; whereas the cruise L/D ratio is approximately 15, as worked out from data in reference [223]. Substituting these inputs in the rearranged Breguet range equation (Equation 2.52), the fuel weight is found to be approximately 6 t. Yet, safety regulations [224] stipulates that reserve fuel should allow 45 minutes of flight. Considering that the cruise fuel flow of the A320 is 0.88 kg/s [79], the reserve fuel weight should roughly be 3 t. Hence, the A320 should be equipped with 9 t of fuel for the 900 nm mission.

9.3.7.3 Weight of array of electric propulsors, W_{pa}

Both the TeDP and the All-Electric e-A320 variations use the same electric propulsors array. This paragraph investigates the weight variation of the electric propulsors array with number of propulsors. This is achieved by decomposing the electric propulsor into its various components (i.e. fan, nacelle, lining and motor) and estimating the weight variation of each component with fan diameter, in accordance with Lolis et al. [225] findings described below.

Numerous methods are available in the public sector for the prediction of conventional gas turbine engines weight. A critical review of them is given by Lolis et al. [225], who classifies methods into whole engine based and component based. The former use public engine data to produce empirical equations that correlate the engine weight with one (thrust or mass flow) or more (fan diameter, BPR, OPR, etc.) design parameters. Component based methods compute analytically each component's weight using some empirical data and numerous input variables. Lolis et al. [225] used existing methods to predict the weight of actual engines. Although he observed notable discrepancies between results, he suggested that engine weight (and size) is mostly determined by the engine diameter, which is in turn established from the fan diameter. The below-derived analogies between fan diameter and weight of components involve some very crud approximations and serve for capturing the trends associated with DEP systems.

Motor weight:

According to Liu et al. [209], the motor weight is related with its power, P_{mtr}, in MW and shaft speed, $N1$, in rpm as follows:

$$W_{mtr} = 2325\sqrt{\frac{P_{mtr}}{N1}}\,. \tag{9.15}$$

It is sensible to assume that P_{mtr} changes with the fan diameter, d_f, and hence, with the number of propulsors. Liu et al. [209] calculated the variation of power per propulsor with fan diameter and his results are reproduced in the left plot of Figure 9.10, along with a quadratic trend curve described by

$$P_{mtr}(d_f) = \alpha d_f^2 + \beta d_f + \gamma \,, \tag{9.16}$$

where α, β, γ are the quadratic equation constants. Also, Figure 4.7 of Chapter 4 indicates that the relationship between $N1$ and fan diameter has the form

$$N1(d_f) = \delta {d_f}^{\varepsilon} \,. \tag{9.17}$$

where constants δ, ε are obtained through linear regression. The values of all constants in the two previous equations are listed in Table 9.4.

Table 9.4: Coefficients for the fitted curves for P_{mtr} and $N1$.

Coefficient	**Value**	**Coefficient**	**Value**	**Coefficient**	**Value**
α	32948	γ	66310	ε	-1.013
β	-80106	δ	8761		

Substituting $P_{mtr}(d_f)$ and $N1(d_f)$ in Equation 9.15 yields the estimated variation between motor weight and number of propulsors that is represented by the right plot of Figure 9.10.

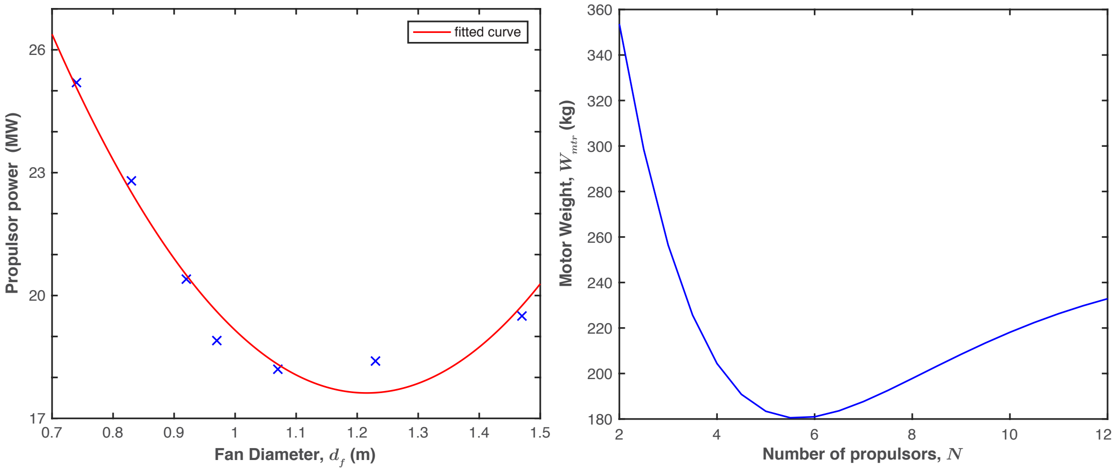

Figure 9.10: Left: Propulsor power variation with fan diameter [209]. Right: Estimated motor weight for different number of propulsors.

Fan weight:

Based on the component based method of Sagerser [226] the fan weight and fan diameter are related with

$$W_{fan} = 135 {d_f}^{2.7} \,. \tag{9.18}$$

This relationship is assumed representative for the electric propulsors fans as well.

Nacelle and lining weight:

The weight of an object is defined as $W = mg = \rho V g$, where ρ is the object's material density and V its volume. The nacelle's volume can be written as its surface area, S_{ncl}, which was previously estimated (Equation 9.4) multiplied by its wall thickness. The lining volume can be expressed similarly. Assuming that the area treated with lining is 20% of the inner nacelle area, the nacelle and lining weight variation with fan diameter approximated with

$$W_{ncl} \approx gS_{ncl}(\rho_n\, z_n + 0.2\, \rho_l\, z_l)\,, \tag{9.19}$$

where z and ρ signify thickness and density respectively, while subscripts n and l refer to the nacelle and the liner. It is assumed that $z_n = 1$ mm , $z_l = 5$ mm, $\rho_n = 2500$ kg/m^3 (corresponding to material like duralumin [227]) and $\rho_l = 9000$ kg/m^3 (corresponding to material like Haynes 25 [169]).

Total weight of propulsors array:

The weight of each propulsor is the sum of its components weights, i.e.

$$W_p = W_{mtr} + W_{fan} + W_{ncl}\,, \tag{9.20}$$

and therefore, the weight of the propulsors array is

$$W_{pa} = N\, W_p\,. \tag{9.21}$$

The variation of propulsor weight with fan diameter is plotted in the left diagram of Figure 9.11. More interestingly, the right plot of Figure 9.11 shows that increasing the number of propulsors, N, reduces the weight of the whole DP array. This agrees with findings by Liu et al. [209]. This indicates that it is beneficiary in terms of weight to seek the maximum possible number of propulsors, i.e. use the smallest possible propulsors.

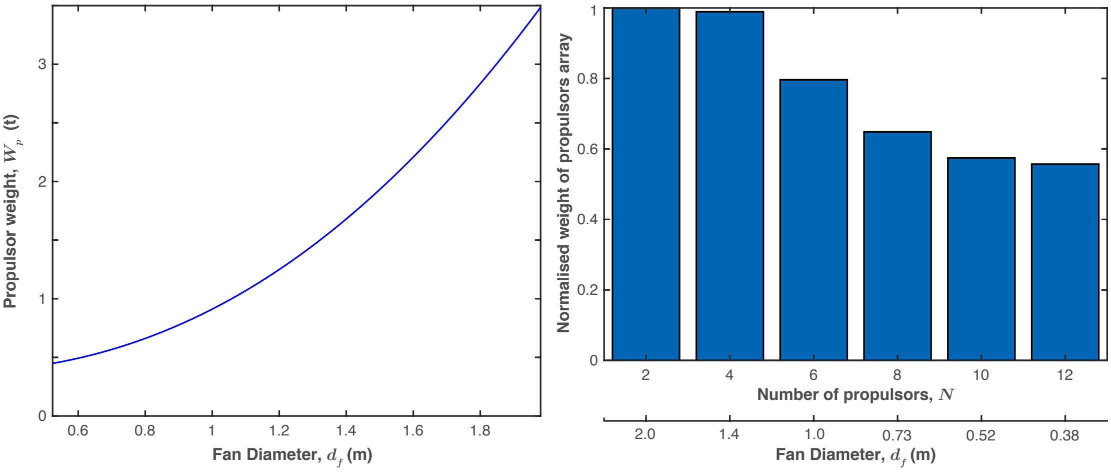

Figure 9.11: Left: Relationship between fan diameter and propulsor weight. Right: Approximated effect of propulsors number on the DP array weight.

9.3.7.4 Power supply weight, W_{pwr}

Power requirements of the e-A320

The aircraft maximum power requirements, P_{max}, determine the power supply unit specifications and weight. According to Equation 9.14, which was used earlier to estimate the P_{max} of the conventional A320, P_{max} is a function of takeoff speed and thrust; both these quantities depend on MTOW, which is affected by the previously described variation of the propulsors array weight, W_{pa}, with number of propulsors, N, indicating that P_{max} varies with N.

Moreover, as illustrated in Figure 9.12, power supply weight itself contributes to the aircraft MTOW creating a loop. Hence, assessing the power supply weight requires several iterations of calculations, until results converge, as shown later in this Section. Concerning the TeDP version of the e-A320, it is sensible to assume that the turboshaft weight is not sensitive to relatively small output power variations, due to the inability to fine-scale all its parts. This conclusion is also extracted from observing the turboshaft engine specification database [210]. Therefore, the selection of turbogenerator type is assumed unrelated to the number of propulsors. In contrast, power requirements variation affects the weight of batteries in an All-Electric e-A320. Hence, the convergence loop is only used for the All-Electric e-A320.

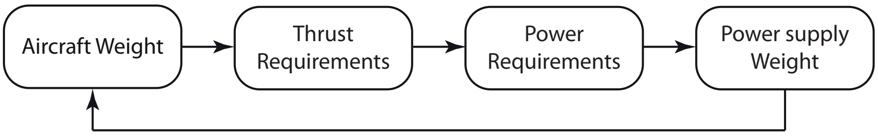

Figure 9.12: Schematic representation of the loop describing the relationship between aircraft weight and power supply weight.

Turboelectric (TeDP) system

Turbogenerator weight:
The turbogenerator consists of a turboshaft engine and a generator. A suitable turbogenerator for the TeDP system should cover the power requirements of the e-A320 aircraft. It is assumed that these are the conventional A320 ones (i.e. 21 MW) plus an additional 10% due to inefficiencies associated with the electric system, as suggested by Welstead et al. [202]. This sets power requirements of the e-A320 at 23 MW. Nevertheless, this value may be overestimated, since electric propulsors developments aim at significantly reducing power consumptions, as pointed out in reference [6].

Based on the turboshaft engine specification database [210] and reference [228] the weight of a suitable turboshaft engine delivering the required power, including the generator, is estimated at 2 t. This weight, which, as previously described, is assumed independent of propulsors number, reflects current technology levels and can be reduced in the future due to technology improvements.

Power generator and inverter weight:
Figure 9.9 implies that the weight of all arrangements increases with shaft power at roughly the same rate. Also, for a fixed power requirement, the turbofan core is heavier than the motor or generator with its cooler. Accurately calculating this weight difference is beyond the scope of the present case study. Using Figure 9.9 the power generator weight, W_{gnr}, can be roughly approximated at 300 kg. In addition, based on estimated weights in [101] and [202], the inverter weight can be approximated as $W_{inv} \approx 0.6 W_{gnr}$, i.e. 180 kg.

Cabling weight:
DEP systems are envisioned to use super-conductive cables and High Temperature Superconducting (HTS) technologies to eliminate electric power transmission losses associated with the resistance of conventional cables [198]. Hence, the size of the cables is only a function of the energy to be transmitted and not a function of losses. Cabling diameter (and hence weight) increases with power requirements [229]. Hence, based on the variation of propulsors power with fan diameter in the left plot of Figure 9.10 cabling weight, $W_{cbl} \propto P_{mtr}$. Any variation of the overall aircraft power requirements due to variation of thrust requirements with number of propulsors is small and can be neglected, since it adds excessive complexity for the purposes of this thesis.

So, assuming a fixed position of the power generator and that the propulsors are connected in series, cabling weight varies only with P_{mtr}. Under this assumption, the cabling weight variation will be negligible compared to the whole aircraft weight and can be disregarded. Alternatively, since $W_{cbl} \propto P_{mtr}$ and $W_{mtr} \propto P_{mtr}$ the effect of W_{cbl} can be taken into account by increasing the motor weight by a small percentage, say 10%. This is the method adopted in this study.

Fuel weight:
In TeDP systems, the fuel weight is determined by the SFC of the turboshaft. The turboshaft engine specification database [210] suggests that the selected turboshaft type SFC $= 1.019 \times 10^{-}5$ kg/Ns, which is roughly equal to the SFC of A320-232 turbofan engine, i.e. the IAE V2527-A5. Hence, it is assumed that the TeDP e-A320 requires the same amount of fuel as the A320-232, i.e 9 t.

All-Electric system

The All-Electric and TeDP e-A320s variants use identical electric propulsors. The difference between them lies in the power supply system; the All-Electric aircraft uses batteries to drive the propulsors, rather than a turbogenerator. While this eliminates the need for a fuel tank, the size and weight of the batteries create a new critical issue. A further concern is that All-Electric aircraft weight remains fixed across the whole flight, as there is no mass variation during flight due to fuel burn as in conventional aircraft. This is unrelated to this case study's calculations but should be generally considered, since it alters performance parameters affecting the cruise and landing flight phases.

Batteries:
The weight of the batteries is inversely proportional to their specific energy, e (i.e. energy stored per unit mass or volume). It is generally acknowledged that significant technological improvements are required to realise even a modest range capability for electric and hybrid-electric aircraft [6]. Both mass and volume of the batteries are important, since the latter determines the available load space of the aircraft, which can be seen as an indirect effect on its (effective) weight. NASA [11] specifies that the specific energy of current batteries need to be significantly increased, while their weight (and size) be notably decreased in order to reach the extreme power-to-weight required in electric civil aviation. According to the same reference, lithium-air (Li-O2) batteries can theoretically reach the specific energy of gasoline, yet, their technology is in early development stages.

Figure 9.13 shows theoretical, practical and expected energy densities of various rechargeable battery types, as found in reference [6]. Also quoted is the effective specific energy of kerosene in combustion engines, which consists just the 14% of the raw kerosene fuel specific energy (which is around 12000 Wh/kg), due to fuel burn inefficiencies [6]. Referring to that figure it is presumed that a specific energy of 1500 Wh/kg will have been achieved by the target EIS of 2035.

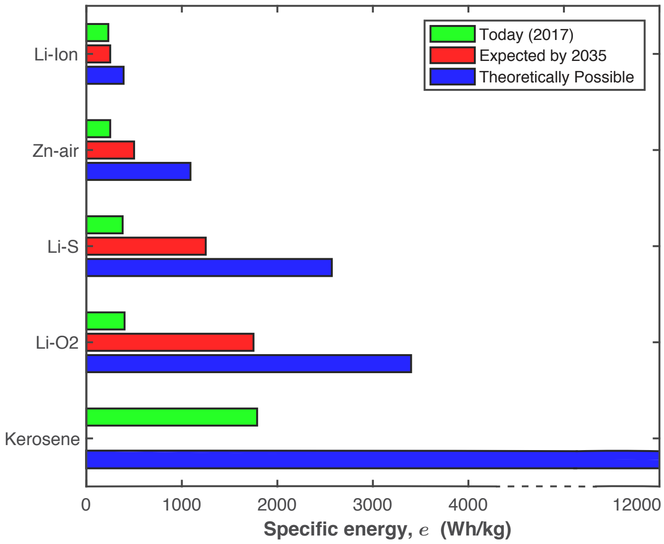

Figure 9.13: Current, expected and theoretically possible specific energy for various types of batteries [6]. Effective and theoretically possible specific energy of kerosene in combustion engines is quoted for comparison [11].

Batteries weight estimation through convergence:

As previously described, batteries weight is estimated using a loop process until the values converge. The starting value for the peak power requirements, P_{max}, is assumed to be that of the TeDP version of the e-A320, i.e. 23 MW. As mentioned in the TeDP case, actual power requirements may reduce dramatically in the future as a result of reducing power consumption of electric propulsors [6]. Comparing to the power and energy requirements for the Ce-Liner aircraft that are analytically specified in reference [190], the minimum energy required by the All-Electric e-A320 with 2 propulsors for the 900 nm mission, including reserve requirements, is estimated at 32 MWh; in which case total weight of the batteries with specific energy of 1500 Wh/kg would be $W_{btr} = 23$ t.

This battery weight is substituted in Equation 9.22 below to yield the aircraft weight, based on which the peak thrust (with Equation 9.23 below) and power requirements are re-calculated yielding a new batteries weight. The procedure is repeated until the values converge, as depicted in the left plot of Figure 9.14. Whereas the right one shows the variation of batteries weight with N.

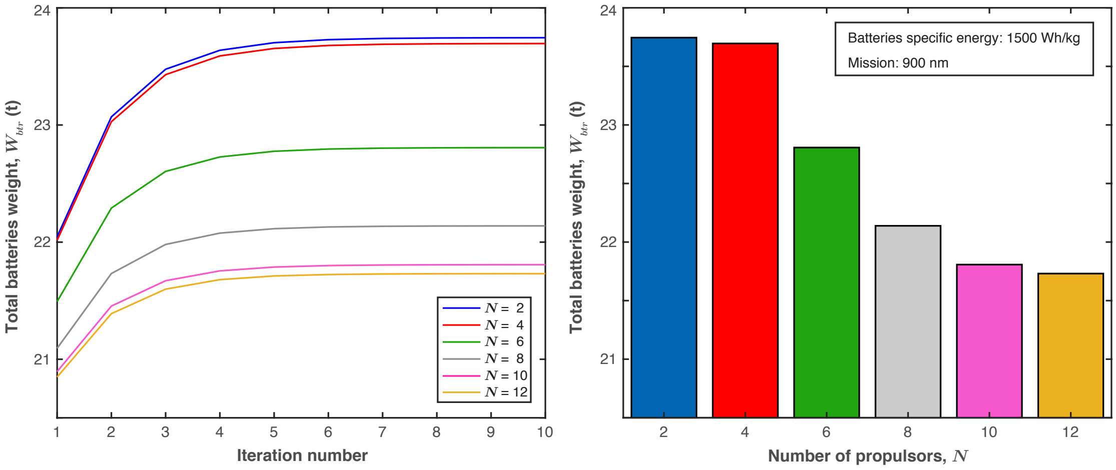

Figure 9.14: Right: Total batteries weight for the 900 nm mission as function of propulsors number, as converged after the 10 iterations shown in the left plot.

9.3.8 Total aircraft weight, W_{ac}

The aircraft total weight is given by

$$W_{ac} = W_{pa} + W_{pwr} + OEW + Payload\,. \tag{9.22}$$

Figure 9.15 shows the estimated weight of the various DEP aircraft, at takeoff and approach. While the TeDP aircraft is lighter in approach due to the fuel consumed throughout the flight, weight remains unchanged for the batteries-powered All-Electric aircraft. Hence, the latter is only represented by a single bar type (grey coloured) in Figure 9.15, whereas plain and dotted blue bars are used to denote the TeDP aircraft weight at takeoff and approach respectively. All the All-Electric variants are heavier than the conventional A320, due to the weight of the batteries. TeDP variants with more than 4 propulsors are lighter than the A320.

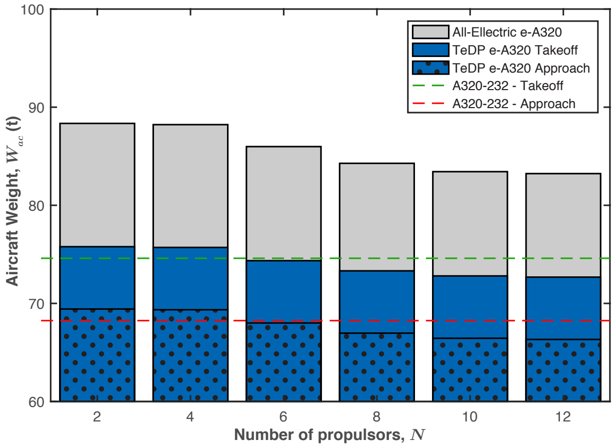

Figure 9.15: Takeoff and landing weight of the e-A320 variations for different number of propulsors. The A320-232 weights are indicated for comparison.

9.4 Thrust variation with number of propulsors

Having estimated the aircraft weight impact, ΔW, of altering the propulsors number, the variation of the aircraft thrust requirements with propulsors number is calculated[4]. As mentioned earlier, the relatively small drag effect is neglected. Based on Equation 2.48, altering the aircraft weight from W_0 to $W_0 + \Delta W$ will result into a thrust requirements difference

$$\Delta F_W = F_0 \frac{\Delta W}{W_0} \,. \tag{9.23}$$

Hence, ΔF_W, between the baseline aircraft (e.g. the conventional A320-232) and the e-A320 variations, for takeoff and approach, is obtained by using the corresponding (takeoff or approach) baseline weight W_0 and thrust F_0, as shown below.

9.4.1 Takeoff

Takeoff thrust per engine for the A32-232 is $F_0 = 112$ kN, as calculated through the SAE-AIR 1845 [45] aircraft performance procedure (similarly to the steeper operations

---

[4] Thrust requirements are calculated under the assumption that all DEP aircraft use the takeoff and/or approach flight profiles of the conventional A320. However, optimum flight profiles for the various DEP aircraft may be different than these of the current A320. This would alter both thrust requirements and noise at CPs. Moreover, an alternative study could keep the thrust fixed, which would cause the takeoff and approach angles to vary with weight variation as suggested by Equation 8.7.

case studies in Chapter 8). Table 9.3 suggests that weight $W_{0,TO} = 74.6$ t; whereas

$$\Delta W_{TO} = W_{ac} - W_{0,TO} \,. \tag{9.24}$$

Substituting these values in Equation 9.23 yields thrust requirements difference, ΔF_W. The takeoff thrust per propulsor is then calculated with

$$F_p = \frac{F_0 + \Delta F_W}{N} \,, \tag{9.25}$$

and must be at least equal to the safety-related minimum thrust per engine, $F_{p,min}$, governed by Equation 9.6. Parameter N in the last-mentioned equation is obtained from Table 9.2, whereas the climb thrust, F_{climb}, is estimated using the SAE-AIR 1845 procedure. More specifically, it is calculated that the baseline A320-232 can maintain a 5° climb if $F_{climb,0} \geqslant 58kN$. This baseline value is inserted in Equation 9.23 for obtaining the climb thrust variation for the various e-A320 types with:

$$\Delta F_{climb} = F_{climb,0} \frac{\Delta W}{W_0} \,, \tag{9.26}$$

where ΔW is the weight difference between the A320-232 and the e-A320 aircraft. Figure 9.16 illustrates the calculated takeoff thrust per propulsor, F_p, along with the associated minimum allowed limits, $F_{p,min}$, for both the TeDP and All - Electric e-A320. The latter is heavier and hence has higher thrust requirements and $F_{p,min}$ than the TeDP versions. Figure 9.16 shows that the condition $F_p \geqslant F_{p,min}$ is satisfied for all the cases examined. Figure 9.17 shows the resulting thrust requirements for the whole aircraft as calculated using the SAE-AIR1845A procedure [45]. The green dashed line represents the baseline A320-232. As expected, the heavier All-Electric aircraft has more demanding thrust requirements than the TeDP and the A320-232.

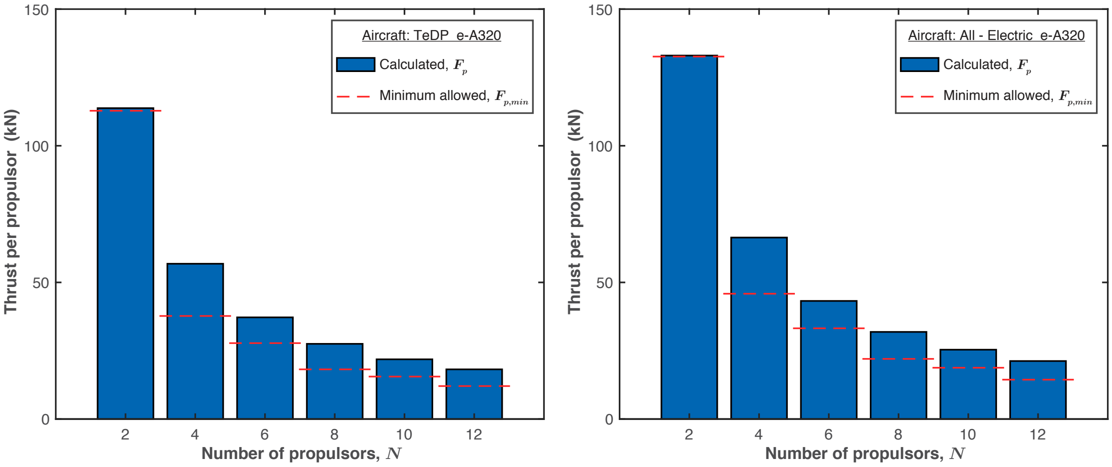

Figure 9.16: Takeoff thrust per propulsor of the e-A320 variations for different number of propulsors. The dashed red lines signify the minimum thrust per propulsor as governed by safety demands.

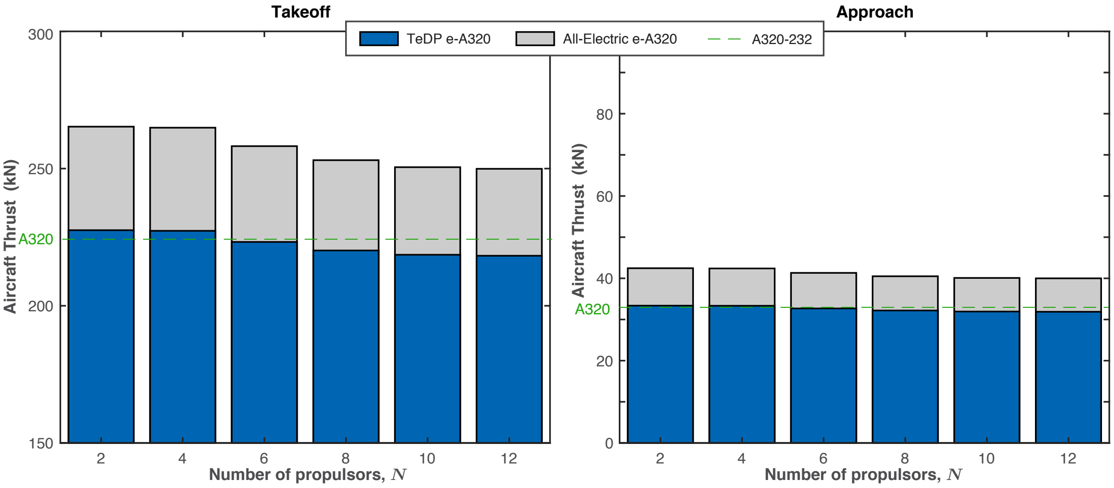

Figure 9.17: Thrust requirements of the different e-A320 variations for performing the default A320 takeoff and approach procedures. The green dashed line represents the baseline A320-232.

9.4.2 Approach

Approach thrust requirements are calculated similarly. Approach thrust per engine for the A32-232 is $F_0 = 16.4$ kN and the approach weight equals the take off weight, $W_{0,TO}$, minus the fuel consumed, which, for the specific 900 nm mission, is $W_{fuel} = 6$ t. Hence,

$$W_{0,AP} = W_{0,TO} - W_{fuel}\,. \tag{9.27}$$

For the TeDP e-A320, approach weight is the takeoff weight W_{ac} minus the fuel consumed, which is the same as that of the baseline aircraft, as explained in Section 9.3.7.4. In contrast, the All-Electric e-A320 weight remains the same throughout the mission, since no fuel is burnt. Hence:

$$\Delta W_{AP} = \begin{cases} (W_{ac} - W_{fuel}) - W_{0,AP} = \Delta W_{TO}, & \text{for TeDP e-A320}\,, \\ \\ W_{ac} - W_{0,AP} = \Delta W_{TO} - W_{fuel}, & \text{for All-Electric e-A320}\,. \end{cases} \tag{9.28}$$

9.5 Noise estimations for DEP aircraft

Above-performed calculations of thrust requirements for the various TeDP and All-Electric aircraft enables noise estimations with the proposed framework. The noise variation with number of propulsors is estimated at source, whereas NPD curves are also constructed. It is reminded that the baseline aircraft is the A320-232.

9.5.1 Noise at source

Figure 9.18 shows the PWL difference between the conventional A320-232 and the e-A320 variations for takeoff and approach. Jet and fan noise changes are estimated with Equations 9.2 and 9.3 respectively, while Equation 5.21 yields airframe noise variations resulting from flap deflection angle changes. To incorporate the effect of weight variation on approach flap setting, it was theoretically assumed that flaps are deflected/retracted by one degree per supplementary/deducted ton.

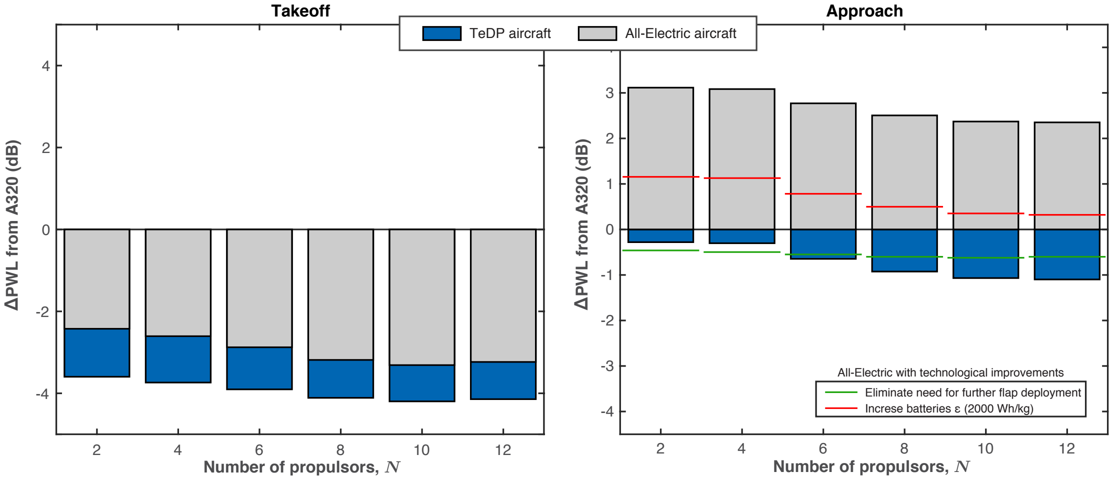

Figure 9.18: Aircraft PWL difference between the conventional A320-232 and the e-A320 variations for takeoff (left) and approach. The horizontal lines at approach depict PWL differences achievable through technological improvements.

At takeoff, where propulsion noise dominates, noise at source is reduced, despite the increased takeoff thrust requirements of the e-A320 demonstrated in Figure 9.17. This is because total airflow traversing the propulsors is larger than the airflow passing through the A320-232 turbofans, as seen in Table 9.1; for instance, while for the 4 propulsors e-A320 the total airflow is $4 \times 233 = 932$ kg/s, it is only $2 \times 355 = 710$ kg/s for the A320-232. This means that for the same thrust, the e-A320 are associated with lower jet velocities than the A320-232 and hence are quieter, as implied by Equation (9.2); apparently, the aforementioned increased thrust requirements of the e-A320 types are relatively small to outweigh the noise impact of this jet velocity difference.

The right plot in Figure 9.18 shows aircraft PWL differences at approach, where the airframe noise contribution dominates. The TeDP e-A320s are slightly quieter than the A320 due to: a) the reduced propulsors' noise, and b) the fact that TeDP with more than 4 propulsors are lighter than the A320 (see Figure 9.15). The significantly heavier All-Electric variations are noisier than the A320-232 because, considering current technology, it is assumed that larger flap deflection angles are required to compensate for their weight and allow them to fulfil the standard approach flight profile; as earlier discussed (e.g. see Equation 5.21), airframe noise increases with flaps deflection angle. This increase significantly affects the whole aircraft noise because at approach, airframe noise prevails. Possible future technologies for reducing All-Electric aircraft approach noise are enhanced lift-to-drag ratio to eliminate further flap deflections, and/or batteries with larger specific energy density to reduce aircraft weight. Figure 9.18 includes the estimated noise impact of these technologies. Further noise reductions are achievable by designing quieter airframes (e-A320 aircraft in this study use the A320 airframe).

Moreover, it is interesting to notice the small PWL differences between the e-A320 variations of the same power source type (TeDP or All-Electric) but different number of propulsors. More specifically, the maximum takeoff PWL difference, which is between the $N = 2$ and $N = 10$ types is 0.5 dB for the TeDP and 0.9 dB for the All-Electric e-A320 (see left plot in Figure 9.18). Whereas during approach, the maximum PWL difference is around 0.8 dB for both e-A320 types. Nevertheless, as will be seen later in the noise contour maps of Figures 9.23 and 9.24, this small PWL difference offers notable benefits in the noise-exposed communities around airports.

Finally, it must be reminded that noise on the ground (e.g. in CP points) also depends on the takeoff and approach flight profiles. As pointed out earlier, optimum takeoff and/or approach flight profiles for DEP aircraft may be different than these of the A320. Hence, noise comparisons would require determining these profiles, which is a task that goes beyond the scope of the present case study.

9.5.2 Effect of batteries specific energy on noise

All-Electric aircraft calculations made thus far assume that state-of-the-art battery technologies will be capable of reaching 1500 Wh/kg of specific energy by the target EIS year, i.e. 2035. This section examines the effect of batteries technological evolution on aircraft noise. Figure 9.19 plots the aircraft PWL at takeoff for different number of propulsors and batteries with specific energy ranging from 800 to 1800 Wh/kg. The minimum PWL value is located when $N = 10$ and $e = 1800$ Wh/kg; this agrees with the trend of Figure 9.18, where takeoff noise minimum occurs when $N = 10$.

The analogue figure for approach is not presented, because aircraft weight increases dramatically for specific energies below 1000 Wh/kg, making the conventional 3° approach operation practically impossible. Assessing the feasible approach operational profiles for such specific energy is irrelevant to the present study.

9.5.3 NPD curves

Estimation of the DEP aircraft PWLs enables the computation of the associated NPD curves and the construction of noise exposure contour maps through the proposed noise estimation framework. As pointed out in Section 5.7, the procedure for computing NPD curves additionally uses aircraft spectral properties, in order to account for atmospheric

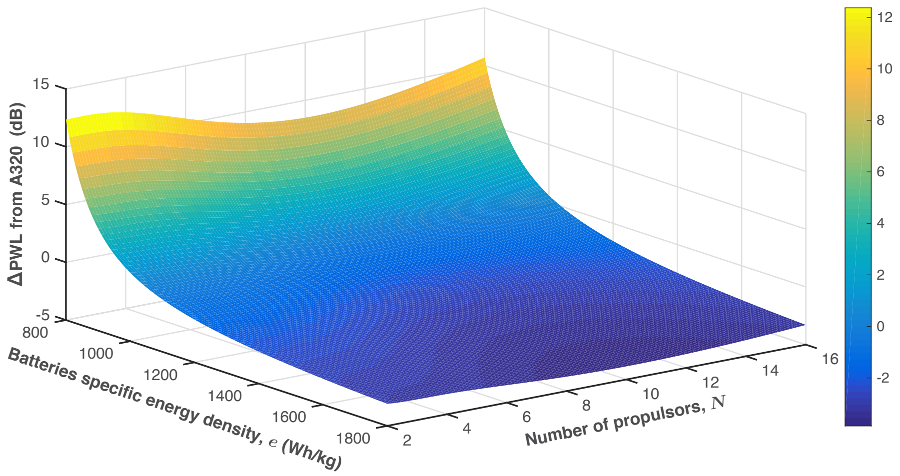

Figure 9.19: Aircraft PWL as a function of number of propulsors, N, and batteries specific energy, e. A minima is located at $N = 10$, $e = 1800$ Wh/kg.

absorption effects. Spectral properties are expected to vary among the examined DEP aircraft; for instance, the fan rotational speed, $N1$, increases with decreasing the fan diameter (and thus increasing the number of propulsors) shifting the blade-passing frequency towards higher frequencies. Thus, the tonal noise component may become more important (but at the same time more absorbable by the atmosphere). This spectral dependancy on fan diameter is approximated and incorporated in NPD calculations based on the spectral classes of existing aircraft that are available in the ANP Database [44]. More specifically, each e-A320 variant is assigned the spectral class of existing aircraft with resembling fan diameters, as summarised in Table 9.5. Clearly, a higher-fidelity model describing the propulsor's spectral variation with fan diameter would be advantageous.

Table 9.5: Turbofan engines of similar dimensions as the electric propulsors.

Propulsor fan diameter (m)	1.98	1.42	1.02	0.73	0.52
Turbofan of similar size	PW2037	CFM56	RR AE3007	GE CF700	PW625F

Figures 9.20 and 9.21 present takeoff and approach NPD curves for the e-A320 variations, as estimated using these spectral classes and the propulsors' geometry and performance data in Table 9.1. The TeDP and All-Electric e-A320s use different descent flap settings and are therefore assigned different approach NPD curves. In contrast they use the same takeoff NPDs. The thrust values in the NPD curves labels vary significantly between e-A320s of different number of propulsors because they express the thrust per propulsor and not that of the whole aircraft (whereas noise values refer to the whole aircraft).

Overall, takeoff and approach NPD curves are almost independent of number of propulsors. This was expected, based on the small differences (< 1 dB) observed in Figure 9.18. In addition, the spectral classes assigned to the propulsors based on their size produced negligible noise difference, even at large NPD distances.

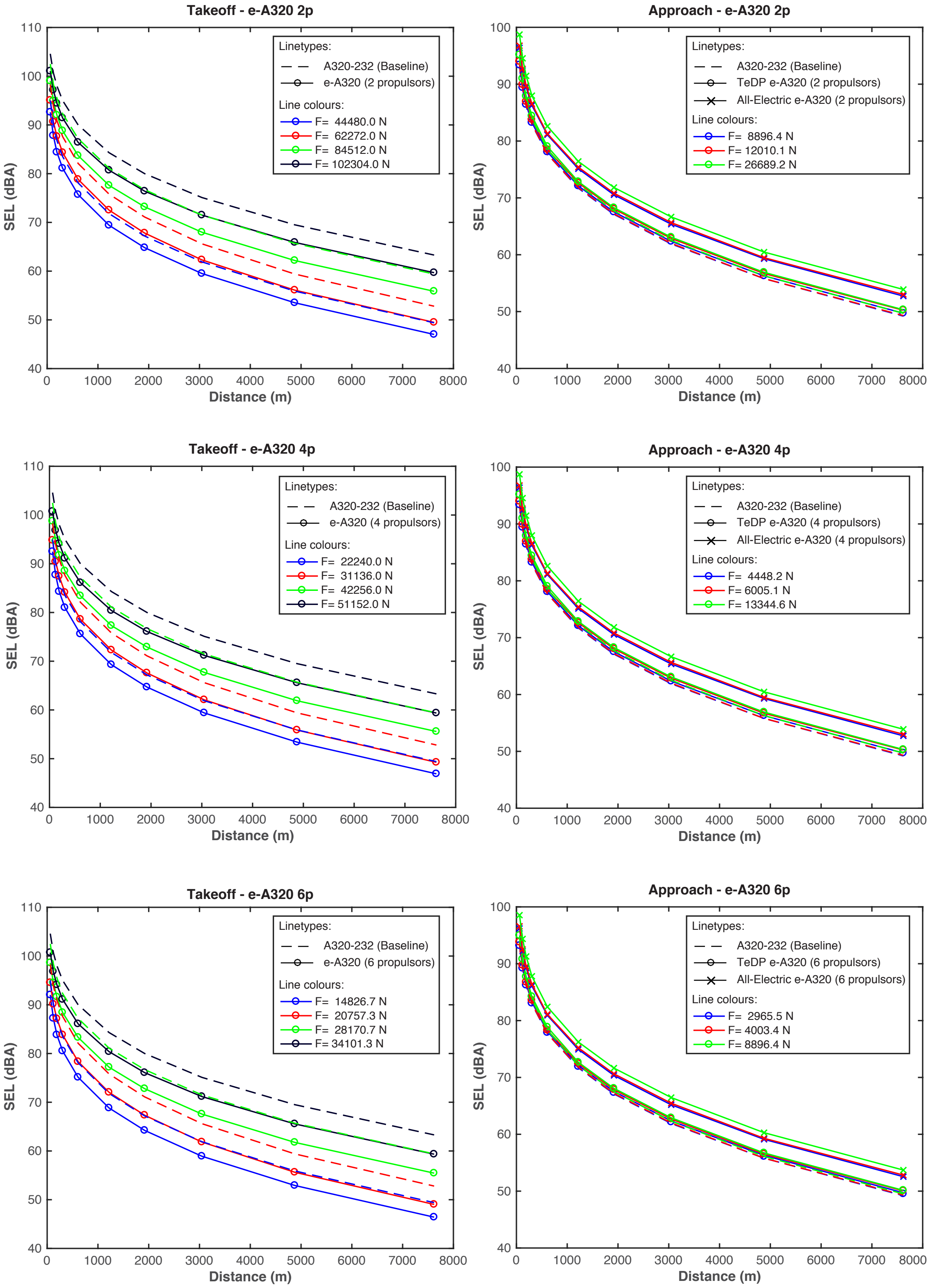

Figure 9.20: Estimated takeoff and approach NPD curves for the e-A320 with 2, 4 and 6 propulsors. Dashed lines represent the baseline aircraft NPD curves.

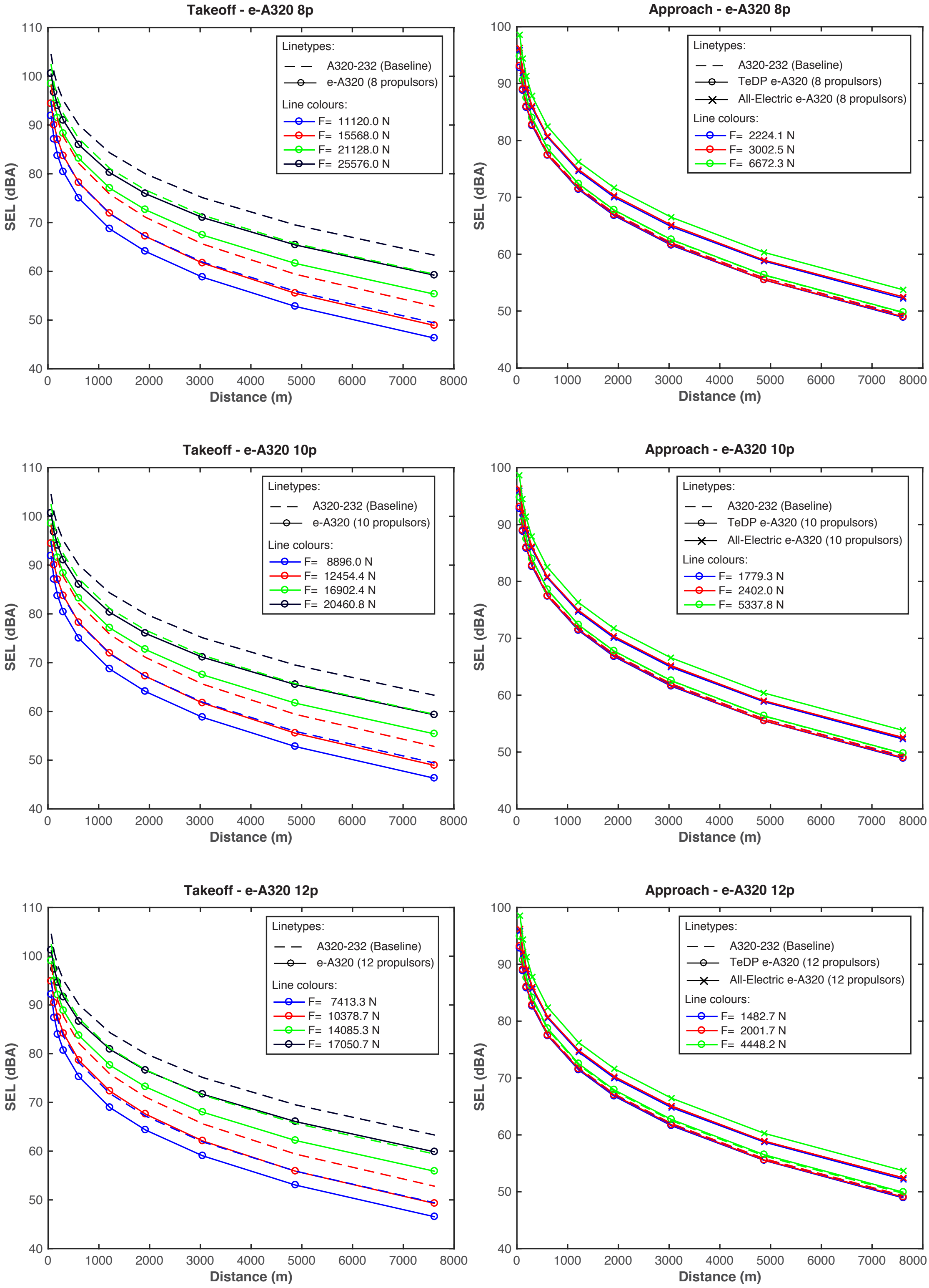

Figure 9.21: Estimated takeoff and approach NPD curves for the e-A320 with 8, 10 and 12 propulsors. Dashed lines represent the baseline aircraft NPD curves.

9.5.4 Noise exposure contour maps

Computationally derived NPD curves through the proposed framework enable assessing the potential benefit of novel aircraft in terms of noise exposure contour maps. Figure 9.22 demonstrates this capability by plotting the estimated 90 dB SEL noise contours for the 6 propulsors DEP aircraft at takeoff, as produced by introducing the respective computed NPDs into RANE airport noise model [115]. For comparison, the Figure includes the respective contours of the conventional A320, indicating that DEP aircraft are generally quieter than the A320 at takeoff. Moreover, the heavier (due to batteries weight) All-Electric variation is noisier than the TeDP one, since it needs more thrust for realising the default A320 takeoff trajectory, leading in increased propulsors' noise.

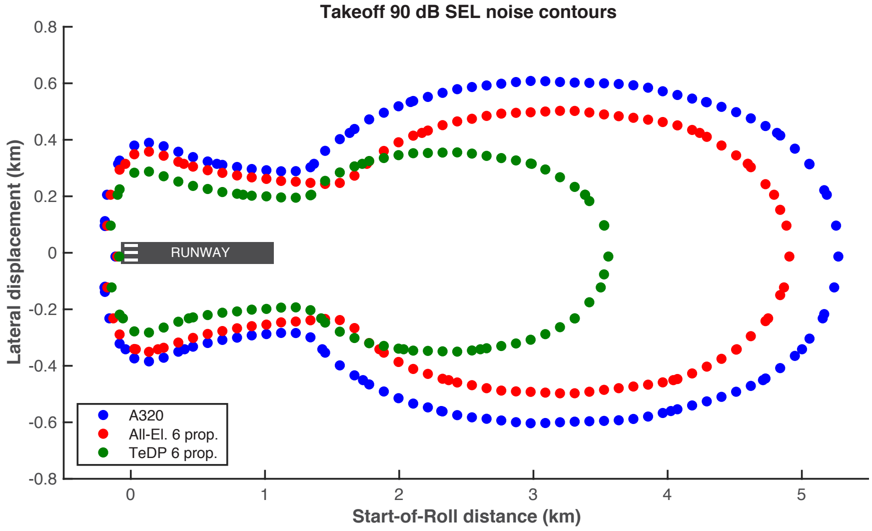

Figure 9.22: Comparison between the estimated 90 dB SEL contours for the 6 propulsors DEP aircraft and contours for the A320 obtained with INM [15].

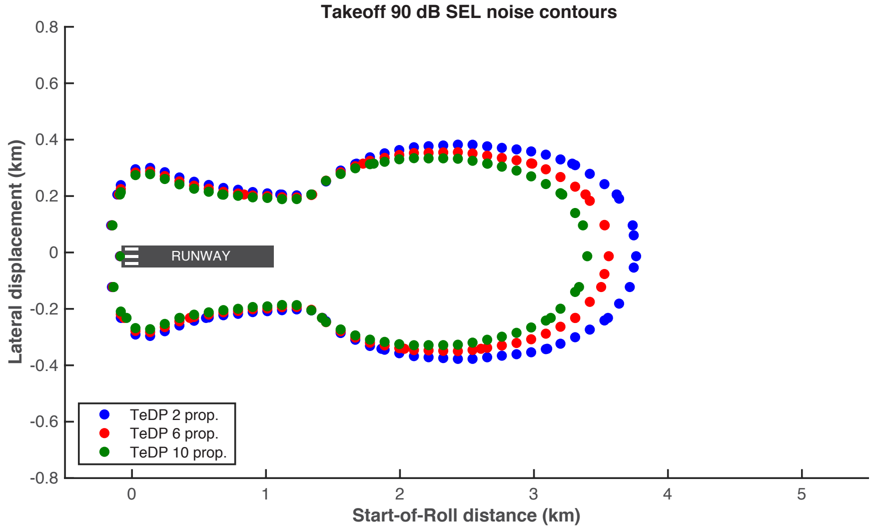

Figure 9.23: Estimated 90 dB SEL contours for the 2, 6 and 10 propulsors TeDP DEP aircraft.

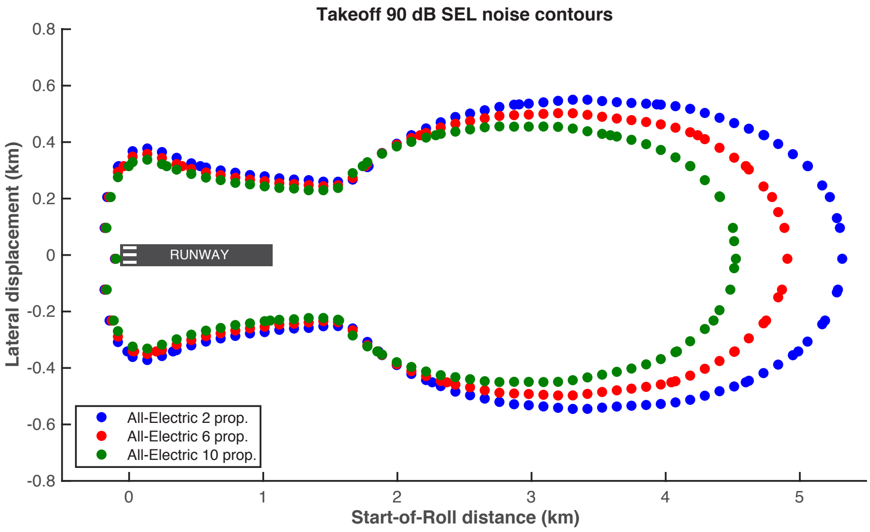

Figure 9.24: Estimated 90 dB SEL contours for the 2, 6 and 10 propulsors All-Electric DEP aircraft.

Figures 9.23 and 9.24 demonstrate the effect of number of propulsors on noise contour areas for the TeDP and All-Electric e-A320s respectively. It is seen that contour areas tend to shrink with increasing the DEP systems number of propulsors, as a result of the PWL variation with number of propulsors noticed in Figure 9.18.

Finally, it is reminded that estimated contours reflect the default approach/takeoff flight profiles. Clearly, further reductions of SEL contour areas can be achieved through operational improvements (e.g. steeper approach/takeoff slopes), propulsive efficiency improvements (e.g. BLI, advanced fans) and technological advances (e.g. quieter airframe, lighter batteries, Blended Wing Body (BWB) designs).

9.6 Blended Wing Body (BWB) aircraft

As a second application of the proposed framework on novel aircraft designs, this Section presents a case study involving impact prediction of a simplified Blended Wing Body (BWB) aircraft model. Being close to reach the efficiency and environmental performance limits of conventional tube and wing aircraft designs [230], the BWB concept is anticipated as one of the most promising novel configurations for achieving the ambitious future environmental goals [188]. Several aircraft concepts featuring DP that was discussed in the previous case study, adopt a BWB design (see Figure 9.2). BWB aircraft are conceived to have their engines/propulsors mounted on top of an airframe providing high lift capabilities (see Figure 9.25). Outstanding assets of the BWB concept are:

- Reduced noise at source due to: a) the shielding of a significant portion of engine noise [121], and b) the reduction of airframe noise due to the high-lift capability of the BWB that can eliminate conventional high-lift devices and enable low-airspeed approach and takeoff procedures (as mentioned in Section 2.1.7, airframe noise scales with the 5th power of airspeed [118]).

- Significantly reduced noise footprint due to: a) the above mentioned reduction of noise at source, and b) the BWB satisfies the NASA STOL concept requirements mentioned in Section 2.4.1, enabling steep climb and steep descent operations that increase the distance between aircraft path and communities. As an example of the potential BWB noise benefits, predictions in NASA by Thomas et al. [231, 232] for several advanced BWB configurations predict ground footprint reductions of up to 94.4% relative to the current technology B777-like.
- BWB aircraft are expected to offer fuel consumption and emissions benefits due to their higher aerodynamic efficiency [233]. Efficiency may be enhanced by advanced high-lift devices, such as Krueger flaps [234], but this will cancel the aforementioned airframe noise benefits resulting from eliminating high-lift devices.
- BWB aircraft offer the prospect of integrating novel and more efficient propulsion concepts, such as electric distributed propulsion systems [194].

9.6.1 Boundary Layer Ingestion (BLI)

In support of the BWB aircraft concept, it is beneficial to partly bury the DP fan array across the upper-rear fuselage area, as shown in Figure 9.25, rather than exposing it to the free stream flow. The result of this arrangement is that the propulsors ingest the upper fuselage boundary layer as their inflow. This idea is termed Boundary Layer Ingestion (BLI) and is also used in ships, torpedoes and missiles [235]. It is noteworthy that for the purpose of exploiting BLI, integrated nacelle configurations are also considered for non-DP tube-and-wing future designs, like the NASA D8 aircraft concept shown in Figure 9.26 [236].

Details of the physical concept and performance of BLI can be found in references [204, 11, 198, 235]. Prominent consequences of BLI are:

- Increased propulsive efficiency, η_p. This increase of η_p is explained in simple terms by looking at its definition in Equation 2.39; the denominator represents the sum of the jet exit velocity and the inlet velocity ($V_{in} + V_j$). In the non-ingestive case, $V_{in} = V_0$ yielding the standard form of propulsive efficiency, i.e. Equation 2.39. In the BLI case, the inlet velocity becomes smaller than the free stream velocity ($V_{in} < V_0$) due to viscous forces and hence η_p increases. Overall, the more the boundary layer ingested the more the propulsive efficiency increase, which means that large aircraft with wide DP fan arrays can profit more from BLI.

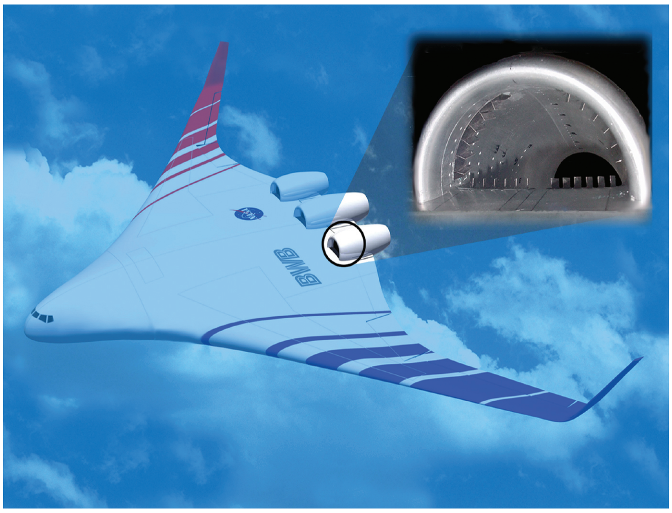

Figure 9.25: Visual representation of boundary-layer-ingesting (BLI) inlet on a BWB aircraft. Taken from [237].

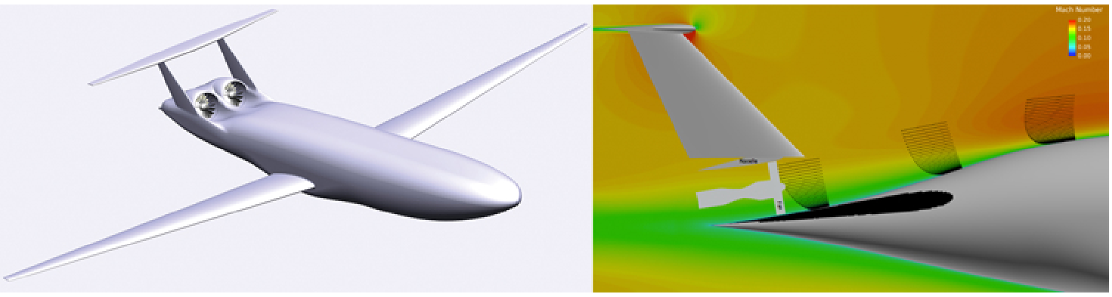

Figure 9.26: Illustration of BLI effects on the NASA D8 concept. Both photos taken from [236].

- Fuel burn reduction. Experiments showed that a fuel burn reduction from 3% to 5% can be achieved compared to a clean-inflow high BPR turbofan engine.
- BLI reduces thrust requirements at design point by about 7% [204].
- Reduced community noise levels due to low-airspeed operations.
- Several integration advantages, such as ram drag reduction.
- Fan performance losses due to the flow becoming non-uniform. According to reference [11], this negative consequence is likely to be overcome.

9.6.2 Noise sources on BWB aircraft

Proposed propulsion solutions for BWB aircraft are either conventional gas turbine engines (e.g. turbofans), or electric propulsors [101]. Therefore, the propulsive noise sources of the BWB aircraft are essentially the same as the ones examined in the previous case studies. Due to the engine noise shielding offered by the airframe, the airframe itself is a major BWB noise source. Hence, as explained by Guo [238], noise reduction technologies are projected for airframe noise sources. More specifically, landing gears are anticipated to be 5 dB quieter, whereas as already mentioned, high-lift devices may be either eliminated [121], which could result in airframe noise reductions of up to 12 dB [239] or replaced by advanced, more efficient and quieter ones; for instance, a 3-4 dB noise reduction is projected for the aforementioned Krueger flaps [238, 232].

Moreover, BWB aircraft like the one in Figure 9.25, that have their propulsors partially buried in the airframe for exploiting BLI benefits feature an additional noise source originating from the fan interaction with the non-uniform inlet flow [235]. This source is anticipated to be either narrowband or tonal, depending on the exact geometry and configuration. The resulting noise could be attenuated with liners, which would lead to further weight considerations. However, as suggested by Plas [235], this noise source is expected to be shielded by the BWB airframe and is therefore neglected in this study.

9.6.3 BWB noise impact estimation

The case study presented in this Section involves predicting the noise impact of a hypothetical BWB aircraft that has identical thrust requirements as the A320-232 and is therefore equipped with the turbofan engines of the A320-232. Hence, it is convenient to use the A320-232 as the baseline aircraft[5]. It is assumed that the airframe shields engine noise radiated at polar angles ranging from 45° to 135°. This range was chosen arbitrarily. Actual shielding range will be affected by diffraction effects but more importantly will be determined by the engine design and its position on the fuselage, as well as on the fuselage dimensions. Such design characteristics are likely to be publicly available, as are currently for the existing aircraft.

For incorporating the airframe shielding effects of BWBs in a simplified manner, the engine noise sources directivity factor within the shielding range is set to zero, resulting in the directivity factors shown in the left plot of Figure 9.27. Substituting these directivities in Equation 5.9 produces a similarly-shaped lumped aircraft directivity, illustrated in the right plot of Figure 9.27, for approach and takeoff. It is seen that the shielding effect is prominent at takeoff, when engine noise dominates. This is also implied by Equation 5.9 that shows that aircraft lumped directivity depends on each source sound level, $Lw_s(j)$, which in turn is a function of engine power setting. For the comparison to be clearer, Figure 9.27 only shows the lumped directivities at the standard A320-232 engine power settings for takeoff and approach that are calculated (as already performed in the earlier case studies) through the recommended SAE-AIR 1845 procedure [45].

Figure 9.28 compares estimated takeoff and approach SEL NPD curves for the hypothetical BWB aircraft with the respective NPDs for the baseline A320-232. As indicated

---

[5] The hypothetical BWB aircraft may feature DEP systems, like the ones defined in the previous case study. In that case, baseline aircraft can either be the conventional A320-232 or the respective e-A320.

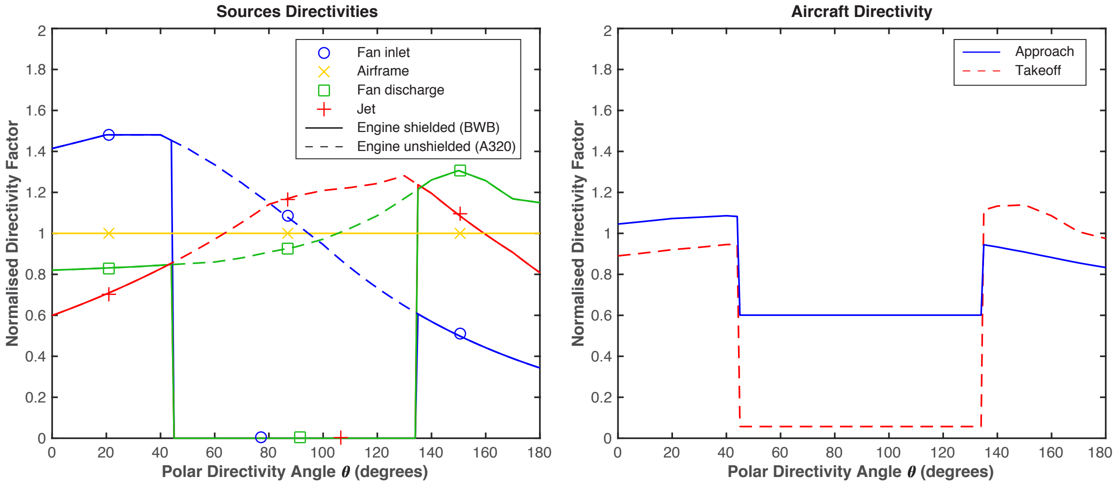

Figure 9.27: Left: Source directivities for the BWB. Right: Lumped aircraft directivity at takeoff and approach, at the default engine power settings.

earlier, these two aircraft have identical engines and thrust requirements and thus, the noise exposure reduction is due to the engine noise shielding. As expected, shielding offers a substantial noise reduction of 6 to 7 dB at takeoff where engine noise dominates. This result is very close to the 6 EPNdB reduction predicted in [171]. At approach where airframe noise dominates, engine noise shielding is unimportant in terms of the whole aircraft noise. In contrast, significant benefits are gained by reducing airframe noise; the dotted lines in the approach plot of Figure 9.28 represent NPDs for the hypothetical BWB including a 4 dB airframe noise reduction due to the aforementioned projected noise reduction technologies for airframe components. Potential airframe noise influence due to the fuselage shape difference between the BWB and the baseline A320 is assumed to be included (or outweighed by) these noise reduction technologies.

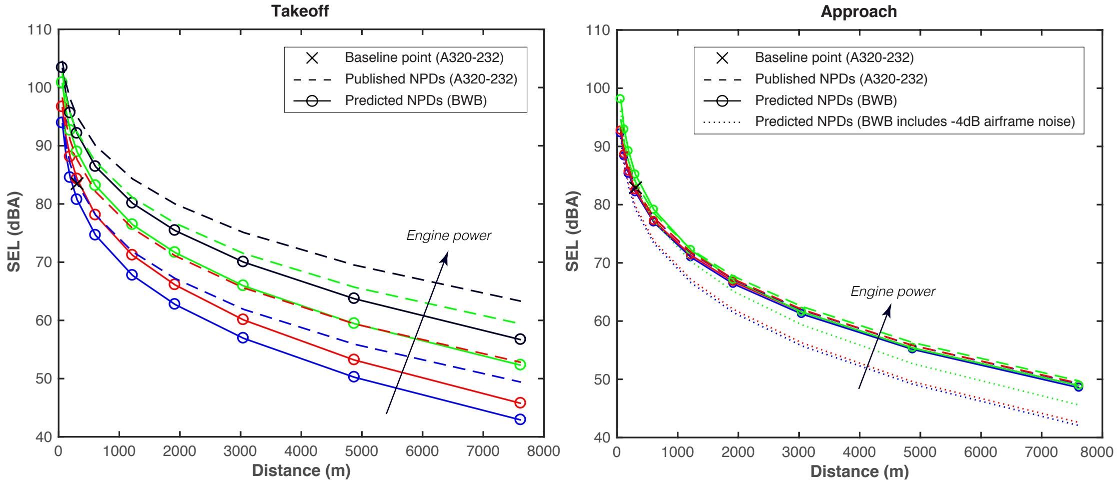

Figure 9.28: Generated NPD curves for a BWB aircraft at takeoff (left), and approach. The A320-232 NPD curves are shown with dashed lines for comparison. Dotted lines represent NPDs for a BWB aircraft configured with projected 4 dB airframe noise reduction technologies.

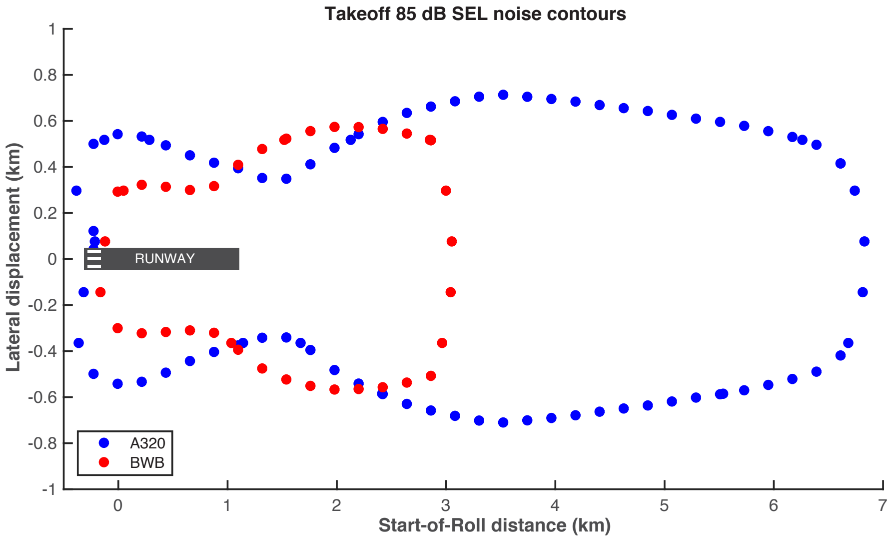

Figure 9.29: Comparison between the 85 dB SEL noise contours for the A320-232 obtained with INM [15] and those estimated with the proposed framework for the BWB aircraft reflecting the default A320-232 takeoff trajectory.

Figure 9.29 illustrates the estimated noise exposure contour maps for the BWB aircraft at takeoff. The noise footprint area reduction with respect to the baseline A320-232 is around 65% that is almost identical to predictions from Thomas and Guo [240], who found a 65.7% reduction in ground noise contour of a BWB as compared to a 2025 technology tube-and-wing aircraft with engines installed under the wing. It is important to note that these noise contours reflect the default takeoff trajectory for the A320-232.

Overall, estimated noise reductions at source in combination with performance enhancements (e.g. by exploiting BLI) and the low-airspeed and steep operations achievable by BWB aircraft are expected to offer the earlier-mentioned dramatic reductions of around 85% predicted by NASA [231, 232].

Chapter 10

Conclusions and future work

10.1 Summary

This thesis presented a new framework for estimating the community noise variation around airports arising from potential mitigation strategies aiming at delivering the challenging noise and emissions reduction goals for aviation set by several organisations worldwide. The framework combines noise prediction methods for individual sources, with aircraft noise and performance data to estimate noise variation with respect to a baseline scenario, where noise levels are known. Being independent of aircraft noise measurements, confidential inputs and specific mathematical models, the framework can be used to appraise the impacts of different technology options, novel aircraft designs and contemporary operations and hence support effective planning and decision making on airport noise abatement. An important feature of the framework is that it enables purely computational construction of NPD curves and hence provides the option of assessing community noise benefits of different strategies through noise exposure contour maps around airports. Also, to facilitate a more holistic environmental assessment of action planning and account for the interdependencies among various environmental concerns, the framework can integrate with emissions prediction models and other airport tools, such as RANE [115]. Furthermore, the fact that noise variation is estimated (rather than absolute noise values) significantly reduces complexity, which in combination with other simplifications (e.g. modelling the aircraft as a lumped noise source) results in low computational requirements; results are therefore promptly obtained (e.g. generating NPD data for a given scenario is a matter of few seconds).

To demonstrate the framework's validity, computed NPD curves for existing aircraft were compared to those found in literature. This process showed an excellent agreement, obtaining a maximum rms error of about 2 dB, which is within the tolerance suggested in ECAC Doc 29 [32] and in similar noise prediction studies in references [241, 242].

The validation process was followed by an error analysis that revealed, discussed and quantified the potential sources of error and limitations of the proposed framework.

The capabilities of the proposed framework were demonstrated by:

- Assessing the community noise impact of technological changes on existing aircraft and of future BWB aircraft.
- Estimating the noise trends of novel Turboelectric (TeDP) and Universally-Electric aircraft concepts that use Distributed Electric Propulsion (DEP) and conducting a parametric study seeking the optimal number of electric propulsors in DEP systems.
- Computing NPD curves for the cases above and constructing noise contour maps through integration with RANE airport noise model [115].
- Estimating the environmentally-optimal (i.e. in terms of noise and emissions) takeoff and approach angles of innovative steep operations for various civil aircraft models.
- Linking the impact of noise and pollutant emissions through a commonly influencing parameter (thrust) in order to describe the associated trade-offs and provide suitable outputs to emission assessment tools.

10.2 Conclusions

Estimations performed with the proposed framework for scenarios involving novel designs, new noise reduction technologies and unconventional operations conform with published data and/or more sophisticated predictions and/or historical trends (e.g. see Figures 8.21, 9.29). Clearly, forecasting the consequences of future scenarios while bypassing the need of measurements and/or confidential data and providing emissions-related outputs are substantial advantages of the framework. Even in the absence of a definite baseline scenario, the framework showed promising capabilities in capturing the correct trends (e.g. in the BWB aircraft example). It is therefore concluded that the proposed framework has great potential in contributing towards designing effective mitigation schemes, under a wider Strategic Environmental Assessment (SEA) process.

As discussed in Section 7.3.5, although the framework is independent of specific noise prediction methods for individual sources, its accuracy does depend on the level of adaptation of such methods to new technologies and/or the development of new ones. The fact that methods are continuously being developed (e.g. higher-fidelity methods introduced by Boeing [174, 173], incorporated in ANOPP2 [120]) is a prominent sign for the relevance and usefulness of the proposed framework. Also, it can be presumed that potential new methods for individual sources will formulate source noise level as a function of stream velocities, just like the existing methods employed in this thesis (e.g. see jet noise expression in Equation 5.18). The thermodynamic cycle analysis performed to estimate these stream velocities showed insignificant error, mainly because the proposed framework uses velocity changes rather than absolute values. Hence, improving the process of obtaining stream velocities is not crucial.

10.3 Future Work

In the case studies of this thesis thrust was used as the linking parameter between noise and emissions, whereas the trade-off between them was depicted in a normalised form (e.g. see Figure 8.19). As mentioned in Section 8.3, normalisation may not be the optimum way of expressing these trade-offs. In this context, it would be very interesting to explore new ways of expressing interdependencies between environmental concerns. Possibly, a unit similar in nature to BPR could be defined, that could describe the propulsion and/or efficiency effects of new configurations (e.g. due to DEP arrangements, BLI, lift capability of BWB, etc.) whilst being indicative of their noise characteristics (e.g. BPR has a major effect on propulsive efficiency [18] but is also an indicator of noise).

Noise levels, $\mathrm{L}w_{0,s}$, of individual noise sources for the baseline aircraft were estimated with the proposed framework using the fitting process described in Section 5.6. This avoids using exact levels that are normally proprietary to manufacturers. Although the estimated baseline levels proved accurate enough for realising the case studies presented in this thesis, the fitting process is associated with uncertainty. Hence, a future task could be the improvement of the fitting process or the development of new techniques for acquiring individual sources baseline levels. Another future study could involve the calculation of these levels from dedicated engineering models, such as Soprano [124] (as mentioned in Section 3.2.1, this requires inputting confidential data). Likewise, the fact that baseline directivity and spectra data were averages provided by NASA did not impede the feasibility of conducting trustworthy noise estimations for future scenarios with the proposed framework. However, progressively creating a database consisting of accurate, aircraft specific directivity and spectra data could enhance estimations' accuracy and determine the relative importance of these data on estimations that in turn could lead to further simplifications.

Finally, a prominent future task of the research presented in this thesis is advancing the method of computationally constructing NPD curves through the proposed framework. This also involves reducing uncertainty associated with NPD curves discussed in Section 7.3. Refurnishing the standard SAE AIR1845 procedure, reducing dependance on fly-over measurements (that as mentioned throughout this thesis are associated with many uncertainties) and even introducing a new aircraft noise metric may not only improve the accuracy of estimated noise exposure contour maps, but also upgrade noise contours to a more meaningful and realistic metric of exposure to airport noise.

Appendix A

Framework analytic flowchart

The next page includes an analytic flowchart of the proposed framework when using the configuration specified in Section 5.5.1. Elements are numbered, wherever possible, as on the flowchart presented in Figure 5.2.

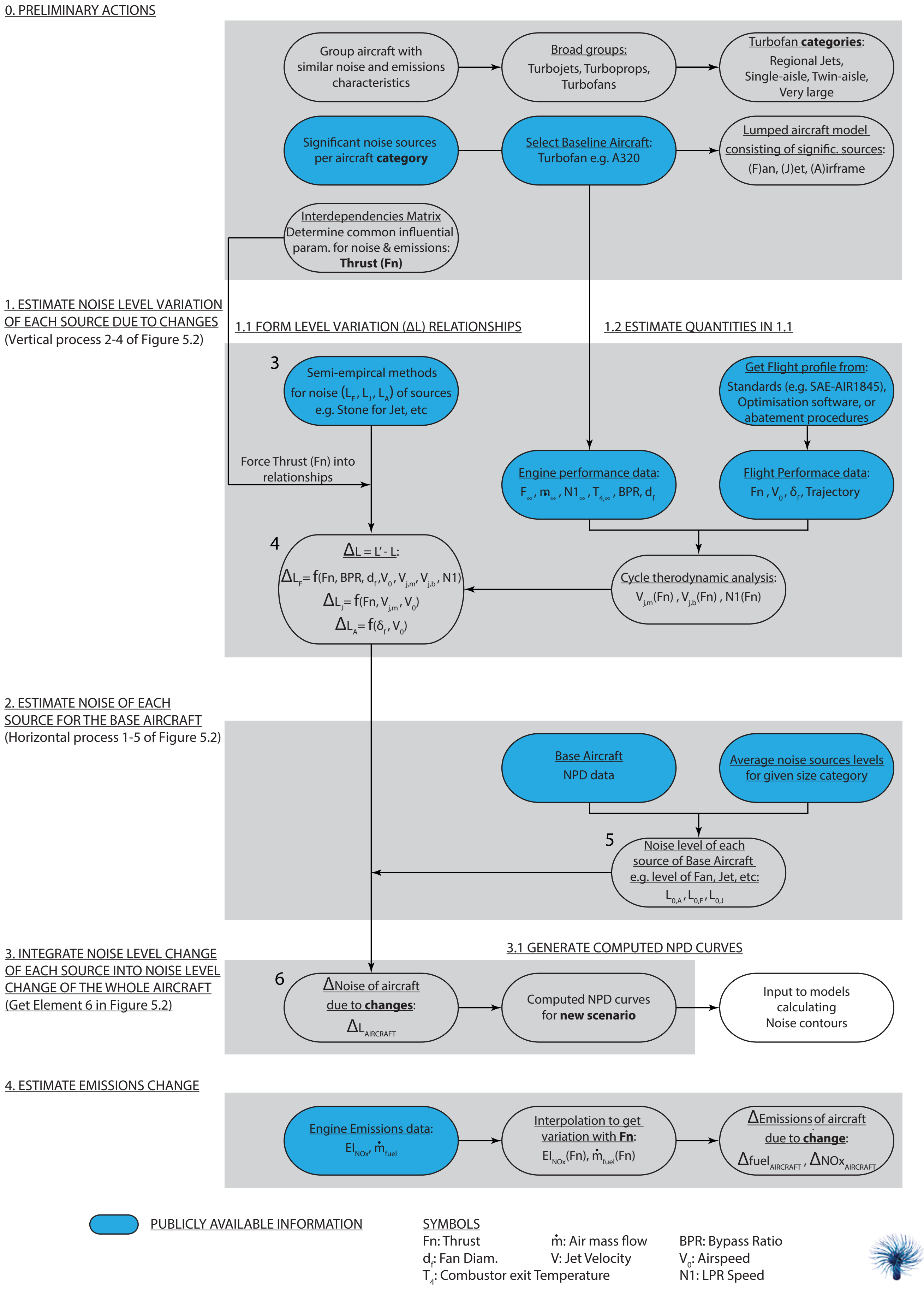
0. PRELIMINARY ACTIONS
Group aircraft with similar noise and emissions characteristics
Broad groups: Turbojets, Turboprops, Turbofans
Turbofan **categories**: Regional Jets, Single-aisle, Twin-aisle, Very large
Significant noise sources per aircraft **category**
Select Baseline Aircraft: Turbofan e.g. A320
Lumped aircraft model consisting of signific. sources: (F)an, (J)et, (A)irframe
Interdependencies Matrix Determine common influential param. for noise & emissions: **Thrust (Fn)**
1. ESTIMATE NOISE LEVEL VARIATION OF EACH SOURCE DUE TO CHANGES (Vertical process 2-4 of Figure 5.2)
1.1 FORM LEVEL VARIATION (ΔL) RELATIONSHIPS
1.2 ESTIMATE QUANTITIES IN 1.1
3
Semi-empircal methods for noise (L_F, L_J, L_A) of sources e.g. Stone for Jet, etc
Get Flight profile from: Standards (e.g. SAE-AIR1845), Optimisation software, or abatement procedures
Force Thrust (Fn) into relationships
Engine performance data: F_∞, $\dot{m}_\infty$, $N1_\infty$, $T_{4,\infty}$, BPR, d_f
Flight Performance data: Fn, V_0, δ_f, Trajectory
4
$\Delta L = L' - L$:
$\Delta L_F = f(Fn, BPR, d_f, V_0, V_{j,m}, V_{j,b}, N1)$
$\Delta L_J = f(Fn, V_{j,m}, V_0)$
$\Delta L_A = f(\delta_f, V_0)$
Cycle therodynamic analysis: $V_{j,m}(Fn)$, $V_{j,b}(Fn)$, $N1(Fn)$
2. ESTIMATE NOISE OF EACH SOURCE FOR THE BASE AIRCRAFT (Horizontal process 1-5 of Figure 5.2)
Base Aircraft NPD data
Average noise sources levels for given size category
5
Noise level of each source of Base Aircraft e.g. level of Fan, Jet, etc: $L_{0,A}$, $L_{0,F}$, $L_{0,J}$
3. INTEGRATE NOISE LEVEL CHANGE OF EACH SOURCE INTO NOISE LEVEL CHANGE OF THE WHOLE AIRCRAFT (Get Element 6 in Figure 5.2)
3.1 GENERATE COMPUTED NPD CURVES
6
ΔNoise of aircraft due to **changes**: $\Delta L_{AIRCRAFT}$
Computed NPD curves for **new scenario**
Input to models calculating Noise contours
4. ESTIMATE EMISSIONS CHANGE
Engine Emissions data: EI_{NOx}, $\dot{m}_{fuel}$
Interpolation to get variation with **Fn**: $EI_{NOx}(Fn)$, $\dot{m}_{fuel}(Fn)$
ΔEmissions of aircraft due to **change**: $\Delta fuel_{AIRCRAFT}$, $\Delta NOx_{AIRCRAFT}$
PUBLICLY AVAILABLE INFORMATION
SYMBOLS
Fn: Thrust
$\dot{m}$: Air mass flow
BPR: Bypass Ratio
d_f: Fan Diam.
V: Jet Velocity
V_0: Airspeed
T_4: Combustor exit Temperature
N1: LPR Speed

Appendix B

Derivation of ΔSEL

This Appendix derives Equation 5.11. Sound exposure level is defined as:

$$\mathrm{SEL} = 10\log\left(\int_0^T 10^{\frac{\mathrm{SPL}}{10}}\,\mathrm{d}t\right) = 10\log\left(\int_0^T \frac{WDC}{R^2}\,\mathrm{d}t\right), \tag{B.1}$$

where W and D are the aircraft total acoustic power and directivity respectively, whereas assuming the lumped model, R is the source-to-observer distance, while C is the constant defined in Section 2.1.1. If acoustic power of sources x and y respectively change to $W_x + \Delta W_x$ and $W_y + \Delta W_y$ then SEL becomes:

$$\begin{aligned}
\mathrm{SEL}' &= 10\log\left[\int_0^T \frac{(WD + \Delta W_x D_x + \Delta W_y D_y)C}{R^2}\,\mathrm{d}t\right] \\
&= 10\log\left(\int_0^T \frac{WDC}{R^2}\,\mathrm{d}t + \int_0^T \frac{\Delta W_x D_x C + \Delta W_y D_y C}{R^2}\,\mathrm{d}t\right) \\
&= 10\log\left[\int_0^T \frac{WDC}{R^2}\,\mathrm{d}t\left(1 + \frac{\displaystyle\int_0^T \sum_{j=1}^{m} \frac{\Delta W_j D_j C}{R^2}\,\mathrm{d}t}{\displaystyle\int_0^T \frac{WDC}{R^2}\,\mathrm{d}t}\right)\right] \\
&= 10\log\left(\int_0^T \frac{WDC}{R^2}\,\mathrm{d}t\right) + 10\log\left(1 + \frac{\displaystyle\int_0^T \sum_{j=1}^{m} \frac{\Delta W_j D_j C}{R^2}\,\mathrm{d}t}{\displaystyle\int_0^T \frac{WDC}{R^2}\,\mathrm{d}t}\right)
\end{aligned}$$

$$= \mathrm{SEL} + 10\log\left(1 + \frac{\displaystyle\int_0^T \sum_{j=1}^{m} \frac{\Delta W_j D_j C}{R^2}\,\mathrm{d}t}{\displaystyle\int_0^T \frac{WDC}{R^2}\,\mathrm{d}t}\right).$$

Noting that $10^{SEL/10} = \displaystyle\int_0^T \frac{WDC}{R^2}\,\mathrm{d}t$ and with i and m being the time increments and number of noise sources respectively, the change of SEL can be expressed as:

$$\Delta\mathrm{SEL} = 10\log\left[1 + \frac{C\Delta t \displaystyle\sum_{i=1}^{T}\sum_{j=1}^{m}\left[\frac{1}{R_i^2}(\Delta W_j D_{j,i})\right]}{10^{SEL/10}}\right]. \tag{B.2}$$

Appendix C

SAE AIR 1845 procedure for developing NPD curves

The main steps of the SAE AIR 1845 [45] experimental procedure for developing NPD curves are:

- Atmospheric conditions for each sound recording are established experimentally.
- The terrain around the microphones is flat and unobstructed.
- The test flight path is parallel to the ground (SAE AIR 1845 describes it as 'nominally level') at a nominal height ranging from 100 m to 800 m.
- Noise measurements are made directly under the flight path so are unaffected by lateral attenuation.
- The aircraft configuration remains constant throughout each flyover duration.
- Flyover effective duration is normally determined by the 10 dB down-time (i.e. the period during which the noise level is within 10 dB of the maximum level).
- The noise is recorded at 0.5 seconds intervals. SPLs are obtained for the 24 1/3-octave-bands with centre frequencies from 50 to 10000Hz.
- Measured SPLs are corrected for instrument calibration and adjusted to account for differences between actual and reference atmospheric conditions.
- A flyover at the nominal height is repeated for each engine power setting.

The noise at the remaining NPD standard distances is then evaluated using extrapolation, accounting for effects of spherical wave spreading, atmospheric absorption as well as for differences on the effective duration.

C.1 NPD data usage

It is apparent that NPD databases derive from flyovers under a standardised experimental environment. Hence, to practically use them, it is necessary to have them adapted into the circumstances and operating conditions of the actual aircraft event of interest. This involves adjustments due to the below-outlined factors:

- The fact that NPD data express information of aircraft along flight paths that are infinitely long and parallel to the ground
- The influence of lateral attenuation when the observer is not directly below the aircraft ground track
- The influence of aircraft speed when this is different from 160 knots
- The influence of a curved flight path.

With L_{AE} being the corrected SEL, SAE-AIR 1845 [45] expresses this correction procedure with the following Equation:

$$L_{AE} = L_{AE}(P, d) + \Delta V - \Lambda(\beta, l) + \Delta\phi + \Delta L\,, \tag{C.1}$$

where $L_{AE}(P, d)$ is the SEL for engine power P and distance d at 160 knots as obtained from NPDs, ΔV is the speed adjustment, whereas Λ and $\Delta\phi$ are the corrections for lateral attenuation and curved flight paths. ΔL refers to a correction that is only applicable for locations behind the start of takeoff roll.

To generate noise contours at the vicinity of airports or the noise level or exposure at an observer location from NPD relationships, the engine power must be evaluated using:

- Aircraft and engine types
- Operating mode (takeoff, landing, flyover); this includes a) flight profiles and aircraft direction along them, and b) aircraft configuration

If noise level at intermediate powers and distances is sought, data interpolation is required between NPD data. While intermediate powers are derived by linear interpolation, logarithmic interpolation is required for determining intermediate distances. This is illustrated in Figure C.1, where intermediate engine power P and distance d are respectively bounded by NPD curves with power P_1, P_2 and NPD distances d_1, d_2. INM Technical Manual [15] gives the following equation for the interpolated (or extrapolated) noise level at these intermediate values P, d:

$$L_{P,d} = L_{P1,d} + \frac{(L_{P2,d} - L_{P1,d})(P - P_1)}{P_2 - P_1}\,, \tag{C.2}$$

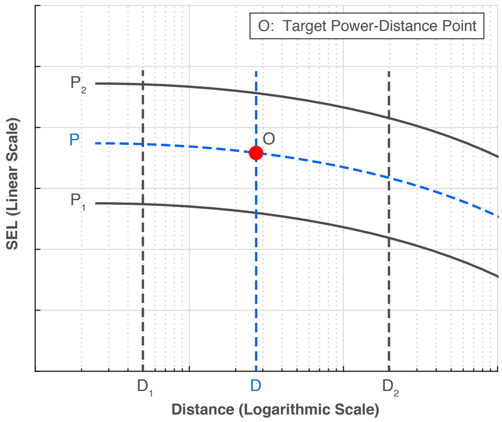

Figure C.1: Schematic representation of NPD data interpolation/extrapolation

where the noise level $L_{P1,d}$ that correspond to distance d and engine powers P_1 is calculated with Equation C.3. Noise level $L_{P2,d}$ is similarly evaluated.

$$L_{P1,d} = L_{P1,d1} + \frac{(L_{P1,d2} - L_{P1,d1})(\log(d) - \log(d_1))}{\log(d_2) - \log(d_1)} \,. \tag{C.3}$$

C.1.1 Comparison between NPD curves and curves accounting for spherical spreading

It is interesting to visualise the difference between NPD curves and some simple curves deriving from only accounting for spherical spreading. The red curve of Figure C.2 represents the L$_{A,max}$ NPD curve for a Boeing 747400 at takeoff, at the lowest thrust setting. Starting from a fixed point on that curve, such as the one corresponding to the distance of 50 m, another curve is drawed, that represents spherical spreading, i.e. derives from Equation 2.6. The deviation between these two curves that increases with distance is addressed to atmospheric effects.

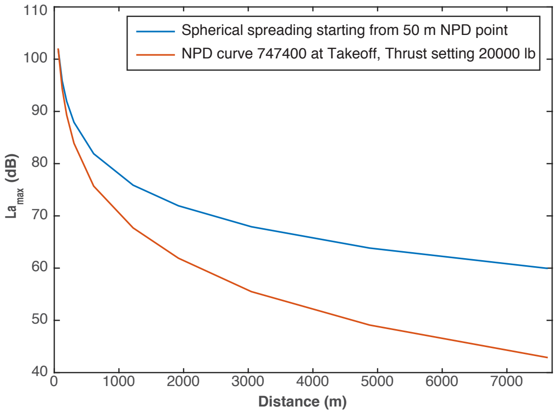

Figure C.2: Comparison between the takeoff L$_{A,max}$ NPD curve for a Boeing 747400 and a curve only accounting for spherical spreading.

Appendix D

Derivation of turbofan velocity ratios

This Appendix contains derivation of turbofan velocity ratios based on reference [163].

D.1 Ideal turbofan

D.1.1 Bypass stream

Considering that $M_0 = \frac{V_0}{c_0}$ and $c_0 = \sqrt{\gamma R T_0}$, then with respect to the numbering system of Figure 6.3 the velocity ratio across the bypass stream is:

$$\frac{V_{19}}{V_0} = \frac{M_{19}}{M_0}\sqrt{\frac{T_{t19}}{T_0}}\,. \tag{D.1}$$

Hence the Mach number and temperature ratios are sought. The procedure to obtain the former starts by writing the stagnation pressure at the bypass exhaust nozzle exit as a function of the variation of stagnation pressure through the engine:

$$P_{t19} = P_0 \frac{P_{t0}}{P_0}\frac{P_{t2}}{P_{t0}}\frac{P_{t13}}{P_{t2}}\frac{P_{t19}}{P_{t13}} = P_0 \pi_r \pi_d \pi_f \pi_{nf}\,. \tag{D.2}$$

Furthermore, by definition:

$$P_{t19} = P_{19}\left(1 + \frac{\gamma - 1}{2}M_{19}^2\right)^{\frac{\gamma}{\gamma-1}}\,. \tag{D.3}$$

Assuming negligible losses in the diffuser and the fan nozzle then $\pi_d = \pi_{nf} = 1$. Also, if the fan behaves isentropically then:

$$\tau_r \tau_f = 1 + \frac{\gamma - 1}{2} M_{19}^2 \,. \tag{D.4}$$

Dividing by the definition of $\tau_r = 1 + \frac{\gamma - 1}{2} M_0^2$ yields:

$$\left(\frac{M_{19}}{M_0} \right)^2 = \frac{\tau_r \tau_f - 1}{\tau_r - 1} \,. \tag{D.5}$$

The temperature ratio is obtained in a similar manner through the stagnation temperature variation through the engine. Noting that $\tau_d = \tau_{nf} = 1$, then:

$$T_{t19} = T_0 \tau_r \tau_f = T_{19} \left(1 + \frac{\gamma - 1}{2} M_{19}^2 \right) \,. \tag{D.6}$$

Comparison with Equation D.5 yields $T_{19} = T_0$, which in fact confirms the assumption of the ideal cycle. Thus, the velocity ratio of the ideal bypass stream is given by:

$$\left(\frac{V_{19}}{V_0} \right)^2 = \frac{\tau_r \tau_f - 1}{\tau_r - 1} \,. \tag{D.7}$$

D.1.2 Core stream

The velocity ratio of the core stream is, again, a function of the Mach number and temperature ratios:

$$\frac{V_9}{V_0} = \frac{M_9}{M_0} \sqrt{\frac{T_{t9}}{T_0}} \,. \tag{D.8}$$

$$P_{t9} = P_0 \frac{P_{t0}}{P_0} \frac{P_{t2}}{P_{t0}} \frac{P_{t3}}{P_{t2}} \frac{P_{t4}}{P_{t3}} \frac{P_{t5}}{P_{t4}} \frac{P_{t9}}{P_{t5}} = P_0 \pi_r \pi_d \pi_c \pi_b \pi_t \pi_n \,. \tag{D.9}$$

The ideal conditions impose isentropic processes and that $\pi_d = \pi_n = 1$, whereas it is assumed that stagnation pressure losses in the burner are negligible, so that $\pi_d = 1$. Additionally, including the definition of stagnation pressure in the above Equation gives:

$$P_{t9} = P_0 \pi_r \pi_c \pi_t = P_9 \left(1 + \frac{\gamma - 1}{2} M_9^2 \right)^{\frac{\gamma}{\gamma - 1}} \,. \tag{D.10}$$

Since the nozzle is assumed to be fully expanded, $P_9 = P_0$; whereas ideally, the compressor and turbine behave isentropically and therefore:

$$\pi_c = \tau_c^{\frac{\gamma}{\gamma-1}} \tag{D.11}$$

$$\pi_t = \tau_t^{\frac{\gamma}{\gamma-1}} \tag{D.12}$$

Substituting these values into Equation D.10 and considering that $\pi_r = \tau_r^{\frac{\gamma}{\gamma-1}}$ leads to the exit Mach number at the core, and in turn, to the Mach number ratio:

$$M_9^2 = \frac{2}{\gamma - 1}(\tau_r \tau_c \tau_t - 1) \tag{D.13}$$

$$\frac{M_9^2}{M_0^2} = \frac{\tau_r \tau_c \tau_t - 1}{\tau_r - 1} \tag{D.14}$$

Working with the temperature ratios as previously ultimately gives:

$$\frac{T_e}{T_0} = \frac{\tau_\lambda}{\tau_r \tau_c} \, . \tag{D.15}$$

Therefore, the velocity ratio across the core is:

$$\left(\frac{V_9}{V_0}\right)^2 = \left(\frac{\tau_r \tau_c \tau_t - 1}{\tau_r - 1}\right) \frac{\tau_\lambda}{\tau_r \tau_c} \, . \tag{D.16}$$

D.2 Non-ideal turbofan

The non-ideal turbofan engine can be described using the polytropic efficiencies of the fan, compressor and turbine, whereas ratios π_d, π_b, π_n and π_{nf} can take values smaller than one. As described in [163], the polytropic relations are:

The velocity ratio for the non-ideal bypass stream is:

$$\left(\frac{V_{19}}{V_0}\right)^2 = \frac{1}{\tau_r - 1}\left[\tau_r \tau_f - \frac{\tau_f^{1-e_f}}{(\pi_d \pi_f)^{\frac{\gamma-1}{\gamma}}}\right] . \tag{D.17}$$

The velocity ratio for the non-ideal core stream is:

$$\left(\frac{V_9}{V_0}\right)^2 = \frac{1}{\tau_r - 1}\left[\tau_\lambda \tau_t - \frac{\tau_\lambda \tau_c^{1-e_c} \tau_t^{1-\frac{1}{e_t}}}{\tau_r \tau_c (\pi_d \pi_b \pi_n)^{\frac{\gamma-1}{\gamma}}}\right] . \tag{D.18}$$

Appendix E

Directivity factor normalisation

Directivity data in NASA ANOPP [16, 134] are provided in the form of directivity indices (DIs) expressed in dB. DI is essentially the logarithmic version of the directivity factor D and therefore the latter is obtained with [22]:

$$D(\theta, \phi) = 10^{DI(\theta,\phi)/10} \,. \tag{E.1}$$

Additionally, $D(\theta, \phi)$ must be normalised to ensure that the acoustic power emitted by the noise sources remains unaffected. This condition is satisfied if integration over a spherical surface S surrounding the source returns the power of that source. Hence, if the surface area is segmented into sub-elements of area dS:

$$\int_0^{4\pi} \frac{W D_S}{4\pi} \, \mathrm{d}S = W \,, \tag{E.2}$$

which means that the sum over all surface sub-elements directivity factor should return unity. If the polar angle varies from 0°to 180°and the azimuthal from 0°to 90°:

$$\sum_{\theta=0}^{180} \sum_{\phi=0}^{90} D(\theta, \phi) = 1 \,. \tag{E.3}$$

Hence, considering angle steps of 1°, directivity factor $D(\theta, \phi)$ is normalised with

$$n = \frac{1}{91 * 181} = \frac{1}{16471} \tag{E.4}$$

Appendix F

Simplified estimates

F.1 Simplification based on Taylor series approximation

Noting that the denominator of the fraction in the bracket of Equation 5.3 expresses the sound power emitted by the whole aircraft it can be assumed that this is comparably very larger than the source change. In which case, the Taylor series approximation $\ln(1+x) \approx x$, for $x << 1$ is applicable[1]. Thus, considering that $\ln(x) = \ln(10)\log(x)$, the PWL change can be estimated as:

$$\Delta \mathrm{L}w,_{Est} \approx \frac{10}{\ln 10} \frac{\sum_{s=1}^{n} \Delta W_s}{\sum_{s=1}^{n} W_s} . \tag{F.1}$$

Using Equation 5.4, the SPL change at a receiver location can be estimated with:

$$\Delta \mathrm{L}p,_{Est} \approx \frac{10^{(1-\mathrm{SPL}/10)}}{\ln(10)} \frac{\Delta W_s D_s}{R^2} , \tag{F.2}$$

where SPL denotes the baseline SPL that can be measured e.g. with a sound level meter. Equation F.2 significantly reduces complexity since the estimated SPL change at the receiver point, under the new conditions, is only dependant on the power change of noise source s. As it is seen in examples of Section F.2, although this simplification leads to calculation time reductions, validity of $\ln(1+x) \approx x$, for $x << 1$ and hence the Equation's applicability is bounded within changes of non-dominant sources or of very small changes of the dominant ones.

---

[1] $\lim\limits_{x\to\infty} \log(1+x) \approx x$

By integrating Equation F.2 over time leads to an expression for the estimated change in $\mathrm{L}_{eq,T}$:

$$\Delta L_{eq,Est} \approx \frac{10}{\ln(10)T}\int_0^T \frac{10^{(-\mathrm{L}_{\mathrm{eq,T}}/10)}\Delta W_s D_s}{R^2}\,\mathrm{d}t\,. \tag{F.3}$$

Equation F.1 implies that quantity $\Delta\mathrm{SPL}_{Est}$ can be assumed constant throughout a flyover with fixed aircraft configuration. This is mostly valid for small directivity variations. In that case, Equation 5.10 can be written as:

$$\begin{aligned}\mathrm{SEL}' &= 10\log\left[\sum_{i=1}^{n} 10^{\frac{SPL_i}{10}}\,10^{\frac{\Delta SPL_i}{10}}\,\Delta t\right]\\ &= \mathrm{SEL} + 10\log\left(10^{\frac{\Delta SPL_{Est}}{10}}\right)\,.\end{aligned} \tag{F.4}$$

F.1.1 Considerations for further simplifications

- Since flyover noise is mainly examined at a relatively low altitude and in the absence of winds, constant atmospheric conditions can be assumed.
- Reflections in the ground can be omitted and a flat ground can be assumed.

F.2 Accuracy of estimated SPL

The following section investigates the validity of Equation F.1 that gives an estimated SPL after exploiting the Taylor series approximation $\ln(1+x) \approx x$, for $x << 1$. Using the notation of Equations 5.8 and F.1, the error e in dB arising from the above approximation is defined as:

$$e = |\Delta\mathrm{L}p - \Delta\mathrm{L}p,_{Est}|\,. \tag{F.5}$$

Figure F.1 illustrates the approximation error when applied to acoustic power variations of individual noise sources, along with the power level of individual sources of two similar aircraft A and B. Both aircraft are assumed to be in the landing configuration, with the fan inlet broadband noise dominating. Yet, while in aircraft B the level difference between fan inlet and airframe is small, the dominance of the fan inlet in aircraft A is definite.

Clearly, due to the logarithmic nature of the decibel scale, a level increase of the definite dominant source is associated with a noise power change which is comparable to that of the whole aircraft and therefore the Taylor series approximation becomes non-applicable. More specifically, the terms $\sum_{s=1}^{n}\Delta W_s$ and $\sum_{s=1}^{n} W_s$ become comparable and thus the fraction of Equation F.1 is not much smaller than unity. Thus a significant error is obtained, as illustrated by the blue curve in Figure F.1.

In contrast, larger level changes are tolerated in the dominant source of aircraft B, because two sources dominate, which makes the term $\sum_{s=1}^{n} \Delta W_s$ large compared to $\sum_{s=1}^{n} \Delta W_s$. Whereas error is negligible when changing non-dominant sources, such as the jet, which is represented by the green line of Figure F.1.

Another example that exposes this behaviour is given next. Considering the ten aircraft of Table F.1 and the associated individual source contributions at landing. Basically, what varies in these contributions is the level difference between the jet, which dominates in the first six aircraft, and the fan discharge, which is the dominant source in the last

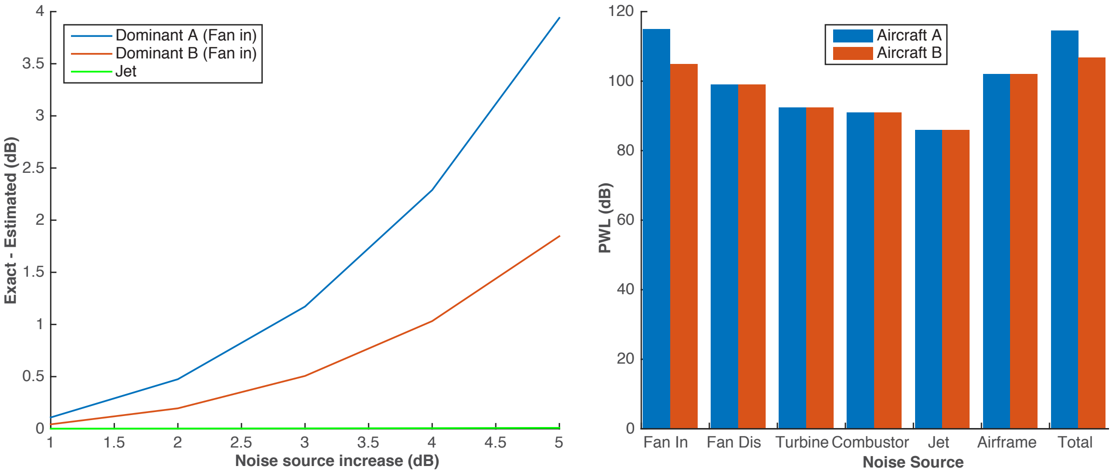

Figure F.1: Mixed velocity (left) and fan pressure ratio variation with BPR.

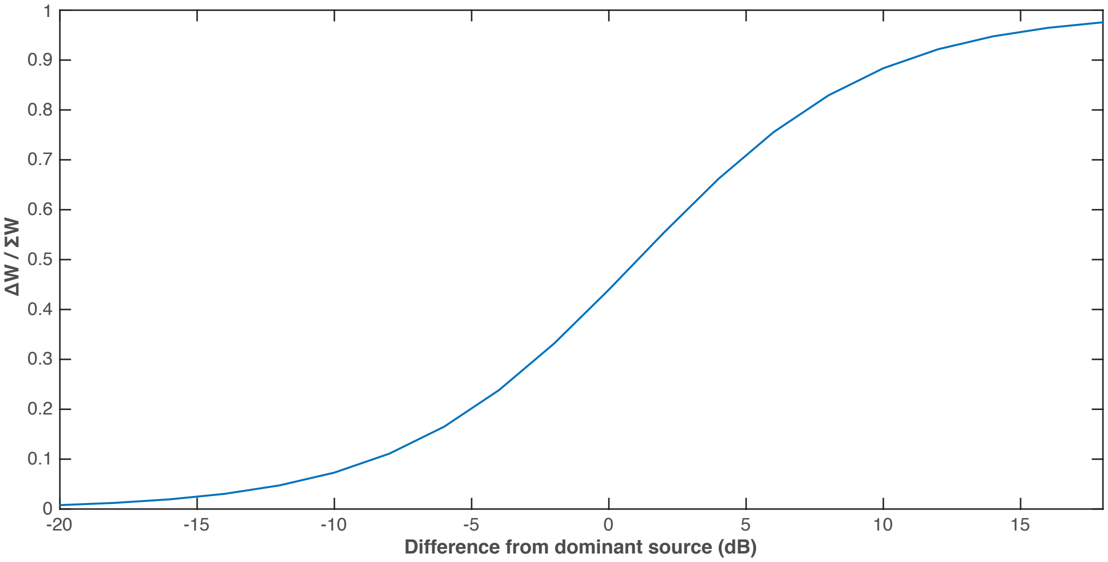

Figure F.2: Value of $\Delta Lw,_{Est}$ depending on relative strength of a source whose level is increased by 3 dB.

Table F.1: Noise source contributions of ten hypothetical different aircraft types at landing.

Aircraft ID	Fan Inlet	Fan Dis.	Turbine	Combust.	Jet	Airframe
1	92	79	70	86	99	80
2	92	83	70	86	99	80
3	92	87	70	86	99	80
4	92	91	70	86	99	80
5	92	95	70	86	99	80
6	92	99	70	86	99	80
7	92	103	70	86	99	80
8	92	107	70	86	99	80
9	92	111	70	86	99	80
10	92	115	70	86	99	80

few aircraft. Figure F.2 plots the value of $\Delta \mathrm{L}w,_{Est}$ versus this level difference when the fan discharge level is increased by 3 dB. This plot illustrates how Equation F.1 becomes obsolete as the fan discharge dominance becomes stronger.

Thus, it is concluded that this simplification method is mostly applicable when:

- Level changes involve non-dominant sources.
- Level changes on dominant sources are small.

Appendix G

Aircraft Directivity Illustrations

Below are shown directivity predictions by Zaporozhets et al. [26], showing the directivity dependance not only on design factors but also on aircraft operational parameters. For example, the top graphs show that jet polar directivity pattern, which generally peaks around the middle of the backward quadrant, is influenced by both jet velocity and flight speed.

Aircraft engine noise sources are directional; their directivity patterns are influenced not only by manufacturing factors, such as the BPR, but also by the aircraft operational parameters, as indicate the attached in Appendix G predictions by Zaporozhets et al. [26]. For example, Figure G.1 shows that jet polar directivity pattern, which generally peaks around the middle of the backward quadrant, is influenced by both jet velocity and flight speed. Likewise, fan noise polar-emission angle, which has a strong forward and a weaker but noteworthy backward radiation, is a function of the aircraft operational engine mode.

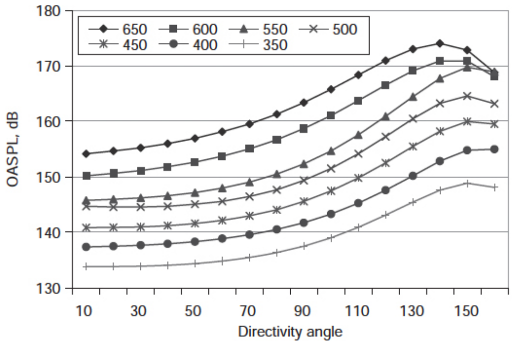

Jet noise directivity pattern for different jet velocities (BPR=1)

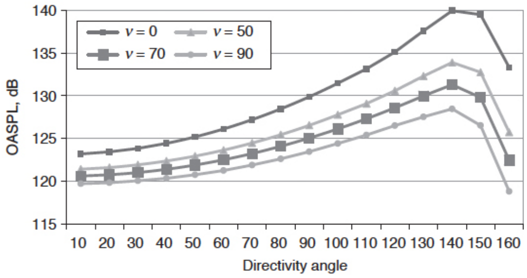

Jet noise directivity pattern for different flight speeds (BPR = 6)

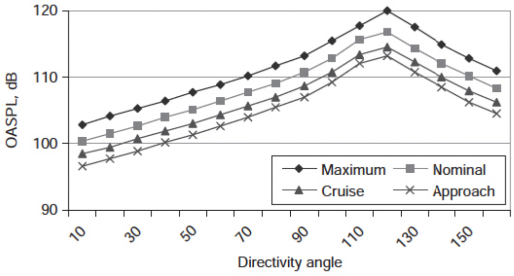

Turbine noise directivity patterns for different engine modes (BPR = 6)

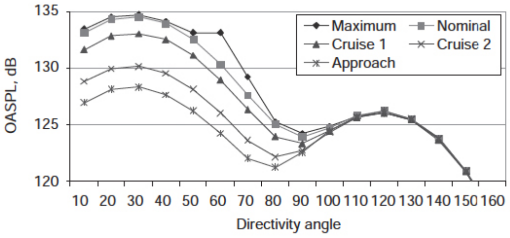

Fan noise directivity patterns for five operational engine modes (BPR = 6)

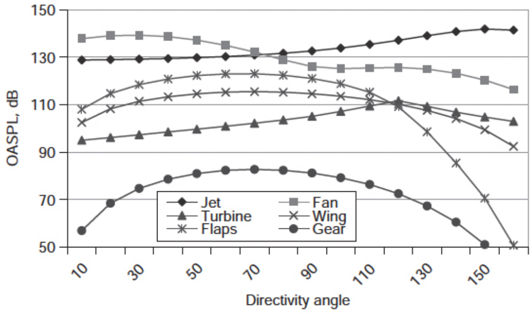

Predicted directivity patterns for the main airframe noise sources on a Tupolev 154M aircraft (BPR = 2.5, u = 70m/s)

Figure G.1: Predicted directivity patterns for aircraft noise sources [26].

Appendix H

Example applications of FANjET

To demonstrate the functionality of the own-developed, simplified noise prediction tool, FANjET, this Appendix contains selected simplified examples carried out throughout the duration of this research. These examples are not linked with the case studies presented in this thesis.

H.1 Single event

The first simulation assesses the sound level received by an observer due to a single aircraft flyover. The aircraft descends from 500 m to 200 m, at a fixed lateral distance of 1500 m from the observer. For simplicity's sake, sources included in this example are the jet, the fan and the landing gears, as well as two coherent[1] fan tones of 1 kHz. Fan and jet directivities are obtained from ANOPP [16], whereas landing gears are regarded as omnidirectional sources. Source powers in Watts are estimated through conversion of typical SPL plots (at unit distance) found on reference [26], (NPD data in ANP Database [44] could have been used instead). Accounting that the aircraft is during the approach procedure, sound powers are set at 13 kW for each engine broadband source, 15 kW for each landing gear and 5 kW for the fan tones. The instantaneous SPL was within 10 dB of L$_{A,max}$ for a period $T = 37$ s; time increment is therefore set at $\Delta t = 0.5$ s

The polar angle (θ) is initialised at 10°, which is - in most cases - an exaggerated value, since SPL values ranging within 10 dB from the L$_{max}$ are expected to occur while the aircraft is relatively near to the observer. Thus, azimuthal angle (ϕ), distance R_{yz}, longitudinal distance x_0 and aircraft - observer distance R can be initialised, as described in Section 6.1.1. Then, as explained in the same Section, distance $x(t)$ is calculated for every time increment Δt, which leads to evaluating the variation with time of angle theta

---

[1] As discussed in Section 2.1.2, aircraft noise sources are generally incoherent. Coherent tones are only included for the sake of completeness in these examples.

($\theta(t)$) and in turn, of distance $R(t)$. SPL calculation is then straightforward, through Equation 2.4.

For the distributed system, each source distance from the aircraft center of gravity (CG) is roughly set as listed in Table H.1. Individual source - observer distances are then calculated as shown in Section 2.13.

Table H.1: Noise sources distances from aircraft CG.

Source	Distance from CG (m)
Jet	-2
Fan	1
Front Gear	10
Rear Gears	-5

Figure H.1 shows the SPL at the observer, as well as the individual contributions from each broadband and tonal noise sources, obtained through the distributed modelling approach. Maximum level encountered is L$_{max}$ = 89.5 dB, while L$_{eq,T}$ and SEL are calculated through Equation 2.14, giving 83 dB and 98 dB respectively.

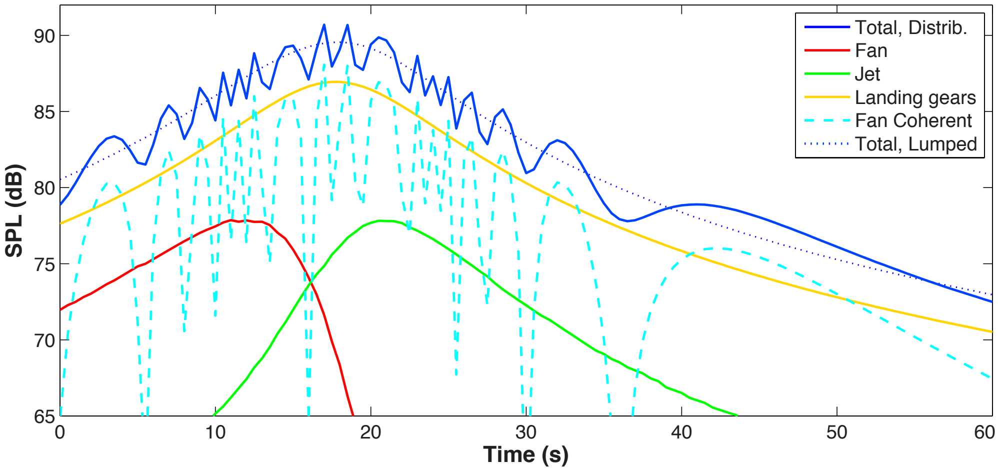

Figure H.1: SPL time history at observer point and contributions from individual noise sources, for a single aircraft descent event.

H.2 Fleets - flight track dispersion example

One possible solution on reducing noise impact on some targeted residential areas may be trajectory optimisation. Figure H.2, illustrates 7 flight tracks and 22 fixed observer positions and describes an hypothetical situation, where the optimum flight track dispersion in terms of noise abatement is sought.

This example examines the distribution of $N = 140$ events occurring within 8 hours, over the different flight tracks. The five dispersion cases examined are displayed in Table H.2;

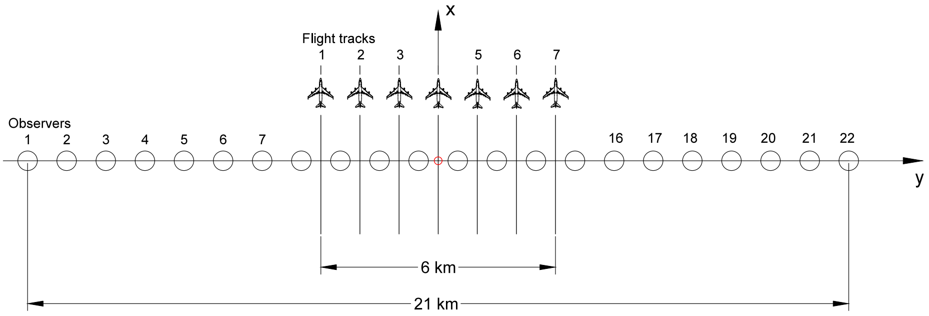

Figure H.2: Illustration of possible pairs of flight tracks and observer points.

cases labelled 'C1' and 'C5' use only one trajectory, the far left and central respectively, whereas the remaining cases examine several distributions over all available flight tracks.

Following the procedure employed for a single event, $\mathrm{L}_{eq,T}$ and SEL values are calculated for each observer-flight track pair. The $\mathrm{L}_{eq,T}$ corresponding to each flight track dispersion and observer location is evaluated with Equation (2.15); for example, considering case 'C1', the equation for observer 1 (O1) becomes:

$$\mathrm{L}_{eqC1,O1} = 10 \log \left[\frac{1}{T} \left(C_{11} 10^{\frac{\mathrm{SEL}_{O1,C11}}{10}} + C_{12} 10^{\frac{\mathrm{SEL}_{O1,C12}}{10}} + ... + C_{17} 10^{\frac{\mathrm{SEL}_{O1,C17}}{10}} \right) \right], \tag{H.1}$$

where $C_{11} - C_{17}$ correspond to the number of flyovers on each of the seven flight tracks. Resulting equivalent levels are shown in the graph of Figure H.3.

Table H.2: Flight track dispersions of N=140 flyovers.

	Flight Track ID							
Case ID	1	2	3	4	5	6	7	SUM
C1	140	0	0	0	0	0	0	140
C2	0	0	0	140	0	0	0	140
C3	20	20	20	20	20	20	20	140
C4	30	20	15	10	15	20	30	140
C5	5	15	25	50	25	15	5	140

Figure H.3 suggests that for the scenario examined, flight track dispersion rearrangements can lead to SEL changes of up to 8 dB. Furthermore, flyovers distribution over all flight tracks is in turn translated into SEL and annoyance distribution, whereas maximum level encountered is reduced. Likewise, a possible alternative -among numerous- could be to arrange dispersion depending on the population density of each location, so that dense locations are associated with SEL minima.

In general, while trajectory optimisation, and in broader terms, the operation of the aircraft, is a competent option for aircraft noise abatement, its effectiveness depends on the criteria and metrics considered. For instance, a commercial zone with offices may be concerned only for a certain day period, whereas another zone may be mostly sensitive on the maximum perceived noise level.

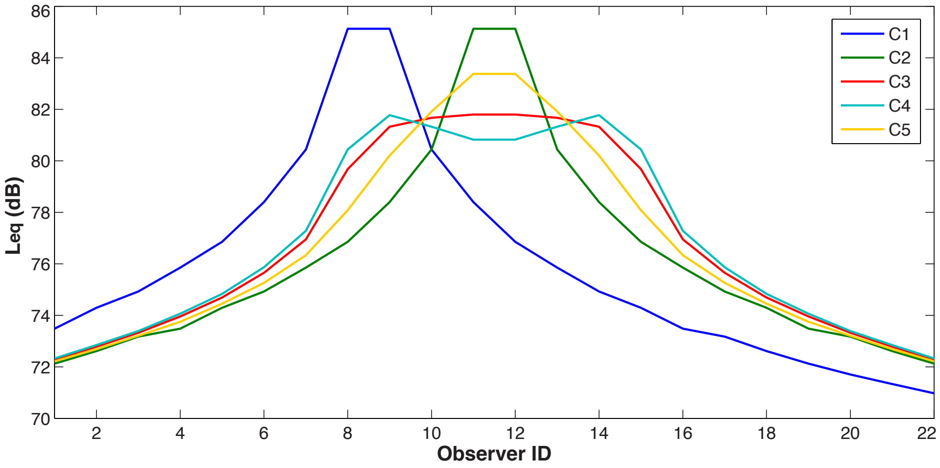

Figure H.3: Results of flight track dispersions at each observer point.

Furthermore, as noise level on the ground is always higher during departure and approach (with the latter dominating between the two), it should be mentioned that several noise trajectory optimisation schemes exist that attempt to limit noise levels during these procedures. Such schemes are generally adaptable to each particular airport requirements and aircraft type.

Lastly, it is worth mentioning that some noise optimised trajectories may be inefficient in terms of other environmental concerns, such as cost and local air quality. For example, an optimum noise trajectory may involve increased flight time, as a result of bypassing a populated residential area; this in turn translates into increased fuel consumption, cost and emissions.

H.3 Steeper approach (Simplified example)

Figure H.4 shows the SPL time histories for both the conventional approach angle of 3° and the steeper one. It can be seen that due to the increase of vertical distance from the observer, which in this case is around 80 m, $L_{A,max}$ is significantly reduced whereas $L_{eq,T}$ and SEL have been found to be reduced by 4 dB and 1.5 dB respectively. This simplified example assumes the same duration for the two events.

Figure H.5 shows noise contour for both events, when the aircraft flies over the approach certification point, which as described in Section 2.1.6, is located on the runway axis, 2 km from the runway threshold. Height difference of 105 m significantly narrows the high-level (yellow) contour. As already mentioned, this trend will result in reducing the overall approach noise foot-print.

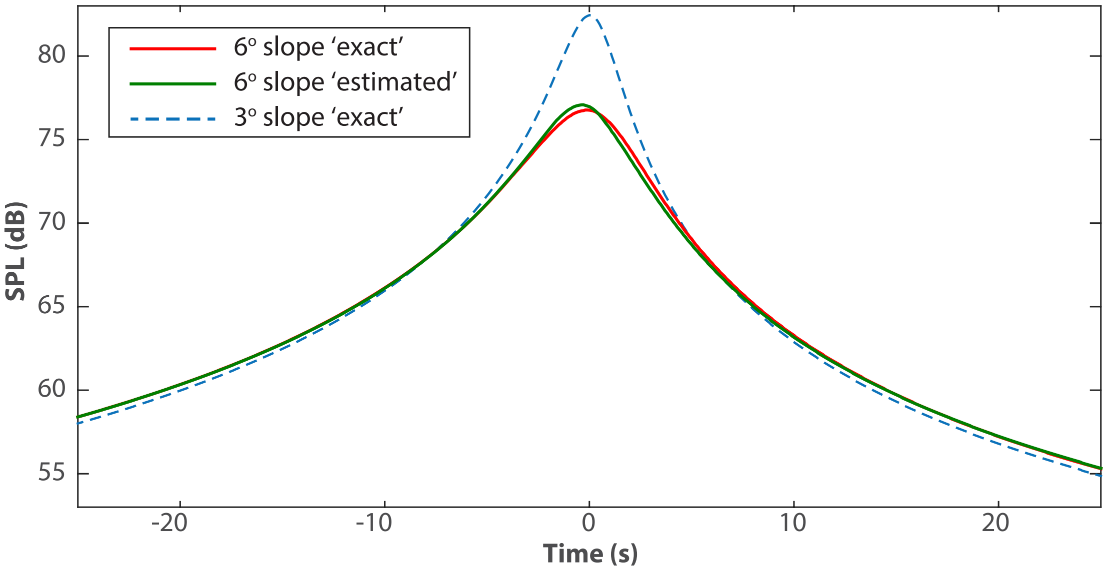

Figure H.4: SPL at observer point for approach angles of 3° and 6°. The estimated SPL is also plotted for the 6° approach.

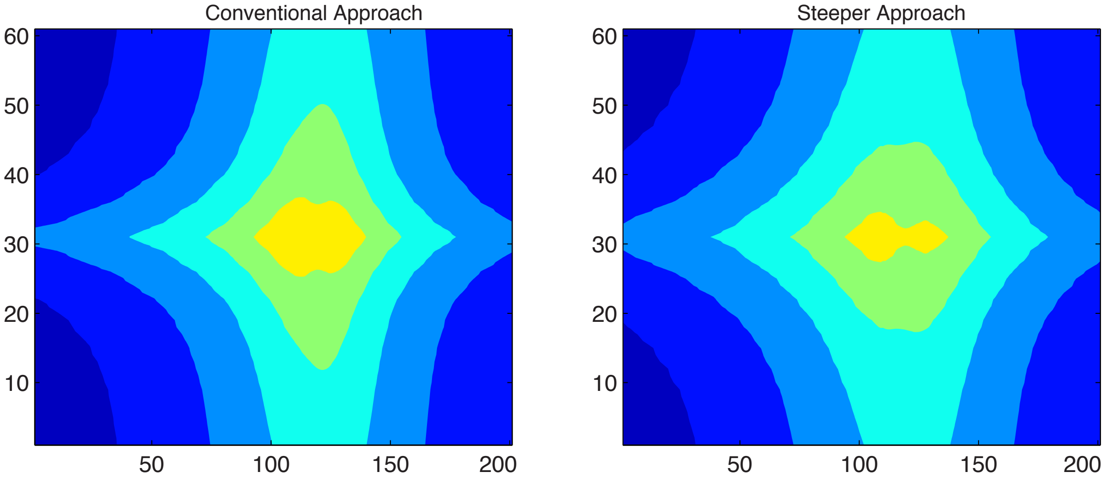

Figure H.5: Noise contours at approach certification point, for different heights.

H.3.1 Simplified estimate of SPL

The green line in Figure H.4 represents the estimated SPL time history for the steeper approach angle of 6°, which was evaluated using Equation F.2. It is seen that it almost matches the calculated, 'exact' one; yet, the important outcome is that computation time was decreased by 10% without generating any noticeable error. The accuracy of this estimation is discussed in Appendix F.

References

[1] Airbus, “Global market forecast 2016-2035,” 2016. [Online]. Available: http://www.airbus.com/company/market/global-market-forecast-2016-2035

[2] Boeing, “Current market outlook 2016-2035,” 2016. [Online]. Available: http://www.boeing.com/resources/boeingdotcom/commercial/about-our-market/assets/downloads/cmo_print_2016_final_updated.pdf

[3] European Environment Agency (EEA)– European Aviation Safety Agency (EASA) – Eurocontrol, “European aviation environmental report 2016,” 2016. [Online]. Available: http://ec.europa.eu/transport/sites/transport/files/modes/air/aviation-strategy/documents/european-aviation-environmental-report-2016-72dpi.pdf

[4] International Civil Aviation Organization (ICAO), “Global air transport outlook to 2030 and trends to 2040,” Tech. Rep. Circular 333, 2016.

[5] “UK aviation forecasts,” 2013. [Online]. Available: https://www.gov.uk/government/publications/uk-aviation-forecasts-2013

[6] M. Hepperle, “Electric flight-potential and limitations,” in *NPU-DLR Workshop, Braunschweig*, 2014.

[7] “Global climate change. Vital signs of the planet.” 2015. [Online]. Available: http://climate.nasa.gov

[8] European Commission (EC), “Flightpath 2050 Europe’s vision for aviation,” Report of the High-Level Group on Aviation Research, Luxembourg, Tech. Rep., 2011.

[9] Advisory Council for Aviation Research and Innovation in Europe (ACARE), “Strategic research and innovation agenda (SRIA),” Brussels, Tech. Rep., 2012.

[10] “European aeronautics: a vision for 2020,” Advisory Council for Aeronautics Research in Europe (ACARE), Tech. Rep., 2001.

[11] S. W. Ashcraft, A. S. Padron, K. A. Pascioni, J. Stout, Gary W., and D. L. Huff, "Review of propulsion technologies for N+3 subsonic vehicle concepts," NASA Glenn Research Center, Cleveland, OH, United States, Tech. Rep. NASA/TM-2011-217239, 2011.

[12] "Clean sky," 2017. [Online]. Available: http://www.cleansky.eu

[13] European Commission (EC), "Clean sky 2: developing new generations of greener aircraft," 2014. [Online]. Available: https://ec.europa.eu/research/press/jti/factsheet_cs2-web.pdf

[14] Royal Aeronautical Society, "Greener by design," 2017. [Online]. Available: https://www.aerosociety.com/get-involved/specialist-groups/air-transport/greener-by-design/

[15] E. R. Boeker, E. Dinges, B. He, G. Fleming, C. J. Roof, P. J. Gerbi, A. S. Rapoza, and J. Hemann, "Integrated Noise Model (INM) version 7.0 technical manual," Federal Aviation Administration, Washington, D.C., Tech. Rep. FAA-AEE-08-01, January 2008.

[16] W. E. Zorumski, "Aircraft noise prediction program theoretical manual," NASA Langley Research Center; Hampton, VA, United States, Tech. Rep. TM-83199, Parts 1 and 2, 1982.

[17] Sustainable Aviation, "Inter-dependencies between emissions of CO_2, NOx and noise from aviation," *Policy Discussion Paper*, September 2010.

[18] N. A. Cumpsty, *Jet Propulsion: A Simple Guide to the Aerodynamics and Thermodynamic Design and Performance of Jet Engines simple guide to the aerodynamics and thermodynamic design and performance of jet engines*, 2nd ed. Cambridge University Press, 2003.

[19] C. A. Hall and D. Crichton, "Engine and installation configurations for a silent aircraft," Cambridge-MIT Institute, Tech. Rep. ISABE-2005-1164, 2005.

[20] "Guidance on the balanced approach to aircraft noise management," International Civil Aviation Organization (ICAO), Tech. Rep. Doc 9829 AN/451, 2008.

[21] "The SA noise roadmap: A blueprint for managing noise from aviation sources to 2050," Sustainable Aviation, Tech. Rep., 2013.

[22] L. E. Kinsler, A. R. Frey, A. B. Coppens, and J. V. Sanders, *Fundamentals of acoustics*, 4th ed. John Wiley & Sons, 2000.

[23] D. A. Bies and C. H. Hansen, *Engineering noise control.* Spon Press, 2009.

[24] A. D. Pierce, *Acoustics: an Introduction to its Physical Principles and Applications.* American Institute of Physics, 1989.

[25] A. Filippone, *Advanced Aircraft Flight Performance.* Cambridge University Press, 2012.

[26] O. Zaporozhets, V. Tokarev, and K. Attenborough, *Aircraft Noise: Assessment, Prediction and Control.* Spon Press, 2011.

[27] M. J. T. Smith, *Aircraft noise.* Cambridge University Press, 1989.

[28] "An introduction to aircraft noise," ESDU, Tech. Rep. ESDU Data Item 02020, 2013.

[29] P. L. Chow, C. H. Liu, and L. Maestrello, "Scattering of coherent sound waves by atmospheric turbulence," in *2nd AIAA aeroacoustics conference.* American Institute of Aeronautics and Astronautics, 1976, pp. 51–66.

[30] "Standard values of atmospheric absorption as a function of temperature and humidity," SAE International, Tech. Rep. SAE ARP-866A, 1975.

[31] L. C. Sutherland, J. E. Piercy, H. E. Bass, and L. B. Evans, "Method for calculating the absorption of sound by the atmosphere," *The Journal of the Acoustical Society of America*, vol. S1, no. 56, 1974.

[32] "Report on standard method of computing noise contours around civil airports," European Civil Aviation Conference (ECAC), Tech. Rep. ECAC.CEAC Doc. 29, 4th ed., 2017. [Online]. Available: https://www.ecac-ceac.org/ecac-docs

[33] K. Jones and R. Cadoux, "Metrics for aircraft noise," Environmental Research and Consultancy Department (ERCD), U.K. Civil Aviation Authority, Tech. Rep. ERCD Report 0904, January 2009.

[34] J.-P. Clairbois and N. V. Oosten, "Airport noise management: Benchmarking of 12 international airports," in *Proceedings of the 45th International Congress and Exposition of Noise Control Engineering (INTER-NOISE)*, Hamburg, Germany, 21 - 24 August 2016.

[35] J. Ollerhead, "The CAA aircraft noise contour model: ANCON version 1," Civil Aviation Authority (CAA) / Department of Transport, Tech. Rep. DORA 9120, 1992.

[36] K. D. Kryter, "The meaning and measurement of perceived noise level," *Noise Control*, vol. 6, no. 5, pp. 12–27, 1960.

[37] *Rolls-Royce. The jet engine.* Rolls-Royce plc, 1996.

[38] Federal Aviation Administration, *Advisory Circular 36-4C: Noise Standards: Aircraft Type and Airworthiness Certification.* Federal Aviation Regulations, July 2003.

[39] Directorate of Operational Research and Analysis, “The noise and number index,” *Civil Aviation Authority DORA Communication 7907*, September 1981.

[40] “Good practice guide on noise exposure and potential health effects,” European Environment Agency (EEA), Tech. Rep. 11/2010, 2010.

[41] D. Southgate, R. Aked, N. Fisher, and G. Rhynehart, “Expanding ways to describe and assess aircraft noise,” *Department of Transport and Regional Services, Commonwealth of Australia*, 2000.

[42] J. Lee, G. Cebrian, L. Edmonds, J. Patel, and D. Rhodes, “Noise exposure contours for Heathrow airport 2015,” Environmental Research and Consultancy Department (ERCD), U.K. Civil Aviation Authority (CAA), Tech. Rep. ERCD 1601, 2017.

[43] NASA Facts, “Making future commercial aircraft quieter,” *NASA Glenn Research Center, Cleveland, OH, United States*, vol. 07, no. 003, 1999.

[44] Eurocontrol Experimental Centre, “Aircraft noise and performance (ANP) database v2.1,” 2016. [Online]. Available: http://www.aircraftnoisemodel.org

[45] “Procedure for the calculation of aircraft noise in the vicinity of airports,” SAE International, Tech. Rep. Aerospace Information Report - SAE AIR1845A, Issued 1986, Revised 2012.

[46] International Standards and Recommended Practices, *Annex 16 - Environmental Protection*. International Civil Aviation Organization (ICAO), 2008, vol. 1.

[47] Federal Aviation Administration (FAA), “Noise standards: Aircraft type and airworthiness certification, title 14, part 36 (FAR 36),” May 2017. [Online]. Available: http://www.ecfr.gov

[48] *ICAO Environmental Report 2016*. International Civil Aviation Organization (ICAO), 2016.

[49] M. J. T. Smith and S. White, “A practical method for estimating operational lateral noise levels,” Environmental Research and Consultancy Department (ERCD), U.K. Civil Aviation Authority, Tech. Rep. ERCD 0206, April 2003.

[50] “ICAO noise certification database,” 2016. [Online]. Available: http://noisedb.stac.aviation-civile.gouv.fr

[51] “EASA type certificates (TCDS),” 2017. [Online]. Available: https://www.easa.europa.eu/document-library/type-certificates

[52] M. J. Lighthill, “On sound generated aerodynamically. I. General theory,” *Proceedings of the Royal Society of London A: Mathematical, Physical and Engineering Sciences*, vol. 211, no. 1107, pp. 564–587, 1952. [Online]. Available: http://rspa.royalsocietypublishing.org/content/211/1107/564

[53] M. J. Fisher, P. A. Lush, and M. H. Bourne, "Jet noise," *Journal of Sound and Vibration*, vol. 28, no. 3, pp. 563–585, 1973.

[54] J. B. Freund, "Jet noise physics and modeling using first-principles simulations," NASA Glenn Research Center, Cleveland, OH, United States, Tech. Rep. NASA/CR-2003-212123, 2003.

[55] L. S. Hultgren and R. O. Arechiga, "Full-scale turbofan engine noise-source separation using a four-signal method," NASA Glenn Research Center, Cleveland, OH, United States, Tech. Rep. NASA/TM-2016-219419, 2016.

[56] M. Howe, "Indirect combustion noise," *Journal of Fluid Mechanics*, vol. 659, pp. 267–288, 2010.

[57] A. P. Dowling and Y. Mahmoudi, "Combustion noise," *Proceedings of the Combustion Institute*, 2015. [Online]. Available: http://www.sciencedirect.com/science/article/pii/S1540748914004003

[58] S. Yifeng, Y. Yi, B. Cyrille, and L. Qiang, "An investigation on screeching noise in the cockpit of a commercial aircraft," in *Proceedings of the 23rd International Congress on Sound and Vibration (ICSV)*, Athens, Greece, 10 - 14 July 2016.

[59] J. Humphreys, William M., M. R. Khorrami, D. P. Lockhard, D. H. Neuhart, and C. J. Bahr, "Characterization of flap edge noise radiation from a high-fidelity airframe model," in *AIAA Aviation 2015*, Dallas, TX, United States, 22-26 June 2015.

[60] Airbus, "Getting to grips with aircraft noise," Flight Operations Support and Line Assistance, Tech. Rep., 2003.

[61] K. Hünecke, *Jet engines : fundamentals of theory, design, and operation.* Motorbooks International, 1997.

[62] H. I. H. Saravanamuttoo, *Gas Turbine Theory*, 6th ed. Pearson Education, 2009.

[63] W. R. Graham, C. A. Hall, and M. Vera Morales, "The potential of future aircraft technology for noise and pollutant emissions reduction," *Transport Policy*, vol. 34, no. Supplement C, pp. 36–51, 2014.

[64] W. Dobrzynski, R. Ewert, M. Pott-Pollenske, M. Herr, and J. Delfs, "Research at DLR towards airframe noise prediction and reduction," *Aerospace Science and Technology*, vol. 12, no. 1, pp. 80–90, January 2008.

[65] H. A. Kumasaka, M. M. Martinez, and D. S. Weir, "Definition of 1992 technology aircraft noise levels and the methodology for assessing airplane noise impact of component noise reduction concepts," NASA Langley Research Center; Hampton, VA United States, Hampton, Virginia, Tech. Rep. CR-198298, June 1996.

[66] A. Filippone, “Aircraft noise prediction.” *Progress in Aerospace Sciences*, vol. 68, pp. 27–63, July 2014.

[67] D. Lyubimov, V. Maslov, A. Mironov, A. Secundov, and D. Zakharov, “Experimental and numerical investigation of jet flap interaction effects,” *International Journal of Aeroacoustics*, vol. 13, no. 3-4, pp. 275–302, 2014.

[68] A. Filippone, “Analysis of carbon-dioxide emissions from transport aircraft,” *Journal of Aircraft*, vol. 45, no. 1, pp. 185–197, 2008.

[69] C. Eriksson, A. Hilding, A. Pyko, G. Bluhm, G. Pershagen, and C. Ostenson, “Long-term aircraft noise exposure and body mass index, waist circumference, and type 2 diabetes: A prospective study,” *Environmental Health Perspectives*, vol. 122, no. 7, pp. 687–694, July 2014.

[70] M. Klatte, J. Spilski, J. Mayerl, U. Moehler, T. Lachmann, and K. Bergstroem, “Effects of aircraft noise on reading and quality of life in primary school children in Germany: Results from the NORAH study,” *Environment and behavior*, vol. 49, no. 4, pp. 390–424, May 2017.

[71] C. N. Jardine, “Calculating the environmental impact of aviation emissions,” Environmental Change Institute, Oxford University Centre for the Environment, Tech. Rep., 2005.

[72] *Climate Impacts of Aviation’s Non-CO2 Emissions.* Sustainable Aviation, 2014.

[73] Federal Aviation Administration, “Aviation emissions, impacts & mitigation a primer,” FAA Office of Environment and Energy, Tech. Rep. 201501, January 2015.

[74] *ICAO Environmental Report 2007.* International Civil Aviation Organization (ICAO), 2007.

[75] R. Torres, J. Chaptal, C. Bes, and J. Hiriart-Urruty, “Optimal, environmentally friendly departure procedures for civil aircraft,” *Journal of Aircraft*, vol. 48, no. 1, pp. 11–22, January 2011.

[76] B. Daley, *Air transport and the environment.* Ashgate Pub. Co., 2010.

[77] International Standards and Recommended Practices, *Annex 16 - Environmental Protection.* International Civil Aviation Organization (ICAO), 2008, vol. 2.

[78] *Airport Air Quality Manual.* International Civil Aviation Organization (ICAO), 2011.

[79] European Aviation Safety Agency EASA, “ICAO Aircraft engine emissions databank,” 2014. [Online]. Available: http://easa.europa.eu/document-library/icao-aircraft-engine-emissions-databank

[80] E. T. Turgut and O. Usanmaz, “NOx, fuel consumption and time effects of flight path angle during descent,” *Journal of Aerospace Engineering*, vol. 225, no. 5, pp. 737–750, 2012.

[81] M. T. Timko, S. C. Herndon, E. C. Wood, T. B. Onasch, M. J. Northway, J. T. Jayne, M. R. Canagaratna, R. C. Miake-Lye, and W. B. Knighton, “Gas turbine engine emissions, Part I: Volatile organic compounds and nitrogen oxides,” *Journal of Engineering for Gas Turbines and Power*, vol. 132, no. 6, 2010.

[82] K. Schäfer, C. Jahn, P. Sturm, B. Lechner, and M. Bacher, “Aircraft emission measurements by remote sensing methodologies at airports,” *Atmospheric Environment*, vol. 37, no. 37, pp. 5261 – 5271, 2003.

[83] A. H. Lefebvre, *GAS Turbine Combustion.* CRC Press, 2nd ed., 1998.

[84] J. Watterson, C. Walker, and S. Eggleston, *Revision to the Method of Estimating Emissions from Aircraft in the UK Greenhouse Gas Inventory.* Global Atmosphere Division, DEFRA, 2004.

[85] N. van Oosten, *ICAO Carbon Emissions Calculator V.7 Methodology*, International Civil Aviation Organization (ICAO), June 2014.

[86] *ICAO Environmental Report 2010.* International Civil Aviation Organization (ICAO), 2010.

[87] “BADA (base of aircraft data),” 2011. [Online]. Available: http://www.eurocontrol.int/eec/public/standard_page/proj_BADA.html

[88] *Scheduled Civil Aircraft Emission Inventories for 1999: Database Development and Analysis.* NASA, 2001.

[89] B. Kim, B. Manning, B. Sharp, J.-P. Clarke, I. Robeson, and J. Brooks, “Environmental optimization of aircraft departures: Fuel burn, emissions, and noise,” Airport Cooperative Research Program (ACRP), Tech. Rep. ACRP 86, 2013.

[90] ICAO, “Aircraft operations, vol. 1, flight procedures,” International Civil Aviation Organization (ICAO), Tech. Rep. Doc 8168 OPS/611, 2006.

[91] J. R. Stone and E. A. Krejsa, “Initial noise assessment of an embedded-wing-propulsion concept vehicle,” NASA Glenn Research Center, Cleveland, OH, United States, Tech. Rep. NASA/CR—2008-215140, 2008.

[92] M. Givoni and P. Rietveld, “Airline’s choice of aircraft size - explanations and implications,” *Transportation Research Part A: Policy and Practice*, vol. 43, 2009.

[93] W. Wei and M. Hansen, “Cost economics of aircraft size,” *Journal of Transport Economics and Policy*, vol. 37, no. 2, pp. 279–296, May 2003.

[94] *ICAO Environmental Report 2013.* International Civil Aviation Organization (ICAO), 2013.

[95] "Aircraft characteristics database," Federal Aviation Administration (FAA), April 2016. [Online]. Available: http://www.faa.gov/airports/engineering/aircraft_char_database/

[96] "Aircraft type designators," International Civil Aviation Organization (ICAO), Tech. Rep. Doc 8643, 2009.

[97] *Mandatory Requirements for Airworthiness.* Civil Aviation Authority CAP 747, November 2014.

[98] L. Jenkinson, P. Simpkin, and D. Rhodes, *Civil Jet Aircraft Design.* Arnold, 1999.

[99] "Specific thrust," May 2015. [Online]. Available: https://www.grc.nasa.gov/www/K-12/airplane/specth.html

[100] "Gas turbine coaxial exhaust flow noise prediction," SAE International, Tech. Rep. SAE AIR 1905A, 2012.

[101] J. L. Felder, H. D. Kim, and G. V. Brown, "Turboelectric distributed propulsion engine cycle analysis for hybrid-wing-body aircraft," in *47th AIAA Aerospace Sciences Meeting including The New Horizons Forum and Aerospace Exposition*, no. AIAA Paper 2009-1132, Orlando, Florida, 5-8 January 2009.

[102] D. Philpott and R. Barnard, *Aircraft Flight: A description of the physical principles of aircraft flight*, 4th ed. Pearson, 2010.

[103] "Aerodynamics index," May 2015. [Online]. Available: https://www.grc.nasa.gov/www/k-12/airplane/short.html

[104] "Report on standard method of computing noise contours around civil airports, vol. 2: Technical guide," European Civil Aviation Conference (ECAC), Tech. Rep. ECAC.CEAC Doc. 29, 3rd ed., December 2005.

[105] M. D. Dahl, "Overview of aircraft noise prediction tools assessment," in *Presentation for the NASA Supersonic and Subsonic Fixed Wing Technical Working Group Meeting*, 4-5 December 2007.

[106] N. van Oosten, *Users manual of Soprano aircraft noise prediction code, Volume I*, version 3 ed., Silence(r) Consortium, March 2006.

[107] *Recommended Method for Computing Noise Contours Around Airports.* International Civil Aviation Organization (ICAO), 2008.

[108] M. Monsrud, *Airplane Noise.* Boeing Flight Operations Engineering, 2009.

[109] J. Page, K. R. Bassarab, C. M. Hobbs, D. H. Robinson, T. D. Schultz, B. H. Sharp, S. M. Usdrowski, I. Wyle Laboratories, and V. Arlington, "Enhanced modeling of aircraft taxiway noise," Airport Cooperative Research Program (ACRP), Tech. Rep. ACRP Project 11-02 Task 08, 2009.

[110] S. Cooper, "INM getting it to work acoustically," in *20th International Congress on Acoustics 2010, ICA 2010 - Incorporating Proceedings of the 2010 Annual Conference of the Australian Acoustical Society*, vol. 3, Sydney, Australia, 23-27 August 2010, pp. 1871–1877.

[111] S. Cooper and J. Maung, "Problems with the INM: Parts 1, 2, 3," in *Proceedings of the 1st Australasian Acoustical Societies' Conference 2006, ACOUSTICS 2006: Noise of Progress*, Christchurch, New Zealand, 20-22 November 2006, pp. 99–104.

[112] J. B. Ollerhead, D. P. Rhodes, M. S. Viinikainen, D. Monkman, and A. C. Woodley, "The UK civil aircraft noise contour model ANCON: Improvements in version 2," Environmental Research and Consultancy Department (ERCD), Civil Aviation Authority (CAA), Tech. Rep. 9842, June 1999.

[113] Brüel & Kjær, "ANOMS - Airport noise monitoring and management system." 2017. [Online]. Available: https://www.bksv.com/en/products/environment-management/airport-environment-monitoring/ANOMS

[114] J. Ollerhead, "Flula - swiss aircraft noise prediction program," in *Annual Conference of the Australian Acoustical Society*, Adelaide, Australia, 13-15 November 2002.

[115] A. J. Torija, R. H. Self, and I. H. Flindell, "A model for the rapid assessment of the impact of aviation noise near airports," *The Journal of the Acoustical Society of America*, vol. 141, no. 2, pp. 981–995, 2017.

[116] J. R. Stone and F. J. Montegani, "An improved prediction method for the noise generated in flight by circular jets," NASA, Tech. Rep. TM-81470, 1980.

[117] M. F. Heidmann, "Interim prediction method for fan and compressor source noise," NASA Lewis Research Center, Cleveland, OH, United States, Tech. Rep. NASA-TM-X-71763, 1979.

[118] M. R. Fink, "Airframe noise prediction method," Federal Aviation Administration, Tech. Rep. FAA-RD-77-29, 1977.

[119] L. Lopes and C. Burley, "Design of the next generation aircraft noise prediction program: ANOPP2," in *17th AIAA/CEAS aeroacoustics conference*, no. AIAA 2011-2854, Portland, Oregon, 5-8 June 2011.

[120] L. V. Lopes and C. L. Burley, "ANOPP2 User's manual: Version 1.2," NASA Langley Research Center; Hampton, VA, United States, Tech. Rep. NASA/TM-2016-219342, 2016.

[121] S. A. Rizzi, A. R. Aumann, L. V. Lopes, and C. L. Burley, “Auralization of hybrid wing-body aircraft flyover noise from system noise predictions,” *Journal of Aircraft*, vol. 51, no. 6, pp. 1914–1926, November 2014.

[122] B. J. Clark, “Computer program to predict aircraft noise levels.” NASA Lewis Research Center; Cleveland, OH, United States, Tech. Rep. NASA-TP-1913, 1981.

[123] July 2014. [Online]. Available: http://www.xnoise.eu/about-x-noise/projects/generation-1-projects/silencer/

[124] A. Vazquez, L. Meliveo, and N. van Oosten, *Users manual Aircraft Noise Studio for Soprano V1.0*, Anotec Consulting, S.L., November 2011.

[125] A. Filippone, “Flight: Aircraft performance software,” August 2014. [Online]. Available: http://www.flight.mace.manchester.ac.uk/

[126] L. Bertsch, W. Dobrzynski, and S. Guérin, “Tool development for low-noise aircraft design,” *Journal of Aircraft*, vol. 47, no. 2, pp. 694–699, July 2010.

[127] J. A. Page, C. Wilmer, T. Schultz, K. J. Plotkin, and J. Czech, “Advanced acoustic model technical reference and user manual,” *SERDP Project WP-1304*, May 2009.

[128] J. R. Stone, D. E. Groesbeck, and C. L. Zola, “Conventional profile coaxial jet noise prediction,” *AIAA Journal*, vol. 21, no. 3, pp. 336–342, 1983.

[129] J. R. Stone, E. A. Krejsa, and B. J. Clark, “Jet noise modeling for supersonic business jet application,” NASA Glenn Research Center, Cleveland, OH, United States, Tech. Rep. CR-2004-212984, 2004.

[130] J. R. Stone, E. A. Krejsa, B. J. Clark, and J. J. Berton, “Jet noise modeling for suppressed and unsuppressed aircraft in simulated flight,” NASA Glenn Research Center, Cleveland, OH, United States, Tech. Rep. TM-215524, 2009.

[131] K. Zaman, J. Bridges, and D. Huff, “Evolution from ‘Tabs’ to ‘Chevron technology’ – a review,” in *Proceedings of the 13th Asian Congress of Fluid Mechanics*, Dhaka, Bangladesh, 17-21 December 2010.

[132] “Report by the second CAEP noise technology independent expert panel: Novel aircraft-noise technology review and medium- and long-term noise reduction goals,” International Civil Aviation Organization (ICAO), Tech. Rep. Doc 10017, 2014.

[133] K. B. Kontos, B. A. Janardan, and P. R. Gliebe, “Improved NASA-ANOPP noise prediction computer code for advanced subsonic propulsion systems,” NASA Lewis Research Center; Cleveland, OH United States, Tech. Rep. NASA Contractor Report 195480, 1996.

[134] J. W. Hough and D. S. Weir, “Aircraft noise prediction program (ANOPP) fan noise prediction for small engines,” NASA, Langley Research Center, Hampton, Virginia, Tech. Rep. NASA Contractor Report 198300, 1996.

[135] J. R. Stone and E. A. Krejsa, “Enhanced fan noise modeling for turbofan engine,” NASA, Cleveland, Ohio 44135, Tech. Rep. CR—2014-218421, 2014.

[136] “Aircraft noise series: Record of documents,” ESDU, Tech. Rep. ESDU Data Item 00010, 2016.

[137] “Prediction of noise generated by fans and compressors in turbojet and turbofan engines.” ESDU, Tech. Rep. ESDU Data Item 98008, 1998.

[138] “Airframe noise prediction,” ESDU, Tech. Rep. ESDU Data Item 90023, 2009.

[139] “ICAO Environmental toolkits,” July 2014. [Online]. Available: http://www.icao.int/environmental-protection/Pages/Tools.aspx

[140] “Emissions and dispersion modeling system (EDMS),” Federal Aviation Administration, August 2014. [Online]. Available: http://www.faa.gov/about/office_org/headquarters_offices/apl/research/models/edms_model/

[141] “Mobile6 vehicle emission modeling software,” 2015. [Online]. Available: http://www3.epa.gov/otaq/m6.htm

[142] “Advanced emission model (AEM),” Eurocontrol Experimental Centre, August 2014. [Online]. Available: https://www.eurocontrol.int/services/advanced-emission-model

[143] “ESDU aircraft performance series,” September 2015. [Online]. Available: https://www.esdu.com/

[144] “GasTurb - Gas turbine performance,” 2017. [Online]. Available: http://www.gasturb.de

[145] “Piano-x,” 2017. [Online]. Available: http://www.lissys.demon.co.uk/PianoX.html

[146] “Aircraft performance program APP,” 2016. [Online]. Available: http://aircraftperformance.software

[147] “Asimptote software GSP-DUT,” 2016. [Online]. Available: http://www.asimptote.nl/software/GSP-DUT

[148] “NASA EngineSim version 1.8a,” May 2015. [Online]. Available: https://www.grc.nasa.gov/WWW/k-12/airplane/ngnsim.html

[149] J. Koopmann, A. Hansen, S. Hwang, M. Ahearn, and G. Solman, "Aviation environmental design tool (AEDT) version 2c technical manual," Federal Aviation Administration (FAA), Tech. Rep. DOT-VNTSC-FAA-16-17, July 2016.

[150] "Managing aviation noise," Civil Aviation Authority (CAA), Tech. Rep. CAP 1165, 2014.

[151] U. Michel, "Noise reduction by aircraft innovations," in *Presentation at the symposium freight needs night*, Frankfurt Airport, 24 June 2010.

[152] H. D. Kim, J. L. Felder, M. T. Tong, J. J. Berton, and W. J. Haller, "Turboelectric distributed propulsion benefits on the N3-X vehicle," *Aircraft Engineering and Aerospace Technology: An International Journal*, 2014.

[153] E. M. Greitzer, P. A. Bonnefoy, E. DelaRosaBlanco, C. S. Dorbian, M. Drela, D. K. Hall, R. J. Hansman, J. I. Hileman, R. H. Liebeck, J. Levegren, P. Mody, J. A. Pertuze, S. Sato, Z. S. Spakovszky, C. S. Tan, J. S. Hollman, J. E. Duda, N. Fitzgerald, J. Houghton, J. L. Kerrebrock, G. F. Kiwada, D. Kordonowy, J. C. Parrish, J. Tylko, and E. A. Wen, "N+3 aircraft concept designs and trade studies. volume 1," NASA Glenn Research Center Cleveland, Ohio, Tech. Rep. NASA/CR-2010-216794/VOL1, E-17419-1, 2010.

[154] M. K. Bradley and C. K. Droney, "Subsonic ultra green aircraft research: Phase I final report," NASA, Tech. Rep. NASA/CR-2011-216847, 2011.

[155] U. Michel, "Correlation of aircraft certification noise levels epnl with controlling physical parameters," in *19th AIAA/CEAS Aeroacoustics Conference*, 2013.

[156] J. L. Kerrebrock, *Aircraft Engines and Gas Turbines, Second Edition.* The MIT Press, 1992.

[157] P. Hill and C. Peterson, *Mechanics and Thermodynamics of Propulsion (2nd Edition).* Prentice Hall, September 1991.

[158] W. Krebs and G. Thomann, "Aircraft noise: New aspects on lateral sound attenuation," *Acta Acustica united with Acustica*, 2009.

[159] J. W. Jewett and R. A. Serway, *Physics for scientists and engineers with modern physics*, 9th ed. Thomson Brooks/Cole, 2015.

[160] "Aircraft technical data and specifications," 2017. [Online]. Available: http://www.airliners.net/aircraft-data/

[161] "Category: Jet engine diagrams," August 2014. [Online]. Available: http://commons.wikimedia.org/wiki/Category:Jet_engine_diagrams

[162] "Aircraft propulsion system performance station designation and nomenclature," SAE International, Tech. Rep. Aerospace Recommended Practice - SAE ARP755C, June 2013.

[163] J. Mattingly, W. H. Heiser, and D. T. Pratt, *Aircraft Engine Design, Second Edition*. American Institute of Aeronautics and Astronautics (AIAA) Education Series, 2002.

[164] "The GE90 - An introduction," General Electric, Tech. Rep.

[165] V. Mollwitz and B. Korn, "Steep segmented approaches for active noise abatement - a flyability study," in *Proceedings of the 2014 Integrated Communications Navigation and Surveillance (ICNS) Conference, Herndon*, 2014.

[166] C. Brady, *The Boeing 737 Technical Guide*. Lulu.com, 2016.

[167] W. Freitag and T. Schulze, "Blended winglets improve performance," *Aero Magazine - Boeing Commercial Airplane Group*, no. 35, pp. 9,12, 2009. [Online]. Available: http://www.boeing.com/commercial/aeromagazine/articles/qtr_03_09/article_03_1.html

[168] "747-8 design highlights," November 2016. [Online]. Available: http://www.boeing.com/commercial/747/

[169] D. L. Huff, "Noise reduction technologies for turbofan engines," NASA, Cleveland, Ohio 44135, Tech. Rep. NASA-TM-214495, 2007.

[170] R. Thomas, M. Czech, and R. Elkoby, "Propulsion airframe aeroacoustic integration effects for a hybrid wing body aircraft configuration," in *16th AIAA/CEAS Aeroacoustics Conference*, no. AIAA Paper 2010-3912. American Institute of Aeronautics and Astronautics, 2010.

[171] M. D. Guynn, J. E. Freh, and E. D. Olson, "Evaluation of a hydrogen fuel cell powered blended-wing-body aircraft concept for reduced noise and emissions," NASA Langley Research Center; Hampton, VA, United States, Tech. Rep. NASA/TM-2004-212989, 2004.

[172] W. Neise and L. Enghardt, "Technology approach to aero engine noise reduction," *Aerospace Science and Technology*, vol. 7, no. 5, pp. 352 – 363, 2003.

[173] Y. Guo, C. L. Burley, and R. H. Thomas, "Modeling and prediction of krueger device noise," in *22nd AIAA/CEAS Aeroacoustics Conference*, no. AIAA Paper 2016-2957. American Institute of Aeronautics and Astronautics Inc, AIAA, 2016.

[174] Y. Guo, "A study on local flow variations for landing gear noise research," in *14th AIAA/CEAS Aeroacoustics Conference (29th AIAA Aeroacoustics Conference)*, no. AIAA Paper 2008-2915, 2008.

[175] K. Viswanathan and M. J. Czech, "Measurement and modeling of effect of forward flight on jet noise," *AIAA Journal*, vol. 49, no. 1, pp. 216–234, 2011.

[176] "Instrument procedures handbook," Federal Aviation Administration (FAA) Flight Standards Service, Tech. Rep. FAA-H-8083-16A, 2015.

[177] J. A. Zalovcik, "Effect of thrust and altitude in steep approaches on ground track noise," NASA, Washington, D.C., Tech. Rep. TN D-4241, 1967.

[178] J. A. Zalovcik and W. T. Schaefer, "NASA research on noise-abatement approach profiles for multiengine jet transport aircraft," NASA, Washington, D.C., Tech. Rep. TN D-4044, 1967.

[179] D. G. Denery, K. R. Bourquin, K. C. White, and F. J. Drinkwater, "Flight evaluation of three-dimensional area navigation for jet transport noise abatement," *Journal of Aircraft*, vol. 10, no. 4, pp. 226–231, 1973.

[180] *London City Airport Noise Action Plan 2013 - 2018.* London City Airport, 2014.

[181] A. Filippone, "Steep-descent maneuver of transport aircraft," *Journal of Aircraft*, vol. 44, no. 5, pp. 1727–1739, October 2007.

[182] H. Toebben, V. Mollwitz, L. Bertsch, R. M. Geister, B. Korn, and D. Kügler, "Flight testing of noise abating required navigation performance procedures and steep approaches," *Journal of Aerospace Engineering*, vol. 228, no. 9, pp. 1586–1597, August 2013.

[183] S. Bauer, "An aerodynamic assessment of micro-drag generators (MDGs)," in *Proceedings of the 16th AIAA Applied Aerodynamics Conference*, no. AIAA-98-2621, Albuquerque, NM, U.S.A, 1998.

[184] N. E. Antoine and I. M. Kroo, "Aircraft optimization for minimal environmental impact," *Journal of Aircraft*, vol. 41, no. 4, pp. 790–797, 2004.

[185] E. T. Turgut, O. Usanmaz, S. Kahvecioglu, and M. A. Rosen, "A preliminary study on relationship between flight path angle and NOx emissions during descent," *Chemical Engineering Transactions*, vol. 42, pp. 109–114, 2014.

[186] V. Mollwitz and B. Korn, "Flight testing steep segmented approaches for noise abatement," in *Proceedings of the 33rd IEEE/AIAA Digital Avionics Systems Conference (DASC)*, Colorado Springs, CO, USA, 5-9 October 2014.

[187] R. Koenig and R. G. Huemer, "Noise saving potential of future approach and departure procedures," in *Proceedings of the 24rth International Congress of the Aeronautical Sciences*, Yokohama, Japan, 29 August - 3 September 2004.

[188] H. Smith and J. Fielding, “New concepts for environmentally friendly aircraft,” in *Connect Research 2009*, OECD Conférence Centre, Paris, France, 12-13 November 2009.

[189] A. T. Isikveren, A. Seitz, J. Bijewitz, A. Mirzoyan, A. Isyanov, R. Grenon, O. Atinault, J.-L. Godard, and S. Stückl, “Distributed propulsion and ultra-high by-pass rotor study at aircraft level,” *The Aeronautical Journal*, vol. 119, no. 1221, pp. 1327–1376, 2015.

[190] M. Hornung, A. T. Isikveren, M. Cole, and A. Sizmann, “Ce-liner - case study for emobility in air transportation,” in *2013 Aviation Technology, Integration, and Operations Conference*, no. AIAA Paper 2013-4302, Los Angeles, CA, USA, 2013.

[191] H. D. Kim, “Distributed propulsion vehicles,” in *Proceedings of the 27th International Congress of the Aeronautical Sciences, 19-24 Sep. 2010, Nice; France.* NASA Glenn Research Center; Cleveland, OH, United States, 2010.

[192] “Aircraft propulsion,” in *Proceedings of conference on aircraft propulsion*, no. NASA-SP-259, NASA Lewis Research Center; Cleveland, OH, United States, January 01 1971.

[193] H. D. Kim, J. J. Berton, and S. M. Jones, “Low noise cruise efficient short take-off and landing transport vehicle study,” NASA Glenn Research Center Cleveland, Ohio, Tech. Rep. NASA/TM—2007-214659, 2007.

[194] H. Smith, “Airframe integration for an LH2 hybrid-electric propulsion system,” *Aircraft Engineering and Aerospace Technology*, vol. 86, no. 6, pp. 562–567, 2014.

[195] N. K. Borer, M. D. Patterson, J. K. Viken, M. D. Moore, J. Bevirt, A. M. Stoll, and A. R. Gibson, “Design and performance of the NASA SCEPTOR distributed electric propulsion flight demonstrator,” in *16th AIAA Aviation Technology, Integration, and Operations Conference*, no. AIAA 2016-3920, Washington, D.C, 13-17 June 2016.

[196] “E-thrust,” 2014. [Online]. Available: http://company.airbus.com/responsibility/airbus-e-fan-the-future-of-electric-aircraft/technology-tutorial/E-Thrust.html

[197] *Greener by Design Annual Report 2014-2015.* Royal Aeronautical Society, 2015.

[198] C. Pornet and A. Isikveren, “Conceptual design of hybrid-electric transport aircraft,” *Progress in Aerospace Sciences*, vol. 79, pp. 114 – 135, 2015.

[199] B. Schiltgen, M. Green, A. Gibson, D. Hall, D. Cummings, and C. Hange, “Benefits and concerns of hybrid electric distributed propulsion with conventional electric machines,” in *48th AIAA/ASME/SAE/ASEE Joint Propulsion Conference & Exhibit*, no. AIAA 2012-3769, Atlanta, Georgia, 30 July - 1 August 2012.

[200] *Sustainable Aviation, A decade of progress.* Sustainable Aviation, 2015.

[201] "Airbus media, Efan 1.0," February 2017. [Online]. Available: http://www.airbusgroup.com/int/en/news-media/media-search.html

[202] J. Welstead and J. L. Felder, "Conceptual design of a single-aisle turboelectric commercial transport with fuselage boundary layer ingestion," in *54th AIAA Aerospace Sciences Meeting*, no. AIAA 2016-1027, San Diego, California, USA, 4-8 January 2016.

[203] C. Liu, E. Valencia, and J. Teng, "Design point analysis of the turbofan-driven turboelectric distributed propulsion system with boundary layer ingestion," *Journal of Aerospace Engineering*, vol. 230, no. 6, pp. 1139–1149, September 2015.

[204] J. L. Felder, H. D. Kim, and G. V. Brown, "An examination of the effect of boundary layer ingestion on turboelectric distributed propulsion systems," in *Proceedings of the 49th Aerospace Sciences Meeting.* Orlando, FL, United States: NASA Glenn Research Center; Cleveland, OH, United States, 4-7 January 2011.

[205] A. Isikveren, A. Seitz, J. Bijewitz, M. Hornung, and A. Mirzoyan, "Recent advances in airframe-propulsion concepts with distributed propulsion," in *Proceedings of the 29th Congrees of the International Council of the Aerautical Sciences (ICAS 2014)*, St-Petersbourg, Russia, 7-12 September 2014.

[206] Clean Sky 2, "Bi-annual work plan and budget 2016-2017," Horizon 2020 EU Research and Innovation programme, Tech. Rep., 2016.

[207] A. Isikveren, S. Kaiser, C. Pornet, and P. Vratny, "Pre-design strategies and sizing techniques for dual-energy aircraft," *Aircraft Engineering and Aerospace Technology*, vol. 86, no. 6, pp. 525–542, 2014.

[208] D. L. Huff, B. S. Henderson, and E. Envia, "A first look at electric motor noise for future propulsion systems," NASA Glenn Research Center; Cleveland, OH, United States, Oral/Visual Presentation GRC-E-DAA-TN31506, April 2016.

[209] C. Liu, X. Si, J. Teng, and D. Ihiabe, "Method to explore the design space of a turbo-electric distributed propulsion system," *Journal of Aerospace Engineering*, vol. 29, no. 5, 2016.

[210] "Jet engine specification database," 2005. [Online]. Available: http://www.jet-engine.net

[211] I. Kroo and R. Shevell, *Aircraft Design: Synthesis and Analysis.* Desktop Aeronautics, Stanford (online version, available at: http://adg.stanford.edu/aa241/AircraftDesign.html), 2017.

[212] "Airworthiness standards: Transport category airplanes, federal aviation administration regulations, title 14, part 25 (far 25)," January 2017. [Online]. Available: http://www.ecfr.gov

[213] EASA, "Certification specifications and acceptable means of compliance for large aeroplanes CS-25, amendment 18," European Aviation Safety Agency, Tech. Rep., 2016.

[214] G. James, *Modern Engineering Mathematics, 5th Ed.* Pearson, 2015.

[215] Federal Aviation Administration, *Advisory Circular 25.1309-1A: System Design and Analysis.* Federal Aviation Regulations, July 1988.

[216] F. D. Gregorio, D. Steiling, E. Benini, and R. Ponza, "ERICA tiltrotor airframe wake characterization," in *Proceedings of the 41st European Rotorcraft Forum*, Munich, Germany, 1-4 September 2015.

[217] C. E. Jobe, "Prediction of aerodynamic drag," Flight Dynamics Laboratory, Air Force Wright Aeronautical Laboratories, Ohio, United States, Tech. Rep. AFWAL - TM-84-203, 1984.

[218] M. Sadraey, *Aircraft Performance: Analysis.* VDM Verlag Dr. Müller, 2011.

[219] "Fluid properties calculator," February 2017. [Online]. Available: http://www.mhtl.uwaterloo.ca/old/onlinetools/airprop/airprop.html

[220] H. Schlichting and K. Gersten, *Boundary-Layer Theory, 9th ed.* Springer, 2017.

[221] M. H. Waters and E. T. Schairer, "Analysis of turbofan propulsion system weight and dimensions," NASA Ames Research Center; Moffett Field, CA, United States, Tech. Rep. NASA-TM-X-73199, 1977.

[222] ICAO, "Agenda item 1: Civil aviation statistics — ICAO classification and definition. Available capacity and average passenger mass." in *10th Session of the statistics division*, no. STA/10-WP/5, Montréal, Canada, 23 - 27 November 2009.

[223] E. Torenbeek, "The initial calculation of range and mission fuel during conceptual design," Delft University of Technology, Faculty of Aerospace Engineering, Tech. Rep. LR-525, 1987.

[224] International Standards and Recommended Practices, *Annex 6 - Operation Of Aircraft.* International Civil Aviation Organization (ICAO), 2016.

[225] P. Lolis, P. Giannakakis, V. Sethi, A. J. B. Jackson, and P. Pilidis, "Evaluation of aero gas turbine preliminary weight estimation methods," *Aeronautical Journal*, vol. 118, no. 1204, pp. 625–641, June 2014.

[226] D. A. Sagerser, S. Lieblein, and R. P. Krebs, “Empirical expressions for estimating length and weight of axial-flow components of VTOL powerplants,” NASA Lewis Research Center, Cleveland, OH, United States, Tech. Rep. NASA-TM-X-2406, 1971.

[227] D. P. Raymer, *Aircraft Design a Conceptual Approach, 5th ed.* American Institute of Aeronautics & Astronautics (AIAA), 2012.

[228] J. L. Felder, “NASA N3-X with turboelectric distributed propulsion,” in *Presentation for the NASA Fixed Wing Project NASA Glenn Research Center*, Cleveland, Ohio, 2009.

[229] V. K. Mehta and R. Mehta, *Basic Electrical Engineering.* S. Chand & Co Ltd, 2017.

[230] R. H. Liebeck, “Design of the blended wing body subsonic transport,” *Journal of Aircraft*, vol. 41, no. 1, pp. 10–25, 2004.

[231] R. Thomas, C. Burley, and E. Olson, “Hybrid wing body aircraft system noise assessment with propulsion airframe aeroacoustic experiment,” in *16th AIAA/CEAS Aeroacoustics Conference*, no. AIAA Paper 2010-3913, Stockholm, Sweden, 7-9 June 2010.

[232] R. H. Thomas, Y. Guo, J. Berton, and H. Fernandez, “Aircraft noise reduction technology roadmap toward achieving the NASA 2035 goal,” in *23rd AIAA/CEAS Aeroacoustics Conference*, no. AIAA Paper 2017-3193, Denver, Colorado, 5-9 June 2017.

[233] A. Arntz and O. Atinault, “Exergy-based performance assessment of a blended wing–body with boundary-layer ingestion,” *AIAA Journal*, vol. 53, no. 12, pp. 3766–3776, 2015.

[234] C. L. Nickol and W. J. Haller, “Assessment of the performance potential of advanced subsonic transport concepts for NASA’s environmentally responsible aviation project,” in *54th AIAA Aerospace Sciences Meeting*, no. AIAA Paper 2016-1030, San Diego, California, USA, 4-8 January 2016.

[235] A. Plas, D. Crichton, M. Sargeant, T. Hynes, E. Greitzer, C. Hall, and V. Madani, “Performance of a boundary layer ingesting (BLI) propulsion system,” in *45th AIAA Aerospace Sciences Meeting and Exhibit*, Reno, Nevada, USA, 8-11 January 2007.

[236] S. A. Pandya, “The D8 aircraft: An aerodynamics study of boundary layer and wake ingestion benefit,” in *Case Studies in Aircraft Design*, Stanford University, CA, USA, 22 April 2015.

[237] "Optimal flow control design," NASA Technology Transfer Program, February 2017. [Online]. Available: https://technology.nasa.gov/patent/LAR-TOPS-105

[238] Y. Guo, C. L. Burley, and R. H. Thomas, "On noise assessment for blended wing body aircraft," in *52nd Aerospace Sciences Meeting, National Harbor, Maryland*, no. AIAA Paper 2014-0365. American Institute of Aeronautics and Astronautics, 2014.

[239] A. Manneville, D. Pilczer, and Z. Spakovszky, "Noise reduction assessments and preliminary design implications for a functionally-silent aircraft," in *10th AIAA/CEAS Aeroacoustics Conference*, no. AIAA Paper 2004-2925, 2004.

[240] R. H. Thomas and Y. Guo, "Ground noise contour prediction for a NASA hybrid wing body subsonic transport aircraft," in *23rd AIAA/CEAS Aeroacoustics Conference*, no. AIAA Paper 2017-3194, Denver, Colorado, USA, 5-9 June 2017.

[241] J. Bernardo, M. Kirby, and D. Mavris, "Development of a rapid fleet-level noise computation model," *Journal of Aircraft*, vol. 52, no. 3, pp. 721–733, 2016/11/04 2015.

[242] S. Pietrzko and R. Hofmann, "Mathematical modelling of aircraft noise based on identified directivity patterns," in *2nd AIAA/CEAS Aeroacoustics Conference*, no. AIAA Paper 1996-1768, State College, PA, USA, 6-8 May 1996.